Barrier Layer Capacitors Based on $CaCu_3Ti_4O_{12}$

Thesis

Timothy B. Adams

Submitted in partial fulfilment of the requirements
for the degree of Doctor of Philosophy

Thesis Supervisors:

Dr. Derek C. Sinclair
Prof. Anthony R. West

Department of Engineering Materials
University of Sheffield

October 2001 – September 2005

Acknowledgements

I wish to express a huge amount of thanks to my supervisors, Dr. Derek Sinclair and Prof. Tony West for their support and words of wisdom over the past 4 or so years.

I also owe a great debt of gratitude to my parents and my big brother, who all take part of the blame for everything.

Thanks to all my former colleagues in the CCL for their camaraderie, slanderous banter, and many entertaining nights out/in - are *you* still here?

Thanks also to Mr. Heather Bagshaw, Mr. Dion Haylock, Mr. Ian What's and Mr. Stuart "Ah, wonderful" Bater for their help with a multitude of technical things, Dr. Catherine Sheilds for assistance with SEM/EDS in Chapters 6/7, Dr. Denis Pasero for assistance with TGA in Chapter 4 and Dr. Nik Reeves for assistance with XRD in Chapter 4. Special thanks to Mr. Andrew "Mouldy" Mould for emergency overnight accommodation.

Whilst completing this thesis, I had already begun a research assistant position at Queen's University Belfast, and I'd like to thank Drs. Marty Gregg, Robert Bowman, Alina Schilling, Xinhua Zhu and the rest of the group for their on-going sympathy and tolerance.

It has recently come to my attention that since 1998 I have had the pleasure of sharing houses, beers, cars, trains, ships and tents with Mr. Robert Carroll, Mr. Kevin Mutter and Mr. Iain Maud.

Thanks to EPSRC for funding.

> “*Ah, what a wonderful experience it is to see one’s work in print for the first time. It was like cutting off one’s nose or moustache and mounting it on a little board for everyone to see.*”
>
> Gerard Hoffnung (1925-1959)

Abstract

$CaCu_3Ti_4O_{12}$ ceramics were prepared by solid state synthesis (solid state reaction of mixed oxides at 1000 °C, following by sintering at 1115 °C) and electrical properties measured by Impedance Spectroscopy. Initially, mixing and grinding of powders was performed using an agate mortar & pestle. The electrical microstructure of these ceramics could be modelled on an Internal Barrier Layer Capacitor (IBLC) model, consisting of semiconducting grains surrounded by thin, insulating grain boundary layer(s). The response could be interpreted in terms of an equivalent circuit of two parallel resistor-capacitor (*RC*) elements connected in series, with one *RC* element representing the bulk impedance and the other representing the grain boundary impedance. At room temperature, the grain boundary resistance, R_{gb}, was ~ 450 kΩ.cm and the grain boundary capacitance, C_{gb}, was ~ 2.2 nF/cm, corresponding to an effective permittivity, ε'_{eff} of ~ 24,850 (where $\varepsilon'_{eff} = C_{gb}/\varepsilon_0$ and ε_0 is the permittivity of free space). The bulk resistance, R_b, was 62 Ω.cm but the bulk capacitance, C_b, could not be measured at room temperature. Cooling the ceramic to 104 K allowed C_b to be measured as ~ 7 - 8 pF/cm, corresponding to a bulk permittivity for $CaCu_3Ti_4O_{12}$ of ~ 80 - 90.

Using planetary ball milling to mix and grind the reagents and reacted powder, and by extending the sintering time from 1 – 5 h up to 24 h, coarse-grained ceramics were obtained with grain sizes in excess of 100 μm and effective permittivity values of up to 300, 000, proving that the observed permittivity is in fact an effective permittivity arising from the grain boundary capacitance. Electron probe micro-analysis and scanning electron microscopy data demonstrated that $CaCu_3Ti_4O_{12}$ ceramics underwent partial decomposition during sintering and EPMA data showed the composition bulk phase was slightly Cu-deficient, with a stoichiometry of $Ca_{0.98}Cu_{2.92}Ti_{4.04}O_{12(+/-0.02)}$. Powder samples decomposed completely to $CaTiO_3$, TiO_2 and Cu (as shown by X-ray diffraction data) by heating to 800 °C in 5 % H_2 – 95 % Ar. By annealing in N_2 and O_2, it was possible to respectively decrease and increase R_{gb}. However, it was not possible to change R_b under such conditions.

Impedance measurements were performed with a dc bias, up to 15 V, on coarse-grained ceramics and the characteristics of the grain boundary impedance was found to correspond to a back-to-back Schottky barrier model with a potential barrier height, ϕ_b, of ~ 0.77 eV. Measurements were taken using InGa and Au electrodes and, in both cases, electrode contact phenomena did not contribute significantly to the electrical response. Fine-grained ceramics showed no such behaviour below 15 V dc bias.

The impedance of fine- and coarse-grained ceramics was also measured as a function of sample thickness. The impedance of fine-grained ceramics exhibited no significant dependence for thicknesses between ~ 2 mm and ~ 0.2 mm whereas the coarse-grained sample showed a noticeable, non-linear dependence in which R_{gb} decreased and C_{gb} increased with decreasing thickness. The behaviour of the coarse-grained ceramic was attributed to the grain size being comparable to the sample thickness and so the number of grain boundaries per unit volume changed significantly with changing sample thickness. Furthermore, the time constant, τ_{gb}, ($\tau = RC$) was also dependent on the thickness of coarse-grained ceramics, suggesting that the grain boundary impedance was affected by an inhomogeneous potential distribution resulting from a distribution of grain sizes, and/or grain boundary electrical properties, within the ceramic.

$CdCu_3Ti_4O_{12}$ and $Na_{1/2}Bi_{1/2}Cu_3Ti_4O_{12}$ ceramics were also prepared via solid state synthesis. These phases were isostructural with $CaCu_3Ti_4O_{12}$ and their respective electrical properties were also consistent with an IBLC-type model. The bulk permittivity of $CdCu_3Ti_4O_{12}$ and $Na_{1/2}Bi_{1/2}Cu_3Ti_4O_{12}$ were ~ 160 and ~ 330, respectively. These values are higher than expected for non-ferroelectric phases and understanding the origin of these permittivity values requires further investigation.

1. Introduction

1.1. Summary

Oxides with crystal structures based on perovskite (general formula ABO_3) are at the heart of various electronic devices from capacitors, positive temperature coefficient resistors, ionic conductors and infrared sensors to actuators, inductors and high temperature superconductors. Such varied properties arise from the ability of the perovskite structure to accept many combinations of ions and to undergo many subtle structural distortions.

The use of thin dielectric layers (usually based on $BaTiO_3$) in multi-layer capacitors forms the largest commercial application of perovskite-structured materials. Although this is a mature technology, the capacitor market is highly competitive and new $BaTiO_3$-based compositions and new materials are constantly being sought to meet the rising demands of consumers, particularly in the automotive industry.

Recently, a perovskite-related compound $CaCu_3Ti_4O_{12}$ was reported to have properties that were highly suited for use in capacitors, having higher overall permittivity and better temperature stability than many commercial compositions. The aim of this work was to characterise and optimise the electrical properties of $CaCu_3Ti_4O_{12}$ and related materials and to establish the origin(s) of their dielectric-type behaviour.

1.2. Structural Features of Perovskites

A large number of oxide and intermetallic phases exist with structures that are related to the high temperature cubic polymorph of the mineral Perovskite ($CaTiO_3$) and this section offers a review of important effects associated with perovskite-type structures.

1.2.1. The Ideal Perovskite Structure

In the generic case of ABX_3, the ideal perovskite cell is considered cubic with the A cations located in the 12-coordinate cube corners (the A-site), the B cation in the 6-coordinate cube centre (the B-site) and the X anions on the cube face centres (the X-site) as shown in Figure 1.1 (a). Since the B-site is octahedrally coordinated by the X-site, the ideal ABX_3 perovskite can be represented, as in Figure 1.1 (b), by a framework structure of corner-sharing BX_6 octahedra extending throughout the crystal with the *A* cations located in the interstices [1].

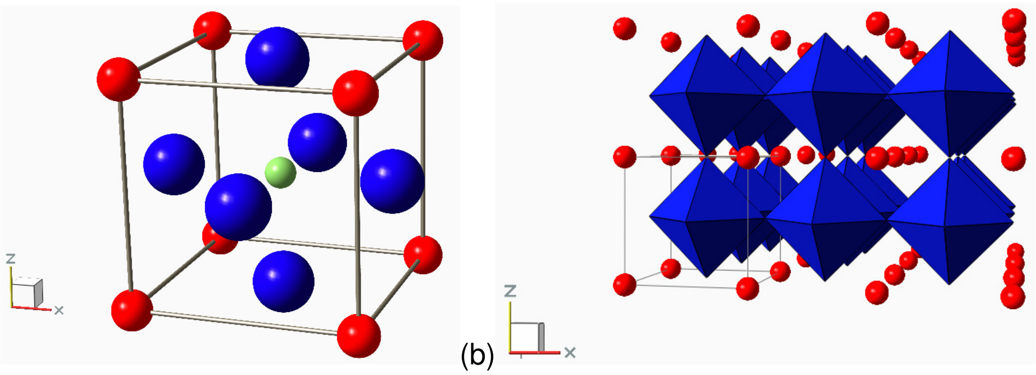

(a) (b)

Figure 1.1: (a) The unit cell of an ideal cubic perovskite, ABX_3 and (b) the framework representation of perovskite (Generated using Balls & Sticks software version 1.51, S.J. Kung, T.L. Ozawa, 2003).

1.2.2. Structural Distortions

The perovskite structure can accommodate many combinations of ions, primarily because it can distort by stretching and/or tilting of the BX_6 octahedra. An indication as to whether a particular perovskite phase is likely to be cubic, tilted or otherwise distorted is given by the tolerance factor, *t*, whereby:

$$t = \frac{\sqrt{2}r_{A-X}}{2r_{B-X}} \tag{1.1}$$

where $r_{A\text{-}X}$ and $r_{B\text{-}X}$ are the bond lengths from the *X* anions to *A* and *B* cations, respectively [1].

Perovskites with $t \sim 1$ tend to adopt the ideal cubic, centrosymmetric symmetry since the ionic radii of *A*, *B*, and *X* species are such that the free volume of the structure is minimised. A phase with $0.85 < t < 0.95$, however, is likely to have tilted octahedra in order to occupy the free space which would otherwise result from the *A* cation being too small with respect to the *B-X* bond distance. If $t > 1$ then the *B*-cation is too small to remain central in the BX_6 octahedra and is displaced from the centrosymmetric position. Alternatively, the *A*-cation may be considered too large with the same effect.

1.2.2.1. Octahedral Tilting

A schematic, 2D, representation of an octahedron tilted in a perovskite ‘cell’ is given in Figure 1.2 (a). Since the octahedra remain corner-sharing, the tilt imparts a periodicity in the lattice as shown in Figure 1.2 (b) and a refined unit cell is required to represent the corresponding change in symmetry.

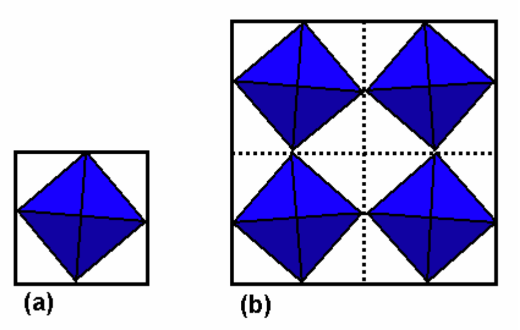

Figure 1.2: (a) Octahedron tilted within a cuboid and (b) subsequent lattice.

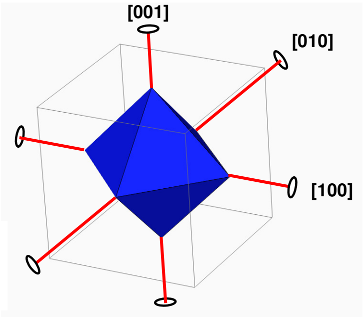

Figure 1.3: The tetrad axes about which an octahedron may tilt.

Any given tilt system can be categorised by Glazer’s notation [2] in which the tilt of the octahedron about each of the tetrad axes shown in Figure 1.3 is represented by a series of 6 symbols. In the notation, the tilt of each axis is represented by a letter *a*, *b* or *c* followed by a superscript 0, + or -, in the order [100], [010], [001]. The letters indicate which axes are equal in terms of their angle of tilt, for instance: *aaa* means all axes are of equal tilt, *aac* indicates that [100] and [010] are equal but [001] is not and *abc* means all axes have unequal tilts. The superscript symbols are defined as follows: ^{0} – no tilt about the axis, $^+$ - octahedra have the same tilt along the axis and $^-$ - octahedra have opposite tilts along the axis.

In all, there are 23 tilt systems as reported by Glazer, yet it was shown by Woodward [3] that several of these also require distortion of the octahedra. Howard [4] subsequently concluded that certain tilt systems indeed facilitated octahedral distortion, but only $a^+a^+c^-$ actually required distortion to maintain corner sharing between the octahedra.

1.2.2.2. Off-centre B-cation Displacement

The reason for off-centering of cations within a comparatively large environment can be found by considering the hypothetical case of a cation, *B*, located centrally between two anions, X_1 and X_2, separated by an ideal distance, *s*, as shown schematically in Figure 1.4 (a). The forces, F_1 and F_2, experienced by *B* are shown in Figure 1.4 (b) in which F_1 acts left to right when positive, whereas F_2 acts right to left when positive. At the central position between X_1 and X_2, forces F_1 and F_2 are of equal magnitude and *B* sits in the centre. If the separation distance, *s*, is increased, however, as in Figure 1.4 (c), *B* can no longer reside in the centre since, with reference to Figure 1.4 (d), there are now 3 positions in which F_1 and F_2 are of equal magnitude. Although both forces remain resolved in the centre, the positions *B'* and *B"* now provide two possible lower energy sites in which the *B* cation can reside [5]. Hence the *B* cation adopts either the *B'* or *B"* positions at random.

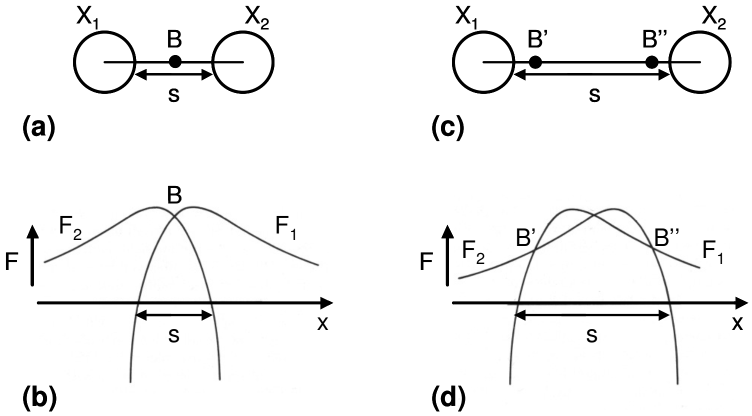

Figure 1.4: (a) Cation *B* centrally located between anions X_1 and X_2, (b) forces F_1 and F_2 experienced by *B*, (c) X_1 and X_2 separated by a greater distance with *B* located in one of the off-centre positions, *B'* and *B"*, (d) forces F_1 and F_2 experienced by *B*. Adapted from Megaw [5].

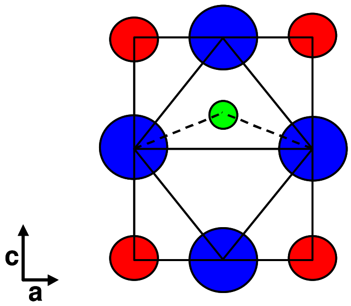

Figure 1.5: Off-centre displacement of *B* cation within a tetragonal *ABX*$_3$ perovskite where red, green and blue represent the *A*, *B* and *X* ions, respectively.

A similar effect occurs in the BX_6 octahedra of a perovskite with $t > 1$ and, since the *B* cation is located between 6 anions, it can move off-centre in any of the six directions towards one of the anions. In response, the octahedra (and hence unit cell) elongate along the axis in which the *B* cation has displaced and hence adopts a lower symmetry, as shown in Figure 1.5 where a tetragonal distortion is represented. Furthermore, the charge distribution within the unit cell is no longer centrosymmetric and a dipole moment occurs across the unit cell; this phenomenon is termed spontaneous polarisation [1].

1.2.2.3. Jahn-Teller Distortions

For an octahedrally coordinated cation, the energy level associated with the *d*-shell electron orbital is split between a higher and lower energy state, e_g and t_{2g}, respectively, as shown in Figure 1.6 (a) for a fully occupied d^{10} configuration. The e_g level consists of the axial d_{x2-y2} and d_{z2} orbitals, represented schematically in Figure 1.6 (b), and the t_{2g} level consists of the inter-axial d_{xy}, d_{yz} and d_{zx} orbitals. In this case, the octahedron remains undistorted.

For a cation with a d^9 configuration, e.*g*. Cu^{2+}, either the d_{z2} or d_{x2-y2} will be singly occupied since they are degenerate (*i.e*. of the same energy), resulting in a deficiency of electron density along the *z*-axis or *x*- and *y*-axes, respectively, in comparison with a d^{10} configuration. The net result of a singly occupied d_{z2} orbital is shortening of the 2 bonds along the *z*-axis while that of a single occupied d_{x2-y2} orbital results in shortening of the 4 bonds on the *xy* plane. In either case, the singly occupied orbital is now of higher energy than the doubly occupied orbital and so the e_g orbitals are no longer degenerate. This, and any other structural distortion that arises from the need to remove orbital degeneracy, is known as Jahn-Teller distortion [6, 7].

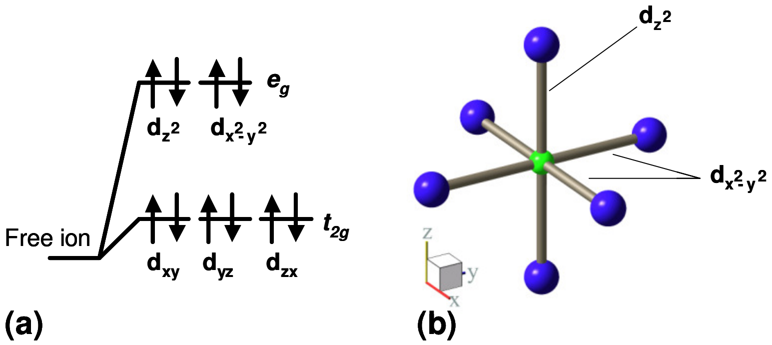

Figure 1.6: (a) energy levels of fully occupied *d*-shell and (b) the corresponding octahedrally coordinated cation.

The presence of Jahn-Teller active ions in perovskites has a significant impact on the structure [8]. $KCuF_3$, for instance, has a tolerance factor of ~ 1.11 and so it can be inferred that the Cu^{2+} ion is too small with respect to the K and F ions to allow such a phase to be stable without significant elongation of the CuF_6 octahedron. Cu^{2+} is Jahn-Teller active, however, and the resultant contraction of the axial Cu-F bonds facilitates the formation of an orthorhombic unit cell with tilted CuF_6 octahedra.

1.2.3. Phase Transitions in Perovskites

The structure of any given crystalline phase may change in response to changes in temperature or pressure. In general, when a phase undergoes several polymorphic phase transitions, the symmetry of a given polymorph decreases with decreasing temperature via a sequence of phase transitions, and may decrease further with increasing pressure. Such phase transitions fall into two categories: reconstructive and displacive. Reconstructive phase transitions involve the extensive breaking of interatomic bonds, leading to a partial collapse of the structure into smaller units; these units are subsequently rearranged and new interatomic bonds formed [5].

By contrast, displacive transitions involve little or no bond breaking and the atoms move by only a fraction of an angstrom from their position prior to undergoing a phase transition, as shown schematically in Figure 1.7 (a), in which the squares rotate to move the atoms from their initial positions at (i) to their new positions in (ii). In the course of the transition, atoms occupying the corner-sites of the square polyhedra in (i) oscillate co-operatively about the centre of their respective polyhedra. For this environment, the corner-occupying atoms oscillate within a double minimum potential well, Figure 1.7 (b) (i). As temperature increases from T_1 to T_3, both the amplitude and anharmonicity of the oscillation increase until, at T_3, the potential energy almost exceeds the potential maximum, M.

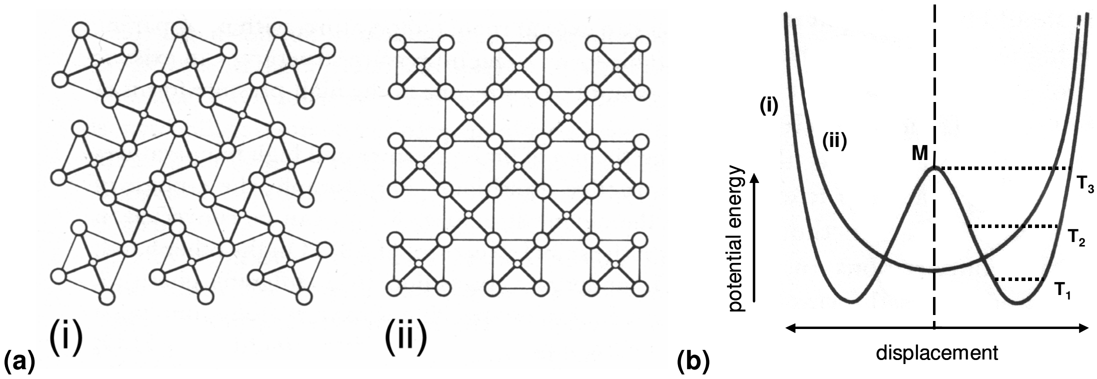

Figure 1.7: (a) Schematic example of a displacive phase transition and (b) change of potential energy curve for displacive phase transition. Adapted from Megaw [5].

If the temperature is increased still further so that the potential energy exceeds M, the amplitude would almost double and, provided the frequency remained constant, a sudden increase in the energy of vibration would occur. This is prevented by transferring the energy into another vibrational mode, such as expansion-compression of the square, and hence the potential energy well changes shape, losing its double minima, as shown in Figure 1.7 (b) (ii). The corner-occupying atoms now vibrate within the new potential well, corresponding to the new positions in Figure 1.7 (a) (ii).

Displacive phase transitions are more common than reconstructive transitions with many perovskites exhibiting transitions from a low symmetry phase at low temperature to the high symmetry cubic aristotype at high temperature. For perovskites with $t < 1$, the transitions involve changes in the octahedral tilt that may, in the special cases described by Woodward [3], also result in distortion of the octahedra. Those perovskites with $t > 1$ experience changes in unit cell dimensions associated with the magnitude and direction of the displacement of the B cation from the central position within the octahedron.

1.2.4. Examples of Perovskites

Selected perovskites are listed in Table 1.1 together with their corresponding tolerance factors and polymorphic phase transition sequences.

Formula	t	Polymorphic phase transition sequence	Ref
$SrTiO_3$	1.00	Tetragonal (*I*4/*mcm*) → 110 K → Cubic (*Pm*-3*m*)	[9-11]
$LaNiO_3$	1.00	Cubic (*Pm*-3*m*)	[12]
$BaTiO_3$	1.06	Rhombohedral (*R*3*m*) → 183 K → Orthorhombic (*Amm*2) → 278 K → Tetragonal (*P*4/*mmm*) → 393 K → Cubic (*Pm*-3*m*)	[13]
$PbTiO_3$	1.02	Tetragonal (*P*4/*mmm*) → 763 K → Cubic (*Pm*-3*m*)	[14]
$CaTiO_3$	0.97	Orthorhombic (*Pbnm*) → 1380 K → Orthorhombic (*Cmcm*) → 1500 K → Tetragonal (*I*4/*mcm*) → 1580 K → Cubic (*Pm*-3*m*)	[15]
$SrZrO_3$	0.96	Orthorhombic (*Pbnm*) → 1020 K → Psedo-tetragonal (*Imma*) → 1110 K → Tetragonal (*I*4/*mcm*) → 1340 K → Cubic (*Pm*-3*m*)	[16, 17]

Table 1.1: Examples of perovskites, their respective tolerance factors and polymorphic phase transitions sequences; tolerance factors were calculated using ionic radii reported by Shannon[18].

$SrTiO_3$ has a tolerance factor of 1.00 and is often thought of as an ideal, cubic perovskite with no polymorphism [1]. It was shown by Lytle [19], however, that slight deviations from cubic symmetry occur upon cooling to ~ 110 K where the unit cell becomes tetragonal with a *c/a* ratio of 1.00056. At 65 K, an orthorhombic cell is adopted with an *a*:*b*:*c* ratio of 0.9998:1:1.0002 and below 10 K, Lytle speculates as to the possibility of a rhombohedral distortion. Shirane and Yamada [9] refined the tetragonal polymorph in *I*4*/mcm* space group symmetry, in which the octahedra are tilted $a^0a^0c^-$, as opposed to being elongated. In contrast, $LaNiO_3$ is more typical of an ideal perovskite with no reported deviations from cubic symmetry [12].

$BaTiO_3$, however, has several distinct polymorphs involving small deviations from cubic symmetry with no tilting of the TiO_6 octahedra [13]; $t > 1$ in this case, so tilting is not expected. Above 1730 K, $BaTiO_3$ undergoes a reconstructive phase transition to an hexagonal polymorph and cooling from below 1730 K reveals 3 displacive phase transitions from: cubic to tetragonal (*c/a* = 1.0100) at 383 K, tetragonal to orthorhombic (*a:b:c* = 0.7026:1:1.0026) at 278 K and finally orthorhombic to rhombohedral at 183 K.

In all but the cubic phase, the Ti cation is displaced from the centrosymmetric position in the TiO_6 octahedral network. There are eight possible directions of displacement corresponding to the eight faces of the octahedron. It is believed that, in rhombohedral and orthorhombic $BaTiO_3$, displacement occurs along the [111] and [011] directions, respectively. Displacement in tetragonal $BaTiO_3$ occurs in the [001] direction whereas, for cubic $BaTiO_3$, displacement is possible in all eight directions since the cubic symmetry implies that no particular direction is energetically preferable.

Having a tolerance factor of 1.03, $PbTiO_3$ exhibits a single phase transition at 763 K from the low temperature tetragonal phase, in which *c/a* ~ 1.06 at room temperature, to the high temperature cubic phase [14]. In both tetragonal $BaTiO_3$ and tetragonal $PbTiO_3$, the off-centering of the Ti cations in the [001] direction and corresponding large *c/a* ratios play an important role in the electrical properties of these compounds, as discussed later.

$CaTiO_3$ has a tolerance factor of 0.97 and has a number of tilt systems that operate throughout, potentially, three displacive phase transitions [15]. Above 1580 K, the octahedra are not tilted and the symmetry corresponds to that of the ideal cubic perovskite with space group *Pm*3-*m*. On cooling below 1580 K a transition to the tetragonal *I*4/*mcm* polymorph occurs, corresponding to an $a^0a^0c^-$ tilt. The octahedra are now distorted such that the axial Ti-O bonds are shorter than the equatorial Ti-O bonds. Below 1500 K, $CaTiO_3$ is orthorhombic but the precise structure above 1380 K is uncertain since, according to Kennedy *et al* [15], diffraction data can be refined in both *Pbnm* and *Cmcm* symmetries. Evidence for the existence of the *Cmcm* polymorph is circumstantial, arising from anomalies in specific heat capacity at ~ 1380 K and ~ 1500 K. Below 1500 K, and assuming the *Cmcm* polymorph is adopted, the octahedra are no longer distorted and are tilted $a^0b^-c^+$. Upon reaching 1380 K a transition to the low temperature *Pbnm* polymorph occurs in which the octahedra are tilted $a^-a^-c^+$.

Similarly, $SrZrO_3$ exhibits a sequence of displacive phase transitions based on changes in tilt systems [16]. As with $CaTiO_3$, the first transition involves distortion from a cubic to tetragonal (*I*4/*mcm*) unit cell associated with the onset of an $a^0a^0c^-$ tilt at 1340 K and subsequent elongation of the octahedra along the *c* axis. Below 1110 K, $SrZrO_3$ is reportedly tetragonal, although experimental data could only be refined in the orthorhombic space group *Imma* with tetragonal unit cell parameters, and so the assignment of this phase transition to tetragonal-tetragonal or tetragonal-orthorhombic symmetry is somewhat ambiguous [17]. Below 1020 K, the low temperature orthorhombic phase, corresponding to *Pbnm* and tilt system $a^-a^-c^+$, is reached.

1.2.5. Complex Perovskites

Perovskites with two cations of different valence occupying the *B*-site in an ordered manner are considered complex perovskites. In general, they fall into 2 categories based on the ratio of *B*-site cations, namely ½:½ with general formula $A_2B'B''O_6$ and 1/3:2/3 with general formula $A_3B'B''_2O_9$. The *B'* and *B"* cations, in both ½:½ and

1/3:2/3 perovskites, are ordered primarily because of charge difference between the *B'* and *B''* cations, giving rise to supercell formation. As for simple perovskites, complex perovskites may be of lower symmetry than the ideal supercell. For instance, the octahedra may tilt or distort if the tolerance factor, based on the average radius of the *B*-site cations, is < 1 or > 1, respectively. Tilting may also arise in complex perovskites if there is a substantial difference in the *B'* and *B''* radii, or if one of the *B*-cations is Jahn-Teller active.

1.2.5.1. $A_2B'B''O_6$ Perovskites

The supercell of a $A_2B'B''O_6$ compound consists of a simple perovskite cell doubled along all three axes with the *B'* and *B''* cations occupying alternate {111} planes, the symmetry of which is represented by the *Fm*3-*m* space group. Alternatively, the overall structure can be regarded as a rocksalt-structured array of $B'O_6$ and $B''O_6$ octahedra with *A* cations situated in the interstices between the octahedra, as shown in Figure 1.8.

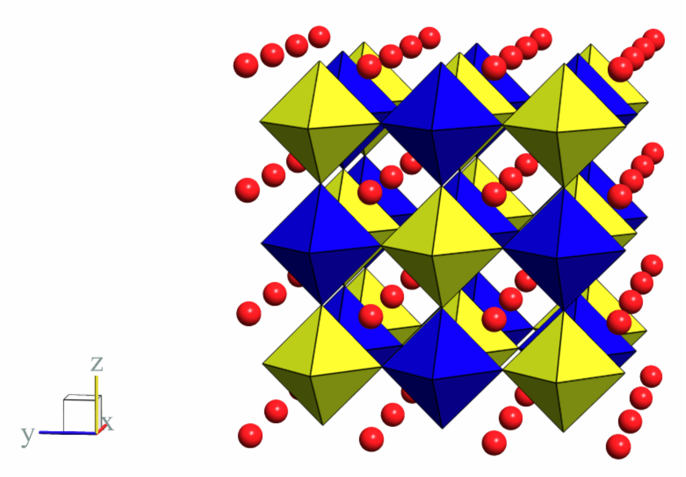

Figure 1.8: Schematic representation of an $A_2B'B''O_6$ perovskite structure. *A* cations are red spheres while the $B'O_6$ and $B''O_6$ environments are represented by yellow and blue octahedra, respectively (Balls & Sticks version 1.51, S.J. Kung, T.L. Ozawa, 2003).

A common example of an $A_2B'B''O_6$ perovskite is Pb_2ScTaO_6 [20]. The structure of Pb_2ScTaO_6 above 295 K corresponds to that shown in Figure 1.8, in which the unit cell is cubic and the symmetry represented by *Fm*3-*m*. Below 295 K, however, a rhombohedral distortion to *R*3 space group symmetry occurs in which the Sc^{3+} and Ta^{5+}

ions are displaced off-centre in the [111] direction, analogous to the off-centering of Ti^{4+} in rhombohedral $BaTiO_3$.

1.2.5.2. $A_3B'B''_2O_9$ Perovskites

Ideally, $A_3B'B''_2O_9$ compounds adopt the trigonal unit cell shown in Figure 1.9, with the *A*-site located on the cell corners and at positions 1/3,2/3,2/3 and 2/3,2/3,1/3 along the *x*,*y* and *z* axis, respectively. The $B'O_6$ and $B''O_6$ octahedra are stacked in a 1:2 ratio along the *z*-axis. $Ba_3SrTa_2O_9$ was the first compound to be refined with this structure [21].

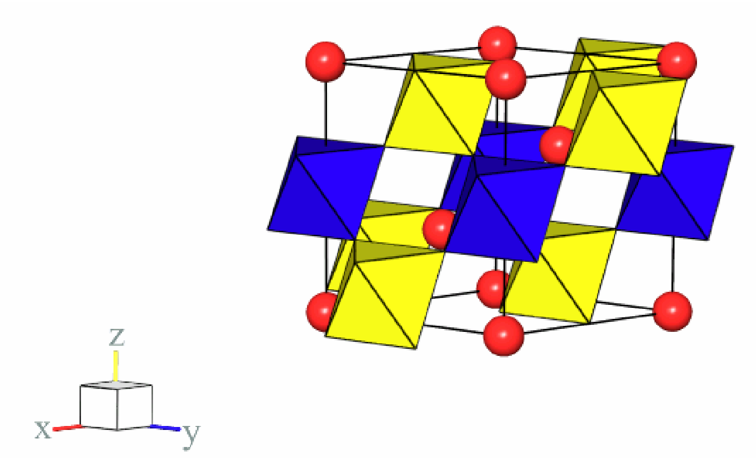

Figure 1.9: Schematic representation of an $A_3B'B''_2O_9$ perovskite. A cations are red spheres while the $B'O_6$ and $B''O_6$ environments are represented by yellow and blue octahedra, respectively (Balls & Sticks version 1.51, S.J. Kung, T.L. Ozawa, 2003).

1.2.5.3. $ACu_3B_4O_{12}$ Perovskites

The first $ACu_3B_4O_{12}$ perovskite to be discovered was $CaCu_3Ti_4O_{12}$, in which Ca^{2+} and Cu^{2+} ions share the *A*-site in a 1:3 ratio [22]. *A*-site occupancy is highly ordered and no structural phase transitions have been observed from 10 K to 1273 K [23-25]. Having a d^9 configuration, Cu^{2+} is Jahn-Teller active and, combined with the *A*-site ordering and size difference between Ca^{2+} and Cu^{2+}, the unit cell is doubled in all three directions and the octahedra are heavily tilted in an $a^+a^+a^+$ formation with the result that the unit cell symmetry is described by the $Im3$ space group. The environment of the Ca^{2+} ion is now slightly distorted from the 12-coordinate site and the Cu^{2+} ion now occupies a site that closely resembles square-planar coordination, as shown in Figure 1.10.

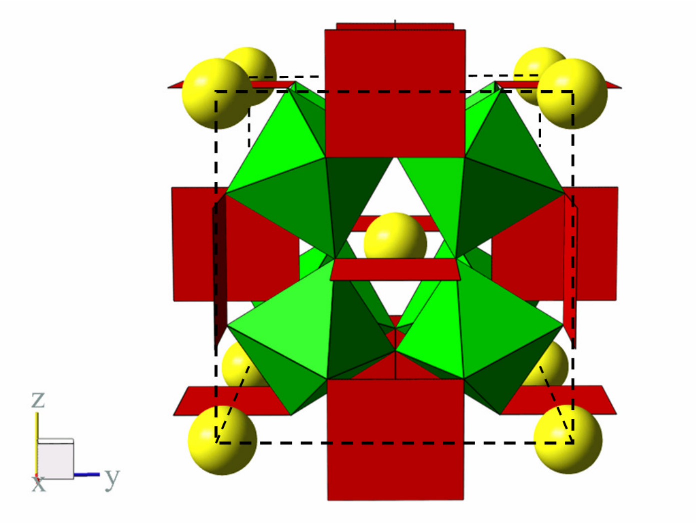

Figure 1.10: Unit cell of $CaCu_3Ti_4O_{12}$. The green octahedra represent the TiO_6 polyhedra, inside which the Ti^{4+} ion is located centrally. The red squares represent the pseudo-square-planar CuO_4 environment and yellow spheres represent the Ca^{2+} ions (Balls & Sticks version 1.51, S.J. Kung, T.L. Ozawa, 2003).

An increasing number of phases with structures analogous to $CaCu_3Ti_4O_{12}$ are known to exist. Those reported on the International Chemical Services Database are listed in Table 1.2 with their respective lattice parameters.

Formula	**a/Å**	**Ref**
$CdCu_3Ti_4O_{12}$	7.390	[26]
$CaCu_3Mn_4O_{12}$	7.241	[27]
$ThCu_3Mn_4O_{12}$	7.359	[28]
$YCu_3Mn_4O_{12}$	7.254	[29]
$Tb_{0.71}Cu_3Ti_4O_{12}$	7.383	[30]
$Bi_{0.667}Cu_3Ti_4O_{12}$	7.418	[31]

Table 1.2: Phases structurally analogous to $CaCu_3Ti_4O_{12}$.

Although the structure is heavily distorted from that of the ideal perovskite, refinement in $Im3$ space group symmetry eliminates the possibility of off-centre displacement of the cations in all $ACu_3B_4O_{12}$ perovskites. Furthermore, compositions with A species of higher valence are also achievable. In the case of B = Mn, the charge compensation mechanism involves partial reduction of Mn^{4+} to Mn^{3+} and, in the case B = Ti, A cation vacancies are required to preserve electroneutrality; neither mechanism has been reported to alter the crystal symmetry.

1.3. Electrical Properties of Perovskites

1.3.1. Electrical Conductivity

Electrical conductivity arises from long-range transport of charge carriers through a material. These charge carriers may be electrons or ions and the conduction can be referred to as being electronic or ionic, respectively, or mixed if both electrons and ions conduct.

	Material	**σ (Scm^{-1})**
Electronic conduction	Metals	10^{-1} - 10^{5}
	Semiconductors	10^{-5} - 10^{2}
	Insulators	$< 10^{-12}$
Ionic conduction	Ionic crystals	$< 10^{-18}$ – 10^{-4}
	Solid electrolytes	10^{-3} – 10^{1}
	Liquid electrolytes	10^{-3} - 10^{1}

Table 1.3: Typical values of ionic conductivity and electronic conductivity, after West [1].

1.3.1.1. Electronic Conduction

Electronic conductors fall into 3 main categories as listed in Table 1.3 and with band gap representations given in Figure 1.11. Metallic conductors are characterised by a partially filled valence band in which electrons are promoted by thermal excitation into a delocalised state within the valence band. Although increasing temperature will excite more electrons, this also leads to increasing phonon activity that tends to disrupt conductivity. Oxides exhibit metallic conductivity when there is orbital overlap between cations, TiO being a common example, and activation energies tend to be of the order 10^{-2} eV with room temperature conductivities of the order 10^{5} Scm^{-1} [1].

In terms of their band structure, semiconductors and insulators are similar; both have filled valence bands and a conduction band separated by a substantial band gap. Semiconductors tend to have band gaps between 0.1 eV and 2.0 eV whereas those of insulators tend to be > 3.0 eV. As a result, fewer electrons can be thermally excited into the conduction band of an insulator. Semiconductors have room temperature conductivity values ranging from 10^{-5} Scm^{-1} up to 10^{2} Scm^{-1}, comparable with some metallic conductors while insulators are considered to have conductivities $< 10^{-12}$ Scm^{-1} at room temperature.

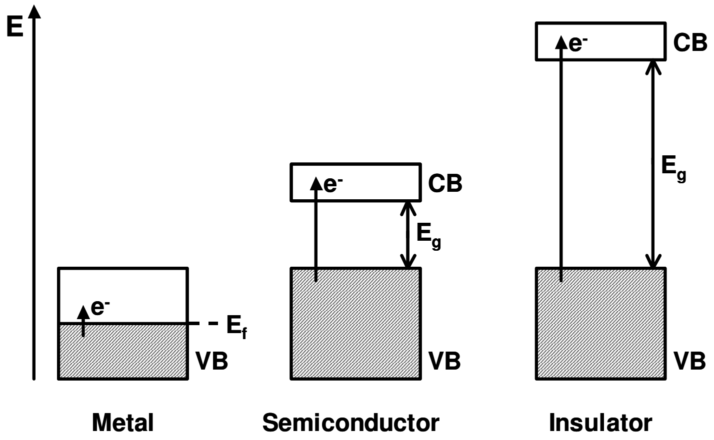

Figure 1.11: Band-gap diagrams for metallic conductors, semiconductors and insulators. VB, CB, E_f and E_g denote the valence band, conduction band, Fermi level and band gap, respectively.

The band structure, and hence conductivity of semiconductors can be modified by partial substitution of aliovalent ions into the lattice (*i.e.* doping). Donor doping occurs when the dopant ion is of higher valence than the host ion, e.g. $Si^{4+} \leftrightarrow P^{5+} + e^-$, such that an extra energy level is formed below the conduction band associated with the excess electrons, as shown in Figure 1.12. The energy gap between the donor level and the conduction band is much less than that between the valence band and the conduction band, so more electrons can be excited into the conduction band. This conduction mechanism is termed *n*-type, since the charge carriers are the negatively charged electrons in the conduction band.

Acceptor doping involves the substitution of an ion of lower valence than the host ion, e.g. $Si^{4+} \leftrightarrow Ga^{3+} + h^+$, in which a positively charge 'hole' is created in the valence band associated with an acceptor level above it. In this case, the charge carriers are the positive holes and so the conductivity mechanism is termed *p*-type, as shown in Figure 1.12.

Similarly, oxide semiconductors can be doped to create *n*- or *p*-type band structures. In such cases, acceptor levels arise from partial substitution of lower valence cations but also from excess oxygen, *i.e.* oxygen located in interstitial sites; close-packing of ions, however, excludes the latter compensation mechanism for perovskite-type oxides. Donor levels arise through partial substitution of higher valence cations or oxygen vacancies and both are plausible mechanisms in perovskites [1].

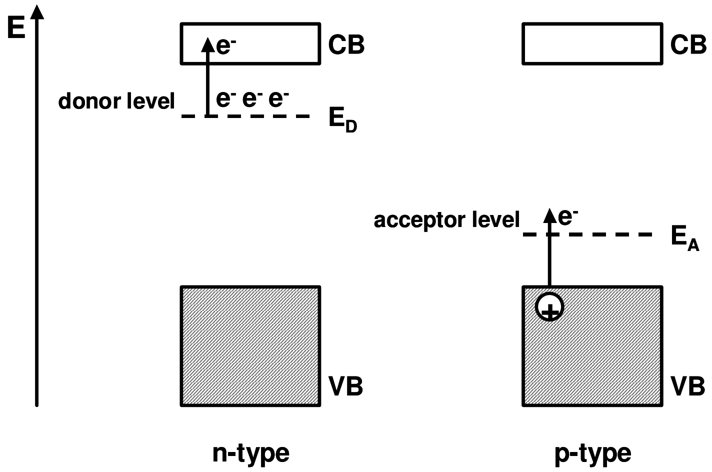

Figure 1.12: Band gap diagram for *n*-type (left) and *p*-type (right) semiconductor.

Aliovalent doping and/or changes in oxygen stoichiometry also facilitate *n*- or *p*-type conductivity in insulating phases by providing a means to transport charge without having to excite electrons directly from the valence band to the conduction band.

Superconductivity is related to metallic conductivity in that charge carriers are delocalised. However, superconductivity is also characterised by the fact that electron-phonon interactions below a certain critical temperature, T_c, result in the formation of co-operative electron pairs that result in zero *dc* resistivity. Upon cooling from above T_c, therefore, superconductors switch at T_c from a metallic state to a superconducting state, although T_c itself is also dependent on pressure, magnetic field and current. T_c was believed to be restricted to temperatures below 23 K until the perovskite-based compound $YBa_2Cu_3O_7$ was found to enter a superconducting state below ~ 91 K [1].

The $YBa_2Cu_3O_7$ structure is shown in Figure 1.13. The unit cell, contained within the black outline, is orthorhombic and represented by the space group *Pmmm*. It contains three perovskite ‘layers’ stacked parallel to the *z*-axis, the net stoichiometry of the top and bottom third being $BaCuO_{2.5}$ and the middle third being $YCuO_2$. The valence of Cu in $YBa_2Cu_3O_7$ is, therefore, variable between 2+ in the $YCuO_2$ layer and 3+ in $BaCuO_{2.5}$ layer. Overall, two *A*-sites exist: the 10 coordinate Ba site and the 8 coordinate Y site. Also two *B*-sites exist: the 5 coordinate Cu^{2+} site and the 4 coordinate Cu^{3+} site represented in Figure 1.13 by the square-pyramidal and square-planar environments, respectively.

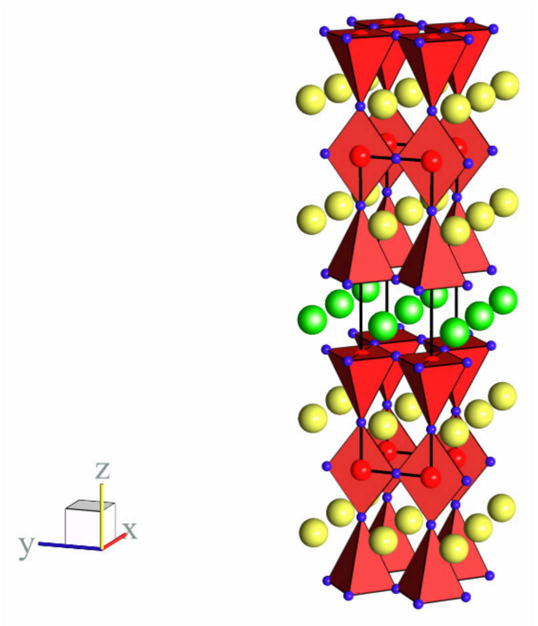

Figure 1.13: Structure of $YBaCu_2O_7$. Green, yellow, red and blue spheres represent Y, Ba, Cu and O ions, respectively (Balls & Sticks version 1.51, S.J. Kung, T.L. Ozawa, 2003).

The conductivity in $YBa_2Cu_3O_7$ in the superconducting state is highly anisotropic, being much higher along the *xy*-plane than the *z*-axis. Furthermore, if $YBa_2Cu_3O_7$ is reduced to the stoichiometry $YBa_2Cu_3O_{6.4}$, despite Cu^{2+} remaining in the square-pyramidal environment, the Cu^{3+} ions are reduced to Cu^{+} and occupy a 2 coordinate site. Such a phase does not exhibit superconductivity and so it is believed the presence of Cu^{3+} in a square-planar site is crucial to obtaining superconductivity in these materials [1, 32].

1.3.1.2. Ionic Conductivity

Ionic conductors fall into 3 categories, listed in Table 1.3. Of these, the highest conductivities are given by liquid electrolytes in which all ions are mobile. The lowest conductivities are given by ionic crystals, in which most of the ions remain in their lattice sites but can diffuse through the crystal by ‘hopping’ into adjacent vacancies. Solid electrolytes yield conductivities of similar magnitude to liquid electrolytes and are a compromise between an ionic crystal and liquid electrolyte. The structure of a solid electrolyte generally comprises a framework of ions featuring long-range channels through which charge-carrying ions are freely mobile. Ionic crystals and solid electrolytes can, therefore, be differentiated as having close-packed and non-close-packed structures, respectively [1].

Since the perovskite structure is close-packed, certain compounds are known to exhibit the former type of ionic conductivity, specifically oxide-ion conduction. Of these the most successful to date are doped-$LaGaO_3$ compositions [33]. At room temperature, the structure of $LaGaO_3$ is similar to $CaTiO_3$ having an orthorhombic unit cell and an $a^-a^-c^+$ octahedral tilt system, described by the *Pbnm* space group symmetry. Above 425 K, $LaGaO_3$ undergoes a phase transition to rhombohedral symmetry, space group *R*-3*c*, arising from an $a^-a^-a^-$ tilt system [34].

Since ionic conductivity relies upon vacancies equivalent to the charge-carrying ion, the volume fraction of such vacancies must be maximised to yield significant conductivity. Vacancies can be formed thermally as Schottky-defects, for instance, and so conductivity increases with temperature. Furthermore, at higher temperatures, thermal vibrations become more vigorous and allow the charge-carrying ions to hop more freely into vacant sites. Doping can increase the volume fraction of vacancies still further, so higher conductivities can be obtained at lower temperatures. In either case, the defects must be stoichiometric to prevent changes in the band structure facilitating an electronic-conductivity short-circuit.

The oxygen deficient composition $La_{0.9}Sr_{0.1}Ga_{0.8}Mg_{0.2}O_{2.85}$ was shown to have oxide-ion conductivity of ~ 10^{-2} Scm^{-1} at 600℃, comparable in magnitude to some solid and liquid electrolytes [33]. In contrast to $LaGaO_3$ at high temperatures, $La_{0.9}Sr_{0.1}Ga_{0.8}Mg_{0.2}O_{2.85}$ adopts the ideal cubic perovskite structure (space group *Pm*3*m*) with the dopant ions and vacancies sufficiently disordered to prevent the formation of a supercell [35].

For certain applications, such as cathodes for solid oxide fuel cells, it is necessary for a material to exhibit both oxide-ion and electronic conductivity. In this case oxide-ion conductivity is required to transport oxide ions to the electrolyte and allow an electrical connection between the external circuit and electrolyte. $LaMnO_{3-\delta}$ is one such perovskite-structured compound that facilitates both conduction mechanisms and is used in commercial Y-stabilised ZrO_2-based fuel cells [1, 36].

1.3.2. Permittivity and Ferroelectric Behaviour

Relative permittivity, ε', is a measure of the charge storing ability of an insulating (or dielectric) material relative to that of a vacuum [1, 37] and is, when the material is placed between two parallel electrodes, related to capacitance, *C*, thus:

$$C = \varepsilon' \varepsilon_0 (A/t) \qquad (1.2)$$

where $\varepsilon_0 = 8.854\times10^{-14}$ Fcm^{-1} (the permittivity of free space), t is the thickness of the material and A is the cross-sectional surface area of the electrodes, as shown in Figure 1.14.

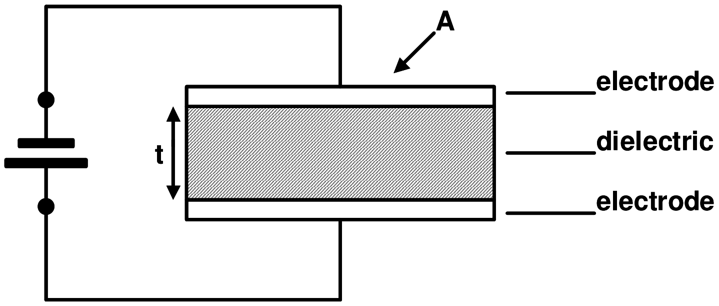

Figure 1.14: Schematic of a capacitor attached to a dc power source.

When connected to a *dc* voltage, V, as in figure 1.14, a charge, Q, is collected on the electrodes according to:

$$Q = CV \tag{1.3}$$

It can be inferred from Equations 1.2 and 1.3 that, in order to increase the charge stored by the capacitor per unit of voltage, the permittivity of the dielectric material must increase and/or the thickness relative to cross-sectional area must decrease.

Permittivity is determined by the extent to which ions are displaced from their lattice positions, *i.e.* polarised, under the influence of an electric field. Consequently, oxides with centrosymmetric structures exhibit permittivities between 10 and 100 since the maximum displacement of cations under an applied field is typically < 0.01 Å. Upon removal of the field, the polarisation is lost; ferroelectric materials, however, retain their polarisation.

Ferroelectric behaviour is observed only in the case where a phase exhibits spontaneous polarisation, such as tetragonal $BaTiO_3$. Initially, the dipoles within a crystal are grouped into domains of differing orientations. A schematic example is given in Figure 1.15, in which each line represents a domain wall between two different dipole orientations [38]. The width of a ferroelectric domain is typically 0.1 μm to 1 μm.

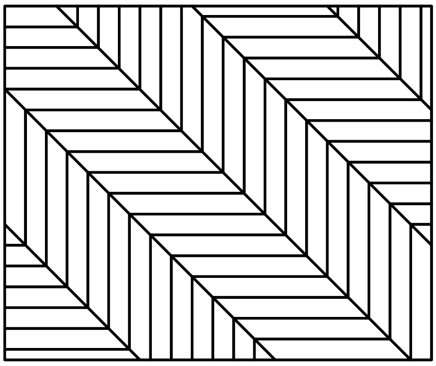

Figure 1.15: Schematic representation of domain walls in a ferroelectric crystal.

The dependence of polarisation, *P*, upon applied field for a ferroelectric is more complex than in the case of a non-ferroelectric, and hysteresis can be observed when the applied field, *E*, is cycled sinusoidally; this is illustrated in Figure 1.16. Initially, with zero applied field, the dipoles are randomised such that there is no net polarisation in the crystal. Upon increasing *E*, the dipoles become oriented in the direction of the field and *P* increases as per the dashed curve in Figure 1.16. Eventually, the saturation polarisation, P_s, is reached, *i.e.* there can be no further increase in polarisation with *E*. Decreasing *E* to zero results in a more gradual decrease in polarisation and, when $E = 0$, a substantial remanent polarisation, P_R, is observable. To reduce the polarisation to zero, such that the dipoles are once again randomised, the field direction must be reversed and its magnitude increased to the coercive field, E_c.

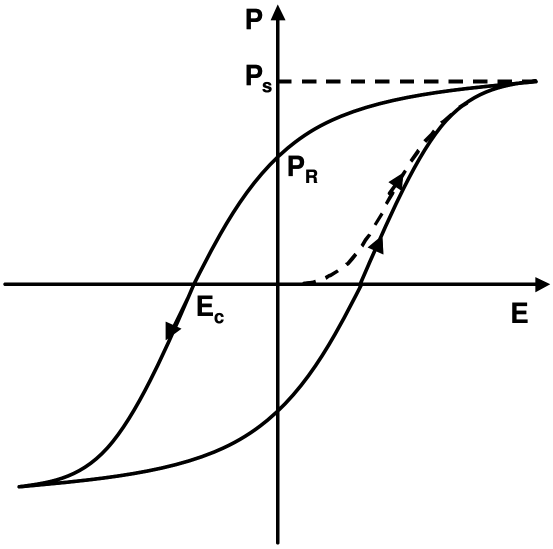

Figure 1.16: Polarisation versus applied field for a ferroelectric, adapted from West [1].

The *P-E* behaviour may also be influenced by phenomena such as changes in the polarisation direction with the domains or growth of domains more closely in alignment with the applied field at the expense of other domains [1].

The presence of phase transitions imparts a significant temperature dependence to the permittivity of ferroelectric materials. Typically, transitions from one ferroelectric phase to another are associated with a minor peak in permittivity whereas transitions from a ferroelectric to a paraelectric phase, in which P_R is reduced to zero, are associated with a major peak; Figure 1.17 (a) is a typical example for $BaTiO_3$.

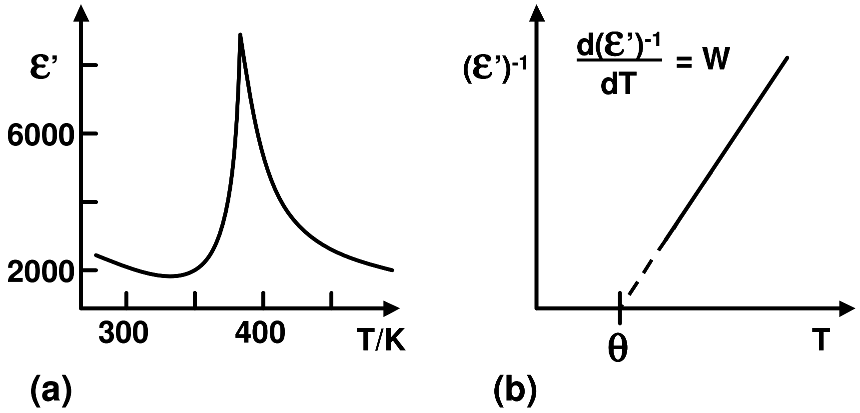

Figure 1.17: (a) Permittivity versus temperature plot of $BaTiO_3$ near the cubic-tetragonal phase transitions and (b) schematic Curie-Weiss plot. Adapted from West [1].

From room temperature to ~ 340 K, the permittivity decreases slightly from ~ 2,500 to ~ 1,900, associated with the orthorhombic-tetragonal phase transition at ~ 280 K. The tetragonal-cubic phase transition at ~ 400 K results in a sharp peak in ε' with $\varepsilon'_{\max}$ ~ 10,000. The cubic polymorph is paraelectric and the permittivity decreases steadily as ordering of the dipoles becomes disrupted by thermal vibrations. Since all the lower symmetry polymorphs of $BaTiO_3$ are ferroelectric, the temperature of the tetragonal-cubic polymorphic phase transition is referred to as the Curie temperature, T_c (not to be confused with the critical temperature used when referring to superconductors).

The temperature dependence above T_c can be modelled on the Curie-Weiss law, Equation 1.4, in which θ is the Curie temperature and W is the Curie constant, as shown in Figure 1.17 (b).

$$\varepsilon' = W/(T-\theta) \qquad (1.4)$$

Ideally, θ corresponds to T_c, yet there is usually a discrepancy arising from impurities and/or chemical inhomogeneities in polycrystalline samples [1].

$CaTiO_3$ and $SrTiO_3$, however, are essentially centrosymmetric yet they have been reported to have permittivities of ~ 10^2 at room temperature. The temperature dependence of ε' in these materials is similar to that of $BaTiO_3$ in the paraelectric state, in that ε' increases with decreasing temperature to the peak at T_c according to the Curie-Weiss law. In the case of $CaTiO_3$ and $SrTiO_3$, however, T_c is never reached since it is effectively < 0 K. Materials exhibiting this phenomenon are classified as incipient ferroelectrics [39].

In practical applications, there is also a lag or phase difference between an alternating current as it enters and leaves the capacitor, arising from energy lost as heat. This energy loss is often quantified as dielectric loss or tan δ in electrical property measurements, and will be discussed further in Chapter 3.

1.3.3. Electrically Heterogeneous Properties

1.3.3.1. Schottky Barriers

Many useful electrical properties arise primarily from electrical heterogeneity between grains and grain boundaries in a ceramic such that the grain boundaries act as an extrinsic source of electrical impedance [37]. In many cases, the resistance can be attributed to the formation of double Schottky potential barriers at the grain-grain interfaces in which charge trapping occurs between adjacent grains, resulting in bending of the conduction band across the grain boundary which produces an effective potential barrier of height, Φ_b, for conducting electrons between adjacent grains, as shown in Figure 1.18.

One possible origin of the charge traps is the formation of dislocations between adjacent grains of different orientations, in which the planes of atoms are mismatched at the grain boundary. Another possibility, more commonly observed in oxides, is a thin (typically ~ 10 Å) diffusion layer of impurity or dopant atoms at the grain surfaces that act either as acceptor or donor levels [37, 40].

For a Schottky-active grain boundary, the activation energy for conduction across the grain boundary is proportional to Φ_b, defined in Equation 1.5, and the resultant grain boundary resistance is, therefore, dependent upon Φ_b as shown in Equation 1.6 [37, 40].

$$\phi_b = \frac{qN_s^2}{8\varepsilon_0\varepsilon' N_T} \qquad (1.5)$$

where q is the excess charge at the grain surface, N_s is the surface charge density and N_T is the trap density in the depletion region

$$R \propto \exp\left(\frac{\phi_b}{kT}\right) \qquad (1.6)$$

In turn, Φ_b decreases under an applied *dc* bias as shown in Equation 1.7 [41]:

$$\phi_b \propto \frac{1}{4}V_c\left[1-\frac{V}{V_c}\right]^2 \qquad (1.7)$$

where V is the voltage of the applied dc bias and V_c is the critical applied bias in which the barrier height is reduced to zero.

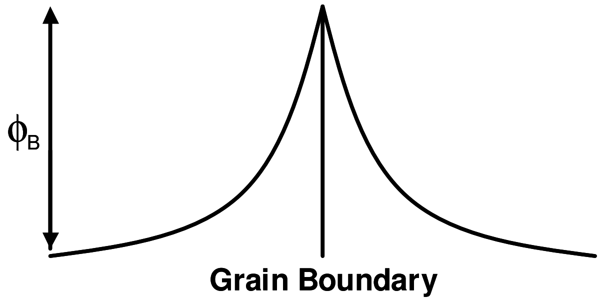

Figure 1.18: Schematic illustration of a double Schottky barrier at a grain boundary.

In the theoretical case of a microstructure consisting of compositionally and geometrically uniform grain boundaries, the number of grain boundaries increases through either increasing sample thickness or decreasing grain size and the dependence of grain boundary resistance upon *dc* bias becomes progressively less pronounced. This is because, with increasing effective thickness, the applied field across each grain boundary is lowered, leading to a less noticeable reduction in Φ_b. In the case of polycrystalline ceramics, even if the *dc* bias exceeds V_c, a substantial grain boundary resistance may still be obtained.

1.3.3.2. PTCRs

Positive temperature coefficient of resistance (PTCR) thermistors find applications in protecting circuits against overheating [37]. Typically, PTCR compositions are based on *n*-type semiconducting $BaTiO_3$ with La^{3+} partially substituted for Ba^{2+}. The aliovalent substitution is believed to impart *n*-type behaviour, but not the high conductivity itself, since the charge difference between Ba^{2+} and La^{3+} is compensated by Ti^{4+} vacancies, according to the solid solution formula $Ba_{1-x}La_xTi_{1-x/4}O_3$. Instead, the conductivity arises from oxygen loss, since ceramics post-annealed with high oxygen partial pressures exhibit dielectric behaviour whereas those post-annealed with low oxygen partial pressures are semiconducting [42, 43].

A PTCR's temperature dependence of resistivity is dominated by the ferroelectric-paraelectric phase transition at ~ 400 K, as shown in Figure 1.19. At room temperature the observed resistivity is ~ 0.1 - 1 Ω.m, commensurate with semiconductivity. On heating above T_c, the resistivity increases suddenly to ~ 10^4 Ω.m at ~ 450 K. The temperature dependence of a PTCR is, therefore, dominated by the potential barrier height being inversely proportional to permittivity, as described in Equation 1.5. Hence, the decrease in permittivity above T_c results in a substantial increase in the barrier height and so the resistivity rises [37, 44].

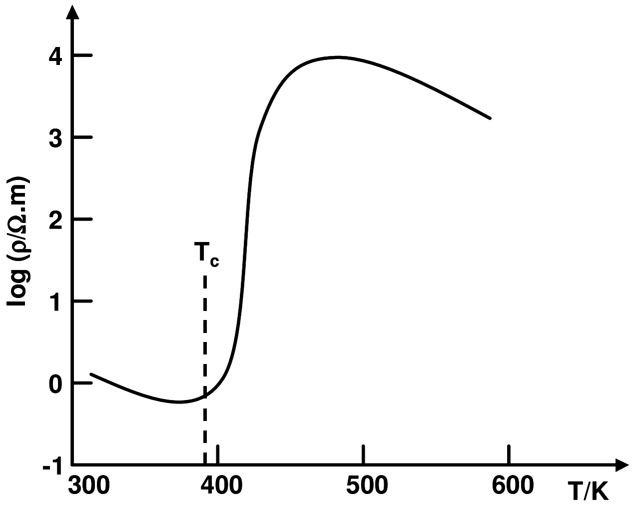

Figure 1.19: Temperature dependence of a PTCR. Adapted from Moulson [37].

Although the PTCR effect is still not fully understood, such devices have found widespread applications for many years. Commercial compositions are more complex, comprising many species of additives to control T_c, sintering behaviour, oxygen loss and density of trap states at the grain boundaries.

1.3.3.3. IBLCs.

Internal barrier layer capacitors (IBLCs) are used in low voltage applications as an alternative to high permittivity ferroelectric devices [37]. Whereas the high permittivity of a ferroelectric arises from off-centre displacement of ions, IBLCs are generally non-ferroelectric and the high permittivity arises from the thin insulating grain boundary regions, the grains themselves being semiconducting. The grain boundaries are thin in comparison to the grains and, according to Equation 1.2, represent regions of high capacitance. Since a macroscopic permittivity measurement cannot account for the geometry of the grain boundaries, their high capacitance results in a high *effective* permittivity. This is illustrated in Figure 1.20, in which a schematic IBLC microstructure is shown with grains of thickness t_g, barrier thickness t_{gb} and overall thickness t. The effective permittivity ε_{eff} is defined thus:

$$\varepsilon_{eff} = \varepsilon'(t_g / t_{gb}) \tag{1.8}$$

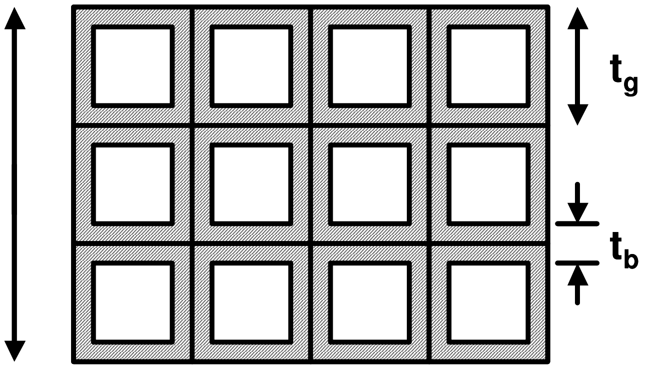

Figure 1.20: Schematic cross-section through an IBLC. The hatched areas represent the insulating barrier regions. Adapted from Moulson [37].

It can be inferred from Equation 1.8 that in order to maximise ε_{eff} it is necessary to maximise the grain size and intrinsic permittivity, ε', of the material, and minimise the barrier thickness. Increasing ε' has the added advantage of increasing the barrier height at the grain boundaries and therefore increasing the *dc* resistance. Reducing barrier thickness and increasing grain size, however, leads to a drop in *dc* resistance and an increase in dielectric loss, as discussed in Chapter 3.

IBLC compositions are often based on $SrTiO_3$ with additives of Nb_2O_5, Al_2O_3, Bi_2O_3, PbO and B_2O_3. The sintered body must be post-annealed in a reducing atmosphere to increase the conductivity of the grains and then reoxidised to limited extent to form insulating grain boundary regions. The typical microstructure of such an IBLC consists of a thin (0.1 – 0.9 μm), glassy intergranular-layer of predominantly Bi_2O_3-based material and semiconducting $SrTiO_3$ grains. On either side of the intergranular layer is a layer of oxidised, and therefore insulating, $SrTiO_3$ from which the effective permittivity arises [45].

1.3.4. Electrical Properties of $CaCu_3Ti_4O_{12}$

Subramanian *et al* reported the first investigations of the electrical properties of $CaCu_3Ti_4O_{12}$ in 2000 [46]. Between room temperature and ~ 400 K, the permittivity measurements, taken at 1 kHz, apparently revealed $CaCu_3Ti_4O_{12}$ ceramics to exhibit an almost constant high permittivity of ~ 10,000 and 2 possible explanations were put forward: 1) the structure of $CaCu_3Ti_4O_{12}$ facilitates an exotic polarisation mechanism that imparts high, temperature-stable permittivity values, or 2) the high permittivity arises from an internal barrier layer-type mechanism, in that the high permittivity is due to high capacitance grain boundary regions.

Ramirez *et al* followed up the findings of Subramanian *et al* by measuring the permittivity and tan δ of $CaCu_3Ti_4O_{12}$ ceramics at selected frequencies between 100 Hz and 1 MHz at temperatures between 10 K and 400 K [47]. Their reported data are shown in Figure 1.21. When measured at 100 Hz, permittivity decreases from ~ 10,000 at 300 K to ~ 8,500 at 210 K. Cooling to 100 K reveals no further change in permittivity. Below 100 K, however, a sharp drop in permittivity to ~ 115 was reported, associated with a peak in tan δ. Increasing the measuring frequency also seemed to increase the temperature at which this apparent transition in permittivity and peak in tan δ occurred. Homes [48] followed this investigation with low temperature permittivity and tan δ measurements of $CaCu_3Ti_4O_{12}$ single crystals at frequencies from 100 Hz up to optical frequencies. It was reported that the permittivity and tan δ values obtained from single crystal samples were almost an order of magnitude higher than for ceramics above the so-called "transition" temperature.

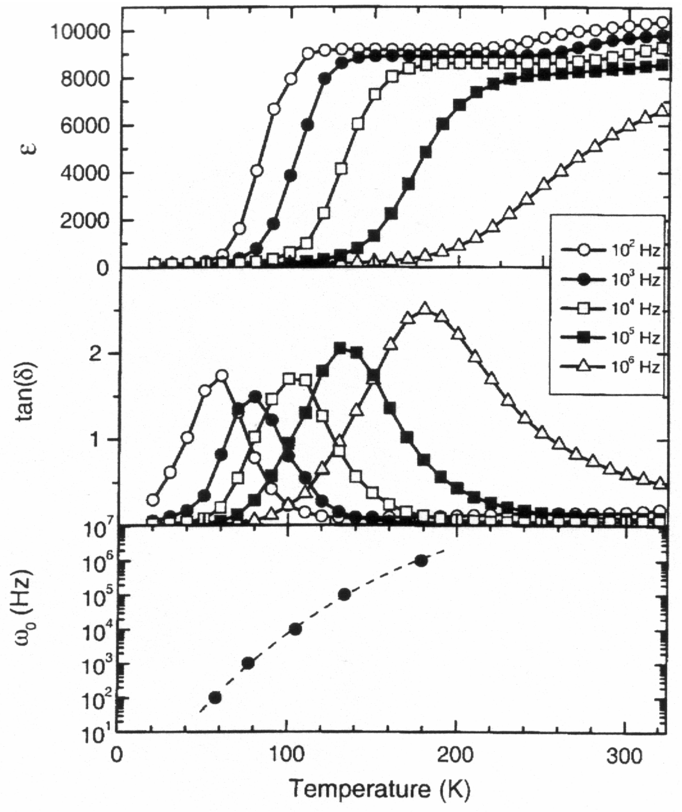

Figure 1.21: Permittivity, tan δ and frequency of the peak in tan δ, ω_0, for $CaCu_3Ti_4O_{12}$ after Ramirez [47].

Homes [48] speculated that the temperature dependence of permittivity and peak in tan δ could be attributed to "a relaxor-like dynamical slowing down of dipolar fluctuations in nanosize domains" and derived supposed relaxation times based on this presumption from the frequency of the peak in tan δ, ω_0. The temperature dependence of the relaxation times of the "dipolar fluctuations" were found to obey the Arrhenius law, with values ranging from 8.2 μs at 150 K to 84 ns at 630 K, corresponding to an activation energy of 54 meV, although it was conceded that the single crystal samples were heavily twinned.

Since similar behaviour had been reported in single-crystals and ceramics of $CaCu_3Ti_4O_{12}$, several investigators began to favour the existence of a new "colossal dielectric constant" phenomenon. Despite numerous publications, no conclusive evidence for either case was forthcoming as to the origin of the observed properties. In this thesis, the electrical properties of $CaCu_3Ti_4O_{12}$ are characterised and the origin of the so-called colossal dielectric constants is revealed.

1.4. Thesis Plan

In Chapter 2, appropriate experimental techniques are described that have been used to synthesise and characterise $CaCu_3Ti_4O_{12}$ ceramics. Chapter 3 focuses on the theory and applications of Impedance Spectroscopy to characterise electroceramics and also reviews potential problems with traditional “fixed frequency” electrical property measurements. Initial impedance studies of $CaCu_3Ti_4O_{12}$ ceramics are discussed in Chapter 4, combined with a tentative description of decomposition processes occurring in these materials at high temperatures. The dependence of impedance characteristics upon pellet thickness, electrode material and *dc* bias is described in Chapter 5. Chapter 6 illustrates decomposition processes occurring in $CaCu_3Ti_4O_{12}$ ceramics at high temperature and low pO_2 and the effect on electrical properties. Finally, Chapter 7 describes the synthesis and impedance characteristics of two phases isostructural with $CaCu_3Ti_4O_{12}$: $CdCu_3Ti_4O_{12}$ and $Na_{1/2}Bi_{1/2}Cu_3Ti_4O_{12}$.

References

1. A.R. West, *Basic Solid State Chemistry*. 2 ed. 1999: John Wiley & Sons.
2. A.M. Glazer, "The Classification of Tilted Octahedra in Perovskites" Acta Crystallographica B, 1972, **28**, 3384
3. P.M. Woodward, "Octahedral Tilting in Perovskites. I. Geometric Considerations." Acta Crystallographica B, 1997, **53**, 32-43
4. C.J. Howard, H.T. Stokes, "Group-Theoretical Analysis of Octahedral Tilting in Perovskites." Acta Crystallographica B, 1998, **54**, 782-789
5. H.D. Megaw, *Crystal Structures: A Working Approach*. 1973: W.B. Saunders Company.
6. H. Krebs, P.H.L. Walter, *Fundamentals of Inorganic Crystal Chemistry*. 1968: McGraw-Hill.
7. D.M. Adams, *Inorganic Solids*. 1974: John Wiley & Sons.
8. M.W. Lufaso, P.M. Woodward, "Jahn-Teller distortions, cation ordering and octahedral tilting in perovskites." Acta Crystallographica B, 2004, **60**, 10-20
9. G. Shirane, Y. Yamada, "Lattice-Dynamical Study of the 110 K Phase Transition in $SrTiO_3$." Physical Review, 1969, **177**(2), 858-863
10. Y.A. Abramov, V.G. Tsirelson, V.E. Zavodnik, S.A. Ivanov, I.D. Brown, "The Chemical Bond and Atomic Displacement in $SrTiO_3$ From X-Ray Diffraction Analysis." Acta Crystallographica B, 1995, **51**, 942-951
11. P.M. Woodward, "Octahedral Tilting in Perovskites. II. Structure Stabilizing Forces." Acta Crystallographica B, 1997, **53**, 44-66
12. S. Rakshit, P.S. Gopalakrishnan, "Oxygen Nonstoichiometry and Its Effect on the Structure of $LaNiO_3$." Journal of Solid State Chemistry, 1994, **110**, 28-31
13. G.H. Kwei, A.C. Lawson, S.J.L. Billinge, S,-W. Cheong, "Structures of the Ferroelectric Phases of Barium Titanate." Journal of Physical Chemistry, 1993, **97**, 2368-2377

14. A. Sani, M. Hanfland, D. Levy, "Pressure and Temperature Dependence of the Ferroelectric-Paraelectric Phase Transition in $PbTiO_3$." Journal of Solid State Chemistry, 2002, **167**, 446-452
15. B.J. Kennedy, C.J. Howard, B.C. Chakoumakos, "Phase Transitions in Perovskite at High Temperatures – A Powder Neutron Diffraction Study" Journal of Physicals: Condensed Matter, 1999, **11**, 1479
16. B.J. Kennedy, C.J. Howard, B.C. Chakoumakos, "High-temperature phase transitions in $SrZrO_3$." Physical Review B, 1999, **59**(6), 4023-4027
17. C.J. Howard, K.S. Knight, B.J. Kennedy, E.H. Kisi, "The structural phase transitions in stronium zirconate revisted." Journal of Physics: Condensed Matter, 2000, **12**, L677-L683
18. R.D. Shannon, "Revised Effective Ionic Radii and System Studies of Interatomic Distances in Halides and Chalcogenides." Acta Crystallographica A, 1976, **32**, 751-767
19. F.W. Lytle, "X-Ray Diffractometry of Low Temperature Phase Transformations in Strontium Titanate" Journal of Applied Physics, 1964, **35**, 2212
20. P.M. Woodward, K.Z. Baba-Kishi, "Crystal structures of the relaxor oxide $Pb_2(ScTa)O_6$ in the paraelectric and ferroelectric states." Journal of Applied Crystallography, 2002, **35**, 233-242
21. F. Galasso, J.R. Barrante, L. Katz, "Alkaline Earth-Tantalum-Oxygen Phases Including the Crystal Structure of an Ordered Perovskite Compound, $Ba_3SrTa_2O_9$." Journal of the American Chemical Society, 1961, **83**, 2830-2832
22. A. Deschanvres, B. Raveau, F. Tollemer, Bulletin de Societie Chemie de France, 1967, **11**, 4077
23. N. Kolev, R.P. Bontchev, A.J. Jacobson, V.N. Popov, V.G. Hadjiev, A.P. Litvinchuk, M.N. Iliev, "Raman spectroscopy of $CaCu_3Ti_4O_{12}$." Physical Review B, 2002, **66**, 132101
24. S.M. Moussa, B.J. Kennedy, "Structural studies of the distorted perovskite $Ca_{0.25}Cu_{0.73}TiO_3$." Materials Research Bulletin, 2001, **36**, 2525-2529
25. Y.J. Kim, S. Wakimoto, S.M. Shapiro, P.M. Gehring, A.P. Ramirez, "Neutron scattering study of anitferromagnetic order in $CaCu_3Ti_4O_{12}$." Solid State Communications, 2002, **121**, 625-629
26. E.G. Fesenko, O.N. Razumovskaya, V.A. Shuvaeva, G.G. Gridneva, O.A. Buinina, "The structure of $CdCu_3Ti_4O_{12}$." Izvestiya Akademii Nauk SSSR, Neorganicheskie Materialy, 1991, **27**, 1991-1992
27. J. Chenavas, J.C. Joubert, M. Marezio, B. Bochu, "The synthesis and crystal structure of $CaCu_3Mn_4O_{12}$: A new ferromagnetic-Perovskite-like compound." Journal of Solid State Chemistry, 1975, **14**, 25-32
28. M.N. Deschizeaux, J.C Loubert, A. Vegas, A. Collomb, J. Chenavas, M. Marezio, "Synthesis and crystal structure of $(ThCu_3)((Mn_2)(3+)(Mn_2)(4+))O_{12}$, a new ferrimagnetic Perovskite-like compound." Journal of Solid State Chemistry, 1976, **19**, 45-51
29. A. Collomb, D. Samaras, J.P. Buevo, J.C. Joubert, "Synthesis, composition-range and structure of the Perovskite-like $YCu_3Mn_4O_{12}$." Journal of Magnetism and Magnetic Materials, 1983, **40**, 75-82
30. B. Bochu, M.N. Deschizeaux, J.C Joubert, A. Collomb, J. Chenevas, M. Marezio, "Synthese et caracterisation d'une serie de titanates Perowskites isotypes de $(CaCu_3)(Mn_4)O_{12}$." Journal of Solid State Chemistry, 1979, **29**, 291-298
31. I. Bryntse, P.E. Werner, "Synthesis and structure of a perovskite related oxide, $Bi_{2/3}Cu_3Ti_4O_{12}$." Materials Research Bulletin, 1990, **25**, 483
32. O.K. Antson, P.E. Husmaki, H.O. Poyry, A.T. Tiitta, K.M. Ullakko, V.A. Trunov, V.A. Ul'yanov, "A High Resolution Neutron Powder Diffraction Study on High-T_c Superconductor $YBa_2Cu_3O_7$." Solid State Communications, 1987, **64**(5), 757-760
33. J.B. Goodenough, "Oxide-Ion Electrolytes." Annual Review of Materials Research, 2003, **33**, 91-128

34. L. Vasylechko, A. Matkovski, A. Suchocki, D. Savytskii, I. Syvorotka, "Crystal Structure of $LaGaO_3$ and (La,Gd)GaO_3 Solid Solutions." Journal of Alloys and Compounds, 1999, **286**, 213-218
35. M. Lerch, H. Boysen, T. Hansen, "High-temperature neutron scattering investigation of pure and doped lanthanum gallate." Journal of Physics and Chemistry of Solids, 2001, **62**, 445-455
36. S.-G. Eriksson, S. Ivanov, J. Eriksen, M. Valkeapaeae, J.-G Johansson, H. Rundloef, R. McGreevy, P. Berastegui, P. Bjoernsson, M. Rubhausen, J. Baeckstroem, M. Kaell, L. Boerjesson, "A neutron powder diffraction and inelastic light scattering study of (La,Sr)MnO_3(+delta)." Materials Science Forum, 2001, **378**, 505-510
37. A.J. Moulson, J.M. Herbert, *Electroceramics Materials, Properties, Applications*. 1991, Wiley.
38. G. Arlt, "Twinning in ferroelectric and ferroelastic ceramics: stress relief." Journal of Materials Science, 1990, **25**, 2655-2666
39. V.V. Lemanov, A.V. Sotnikov, E.P. Smirnova, W. Weihnacht, R. Kunze, "Perovskite $CaTiO_3$ as an incipient ferroelectric." Solid State Communications, 1999, **110**, 611-614
40. F. Greuter, G. Blatter, "Electrical properties of grain boundaries in polycrystalline compound semiconductors." Semiconductor Science & Technology, 1990, **5**, 111-137
41. G. Blatter, F. Greuter, "Carrier transport through grain boundaries in semiconductors." Physical Review B, 1986, **33**(6), 3952-3966
42. F.D. Morrison, D.C. Sinclair, A.R. West, "Characterization of Lanthanum-Doped Barium Titanate Ceramics Using Impedance Spectroscopy." Journal of the American Ceramic Society, 2001, **84**(3), 531-538
43. F.D. Morrison, D.C. Sinclair, J.M.S. Skakle, A.R. West, "Novel Doping Mechanism for Very-High-Permittivity Barium Titanate Ceramics." Journal of the American Ceramic Society, 1998, **81**(7), 1957-1960
44. C.T. Chao, D.P. Cann, R.B. Gall, Y. Palaci, "High-field grain boundary transport in semiconducting $BaTiO_3$ ceramics." Journal of Physics D: Applied Physics, 2004, **37**, 416-421
45. P.E.C. Franken, M.P.A. Viegers, A.P. Gehring, "Microstructure of $SrTiO_3$ Boundary-Layer Capacitor Material." Journal of the American Ceramic Society, 1981, **62**(12), 687-690
46. M.A. Subramanian, D. Li, N. Duan, B.A. Reisner, A.W. Sleight, Journal of Solid State Chemistry, 2000, **151**, 323
47. A.P. Ramirez, M.A. Subramanian, M. Gardel, G. Blumberg, D. Li, T. Vogt, S.M. Shapiro, "Giant dielectric constant response in a copper-titanate." Solid State Communications, 2000, **115**, 217-220
48. C.C. Homes, T. Vogt, S.M. Shapiro, S. Wakimoto, A.P. Ramirez, "Optical Response of High-Dielectric-Constant Perovskite-Related Oxide." Science, 2001, **293**(5530), 673-676

2. Experimental Techniques

2.1. Solid State Synthesis

Solid state synthesis is a widely used and relatively simple method for preparing inorganic phases by mixing appropriate quantities of starting materials (or reagents) into a 'batch', milling the batch to reduce the average particle size of the reagents before reacting the mixture at high temperatures. The reacted powder can then be pressed into a cylindrical shape, the 'green body', and sintered to produce a dense pellet [1].

2.1.1. Batching

Reagents are oxide or carbonate phases containing one of the required cation species. For example, a batch intended for the synthesis of $CaCu_3Ti_4O_3$ will contain $CaCO_3$, CuO and TiO_2, where the overall reaction proceeds as follows:

$CaCO_3 + 3CuO + 4TiO_2 \rightarrow CaCu_3Ti_4O_{12} + CO_2$

A batch calculation determines the quantity of each reagent needed to achieve the required stoichiometry. These quantities are calculated as the ratio of atomic mass of the reagent to atomic mass of the total products, multiplied by the required mass of product. Thus for a 10 g starting batch:

Products:
$[CaCu_3Ti_4O_{12}] + [CO_2] = 614.31 + 44 = 658.31$

Reactants:
$[CaCO_3] = 100.08$
$[3CuO] = 79.54$
$[4TiO_2] = 79.9$

$[CaCO_3] / [CaCu_3Ti_4O_{12} + CO_2] = 0.152$
$[CuO] / [CaCu_3Ti_4O_{12} + CO_2] = 0.363$
$[TiO_2] / [CaCu_3Ti_4O_{12} + CO_2] = 0.486$

Hence:

Batch quantity of $CaCO_3$ = 1.52 g
Batch quantity of CuO = 3.63 g
Batch quantity of TiO_2 = 4.86 g
Total batch weight = 10 g

Although reagents used in solid state synthesis are high purity they nevertheless contain a finite quantity of impurity ions that may make extrinsic contributions to physical properties of the final phase, such as conductivity or permittivity, or be detected in analytical techniques. Sigma-Aldrich Chemical Company supplied all reagents used in this study and Table 2.1 lists the reagents used and their respective impurity levels.

Reagent	Sigma-Aldrich Product Number	Total Metallic Impurities
$CaCO_3$	481807	< 10 ppm
CuO	203130	< 2 ppm
TiO_2	204730	< 20 ppm

Table 2.1: Purity of reagents (source: www.sigmaaldrich.co.uk).

2.1.2. Milling

During the milling process, particles within a batch are abraded by milling media and by adjacent particles; as a result, contamination of the batch by spallation of the milling media is inevitable. Hand grinding is the simplest milling technique, in which the batch is mixed with acetone and ground in an agate mortar and pestle. Hand grinding generally results in low contamination levels (< 1 wt%) but reproducibility is often poor and particle sizes of < 10 μm cannot always be achieved. Furthermore, batch weights are limited to < 10 g. Despite these drawbacks, the technique is widely used in speculative solid state chemistry where low contamination is required [1].

Planetary ball milling is an automated milling technique, illustrated in Figure 2.1. The batch is mixed with acetone and spherical agate media in a cylindrical agate pot. The pot is seated on the end of a rotating arm and driven around in an ‘orbit’ at a selected speed, typically between 200 and 500 rpm. For every rotation of the arm, the pot is rotated once in an epicycle and so the motion is analogous to that of planetary motion.

The epicycle causes the media to collide vigorously, crushing the batch particulates into progressively smaller sizes, while the orbital motion prevents the batch and media being forced against the pot wall. Milling conditions are highly reproducible, since rotation speed and milling time can be pre-programmed and automatically controlled, and particle sizes of 1 μm or less are readily achievable. Batch contamination levels, however, tend to be higher than for hand-ground powders and using rotation speeds of 500 rpm can disrupt the crystallinity of an emerging phase [2].

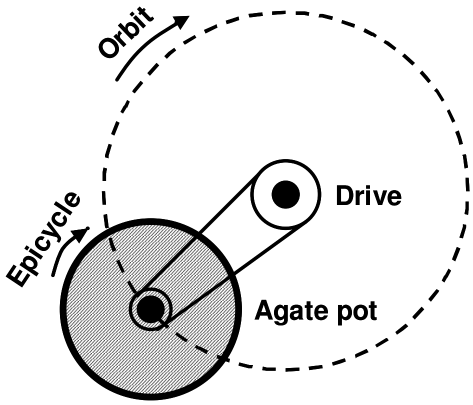

Figure 2.1: Schematic layout of a planetary ball mill.

2.1.3. Solid State Reaction

Reactions in the solid state occur at high temperatures, often in excess of 1000℃, and in two stages, namely nucleation and growth of the intended phase, both of which represent significant kinetic barriers to formation of the product. High temperatures are needed since ions must be able to diffuse between contacting particles in the batch, requiring high thermal energy and high defect concentration. In the nucleation stage, small crystals of the required stoichiometry and structure form. The nuclei are unstable and spontaneously disintegrate if not of a critical size; the driving force for disintegration arises from the difference between the negative free energy for formation of the phase inside the nuclei and the positive surface energy surrounding the nuclei. Typically, the critical size is in the order of tens of angstroms, hence many hundreds of ions from each reactant must become arranged so as to form a product nucleus [1].

Given that nuclei of a theoretical product, *AB*, have formed at the interface between two reagent particles, *A* and *B*, the growth of the product now requires interdiffusion of *A* and *B* species through the *AB* layer, as shown in Figure 2.2. *A* and *B* ions diffuse through the *AB* layer to the reaction interfaces at *B* and *A*, respectively. As the reaction proceeds, the reaction interfaces move further into the reactant particles and the diffusion pathlengths for *A* and *B* become longer, thus slowing the rate of reaction. Even with a well-mixed batch of < 1 μm-size particles, reactions are slow since mixing on the atomic scale is poor, *i.e.* the surface area of *A* in contact with *B* is low, and the batch may take several tens of hours to fully react. During solid state reactions, therefore, frequent regrinding is necessary to break up the larger *AB* layers and create new reaction interfaces between unreacted *A* and *B* surfaces.

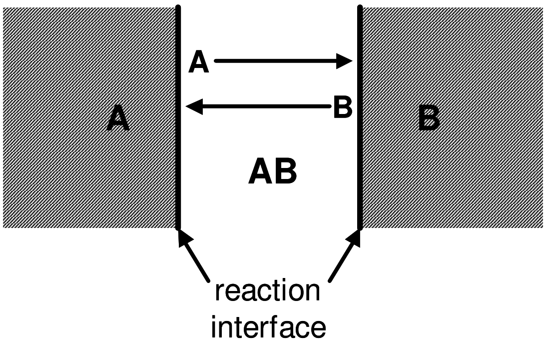

Figure 2.2: Growth of product AB between reactants A and B.

In certain systems, the solid-state diffusion of *A* and *B* may be bypassed by faster transport mechanisms facilitated by a gas or liquid phase. In such cases, the reaction rates are significantly increased [1].

2.1.4. Sintering

Sintering occurs above the reaction temperature, and involves bonding of particles and elimination of pores, decreasing the volume of the green body and, therefore, increasing density. There are two groups of variables that can control the overall sintering processes: processing variables and characteristic properties of the green body. Processing variables include furnace heating/cooling rates, final temperature, dwell time and atmosphere. Characteristic properties of the green body include density before firing, size and shape of particles and the nature and quantity of impurity ions [2].

2.1.4.1. Driving Force

The driving force for sintering is reduction of surface free energy of the particles, primarily by reduction of the total surface area. Surface energy originates from atoms located at the surface being weakly bonded compared with atoms located within the bulk. Surface topography also affects surface energy, as shown schematically for 2 planes of cubic "atoms" in Figure 2.3, where plane A is located above the infinite plane B. The atoms on plane B are all 5 coordinate, apart from those located under plane A that are in the bulk-like 6 coordinate environments. However, atoms located on the edge of plane A occupy 4 coordinate sites and atoms located on the corners only have a 3 coordinate site.

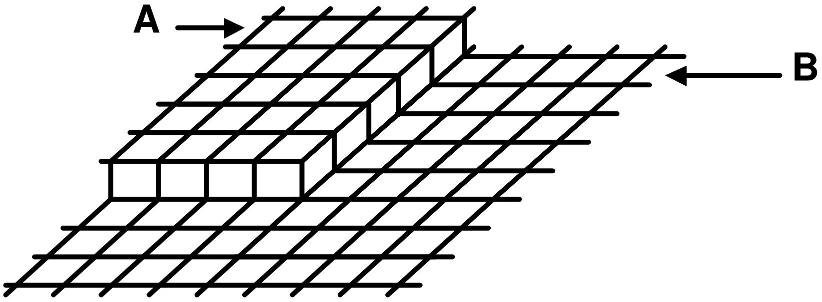

Figure 2.3: Schematic illustration of 2 planes of cubic "atoms" on a surface.

Surface energy is, therefore, greater for convex surfaces where there is a higher proportion of 3-coordinate corner-occupying atoms than for concave surfaces, where the lower energy 4-coordinate edge sites are predominant over corner sites. As a result, the particles in the green body should ideally by μm-size spheres since this geometry has high surface area [2].

2.1.4.2. Stages of Sintering

In general, the sintering process occurs in 3 stages [2], as shown in Figure 2.4. Firstly, when the temperature of the green body has reached the sintering temperature, 'necks' are formed at point contacts between particles, Figure 2.4 (a). In the initial stage, Figure 2.4 (b), necks continue to grow and the pore volume is reduced. By the intermediate stage, Figure 2.4 (c), grain boundaries replace the point contacts between particles, although the pores remain interconnected at the grain boundary junctions until the final stage, Figure 2.4 (d), when grain growth has decreased the pore volume further, causing the pores to become isolated along grain boundaries, grain boundary junctions or within the grains themselves.

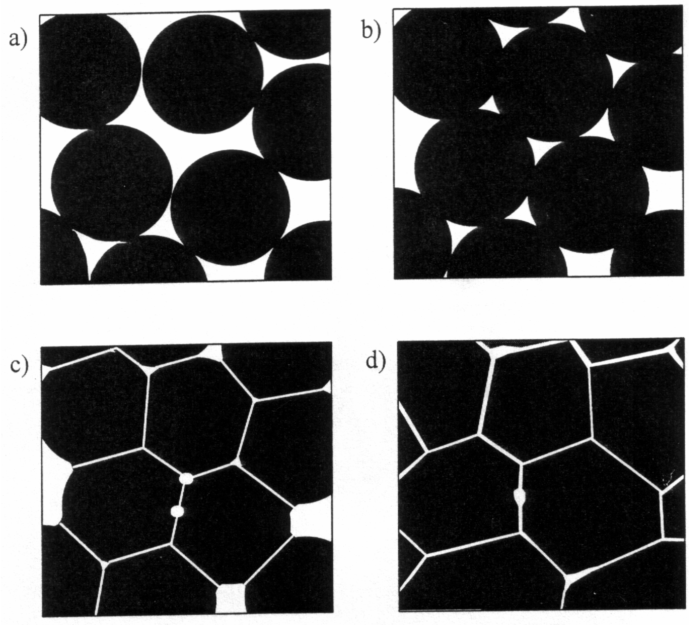

Figure 2.4: Microstructural evolution during sintering showing (a) neck growth between particles, (b) pore volume shrinkage, (c) grain boundary formation and (d) final microstructure. Reproduced from [2].

During the initial stage, transport occurs by surface diffusion, as opposed to bulk diffusion. In the ideal case of two spherical particles in contact, as shown in Figure 2.5 (a), the spherical surfaces of the particles represent regions of high vapour pressure while the concave surface of the neck corresponds to a region of low vapour pressure. Neck growth, therefore, arises as a result of evaporation from the spherical surface from both particles and subsequent condensation on the concave surface of the neck, as indicated by the arrows. Densification by surface transport is limited, however, since the particles do not approach one another and so there is no change in volume.

As the intermediate stage approaches, material is transported from within the particle to the neck region, resulting in shrinkage, and therefore densification, as the particles approach one another, as shown in Figure 2.4 (b). Bulk transport occurs by volume diffusion and grain boundary diffusion, although plastic flow and viscous flow tend to be observed in amorphous materials. Volume diffusion is facilitated by migration of vacancies from within the bulk to the surface. Grain boundaries have an intrinsically high concentration of vacancies and, as such, represent regions of high diffusivity along which the material diffused from within the bulk can be transported to the neck regions.

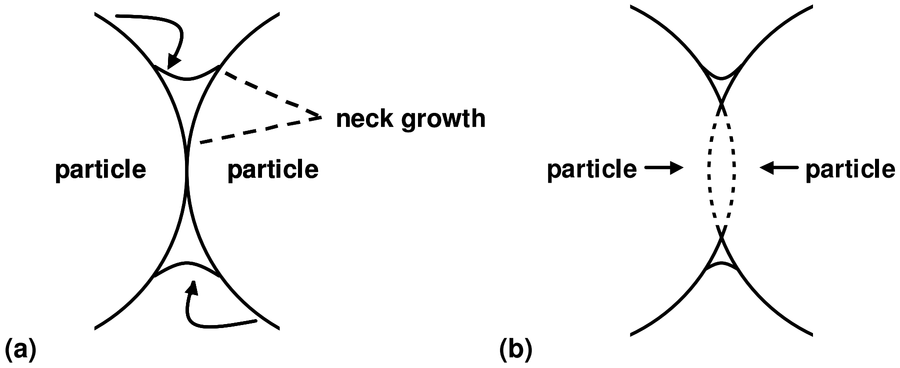

Figure 2.5: Schematic illustration of neck growth between two particles by (a) surface transport and (b) vacancy diffusion. Adapted from [2].

Grain growth occurs as the intermediate stage progresses, reducing poor volume until, at the final stage, the pores are no longer interconnected and lie isolated within grains, along grain boundaries or at grain boundary triple junctions, as shown in Figure 2.4 (d). Pores located within grains restrict densification since diffusion of ions through the bulk does not occur as readily as diffusion along grain boundaries, hence such pores shrink more slowly than those located on grain boundaries. Pore shrinkage may be further restricted if they contain a gas phase. As shrinkage progresses, the pressure in the pore will increase until no further shrinkage is possible. It may be, however, that the gas is soluble such that the gas diffuses away from the pore to a larger pore of lower pressure. Eventually the larger pore may begin to grow and the density of the ceramic will decrease with sintering time.

2.1.4.3. Uniform and Abnormal Grain Growth

During the intermediate stage, the mean grain size increases steadily with time to minimise the total grain boundary surface area, and hence minimises the grain boundary surface energy. For most ceramics, the increase in grain size (*i.e.* diameter of the grain) occurs according to:

$$G^n = G_0^n + Kt \qquad (1.1)$$

where G is the grain size at time t, G_0 is the initial particle size, n is a constant between 1 and 4 and K is a constant associated with the geometry and material properties of the grains.

Although the mean grain size increases during sintering, grain growth occurs by large grains growing into adjacent small grains [2]. Shrinkage of smaller grains is contradictory to their thermodynamically driven need to reduce surface, and occurs by large grains exerting a greater effective pressure on the smaller grains. The pressure originates from the interaction of surface tensions (the force exerted by surface energy) from grain boundaries at triple junctions. In 2-dimensions, these can be considered as 3 line tensions, γ_1, γ_2 and γ_3, radiating from the centre of the junction as shown in Figure 2.6. The tensions are isotropic when angle $\gamma_3\gamma_2 = \gamma_2\gamma_1 = \gamma_1\gamma_3 = 120°$. If $\gamma_3\gamma_2 < 120°$ then an effective tension occurs towards the centre of grain *A* from each triple junction, causing the grain boundaries of *A* to become concave (when viewed from the centre of the grain).

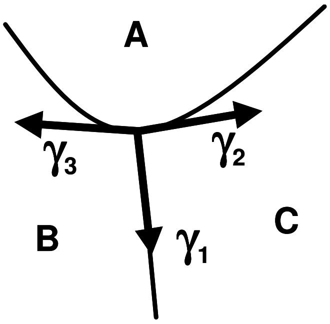

Figure 2.6: Line tensions at a grain boundary triple junction by grains A, B and C.

The concave surface of *A* implies that the pressure surrounding *A* is greater than the pressure within *A* and so there is a driving force to diffuse atoms from *A* and into the surrounding grains, causing *A* to shrink. Conversely, if $\gamma_3\gamma_2 > 120°$ then the effective tension pulls away from grain *A* at each triple junction and the grain boundaries become convex, when viewed from *A*. In this case, the pressure is greater within *A*, and atoms diffuse from the surrounding grains into *A*, such that *A* grows at the expense of its neighbours.

Abnormal or discontinuous grain growth results in a broad and/or bimodal grain size distribution, in which a number of grains have grown faster than the other grains. This can occur as a result of the abnormal grains having a higher coordination number early in the initial stage and therefore having a greater degree of curvature. In many systems, however, abnormal grain growth is poorly understood and may restrict densification [2].

2.1.4.4. Grain Growth Retardation

The rate of grain growth can be limited (or retarded) by segregation of impurity ions to the grain boundaries or by isolated pores or second phase precipitates. In the former case, it is energetically favourable for impurity ions to segregate to the grain boundaries rather than be incorporated into the bulk lattice. As the grain boundary moves during grain growth, the impurity ions must either diffuse cooperatively with the grain boundary or occupy higher energy sites within the bulk as the boundary passes. Since the segregated impurity ions occupy the vacancies that facilitate grain boundary diffusion, their presence significantly retards grain growth [2].

Precipitates and pores can retard grain growth by ‘pinning’ the grain boundaries. As such, when a grain boundary intersects a pore or precipitate, the grain boundary surface area, and therefore surface energy, is reduced so there is a strong driving force for intersection to occur. To leave the precipitate behind, however, would require an increase in surface energy so there is a tendency to impede the grain boundary motion as the precipitate is effectively ‘dragged’ through the lattice. Since grain boundary surface energy increases with increasing degree of curvature, pinning tends to occur towards the final stage of sintering when significant growth has occurred and the overall grain boundary curvature has decreased [2].

2.1.4.5. Liquid Phase Sintering

Liquid phase sintering (LPS) occurs when liquid is present at the sintering temperature and assists densification by improving sintering kinetics. Aside from the presence of liquid, LPS requires that the liquid fully wets solid particles and that the solid phase has significant solubility in the liquid. Furthermore, the volume fraction of liquid is usually < 20% to prevent flow of the body at high temperature [2, 3].

The stages of LPS are shown schematically in Figure 2.7. Initially (stage 0), particles are loose packed in the green body and liquid phase evolves, wetting the solid particles as the body is heated to the sintering temperature. At stage 1, the particles rearrange, becoming more closely packed. During stage 2, solution-precipitation occurs whereby the particles are pulled together and dissolution occurs at the interface while precipitation occurs at the edge of the interface, as shown in Figure 2.8 (a). The solution-precipitation process aids densification by transferring material into the pores between particles and reducing curvature of the grains, as shown in Figure 2.8 (b).

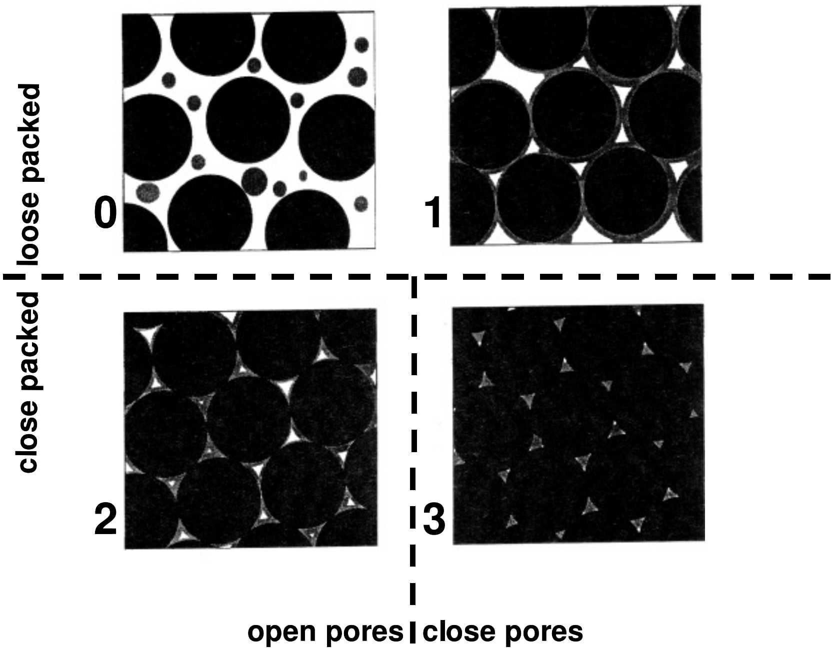

Figure 2.7: Stages of liquid phase sintering, reproduced from [2].

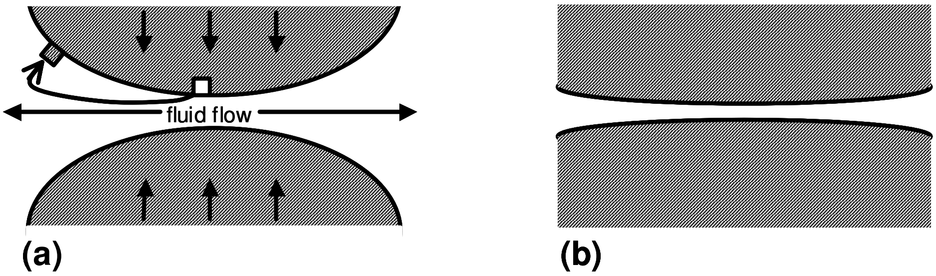

Figure 2.8: (a) Solution-precipitation during stage 2 and (b) resulting decrease in curvature at particle-liquid-particle interface. Adapted from [3].

For a fully wetted LPS system, grain growth occurs during stage 2 by diffusion of material from small grains to large grains, as in solid state sintering, but this occurs via the liquid phase. The rate of growth may, therefore, depend not only on the mobility of ions in the lattice, but also mobility in the liquid phase and dissolution reactions at the particle-liquid interface.

As with solid state sintering, the final stage (stage 3 in Figure 2.7) is reached when the pores are no longer interconnected. Pores may contain gas and/or liquid and so the phenomenon of decreasing density observed in solid state systems may also occur in LPS. Upon cooling, the liquid solidifies into an amorphous or crystalline 2nd phase present along the grain boundaries, in pores and at grain boundary triple junctions.

2.2. Analytical Techniques

2.2.1. X-ray Diffraction

X-ray Diffraction (XRD) facilitates the identification of crystalline phases in a sample and refinement of corresponding unit cell/lattice parameters. The technique is commonly used to determine crystal structures, study phase assemblage following a solid state reaction and detect secondary or impurity phases in reacted samples [1].

2.2.1.1. X-ray Generation

X-rays occur when electrons accelerated by a potential difference of ~ 30 kV – 40 kV collide with a metal target. Production of x-rays is facilitated by an x-ray tube, shown schematically in Figure 2.9, containing a tungsten filament and metal target in high vacuum. The filament is heated by applying a small current and a high voltage generator applies a large positive bias to the target. Cooling water is circulated around the target to prevent melting. The large potential difference between the filament and the target causes electrons to be emitted from the filament and accelerated toward the target. A broad spectrum of x-rays, referred to as ‘white’ or Bremsstrahlung radiation, is produced as a result of loss of kinetic energy by the electrons during impact. X-rays also occur at certain discrete wavelengths, arising from ionisation of outer shell electrons in the metal atoms of the target; the wavelengths of such x-rays are characteristic of the metal [1].

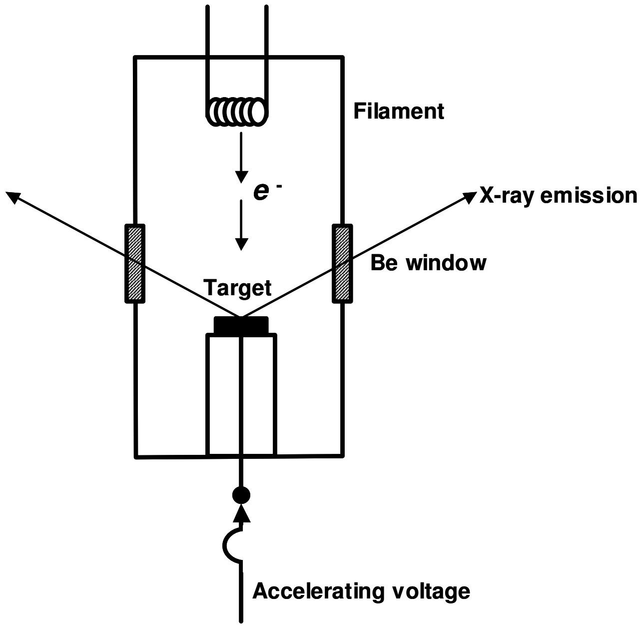

Figure 2.9: Schematic diagram of an x-ray tube, adapted from [1].

The x-rays are emitted from the tube via Be windows with little change in intensity, while the tube casing absorbs all x-rays not directed at the windows. For XRD, monochromatic x-rays are required and so a monochromator and/or metal foil filter are often used to eliminate all x-rays apart from those occurring at the most intense wavelength, usually associated with the characteristic Kα_1 edge. Targets commonly used in XRD at Cu, Cr and Mo with Kα_1 wavelengths of 1.5405 Å, 2.2896 Å and 0.7093 Å, respectively [1].

2.2.1.2. Diffraction of X-rays in Crystals

Waves tend to be diffracted from their incident angle if passed between two points that are separated by a distance of approximately one wavelength, λ. In the case of crystalline phases, these point diffraction sources are atoms separated by distances between 1 - 3 Å, equivalent to wavelengths of characteristic x-ray radiation.

In Figure 2.10 (a), a beam of x-rays is shown passing through a plane of atoms and being re-radiated in all directions as a consequence of individual waves being diffracted. Depending on the angle of diffraction, two waves may become out-of-phase or remain in-phase with one another, as shown in Figure 2.10 (b). Viewed along direction 1, the waves are in-phase and interfere constructively, such that a beam of x-rays is present in this direction. A beam also occurs in direction 3, since the two waves are again in-phase. In direction 2, however, the waves are 180° out-of-phase and no beam can occur in this direction since the two waves interfere deconstructively and cancel each other. Between directions 3 and 2, and direction 2 and 1, the two waves are out-of-phase but the interference is insufficient to achieve cancellation and so the beam intensity decreases gradually to zero when viewed from direction 3 or 1 through to 2.

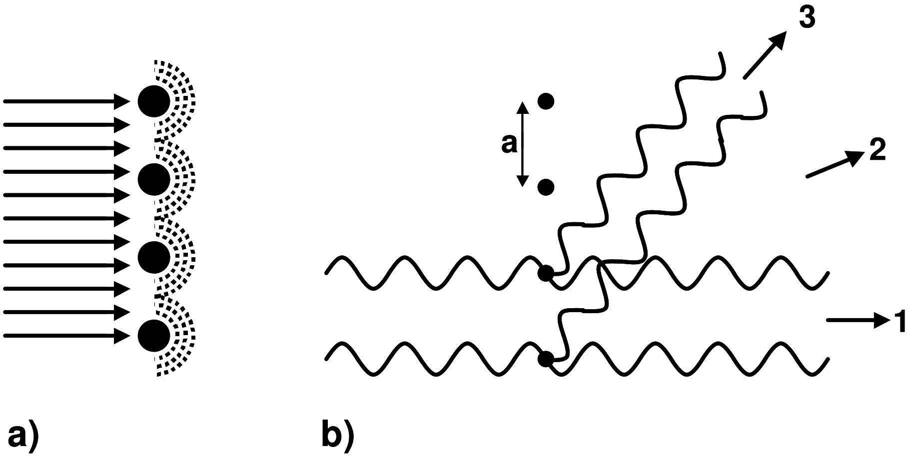

Figure 2.10: Diffraction of X-rays in a crystalline solid showing (a) incident X-rays diffracted by a plane of atoms and (b) constructive and deconstructive interference between diffracted waves. Adapted from [1].

In the case of a large plane of atoms, however, the diffracted beam only occurs at certain angles for which the waves are in-phase. Bragg's law of diffraction determines the angle at which a diffracted beam occurs, θ, according to the interatomic spacing between adjacent planes, d, and wavelength of the incident beam, λ, as defined in Equation 2.2:

$$2d \sin \theta = n\lambda \qquad (2.2)$$

where n is the diffraction order of the diffracting plane, and is usually unity for XRD [1].

Provided the symmetry of the unit cell is know, Miller indices can then be assigned to the observed reflection from a set of parallel planes separated by a distance d, and then unit cell parameters refined. Identification of an unknown phase can also be achieved using the Powder Diffraction File, in which patterns of all known crystalline phases are recorded [1].

2.2.1.3. X-ray Diffraction Techniques

Two common XRD techniques are diffractometry and the Guinier focussing method [1], shown schematically in Figure 2.11 (a) and (b), respectively. In both systems, a beam of monochromatic x-rays is produced by passing the emission from an x-ray tube through a series of slits and on to a monochromator. In a diffractometer, however, the beam is usually transmitted through the monochromator and towards the sample. The diffractometer in Figure 2.11 (a) is of the transmission type although reflection type instruments are common. The intensity of the diffracted beams are registered by a detector as it moves along the arc indicated in the diagram. The sample stage rotates contrary to the detector, so that the angle between the incident beam and the detector is 2θ. The data are stored by a computer and can be plotted as intensity vs. 2θ or *d*. A beam stop prevents the transmitted beam damaging the detector, and so the sample stage may be rotated to avoid discontinuity in the data.

In the Guinier-focussing camera, a convergent monochromatic beam is reflected from a curved monochromator to the sample and diffracted within a circular film case, as shown in Figure 2.11 (b), exposing photographic film placed around the circumference. Upon developing and fixing the film, sharp lines are observed where the diffracted beams have converged. Measuring the distance from a reference point on the film, or 'back-stop', to each line can then be used to determine *d*-spacing or 2θ values by comparison with a conversion table.

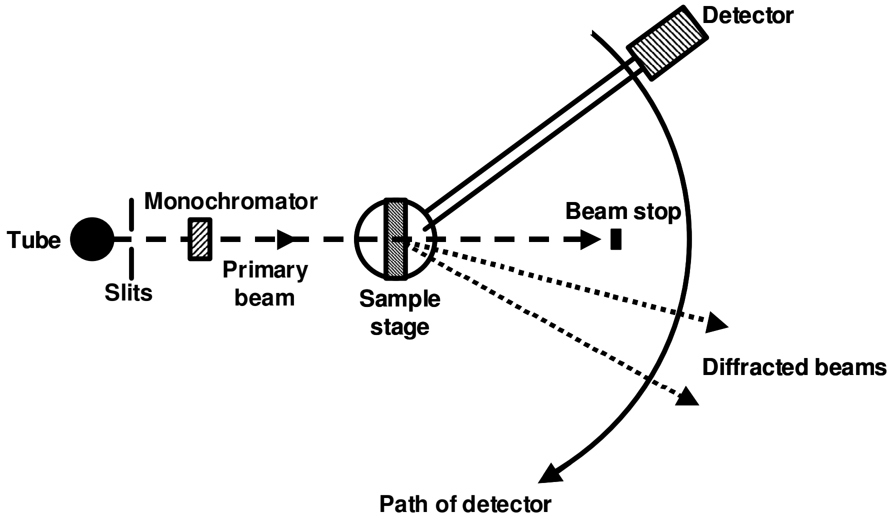

(a)

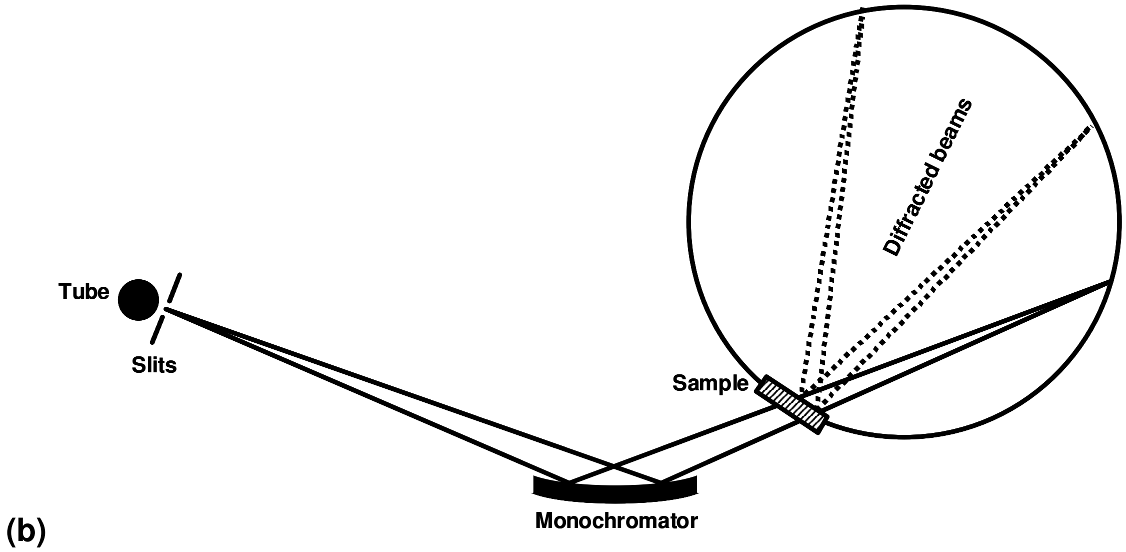

Figure 2.11: Schematic layout of (a) X-ray diffractometer and (b) Guinier-focussing camera. Adapted from [1].

2.2.2. Electron Microscopy

Several advantages are held by electron microscopy over optical microscopy. The wavelengths of electrons are less than those of photons, allowing finer detail to be resolved and electron-sample interactions facilitate localised characterisation of chemical composition, crystal structure and crystal defects [4].

2.2.2.1. Resolution

The focussing of an electron beam by electromagnetic ‘lenses’ is analogous to focussing a beam of light [4], as shown in Figure 2.12. The resolution limited by Rayleigh diffraction, R_d, for this configuration is given by Equation 2.3:

$$R_d = (0.61\ \lambda)/\mu \sin \alpha \qquad (2.3)$$

where λ is wavelength, μ is refractive index and α is the aperture semi-angle as shown in Figure 2.12. The wavelength, λ, of an electron in a vacuum accelerated by a voltage, V, is given by:

$$\lambda = 1.23 / \sqrt{V}\ \text{nm} \qquad (2.4)$$

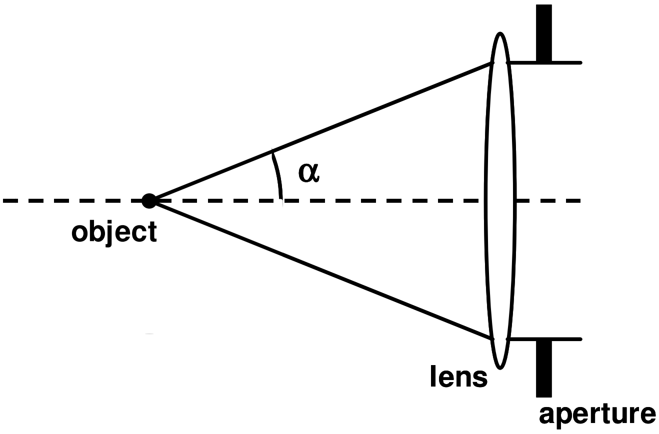

Figure 2.12: Focussing of light by a convex lens. Adapted from [4].

Electrons are unrefracted in the high vacuum conditions of an electron microscope and so $\underline{\mu}$ is considered unity [4]. Furthermore, deflection angles in an electron microscope are considered small enough that Equation 2.3 can be simplified to:

$$R_d = 0.61\ \lambda/\alpha \qquad (2.5)$$

The resolution limit can be reduced, therefore, by decreasing wavelength (hence increasing accelerating voltage) and increasing α, e.g. by widening the aperture.

For any microscope, the resolution is further restricted by lens imperfections, *i.e.*: chromatic aberration, astigmatism and spherical aberration [4]. Chromatic aberration occurs as a result of the refracting power of a lens varying with wavelength, such that a spectral beam is brought to focus at different points, so there is no longer a unique focal point. The effect is minimised by using a monochromatic electron beam, but minor chromatic aberration arising from inelastic scattering events between the beam and sample are unavoidable. Astigmatism occurs as a result of variation in diffracting properties between the horizontal and vertical planes. In electron microscopy, astigmatism can be corrected such that it does not impinge on the effective resolution. Spherical aberration is of greater significance in terms of determining the resolution limit, and arises when rays close to the optic axis are brought to focus at a different point to rays far from the central optic axis. Spherical aberration is limited by reducing α, contrary to Equation 2.5, and so the aperture size must be optimised to minimise Rayleigh diffraction and spherical aberration [4].

2.2.2.2. Electron-Specimen Interactions

Upon reaching the specimen, electrons in a focussed beam undergo a number of interactions or scattering events [1, 4]. The nature of the scattering implies that excitation also occurs beneath the sample surface in a region below the beam called the interaction volume. Interaction volume increases with accelerating voltage and decreases as the density or atomic number increases. For accelerating voltages > 20 kV, the interaction volume is in the order of 10 μm^3. Electron-specimen interactions can be described as inelastic or elastic, depending on whether the electrons scatter with or without a significant loss in energy, respectively. Phonon and plasmon scattering are two inelastic scattering events that may be detrimental to electron microscopy. In the former case, electrons from the primary beam excite phonons in the sample, resulting in localised heating and possible sample degradation. In the latter case, primary beam electrons excite plasmons (or pulses) in the sample's free electron 'gas' yet the effect tends to be unnoticeable apart from adding to background noise in certain techniques.

If an electron achieves a 'direct hit' on the atomic nucleus, there is the possibility of displacing the atom and degrading the sample. For accelerating voltages < 100 kV, this is more likely to happen in polymers than in tightly-bound crystalline ceramics. An electron may be inelastically scattered as it passes close to the nucleus; those that are deflected back towards the primary beam are termed backscattered electrons. Backscattered electrons have high energy and tend to escape from deep within the interaction volume. Inelastically scattered electrons occur as a result of primary beam electron interactions with the atomic orbitals and tend to be deflected at lower angles than elastically scattered electrons [1].

The energy loss experienced by the electrons during inelastic scattering occurs by emission of Bremsstrahlung X-rays, as described in Section 2.2.1.1. Associated with inelastic scattering is the ejection of tightly bound electrons in the form of lower energy secondary electrons. Characteristic X-rays and Auger electrons are then emitted as the ion decays from the excited state. Secondary electrons tend to emerge from only the surface of the interaction volume, since they have too low an energy to escape from below the surface without being absorbed [1].

2.2.2.3. Scanning Electron Microscopy

The principle of operation of an SEM is shown in Figure 2.13. The sample is mounted on a stage in a high vacuum (1×10^{-5} Torr) at the base of a column. An electron 'gun', located at the top of the column, emits a beam of electrons focussed electromagnetically by the condenser lens, then the objective lens. Below the objective lens, the beam is deflected by a system of scanning coils, controlled by an external generator, such that the focussed beam 'scans' the sample surface line-by-line. A positively charged detector located near the sample collects the emitted electrons and, via an amplifier, sends an 'intensity' signal to a cathode-ray-tube display [4].

In most SEM columns, two detectors are present, one dedicated to the detection of secondary electrons and the other to detecting backscattered electrons. Secondary electron image (SEI) mode provides a topographical view of the specimen, whereby edges and protrusions on the sample surface appear brighter than flat regions while pits and grooves appear darker, since fewer secondary electrons can escape from these features, as shown in Figure 2.14. Backscattered electron image (BEI) mode forms an image based on atomic number contrast, since the backscatter effect is a result of deflection of electrons by the nucleus and is therefore dependent on atomic weight. BEI mode is also affected by surface topography and so it is necessary for the surface to be polished flat with a roughness of < 1 μm in order to eliminate topographical contrast [4].

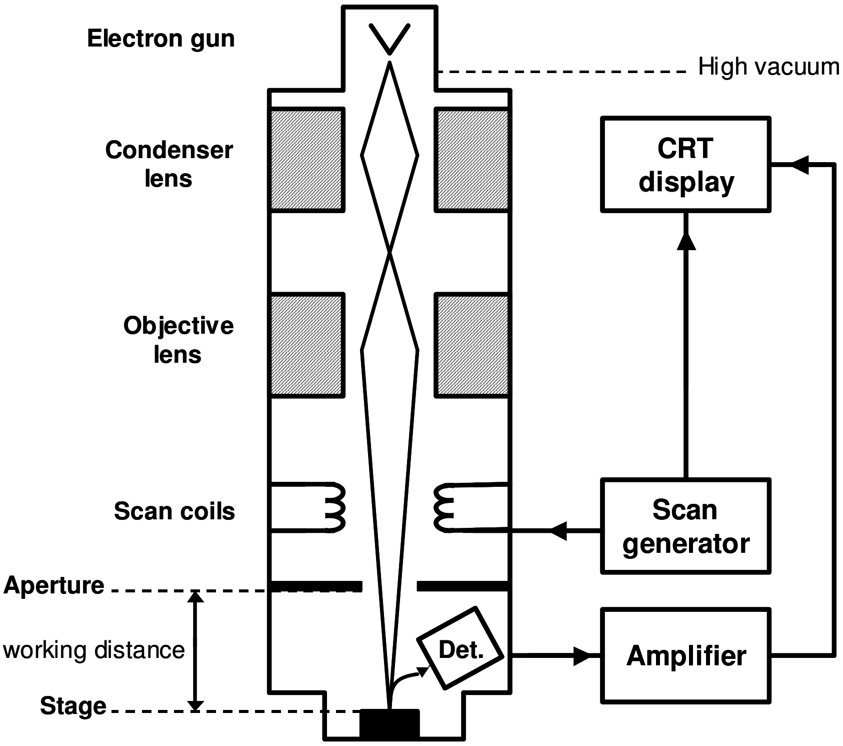

Figure 2.13: Typical layout of an SEM, adapted from [4].

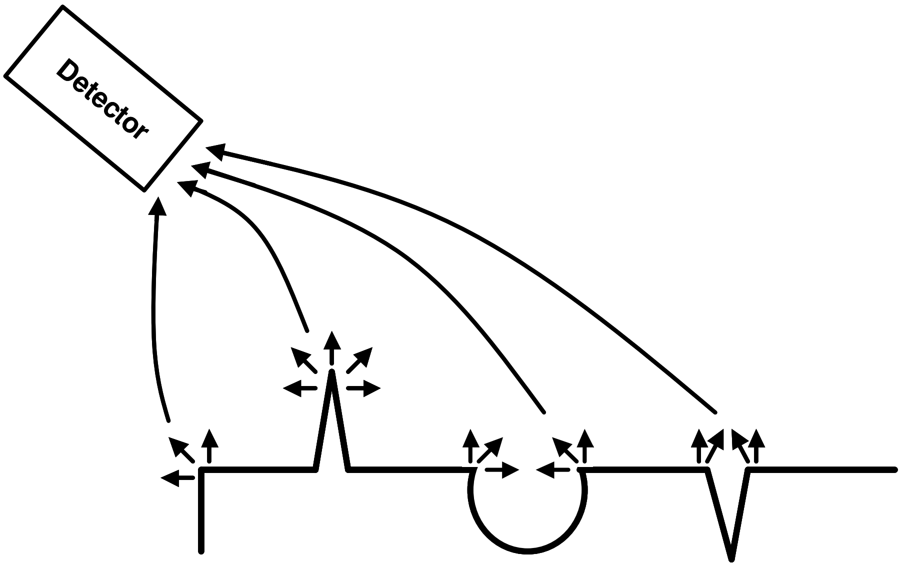

Figure 2.14: Schematic illustration of electron emission from topographic features, adapted from [5].

2.2.2.4. Chemical Analysis in Electron Microscopy

The characteristic X-rays emitted as a result of electron beam-specimen interactions provide information regarding the chemical composition within the interaction volume. Such X-rays can be detected and characterised qualitatively by energy dispersive spectroscopy (EDS) or quantitatively by wavelength dispersive spectroscopy (WDS) [4].

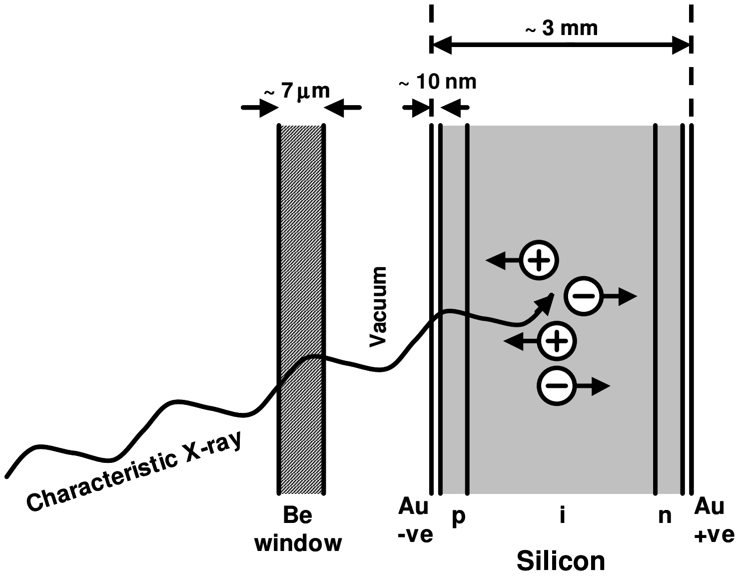

Figure 2.15: Principle of an EDS detector. Adapted from [4].

The EDS detector consists of doped *p-i-n* silicon wafer sandwiched between two gold electrodes, as shown in Figure 2.15. X-rays enter the detector through a Be window and excite electrons in the wafer, leaving positive holes in the outer shells (the detector is cooled to 77 K, minimising noise arising from thermal excitations). The electrons and positive holes migrate to the *n*-type and *p*-type layers, respectively, such that a current flows in an external circuit between the electrodes. Since the characteristic wavelength of each X-ray determines the number of electrons excited in the wafer, the measured current can be converted to wavelength and compared with known values in order to identify the elements present.

The technique is limited to detecting only elements heavier than Na, since the window absorbs X-rays emitted from lighter elements. EDS also detects Bremsstrahlung radiation, giving rise to substantial background noise, and characteristic X-rays of similar wavelengths tend to be poorly resolved. Furthermore, X-rays may be absorbed in the sample if they originate from relatively light elements located within the interaction volume, and so heavier elements nearby are likely to give a disproportionately greater EDS signal. EDS is, therefore, more suited to qualitative identification of elements, rather than accurate quantitative analysis. It can also be implemented in TEM and SEM [4].

WDS is commonly implemented in a dedicated microscope, similar in principle to the SEM, and used in electron-probe microanalysis (EPMA). Whereas EDS passively detects x-rays over a spectrum of wavelengths, WDS selectively filters all wavelengths apart from one that is characteristic of the specified element. The filter is an x-ray spectrometer, shown schematically in Figure 2.16.

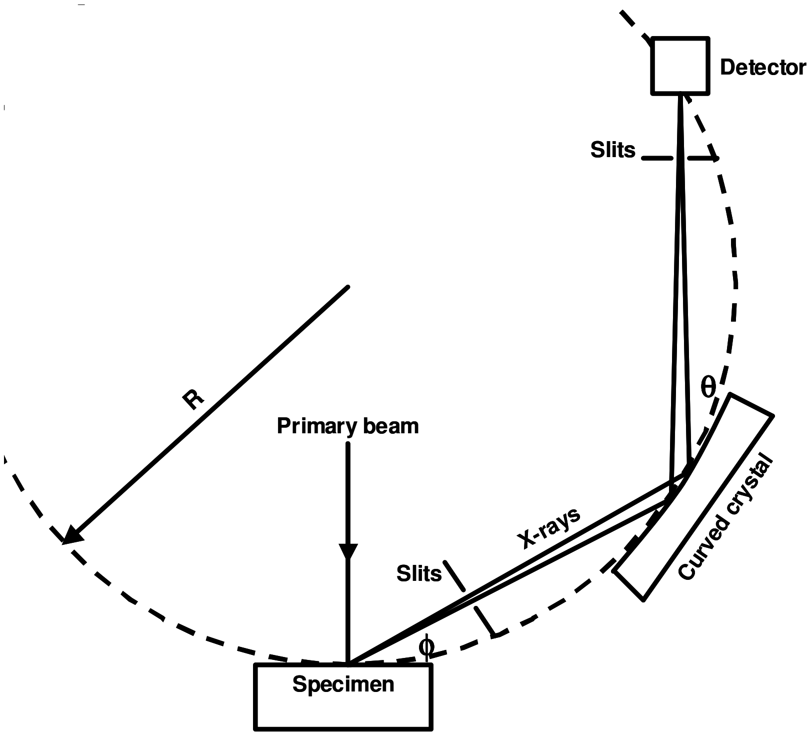

Figure 2.16: Layout of an X-ray spectrometer used in WDS/EPMA. Adapted from [4].

X-rays leaving the sample at the take-off angle, ϕ, pass through a set of slits and reach the curved crystal. At this point, only those x-rays with a wavelength corresponding to θ (according to Bragg's law) reach the detector. θ can, therefore, be set to a specific angle corresponding to a wavelength characteristic of the required element. As a result, the accuracy of the techniques is sufficient for reliable quantitative analysis [4].

2.2.3. Thermogravimetric Analysis and Differential Thermal Analysis

Thermogravimetric analysis (TGA) and differential thermal analysis (DTA) are used to investigate thermally activated phenomena in materials [1]. Both methods allow, in principle, study of thermal behaviour in various atmospheres provided by flowing O_2, N_2, H_2/Ar, etc. through the sample chamber. TGA is shown schematically in Figure 2.17 (a) in which the sample is located in a crucible within a furnace and is connected to a balance. The furnace is heated to a set temperature at a predefined ramp rate and the temperature within the sample chamber is monitored by a thermocouple placed near the crucible, allowing the mass of the sample to be recorded as a function of temperature as shown in Figure 2.17 (b). Any changes in sample mass occurring as a function of temperature by dehydration or decomposition, for example, can be detected and quantified. The example in Figure 2.17 (b) is typical of a decomposition process such as loss of CO_2 from $CaCO_3$ in which the onset of decomposition for a sample of mass M_i commences at T_i and finishes at T_f when no further change in mass is evident. The mass lost by decomposition can, therefore, be quantified as the difference between M_i and the final mass, M_f.

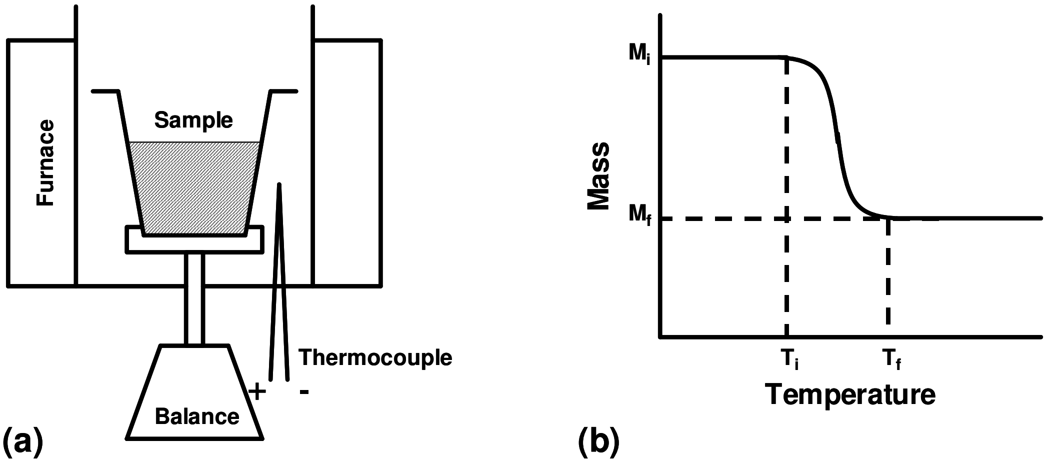

Figure 2.17: Schematic illustration of (a) TGA apparatus and (b) data from a TGA experiment. Adapted from [1].

DTA is used to detect thermal events that may not affect sample mass, such as phase changes or crystallisation, and compares the difference in temperature between the sample and a reference during a heating cycle, since exothermic and endothermic reactions cause the sample temperature to lead or lag that of the reference, respectively. The apparatus is shown schematically in Figure 2.18 (a).

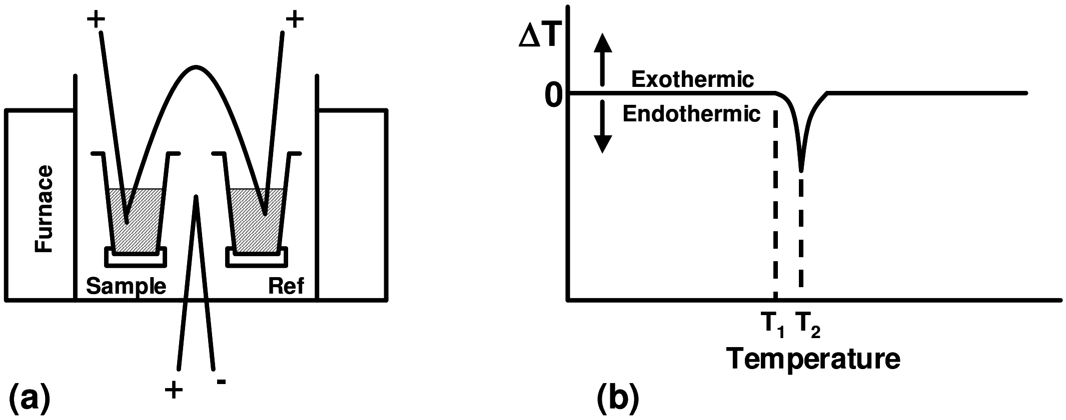

Figure 2.18. Schematic illustration of (a) DTA apparatus and (b) data from a DTA experiment. Adapted from [1].

The sample and reference are located in a furnace. Similar to TGA, the furnace is heated to a set temperature at a given ramp rate and the temperature in the sample chamber is measured by a thermocouple and recorded. Two more thermocouples are placed in the sample and reference, respectively, and connected 'back-to-back' as shown in Figure 2.18 (a). As a result, a signal is generated when there is a difference in temperature, ΔT, between the sample and reference. ΔT can then be plotted as a function of temperature as shown in Figure 2.18 (b), although data can also be plotted to show endothermic events as positive peaks and exothermic events as negative. Furthermore, although the area of the peaks is related to the magnitude of the changes in enthalpy during a given thermal event, most DTA experiments allow for only qualitative analysis.

2.2.4. Impedance Spectroscopy Measurements

Two principal approaches to measuring the impedance of a given sample are the bridge method and the current-voltage (I-V) method[6], shown schematically in Figures 2.19 (a) and 2.19 (b), respectively. In the bridge method, the unknown impedance of the sample, Z_x, can be determined from the relationship between the bridge elements Z_1, Z_2, Z_3, which may be various combinations of perfect resistor, capacitor or inductor components. In the I-V method, the current flowing through the sample is determined from the voltmeter reading, V_2, across a standard, low value resistor, and the voltage across the sample measured by the voltmeter V_1.

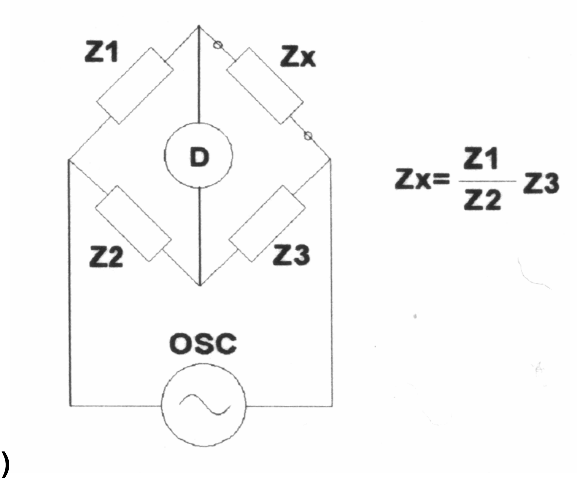

(a)

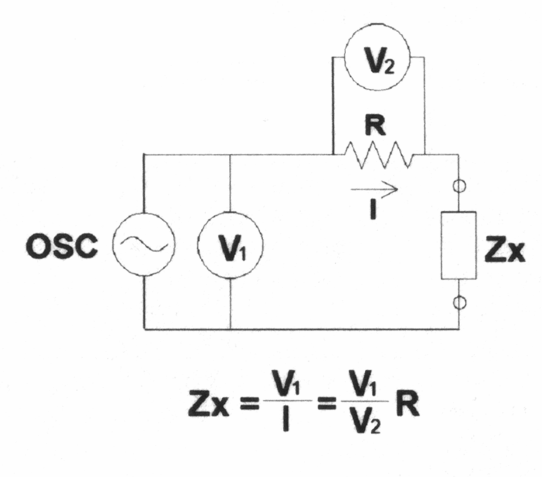

(b)

Figure 2.19: Impedance measurement by (a) bridge and (b) I-V method, after Okada [6].

2.3. Methodologies

2.3.1. Solid State Synthesis and Sintering

Resistance furnaces provided the high temperatures required for solid-state synthesis and sintering. All samples were reacted in Pt crucibles to prevent reaction with the furnace linings and in the case of compositions based on volatile species (i.e. Bi and Cd) the crucibles were also covered. A furnace can be regarded as a reaction vessel and, as such, separate furnaces are used to prevent cross-contamination of volatile species. Dedicated furnaces were available for transition metal-based compositions and Cd/Bi-based compositions.

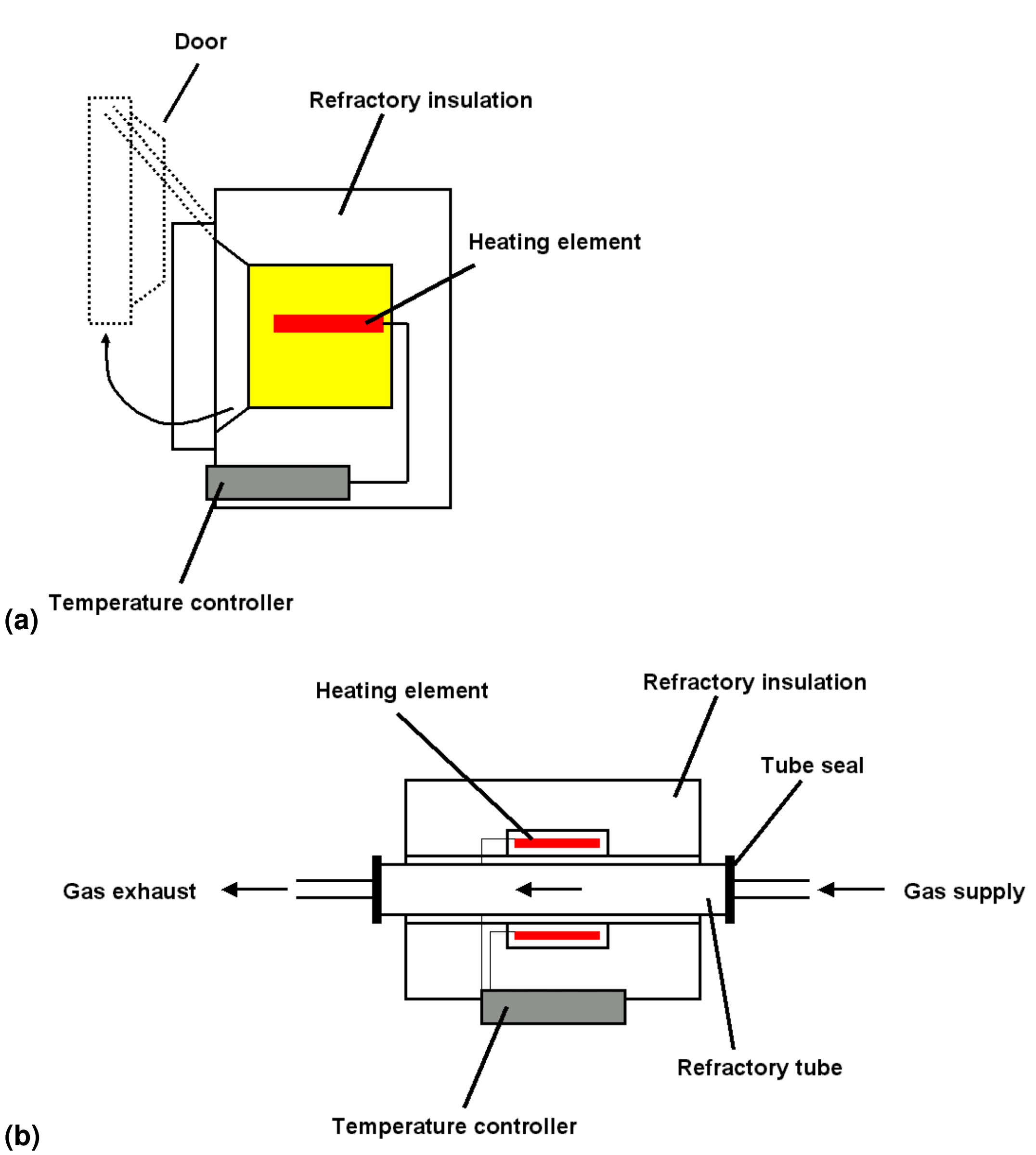

Figure 2.20: Schematic diagram of (a) muffle and (b) tube furnace configurations.

The muffle and tube furnaces are two configurations of furnace in common use, shown in Figure 2.20. Both types achieve high temperature by electrical resistance heating elements. The current supplied to the elements is controlled by a temperature controller that may be programmed with dwell times and heating and cooling rates. The atmosphere within the chamber of a typical muffle furnace is air, with no control over oxygen partial pressure. The tube furnace, however, allows limited control over pO_2 by flowing gas through the tube. If a low pO_2 is required then oxygen is purged from the tube by flowing N_2 or H_2 – Ar, for example. When high pO_2 is required, therefore, pure oxygen is flowed through the tube. The major disadvantage of the tube furnace configuration is that a substantial thermal gradient exists along the tube, such that the sample must be located centrally in the “hot spot” where the target temperature is actually reached. This is further complicated by the fact that the position of the hot spot is somewhat dependent on the flow of gas through the tube.

2.3.2. Sample Preparation for SEM, EPMA and XRD

For analysing grain size and porosity, sintered samples were stuck on aluminium discs using silver electrode paste and coated with a thin (~ 100 – 200 nm) layer of Au, deposited by sputter coating. Polished sections of sintered pellets were also prepared by mounting in epoxy resin, grinding with SiC paper and polishing with 3 – 1 μm diamond paste on silk polishing laps. Optically transparent sections of sintered pellets were required for EPMA. These were prepared by mounting on a glass slide with wax and grinding the pellet to < 1 μm thickness with SiC paper. The section was then polished using a 3 mm diamond paste on a silk polishing lap until optically transparent, and then briefly polished with a 1 μm diamond paste.

Samples were prepared for powder XRD by grinding to a fine (< 10 mm) powder in an agate mortar & pestle with acetone. The powder was then dried. Powder samples intended for the Hagg-Guiner camera were prepared by dusting onto Magic Tape and stuck to brass mounting rings. Samples intended for the STOE StadiP position sensitive diffractometer were prepared by mixing the powder in a water-based suspension and adding a droplet to an acetate disc. The sample was left to dry for ~ 15 – 20 minutes before being placed in a steel holder for mounting in the diffractometer.

2.3.3. IS Measurements

Prior to taking impedance measurements, the major pellet faces of the sample were lightly polished to eliminate the slight curvature commonly observed after sintering. A thin, conductive coating (the electrode) was then applied to the major faces. Electrodes were mainly metal-based compositions such as Au, Pt, Ag or InGa alloy. Magnetron sputtering may be used to deposition Au or Pt but electrodes based on noble metals, including Ag, may be fabricated by “painting” a liquid suspension of metal particles onto the major pellet faces and sintering the particles together at temperatures > 500 ℃. InGa (60:40 mol ratio) alloy is a convenient electrode material for use at temperatures < ~ 200 °C since it exists as a viscous liquid at room temperature and may be applied by spreading over the major pellet faces with a spatula.

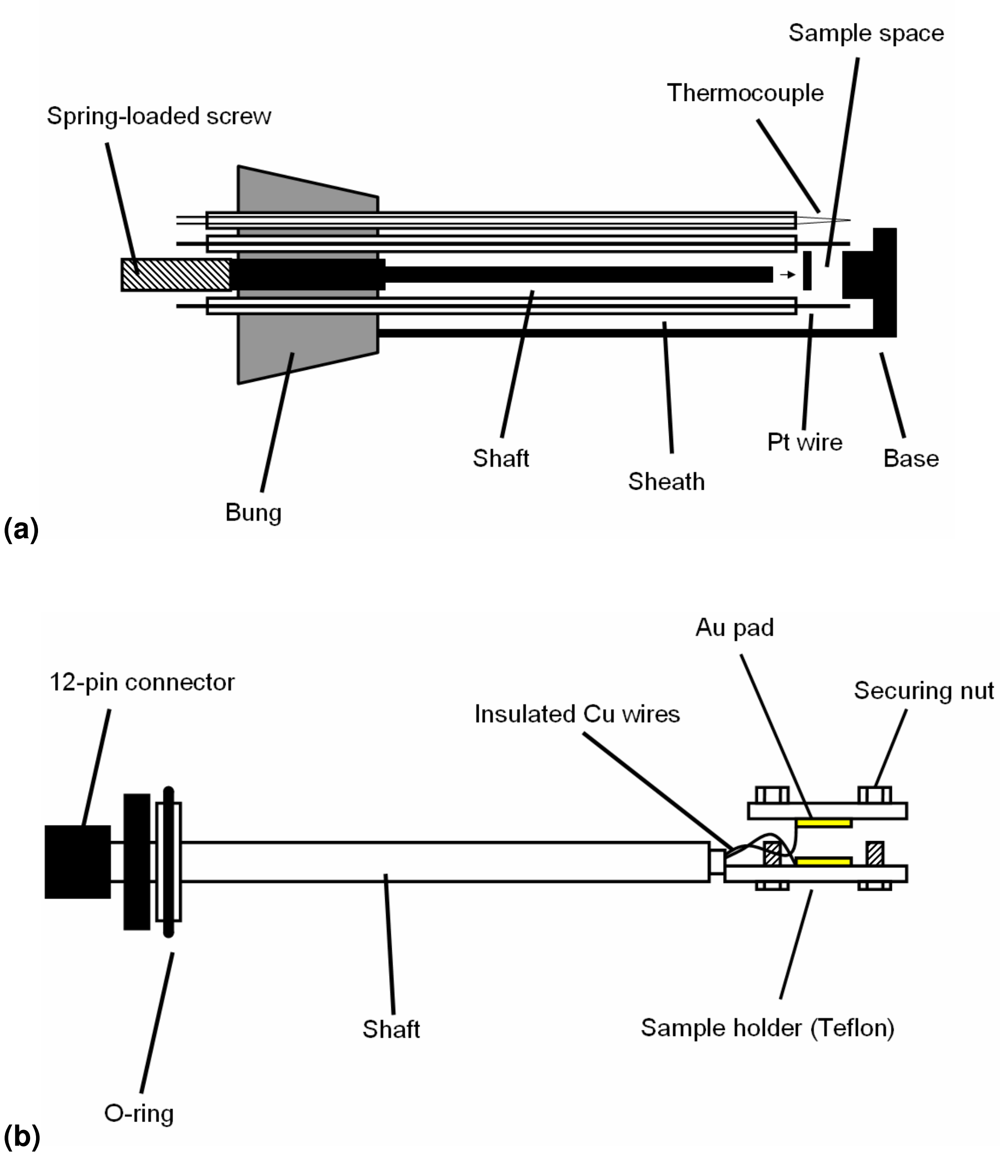

Figure 2.21: Compression-type conductivity jigs used in (a) high temperature measurements (< 500 °C) and (b) low temperature cryostat measurements (77 – 300 K).

The electroded sample was loaded into a conductivity jig to allow connection to the impedance analyser. Two conductivity jigs are shown in Figure 2.21; both were of the compression-type in which the sample electrodes were connected to the jig by pressing contact pads against the major pellet surfaces. In the high temperature jig, Figure 2.21 (a), the contact pads were usually small strips of Pt or Au foil that were crimped around the Pt wires, forming an electrical contact between the Pt wire and the sample electrodes. The jig is then loaded into a tube furnace, similar to that shown in Figure 2.21 (b), and heated to the required temperature. Once the target temperature is reached, a dwell of 15 – 30 minutes was usually required to allow the sample to thermally equilibrate prior to measurement. A thermocouple located close to the sample space allowed more accurate temperature readings than would be available from the furnace's temperature controller. The jig shown in Figure 2.21 (b) was used in conjunction with a liquid nitrogen cryostat for low temperature measurements (70 – 300 K). In this case, the electroded sample was placed between Au pads on opposite Teflon blocks and held in place by tightening the securing screws.

References

1. A.R. West, *Basic Solid State Chemistry*. 2 ed. 1999: John Wiley & Sons.
2. W.E. Lee, W.M. Rainforth, *Ceramic Microstructures: Property Control by Processing*. 1994: Chapman & Hall
3. R.J. Hand, *Sintering (Advanced Materials lecture course, Department of Engineering Materials, University of Sheffield)*, 2001: University of Sheffield
4. P.J. Goodhew, F.J. Humphreys, *Electron Microscopy and Analysis*. 2 ed. 1988.
5. W.M. Rainforth, *Principle of Electron Microscopy (Characterisation of Materials lecture course, Department of Engineering Materials, University of Sheffield)*, 2001: University of Sheffield
6. K. Okada, T. Sekino, *Agilent Technologies Impedance Measurement Handbook*. 2003, Agilent Technologies Co. Ltd.

3. Impedance Spectroscopy - Theory

3.1. Background

The electrical properties of a material may arise from a combination of intrinsic and extrinsic phenomena occurring over a wide range of frequencies. At room temperature, electrical property measurements near 0 Hz (*dc*) are likely to be affected, to some extent, by electrode contact phenomena or long range migration of carriers (in the case of ionic conductors, for example). At frequencies up to ~ 10^4 Hz, the response may be attributable to grain boundary and/or constriction-type impedances. Above ~ 10^5 Hz, the response tends to correspond to intrinsic phenomena in the bulk phase associated with lattice polarisation.

Impedance spectroscopy involves measuring the complex impedance, Z^*, of a sample over a wide range of frequencies (typically 10^{-2} – 10^6 Hz) and temperatures, often from room temperature up to ~ 1000 K. Samples with high conductivity, however, may require measurements at sub-ambient temperatures to obtain the required data. Impedance data can be modelled on an equivalent circuit to identify possible extrinsic and intrinsic responses. Such interpretation requires representation of the data not only in Z* but in several complex formalisms: electric modulus, M^*, admittance, Y^*, and permittivity, ε^*. The formalisms are related to one another thus:

$$Y^* = 1/Z^* \qquad (3.1)$$

$$\varepsilon^* = \frac{1}{j\omega C_0 Z^*} \qquad (3.2)$$

$$M^* = 1/\varepsilon^* = j\omega C_0 Z^* \qquad (3.3)$$

where $j = \sqrt{-1}$, C_0 = 8.854x10^{-14} Fcm^{-1} and ω is the angular frequency in rads^{-1}. ω is related to frequency in Hz, f, by $\omega = 2\pi f$.

NB – Equation 3.3 corresponds to the *relative* electric modulus. An alternative representation used in the following chapters is *absolute* electric modulus where the C_0

term is omitted and the units are in F^{-1}. Similarly, ε^* can be represented as complex capacitance, C^*, in Farads by omitting the C_0 term.

Dielectric loss, or tan δ, is often used as a measure of a capacitor's efficiency and is proportional to the energy converted to heat when an *ac* field is applied to the capacitor. Capacitors based on high permittivity dielectric phases, such as $BaTiO_3$, tend to have tan δ values of ~ 0.01 at 1 kHz whereas microwave dielectrics may have tan δ values several orders of magnitude lower. tan δ is related to complex permittivity, thus:

$$\tan\delta = {\varepsilon''}/{\varepsilon'} \tag{3.4}$$

3.2. Equivalent Circuits

Impedance data can be modelled, to a first approximation, on an equivalent circuit composed of ideal resistors and capacitors. Two circuits, one consisting of a resistor and the other a capacitor, are shown in figures 1 (a) and 1 (b), respectively.

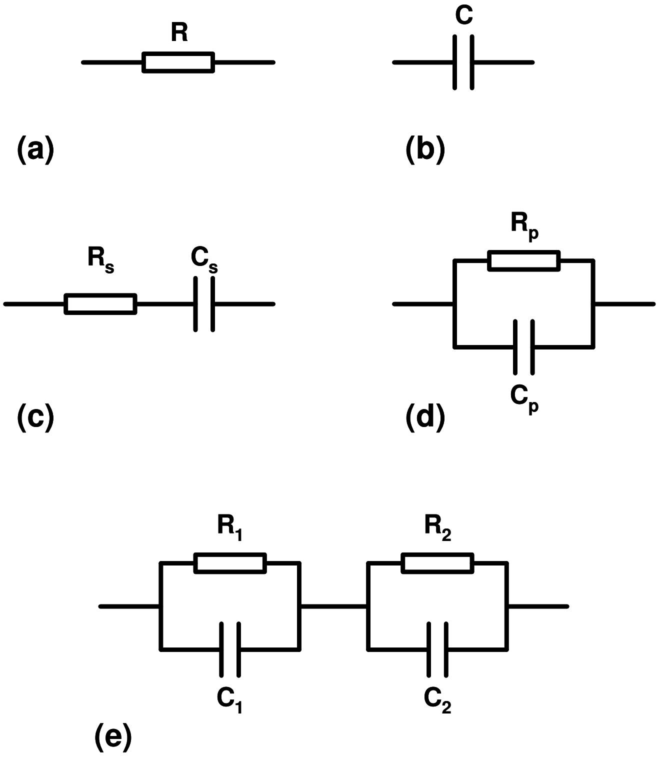

Figure 3.1: Equivalent circuits composed of (a) a resistor, (b) a capacitor, (c) a series *RC* element, (d) a parallel *RC* element and (e) two parallel *RC* elements in series.

The resistance, *R*, of a resistor is independent of frequency and the current and voltage remain in-phase with respect to one another. As such, the resistor has no capacitive characteristics. Hence for this circuit only the real components of Z^* and Y^* and imaginary components of M^* and ε^* are non-zero:

$$Z^* = R \tag{3.5}$$

$$Y^* = R^{-1} \tag{3.6}$$

$$M^* = j\omega C_0 R \tag{3.7}$$

$$\varepsilon^* = {}^{j}\!/_{\omega C_0 R} \tag{3.8}$$

The capacitance, *C*, of a capacitor is independent of frequency but the associated resistance, or reactance, *X*, is frequency dependent. The reactance arises from the voltage leading the current by 90°. As frequency tends to zero, reactance tends to infinity, viz. Equation 3.9.

$$X = {}^{1}\!/_{\omega C} \tag{3.9}$$

For an ideal capacitor, the four formalisms are written thus:

$$Z^* = {}^{-j}\!/_{\omega C} \tag{3.10}$$

$$Y^* = j\omega C \tag{3.11}$$

$$M^* = {}^{C_0}\!/_{C} \tag{3.12}$$

$$\varepsilon^* = {}^{C}\!/_{C_0} \tag{3.13}$$

The convention for deriving complex formalisms for circuits consisting of several elements is that the impedance of each element is added according to Equation 3.14 if the elements are connected in series, or the admittance added according to Equation 3.15 if the elements are connected in parallel. The remaining formalisms and tan δ can then be derived according to Equations 3.1 – 3.4.

$$Z^* = Z^*_1 + Z^*_2 + \ldots \tag{3.14}$$

$$Y^* = Y^*_1 + Y^*_2 + \ldots \tag{3.15}$$

The physical meaning of a resistor and capacitor connected in series or parallel is that the phenomenon being represented has both resistive and capacitive qualities. Furthermore, the phenomenon may exhibit a frequency at which the phase difference between current and voltage reaches a maximum. This particular frequency is referred to as the frequency of maximum loss, ω_{max} (or f_{max} in Hz), or the reciprocal of the time constant, τ^{-1}, as shown in Equation 3.16:

$$\tau = RC = {}^{1}\!/_{\omega_{\max}} \tag{3.16}$$

Complex formalisms and tan δ expressions for the circuits in Figure 3.1 are derived below. It will be shown that Y'' and ε'' feature Debye functions corresponding to series circuits and Z'' and M'' feature Debye functions corresponding to parallel circuits. The general form of a Debye function can be written as:

$$F(\omega) = B\left[\frac{\omega RC}{(\omega RC)^2 + 1}\right] \tag{3.17}$$

The function $F(x)$ peaks at $B/2$ (where B is a constant) when $\omega = RC^{-1}$. When plotted as log F vs log ω, the gradient either side of the peak is |1|.

3.2.1. Series RC Circuit

3.2.1.1. Derivation of Z, Y*, M*, ε* and tan δ.*

The complex formalisms for a resistor, R_s, connected in series to a capacitor, C_s, as shown in Figure 3.1 (c), are deduced as follows:

Determine Z^* by addition Z^* of a resistor and Z^* of a capacitor, according to Equation 3.14:

$$Z^* = R_S - {}^{j}\!/_{\omega C_S} \tag{3.18}$$

Admittance is derived by combining Equations 3.1 and 3.18:

$$Y^* = \frac{1}{R_S - j(\omega C_S)^{-1}} \tag{3.19.1}$$

$$= \frac{\omega C_S}{\omega R_S C_S - j} \times \frac{\omega R_S C_S + j}{\omega R_S C_S + j} \tag{3.19.2}$$

$$= \frac{\omega^2 R_S C_S{}^2 + j\omega C_S}{(\omega R_S C_S)^2 + 1} \tag{3.19.3}$$

$$= \frac{\omega^2 R_S C_S{}^2}{(\omega R_S C_S)^2 + 1} + \frac{j\omega C_S}{(\omega R_S C_S)^2 + 1} \tag{3.19.4}$$

$$= \left(\frac{1}{R_S}\right)\frac{(\omega R_S C_S)^2}{(\omega R_S C_S)^2 + 1} + j\left(\frac{1}{R_S}\right)\frac{\omega R_S C_S}{(\omega R_S C_S)^2 + 1} \tag{3.19.5}$$

Electric modulus is then derived by combining Equations 3.3 and 3.18:

$$M^* = j\omega C_0 R_S - jj\frac{\omega C_0}{\omega C_S} \tag{3.20.1}$$

$$=\frac{C_0}{C_S}+j\omega C_0 R_S \tag{20.2}$$

And permittivity derived by combining Equations 3.2 and 3.19.5:

$$\varepsilon^* = \frac{\left(\dfrac{1}{R_S}\right)\dfrac{(\omega R_S C_S)^2}{(\omega R_S C_S)^2+1}+j\left(\dfrac{1}{R_S}\right)\dfrac{\omega R_S C_S}{(\omega R_S C_S)^2+1}}{j\omega C_0} \tag{3.21.1}$$

Let $\varepsilon' = \left(\dfrac{j}{j\omega C_0 R_S}\right)\dfrac{(\omega R_S C_S)^2}{(\omega R_S C_S)^2+1}$ (3.21.2)

$$=\left(\frac{-1}{\omega C_0 R_S}\right)\frac{\omega R_S C_S}{(\omega R_S C_S)^2+1} \tag{3.21.3}$$

$$=\frac{1}{C_0 \big/ {C_S}^2+\omega^2 {R_S}^3 C_S C_0} \tag{3.21.4}$$

$$=\left(\frac{C_S}{C_0}\right)\frac{1}{(\omega R_S C_S)^2+1} \tag{3.21.5}$$

From Equation 3.21.1, let $j\varepsilon'' = \dfrac{\omega^2 R_S {C_S}^2}{j\omega C_0\left[(\omega R_S C_S)^2+1\right]}$ (3.21.6)

$$=\frac{\omega^2 R_S {C_S}^2}{j\omega C_0\left[(\omega R_S C_S)^2+1\right]}\times\frac{j\omega C_0\left[(\omega R_S C_S)^2-1\right]}{j\omega C_0\left[(\omega R_S C_S)^2-1\right]} \tag{3.21.7}$$

$$=\frac{j\omega^3 R_S {C_S}^2 C_0\left[(\omega R_S C_S)^2-1\right]}{-\omega^2 {C_0}^2\left[(\omega R_S C_S)^2+1\right]\left[(\omega R_S C_S)^2-1\right]} \tag{3.21.8}$$

$$=\frac{j\omega R_S {C_S}^2}{-{C_0}^2\left[(\omega R_S C_S)^2+1\right]} \tag{3.21.9}$$

$$= -j\left(\frac{C_S}{C_0}\right)\left(\frac{\omega R_S C_S}{(\omega R_S C_S)^2 + 1}\right) \qquad (3.21.10)$$

Hence:

$$\varepsilon^* = \left(\frac{C_S}{C_0}\right)\frac{1}{(\omega R_S C_S)^2 + 1} - j\left(\frac{C_S}{C_0}\right)\left(\frac{\omega R_S C_S}{(\omega R_S C_S)^2 + 1}\right) \qquad (3.21.11)$$

tan δ is therefore deduced as follows:

$$\tan\delta = \frac{\dfrac{C_S}{C_0}\left(\dfrac{\omega R_S C_S}{(\omega R_S C_S)^2 + 1}\right)}{\dfrac{C_S}{C_0}\dfrac{1}{(\omega R_S C_S)^2 + 1}} \qquad (3.22.1)$$

$$= \omega R_S C_S \qquad (3.22.2)$$

3.2.1.2. Frequency Dependence of Z^*, Y^*, M^*, ε^* and tan δ.

Referring to the expressions for Z^* and M^* in Equations 3.18 and 3.20.2, respectively, the real terms in both formalisms are frequency independent and the imaginary terms are frequency dependent. In the case of Z^*, Z' is fixed at R_s while Z'' decreases from ∞ at *dc* as frequency tends to ∞, as shown in Figure 3.2 (a). Similarly, the real term in M^* is fixed at C_s^{-1} while M'' increases from 0 at *dc* and tends to ∞ as frequency tends to ∞, shown in Figure 3.2 (c).

Inspection of Equation 3.19.5 reveals the Y'' term to be in the form of a Debye function, as described previously. By comparison with Equation 3.17, Y'' peaks when $\omega = (R_sC_s)^{-1}$, i.e. at ω_{max}, and the peak height corresponds to $(2R_s)^{-1}$. Y' increases from 0 to R_s^{-1} as frequency increases from *dc* to $\omega > \omega_{max}$. At higher frequencies, Y' becomes constant at R_s^{-1}, as shown in Figure 3.2 (b). Similarly, Equation 3.21.10 reveals the ε'' term to be in the form of a Debye function with the peak maximum occurring at ω_{max}, where the value of ε'' is $(2C_0)^{-1}C_s$. ε' tends to 0 from C_s/C_0 as frequency increases from ω_{max} to ∞. At frequencies less than ω_{max}, ε' remains fixed at C_s/C_0, as shown in Figure 3.2 (d).

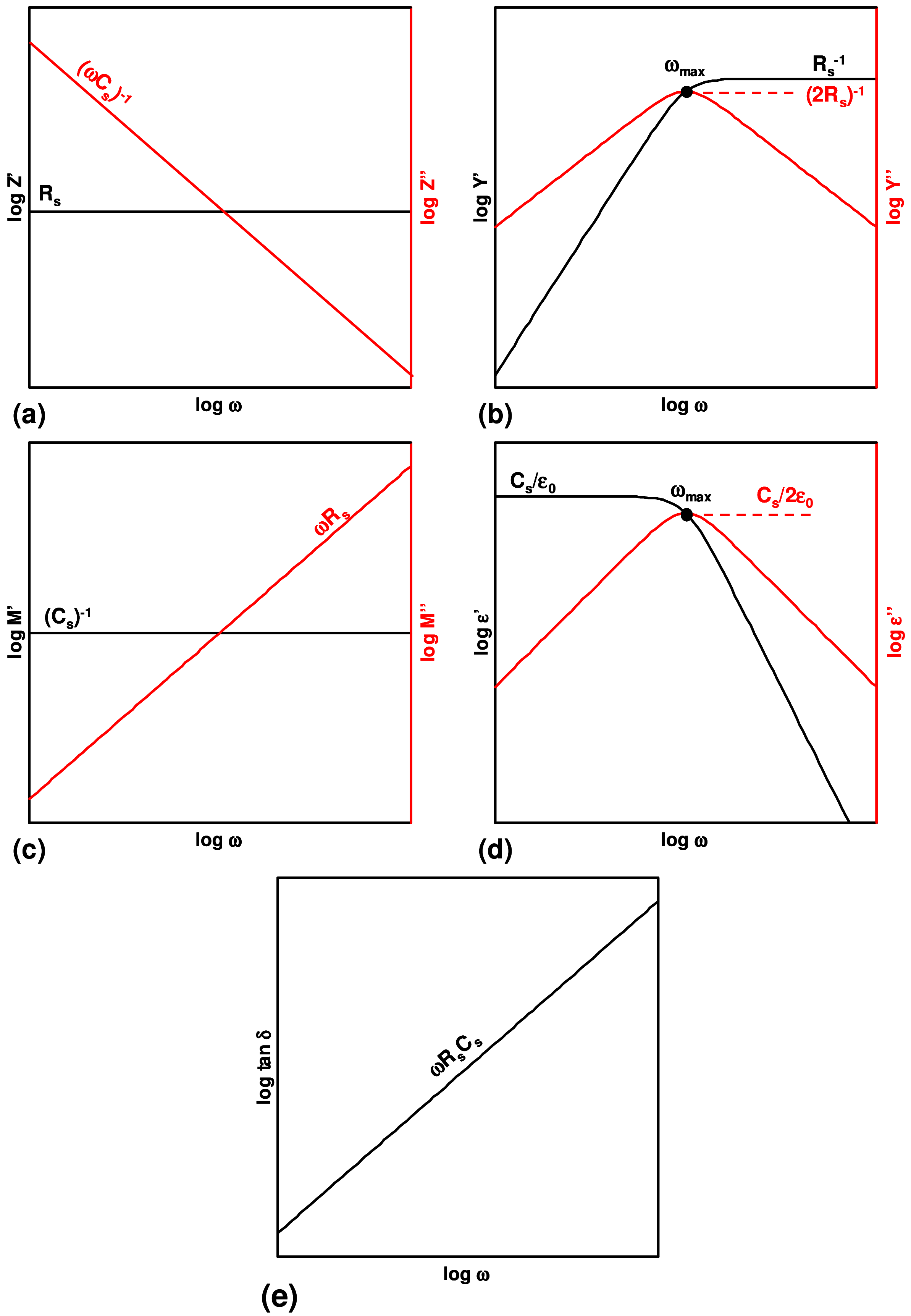

Figure 3.2: Frequency dependence of (a) Z^*, (b) Y^*, (c) M^*, (d) ε^* and (f) tan δ for a series *RC* circuit.

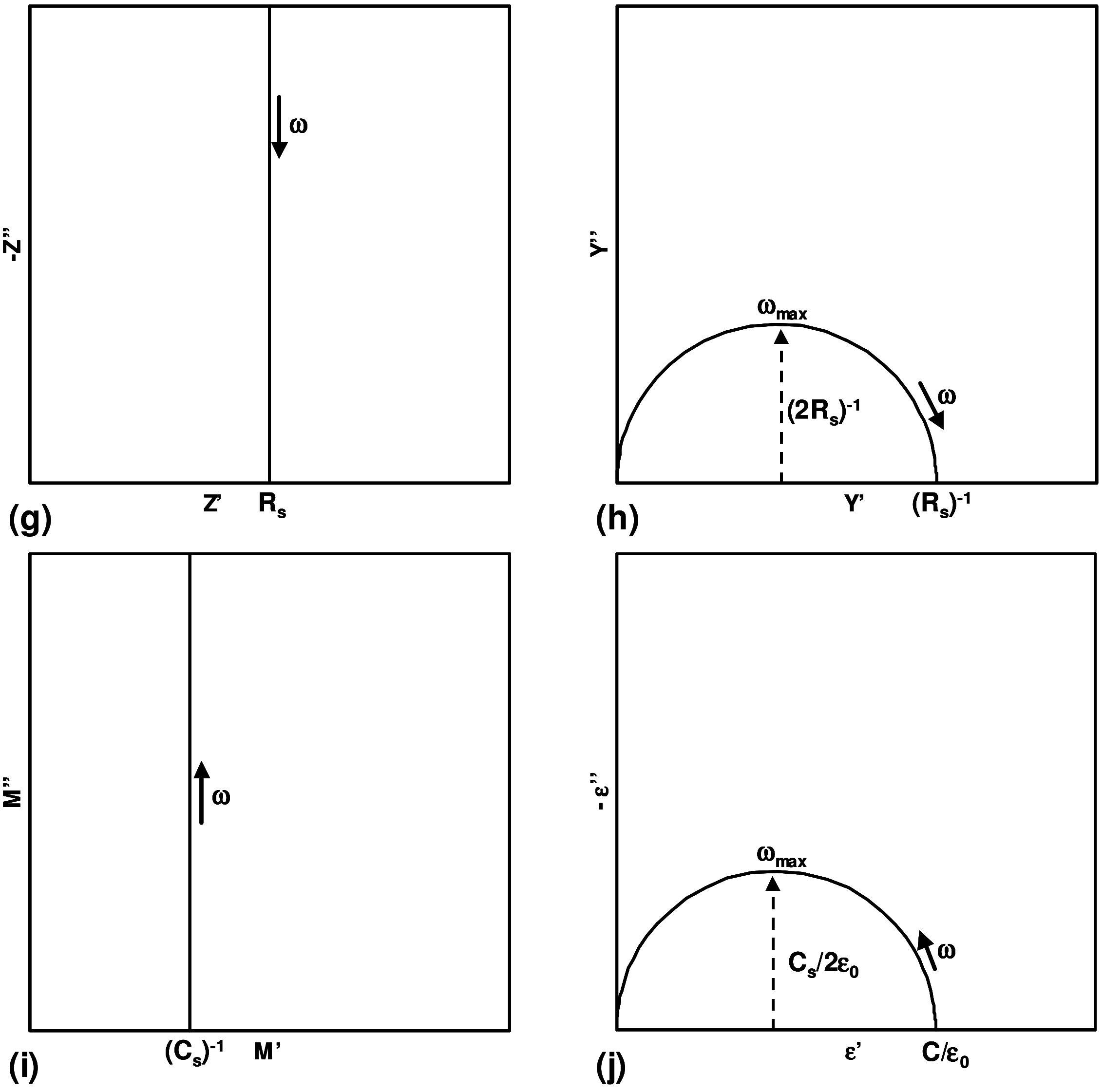

Figure 3.2 (contd.): Complex plane plots of (g) Z^*, (h) Y^*, (i) M^*, (j) ε^* for a series *RC* circuit.

tan δ is proportional to frequency, according to Equation 3.22.2, and so a series *RC* circuit can be characterised by observing a positive slope in a plot of log tan δ vs log ω, as shown in Figure 3.2 (e).

Complex plane plots of Z^* and M^* are shown in Figure 3.2 (g) and 3.2 (i), respectively. Both plots feature a single 'spike' corresponding, in Z^*, to $Z' = R_s$ and, in M^*, to $M' = C_0/C_s$. Y^* and ε^* complex plane plots both exhibit a single semicircle intercepting the real axis at 0, as shown in Figures 3.2 (h) and 3.2 (j). In Y^*, frequency increases from left to right, as indicated by the arrow, with ω_{max} at the apex of the semicircle. The diameter of the semicircle is R_s^{-1}, hence R_s can be determined from the semicircle diameter and C_s can be calculated by substituting the values of ω_{max} and R_s into Equation 3.16.

In ε^*, frequency increases from right to left, and the diameter of the semicircle corresponds to C_s/C_0. As such, C_s can be determined from the diameter and R_s found by substituting the values of ω_{max} and C_s in Equation 3.16. For the series *RC* circuit, therefore, values of both R_s and C_s can be extracted from either Y^* or ε^*, since Z^* and M^* allow only extraction of R_s or C_s, respectively.

3.2.2. Parallel *RC* Circuit

3.2.2.1. Derivation of Z, Y*, M*, ε* and tan δ.*

A similar approach to that described in Section 3.1.1 is used to derive complex expressions for the impedance of a resistor and capacitor connected in parallel, as shown in Figure 3.1 (d).

Determine Y^* by summation of Y^* for R_p and Y* for C_p, according to Equation 3.15:

$$Y^* = {}^{1}\!/_{R_P} + j\omega C_P \tag{3.23}$$

Then derive impedance by combining Equations 3.1 and 3.23:

$$Z^* = \left({}^{1}\!/_{R_P} + j\omega C_P \right)^{-1} \tag{3.24.1}$$

$$= \frac{R_P}{j\omega R_P C_P + 1} \times \frac{j\omega R_P C_P - 1}{j\omega R_P C_P - 1} \tag{3.24.2}$$

$$= \frac{R_P - j\omega R_P{}^2 C_P}{(\omega R_P C_P)^2 + 1} \tag{3.24.3}$$

$$= \frac{R_P}{(\omega R_P C_P)^2 + 1} - j\frac{\omega R_P{}^2 C_P}{(\omega R_P C_P)^2 + 1} \tag{3.24.4}$$

$$= \frac{R_P}{(\omega R_P C_P)^2 + 1} - jR_P \frac{\omega R_P C_P}{(\omega R_P C_P)^2 + 1} \tag{3.24.5}$$

Derive electric modulus by combining Equations 3 and 3.24.5:

$$M^* = j\omega C_0 \left[\frac{R_P}{(\omega R_P C_P)^2 + 1} - jR_P \frac{\omega R_P C_P}{(\omega R_P C_P)^2 + 1} \right] \tag{3.25.1}$$

$$= \omega C_0 R_P \left(\frac{\omega R_P C_P}{(\omega R_P C_P)^2 + 1} \right) + j \frac{\omega C_0 R_P}{(\omega R_P C_P)^2 + 1} \tag{3.25.2}$$

$$= \omega C_0 R_P \left(\frac{\omega R_P C_P}{(\omega R_P C_P)^2 + 1} \right) + j \left(\frac{C_0}{C_P} \right) \frac{\omega C_0 R_P}{(\omega R_P C_P)^2 + 1} \tag{3.25.3}$$

And derive permittivity from Equations 3.2 and 3.23:

$$\varepsilon^* = \frac{1/R_P + j\omega C_P}{j\omega R_P C_0} \tag{3.26.1}$$

$$= \frac{1}{j\omega R_P C_0} \times \frac{-j\omega R_P C_0}{-j\omega R_P C_0} - \left(\frac{C_P}{C_0} \right) \tag{3.26.2}$$

$$= \left(\frac{C_P}{C_0} \right) - j \left(\frac{1}{\omega R_P C_0} \right) \tag{3.26.3}$$

tan δ is therefore deduced as follows:

$$\tan \delta = \frac{(\omega R_P C_0)^{-1}}{C_P / C_0} \tag{3.27.1}$$

$$= \frac{1}{\omega R_P C_P} \tag{3.27.2}$$

3.2.2.2. Frequency Dependence of Z^*, Y^*, M^*, ε^* and tan δ.

For a parallel *RC* circuit, the real terms of Y^* and ε^* are fixed at R_p^{-1} and C_p/C_0, respectively. Y'' increases with frequency, according to ωC_p, whereas ε'' is inversely proportional to frequency, according to $(\omega R_p C_0)^{-1}$, as shown in Figures 3.3 (b) and 3.3 (d), respectively.

Both Z'' and M'' are in the form of Debye functions with the respective peak maxima occurring at ω_{max}, as shown in Figures 3.3 (a) and 3.3 (c). Z'' and M'' at ω_{max} correspond to values of $R_p/2$ and $C_0/2C_p$, respectively. Z' is fixed at R_p at frequencies below ω_{max}. As frequency tends from ω_{max} to ∞, Z' tends to 0. M' is fixed at C_0/C_p at frequencies > ω_{max}. As frequency decreases below ω_{max} and tends to 0, M' tends to 0.

Contrary to the case for a series *RC* circuit, tan δ is inversely proportional to frequency, according to Equation 3.27.2, and so a parallel *RC* circuit can be characterised by a negative slope in a plot of log tan δ vs log ω, as shown in Figure 3.3 (e).

Z^* and M^* complex plane plots are shown in Figures 3.3 (g) and 3.3 (i), respectively. Both plots contain a semicircle intercepting the real axis at zero, corresponding to the impedance of the parallel R_pC_p circuit. In Z^*, frequency increases from right to left and the diameter of the semicircle corresponds to R_p. Z^* facilitates extraction of R_p from the semicircle diameter and C_p by substituting R_p and ω_{max} into Equation 3.16.

In M^*, frequency increases from left to right and the diameter corresponds to C_p^{-1}. M^*, therefore, facilitates extraction of C_p from the semicircle diameter and R_p by substituting C_p and ω_{max} into Equation 3.16.

Y^* and ε^* complex plane plots, however, exhibit only a spike occurring at $Y' = R_p^{-1}$ and $\varepsilon' = C_p/C_0$, respectively, as shown in Figures 3.3 (h) and 3.3 (j). Hence, for a parallel *RC* circuit, both Y^* and ε^* are required to extract R_p and C_p whereas either Z^* or M^* permit extraction of both values.

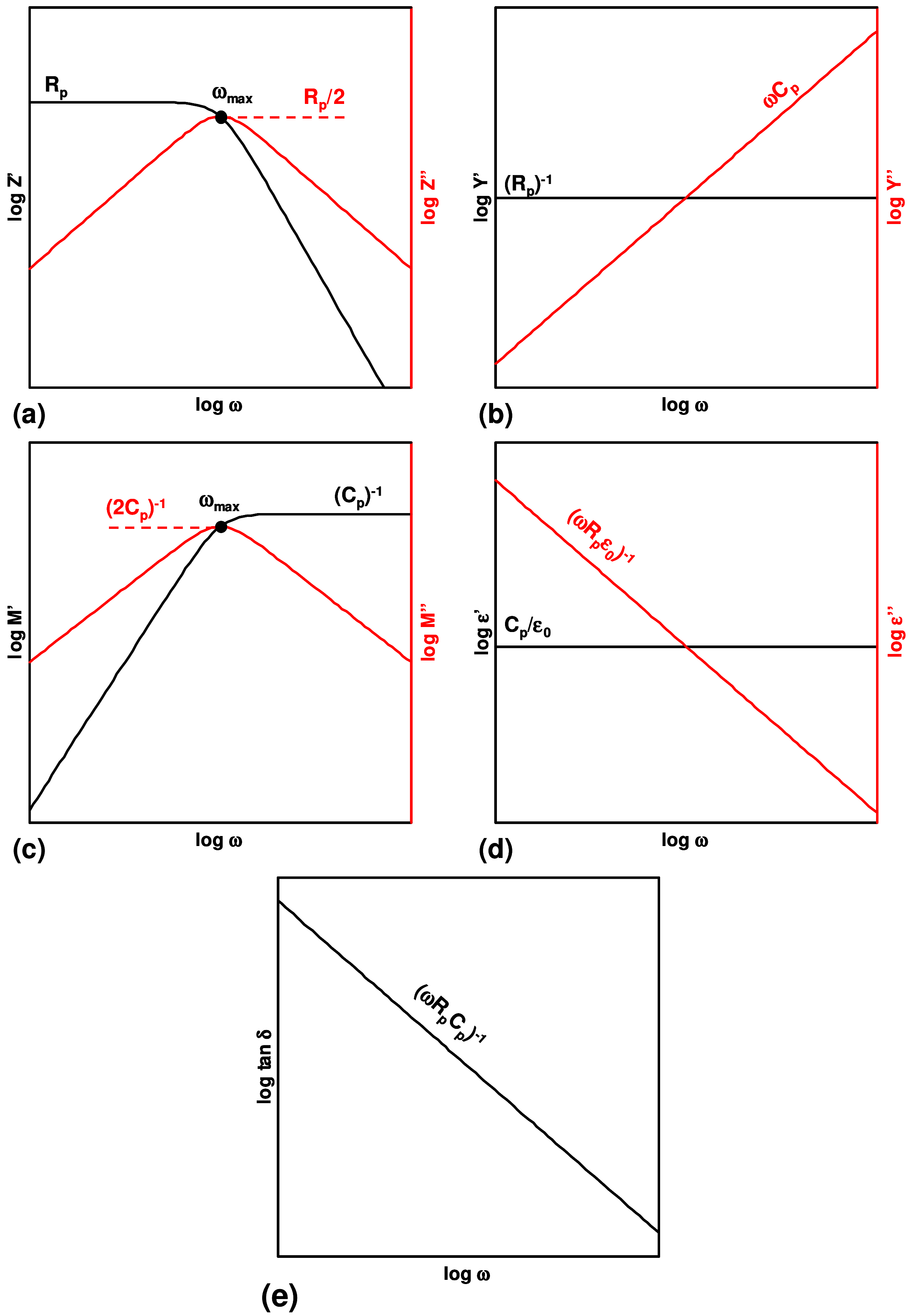

Figure 3.3: Frequency dependence of (a) Z^*, (b) Y^*, (c) M^*, (d) ε^* and (f) tan δ for a parallel *RC* circuit.

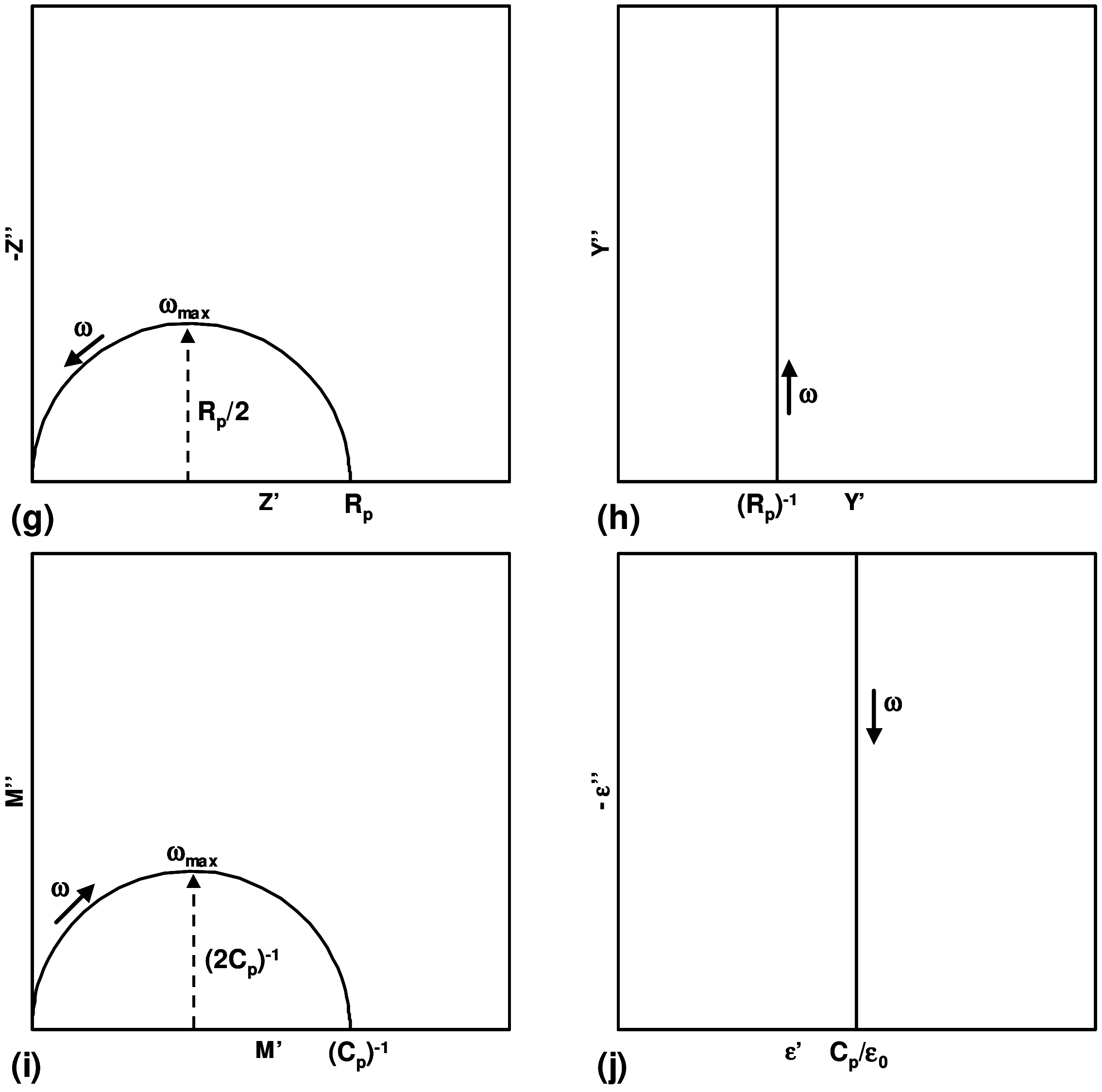

Figure 3.3 (contd.): Complex plane plots of (g) Z^*, (h) Y^*, (i) M^*, (j) ε^* for a parallel *RC* circuit.

3.2.3. Parallel *RC* Elements Connected in Series

3.2.3.1. Derivation of Z^*, Y^*, M^*, ε^* and tan δ.

The circuit in Figure 3.1 (e) may be described as two parallel *RC* elements connected in series. In this way, complex expressions can be derived as before for the impedance of such a circuit. For this circuit, however, the derivations are somewhat corpulent and are given in Appendix A1, with the final equations given below:

$$\begin{aligned} Z^* = {} & \frac{R_1}{(\omega R_1 C_1)^2 + 1} + \frac{R_2}{(\omega R_2 C_2)^2 + 1} \\ & - j\left(R_1 \frac{\omega R_1 C_1}{(\omega R_1 C_1)^2 + 1} + R_2 \frac{\omega R_2 C_2}{(\omega R_2 C_2)^2 + 1} \right) \end{aligned} \tag{3.28}$$

$$\begin{aligned} M^* = {} & \omega C_0 \left[R_1 \frac{\omega R_1 C_1}{(\omega R_1 C_1)^2 + 1} + R_2 \frac{\omega R_2 C_2}{(\omega R_2 C_2)^2 + 1} \right] \\ & + jC_0 \left[\left(\frac{1}{C_1} \right) \frac{\omega R_1 C_1}{(\omega R_1 C_1)^2 + 1} + \left(\frac{1}{C_2} \right) \frac{\omega R_2 C_2}{(\omega R_2 C_2)^2 + 1} + \right] \end{aligned} \tag{3.29}$$

$$\begin{aligned} Y^* = {} & \frac{\frac{1}{R_1 R_2}\left(\frac{1}{R_1} + \frac{1}{R_2} \right) + \omega^2 C_1 C_2 \left(\frac{1}{R_1} + \frac{1}{R_2} \right) + \omega^2 (C_1 + C_2)\left(\frac{C_2}{R_1} + \frac{C_1}{R_2} \right)}{\left(\frac{1}{R_1} + \frac{1}{R_2} \right)^2 + \omega^2 (C_1 + C_2)^2} \\ & + \frac{j}{\left(\frac{1}{R_1} + \frac{1}{R_2} \right)^2 + \omega^2 (C_1 + C_2)^2} \left[\omega \left(\frac{C_2}{R_1} + \frac{C_1}{R_2} \right)\left(\frac{1}{R_1} + \frac{1}{R_2} \right) \right. \\ & \left. - \frac{\omega}{R_1 R_2}(C_1 + C_2) + \omega^3 C_1 C_2 (C_1 + C_2) \right] \end{aligned} \tag{3.30}$$

$$\begin{aligned} \varepsilon^* = {} & \frac{\omega^2 C_1 C_2 (C_1 + C_2) + \left(\frac{1}{R_1} + \frac{1}{R_2} \right)\left(\frac{C_2}{R_1} + \frac{C_1}{R_2} \right) - \left(\frac{C_1 + C_2}{R_1 R_2} \right)}{C_0 \left(\frac{1}{R_1} + \frac{1}{R_2} \right)^2 + \omega^2 C_0 (C_1 + C_2)^2} \\ & - \frac{j}{C_0 \left(\frac{1}{R_1} + \frac{1}{R_2} \right)^2 + \omega^2 C_0 (C_1 + C_2)^2} \left[\omega C_1 C_2 \left(\frac{1}{R_1} + \frac{1}{R_2} \right) - \right. \\ & \left. - (C_1 + C_2)\left(\frac{\omega C_2}{R_1} + \frac{\omega C_1}{R_2} \right) - \frac{1}{\omega}\left(\frac{1}{R_2} + \frac{1}{R_2} \right)\left(\frac{1}{R_1 R_2} \right) \right] \end{aligned} \tag{3.31}$$

$$\tan\delta = \frac{R_1 + R_2 + R_1(\omega R_1 C_1)^2 + R_2(\omega R_2 C_2)^2}{\omega R_1{}^2 C_1 + \omega R_2{}^2 C_2 + \omega R_2{}^2 C_2(\omega R_1 C_1)^2 + \omega R_1{}^2 C_1(\omega R_2 C_2)^2} \tag{3.32}$$

3.2.3.2. Overview of Characteristic Frequencies

The frequency dependence of impedance for the circuit described above displays both series and parallel characteristics. These are evident when the variation in current pathway as a function of frequency is described qualitatively, as shown in Figure 3.4 in which $R_2 >> R_1$ and $C_2 >> C_1$. At *dc*, the reactance of both capacitors, X_1 and X_2, is significantly higher than the resistance of either resistor, R_1 and R_2, and so the circuit is effectively two resistors in series. As frequency increases, reactance X_2 becomes equivalent in magnitude to R_2 and the effective circuit now consists of the parallel R_2C_2 element connected in series to R_1, with a frequency of maximum loss at $\omega_{max(2)}$. A further increase in frequency results in X_2 becoming significantly less than R_2. Above ω_b the effective circuit now resembles a 'parasitic' series R_1C_2 circuit, analogous to the circuit described in Section 3.2.1, with a frequency of maximum loss at ω_c.

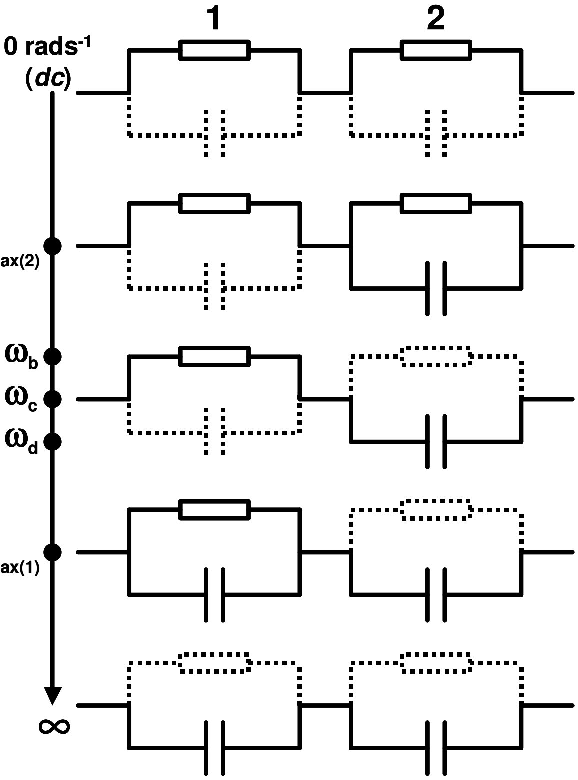

Figure 3.4: Schematic representation of current path (solid line) as a function of frequency.

As frequency increases to ω_d, X_1 becomes comparable in magnitude to R_1 and the effective circuit corresponds to the single parallel R_1C_1 circuit with frequency of maximum loss at $\omega_{max(1)}$ described in Section 3.1.2, in series with the capacitor C_2. As frequency tends to ∞, the magnitude of X_1 becomes significantly less than R_1 and the effective circuit becomes two capacitors, C_1 and C_2, connected in series. This empirical model can be confirmed by provisionally investigating certain aspects of the frequency dependence of tan δ, Y'' and ε'' prior to more detailed analysis in the following section:

It was shown previously that tan δ for a series RC circuit is directly proportional to frequency, whereas tan δ for a parallel circuit RC circuit is inversely proportional to frequency. Based on the above argument, it can be assumed that, for 2 parallel RC elements in series, the slope of tan δ versus frequency is negative for $\omega < \omega_b$, positive for $\omega < \omega_b < \omega_d$, and negative for $\omega > \omega_d$. In effect, ω_b and ω_d must correspond to positive and negative inflections in tan δ, respectively. ω_b and ω_d can therefore be quantified by analysis of equation 3.32:

For $0 < \omega < \omega_b$, R_2 is the dominant term in the numerator of Equation 3.32, and $\omega R_2^2C_2$ is the dominant term, and so tan δ can be written:

$$\tan\delta = \frac{R_2}{\omega R_2{}^2 C_2} = \frac{1}{\omega R_2 C_2} \text{ when } \omega < \omega_b \qquad (3.32.1)$$

For $\omega_b < \omega < \omega_d$, the dominant terms in the numerator and denominator of Equation 3.32 are $R_1(\omega R_2C_2)^2$ and $\omega R_2^2C_2$, respectively. tan δ can then be written:

$$\tan\delta = \frac{R_1(\omega R_2 C_2)^2}{\omega R_2{}^2 C_2} = \omega R_1 C_2 \text{ when } \omega_b < \omega < \omega_d \qquad (3.32.2)$$

Above ω_d, $R_1(\omega R_2C_2)^2$ remains dominant in the numerator and $\omega R_1^2C_1(\omega R_2C_2)^2$ is now dominant in the denominator, such that tan δ can be written:

$$\tan\delta = \frac{R_1(\omega R_2 C_2)^2}{\omega R_1{}^2 C_1(\omega R_2 C_2)^2} = \frac{1}{\omega R_1 C_1} \text{ when } \omega > \omega_d \qquad (3.32.3)$$

An expression for ω_b is determined from the intersection of Equations 3.32.1 and 3.32.2:

$$\frac{1}{\omega_b R_2 C_2} = \omega_b R_1 C_2 \tag{3.32.4}$$

$$1 = \omega_b{}^2 R_1 C_2{}^2 \tag{3.32.5}$$

$$\omega_b = \frac{1}{C_2 (R_1 R_2)^{1/2}} \tag{3.32.6}$$

And similarly, ω_d is determined from the intersection of Equations 3.32.2 and 3.32.3:

$$\frac{1}{\omega_d R_1 C_1} = \omega_d R_1 C_2 \tag{3.32.7}$$

$$1 = \omega_d{}^2 R_1{}^2 C_1 C_2 \tag{3.32.8}$$

$$\omega_d = \frac{1}{R_1 (C_1 C_2)^{1/2}} \tag{3.32.9}$$

It may also be assumed that, due to the parasitic R_1C_2 series circuit, both Y' and ε'' exhibit a Debye-like peak corresponding to the time constant R_1C_2. Y' and ε'' have identical denominators determining the frequency of the peak maximum, when both terms are of equal magnitude, *i.e.*:

$$\left(\frac{1}{R_1} + \frac{1}{R_2}\right)^2 = \omega^2 (C_1 + C_2)^2 \tag{3.33.1}$$

Therefore both Y' and ε'' reach a negative inflection when:

$$\omega = \frac{1}{R_1 (C_1 + C_2)} + \frac{1}{R_2 (C_1 + C_2)} \tag{3.33.2}$$

$$= \frac{R_2 + R_2}{R_1 C_1 R_2 + R_1 R_2 C_2} \qquad (3.33.3)$$

$$\sim \frac{R_2}{R_1 R_2 C_2} = \frac{1}{R_1 C_2} = \omega_C \qquad (3.33.4)$$

corresponding to the time constant of the parasitic series circuit.

3.2.3.3. Frequency Dependence of Z^*, M^*, Y^*, ε^* and tan δ

Analysis of the impedance equations derived for 2 parallel *RC* elements in series is given in Appendix A2. The real and imaginary components of Z^*, M^*, Y^* and ε^* are plotted as a function of frequency in Figures 3.5 (a), 3.5 (c), 3.5 (b) and 3.5 (d), respectively. tan δ is also plotted as a function of frequency in Figure 3.5 (e). Complex plane plots of Z^*, M^*, Y^* and ε^* are shown in Figures 3.5 (g), 3.5 (i), 3.5 (h), 3.5 (j), respectively.

Values of R_1, R_2, C_2 and C_1 are obtainable from either Z^* or M^*, as shown in Figures 3.5 (g) and 3.5 (i), respectively. Z^* plots allow direct extraction of R_1 and R_2 from the diameter of semicircles corresponding to each parallel *RC* element, where the low frequency semicircle corresponds to R_2C_2 and the high frequency semicircle (see inset) corresponds to R_1C_2. C_1 and C_2 can then be determined by substituting R_1 and $\omega_{max(1)}$, or R_2 and $\omega_{max(2)}$, into Equation 3.16, respectively. Conversely, C_0/C_1 and C_0/C_2 correspond to the diameter of the respective semicircles in M^* plots with R_1 and R_2 available by substituting C_1 and $\omega_{max(1)}$ or C_2 and $\omega_{max(2)}$ into Equation 3.16, respectively.

Y^* plots exhibit a single semicircle and a high frequency 'spike' where Y' tends to ∞. At *dc*, the semicircle intercepts the Y' axis at $(R_1 + R_2)^{-1}$. R_1 may be determined from the diameter of the semicircle (corresponding to the parasitic series circuit described previously) and/or by extrapolating the high frequency spike to the Y' axis. As such, Y^* allows direct extraction of R_1 and R_2, while C_2 may be determined by substituting R_1 and ω_C into Equation 3.16; C_1, however, is unavailable. ε^* plots feature a low frequency spike and a single semicircle, again corresponding to the parasitic series circuit. At high frequencies, the semicircle intercepts the ε' axis at C_1/C_0. C_2 may be determined from the diameter of the semicircle and/or by extrapolating the low frequency spike to intercept the ε' axis. R_1 can be extracted by substituting C_2 and ω_c into Equation 3.16, whereas C_1 is unavailable.

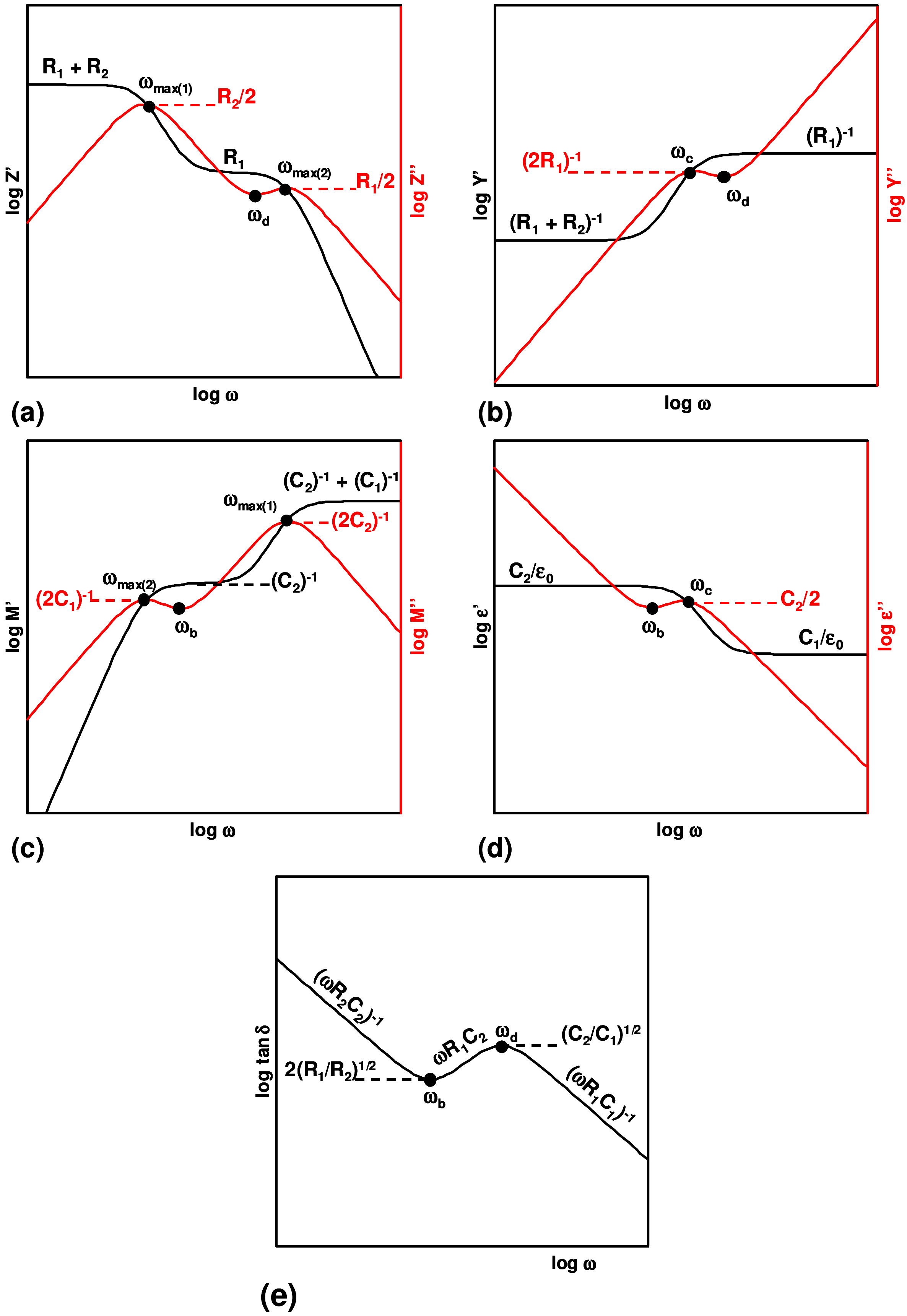

Figure 3.5: Frequency dependence of (a) Z*, (b) Y*, (c) M*, (d) ε* and (f) tan δ for a 2 parallel *RC* elements in series circuit.

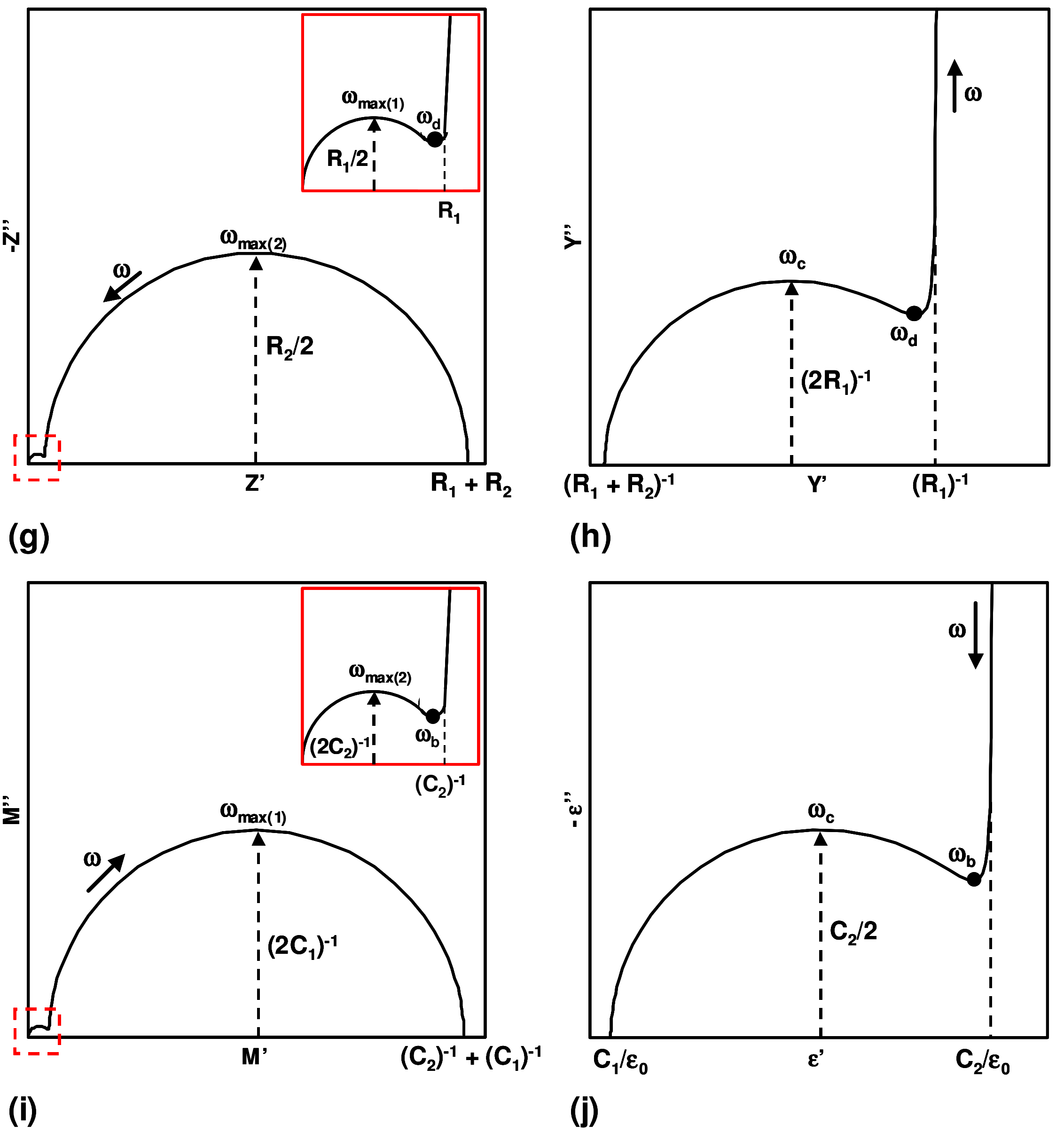

Figure 3.5 (contd.): Complex plane plots of (g) Z*, (h) Y*, (i) M*, (j) ε* for a 2 parallel *RC* elements in series circuit.

3.3. Interpretation of Impedance Data

3.3.1. Overview

A starting point for the interpretation of impedance data, particularly where electrical characterisation of electroceramics is concerned, is to compare the measured data with the theoretical response of 2 parallel *RC* elements connected in series, described previously. Typically, the grain boundaries in a polycrystalline sample exhibit electrical properties that differ from the intrinsic properties of the bulk material. This is often the case since grain boundaries tend to differ both compositionally and geometrically from the bulk, as described by the “brick layer” (BL) model, in which grains are represented by cubic blocks cemented together by the grain boundary layer. The brick layer model assumes no distribution in grain size and that the grains and grain boundaries are themselves electrically homogeneous[1, 2].

On this basis, the geometry of the grain boundary layer is such that the current path length in the grain boundaries is significantly greater than in the bulk. As a result, the grain boundary resistance tends to be greater than the bulk resistance. Furthermore, since the grain boundaries are thin layers, the grain boundary capacitance is often greater than that of the bulk, according to Equation 1.2. As a result, the grain boundary impedance tends to correspond to $\omega_{max(2)}$ as defined previously, whereas the bulk response tends to correspond to $\omega_{max(1)}$. Having distinguished between the two responses, more detailed electrical characterisation may be performed by obtaining resistance and capacitance values over a wide range of temperatures to determine, for example, activation energies and investigate ferroelectric phenomena.

3.3.2. Experimental Limitations

In many experimental situations, however, the electrical microstructure of a given sample cannot be accurately represented by the brick layer model due to variations in grain size and electrical heterogeneity in the bulk and grain boundaries. These deviations from the ideal situation typically result in a departure from Debye-like behaviour, such that the semicircles observed in complex plane plots appear distorted in some way. However, it may still be possible to ‘hand-fit’ the data in order to reasonably estimate grain boundary/bulk resistances and capacitance. Alternatively, software is available to perform linear-regression analysis of data and fit to more complex equivalent circuits. One common approach is to substitute the ideal capacitors in an equivalent circuit for ‘distributed elements’, such as a constant phase element (CPE). Whichever approach is applied, it is particularly important to ensure the raw data are analysed in all four formalisms and that the fitted data are consistent in each case [3].

Fleig and Maier [4-6] have extensively investigated the limitation of standard BL interpretation using finite element studies of simulated microstructures of varying grain shape, grain-grain connectivity, grain boundary conductivity, electrode contact area and grain size distributions. Their work has demonstrated that, although BL interpretation of the bulk response is unaffected by deviations from the BL-model, interpretation of the grain boundary response may be subject to significant errors in cases where the BL model is not adhered to. For most cases, however, where the grain size distribution is not bimodal and the grain boundary conductivity does not vary by more than an order of magnitude throughout the sample, the grain boundary R, C and f_{max} values can be considered to be accurate to within at least +/- 10%.

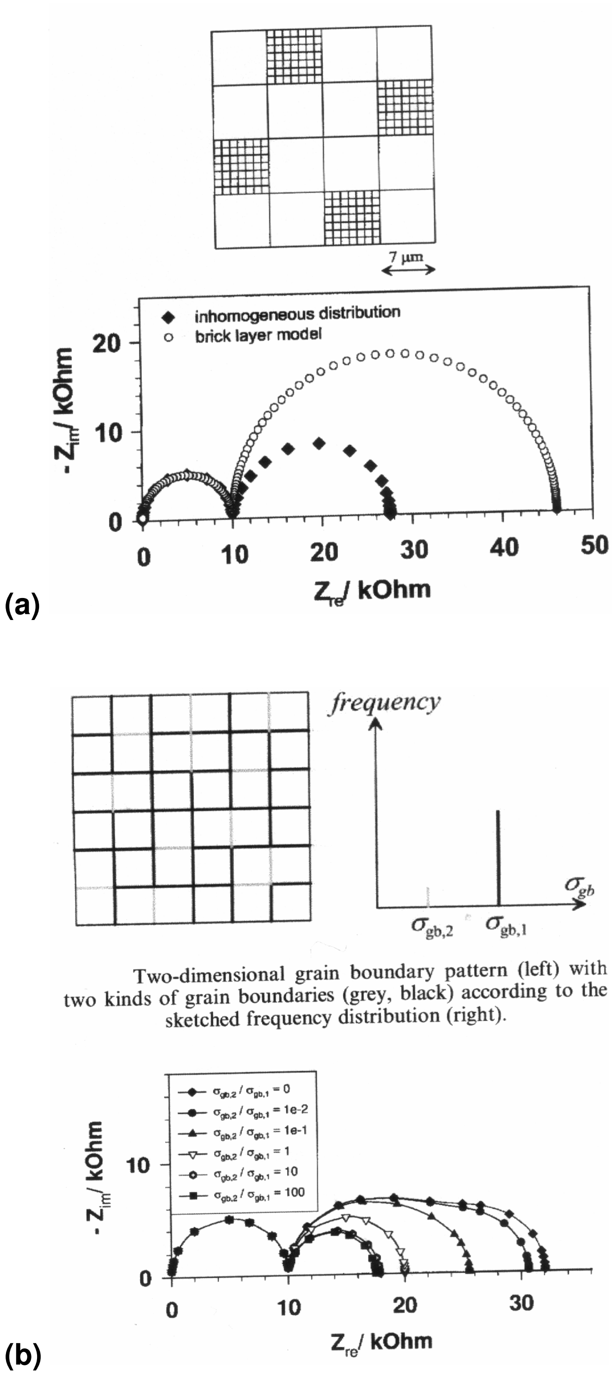

Two-dimensional grain boundary pattern (left) with two kinds of grain boundaries (grey, black) according to the sketched frequency distribution (right).

Figure 3.6: Simulated impedance spectra from (a) bimodal grain size distribution and (b) inhomogeneous distribution of grain boundary conductivity, after Fleig and Maier[5].

In Figure 3.6, two extreme examples of simulated impedance spectra of microstructures that exceed the limitations of the BL model are given. Figure 3.6 (a) represents a microstructure of bimodal grain size, in which fine grain regions exist in a matrix of coarse grains. The BL data are generated assuming a mean grain size of 1.9 μm whereas the inhomogeneous distribution data are generated by the finite element model. In this case, the BL model over-estimates the grain boundary impedance since it does not take into account current detours around the fine-grained regions. The finite element simulations show that the potential current distribution at low frequencies is inhomogeneous and allows the current to bypass the fine-grained regions through the coarse grains.

Figure 3.6 features an example of a microstructure of uniform grain size, but with a spatial distribution of grain boundary conductivities such that 80% of grain boundaries have a conductivity of σ_{gb1} and 20% have σ_{gb2}. Trivially, the grain boundary response is homogenous when $\sigma_{gb1} = \sigma_{gb2}$. The grain boundary impedance can decrease slightly, however, when $\sigma_{gb1} < \sigma_{gb2}$, or increase significantly when $\sigma_{gb1} > \sigma_{gb2}$. The finite element simulations again show that these differences are attributable to current detours arising from an inhomogeneous potential distribution.

3.3.3. Fixed Frequency Capacitance and tan δ measurements vs Impedance Spectroscopy: A Simulated Scenario.

Impedance data were simulated over a frequency range 1 μHz – 2 MHz using ZView 2 software (Scribner Associates) for the equivalent circuit in Figure 3.1 (e). C_1 and C_2 were fixed at 1.27 pF/cm and 25.5 nF/cm, respectively, based on experimentally determined values for bulk and grain boundary capacitances for CCTO ceramics[7, 8] (this will be discussed in greater detail in Chapter 4). R_1 and R_2 for each temperature were obtained from both experimentally determined values and estimated values, based on previously reported bulk and grain boundary activation energies of 0.06 eV and 0.66 eV, respectively[7].

T/K	R_2/Ω	R_1/Ω	τ_2/s	$f_{max(2)}$/Hz	τ_1/s	$f_{max(1)}$/Hz
300	1.27×10^{6}	20	3.23×10^{-2}	4.93	2.55×10^{-10}	6.24×10^{8}
120	1.62×10^{21}	2.07×10^{3}	4.12×10^{13}	3.86×10^{-15}	2.63×10^{-8}	6.04×10^{6}
70	1.55×10^{39}	5.18×10^{5}	3.96×10^{31}	4.02×10^{-33}	6.58×10^{-6}	2.42×10^{5}

Table 3.1: Simulated impedance data at selected temperatures.

The simulated impedance data at selected temperatures are summarised in Table 3.1. At 70 K, element 2 cannot be resolved since $f_{max(2)}$ is 27 orders of magnitude lower than the simulated frequency range. $f_{max(1)}$ is 242 kHz, which is within the simulated frequency range and so element 1 can be resolved at 70 K. As a result, the Z^* plot in Figure 3.7 (a) appears as a single arc of diameter 518 kΩ.cm, corresponding to element 1, and a low frequency spike associated with an 'incomplete' arc corresponding to element 2.

At 120 K, $f_{max(2)}$ remains several orders of magnitude below the frequency range but $f_{max(1)}$ has now increased to 6 MHz, which is beyond the upper frequency limit of the simulation. In this respect, the response of element 2 can still be observed only as a spike in Z^* but the bulk is no longer fully resolved since, higher frequencies are required to exceed $f_{max(1)}$ and intercept the origin, as shown in Figure 3.7 (b). At 300 K, $f_{max(2)}$ is within the frequency range at ~ 5 Hz and the Z^* plot in Figure 3.7 (c) reveals a low frequency arc of diameter 1.27 MΩ.cm corresponding to the response of element 2. $f_{max(1)}$, however, is nearly 2 orders of magnitude higher than the upper frequency limit, resulting in a non-zero intercept with the Z' axis at high frequencies, as shown in the insert in figure 3.7 (c). R_1 can be regarded as the distance from the origin in Z^* to the non-zero intercept, but C_1 is unobtainable at this temperature since $f_{max(1)}$ cannot be measured.

The frequency dependence of the real, C', and imaginary, C'', components of C^* at 70 K, 120 K and 300 K are plotted in Figure 3.8. For C', the equivalent circuit in figure 1 should show a low frequency, high capacitance plateau corresponding to the response of C_2, and a dispersion to a high frequency, low capacitance plateau corresponding to the response of C_1. The frequency at which the dispersion occurs is determined by the Debye peak in C'', ω_c. Given that C_1 and C_2 are fixed, ω_d is inversely proportional to R_1 and is, therefore, strongly dependent on temperature. For instance, at 70 K the high capacitance plateau can be observed up to ~ 1 Hz before dispersing to the low capacitance plateau, as shown in Figure 3.8 (a). At 120 K, the high capacitance plateau extends to ~ 635 Hz, and, at 300 K, it extends to ~ 54 kHz. The peak in C'' occurs at 10 Hz, 2.8 kHz and 380 kHz at 70 K, 120 K and 300 K, respectively, as shown in Figure 3.8 (b). Associated with C^* is tan δ, plotted in Figure 3.8 (c). The peak in tan δ is related to the peak in C'' (see table 3.1), being inversely proportional to R_1, but occurs at higher frequency, *i.e.* at 440 Hz, 180 kHz and 16 MHz at 70K, 120K and 300K, respectively.

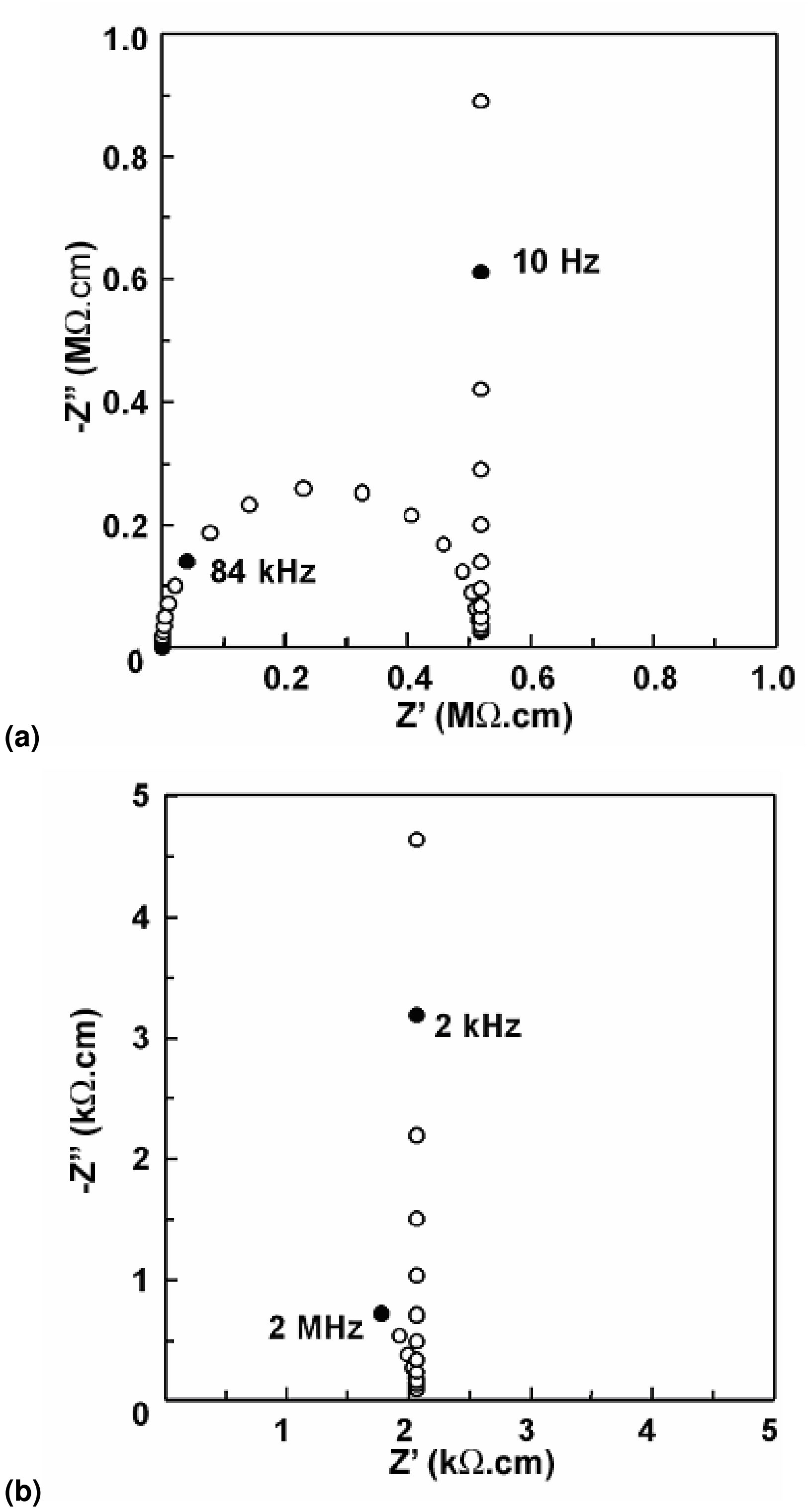

Figure 3.7: Simulated impedance spectra at (a) 70 K, (b) 120 K.

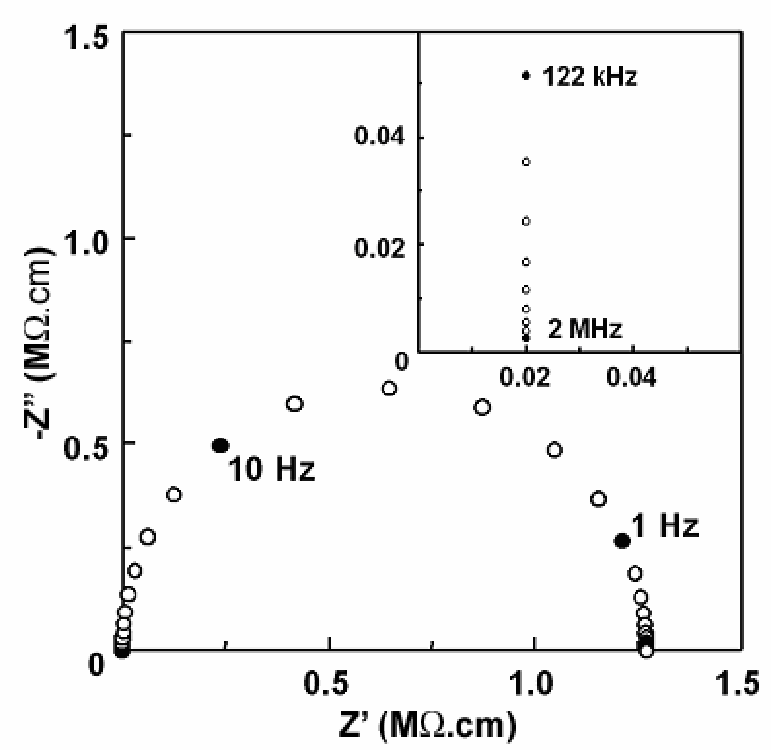

(c)

Figure 3.7 (contd.): Simulated impedance spectrum at (c) 300 K.

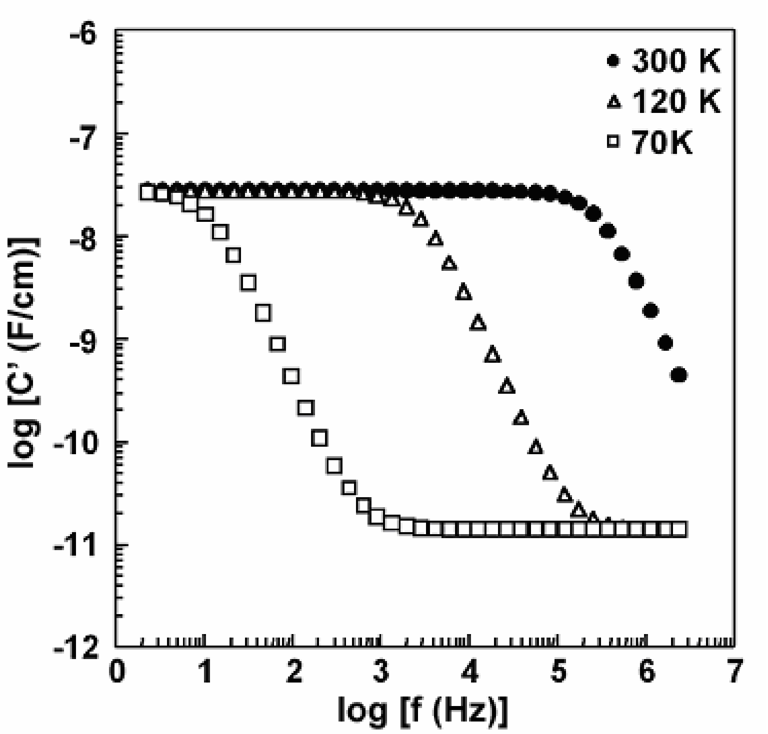

(a)

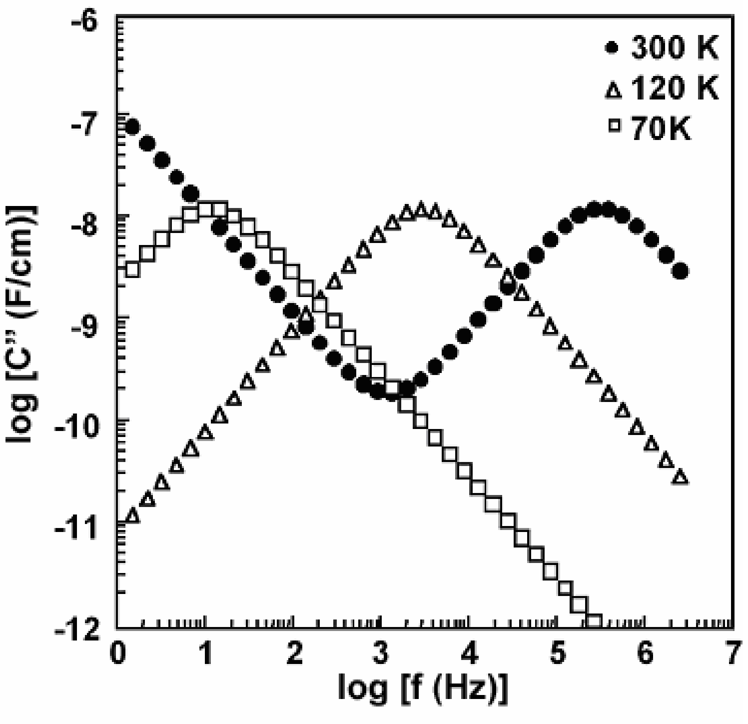

(b)

Figure 3.8: Spectroscopic plots of (a) *C*' and (b) *C*'' at 300 K, 120 K and 70 K.

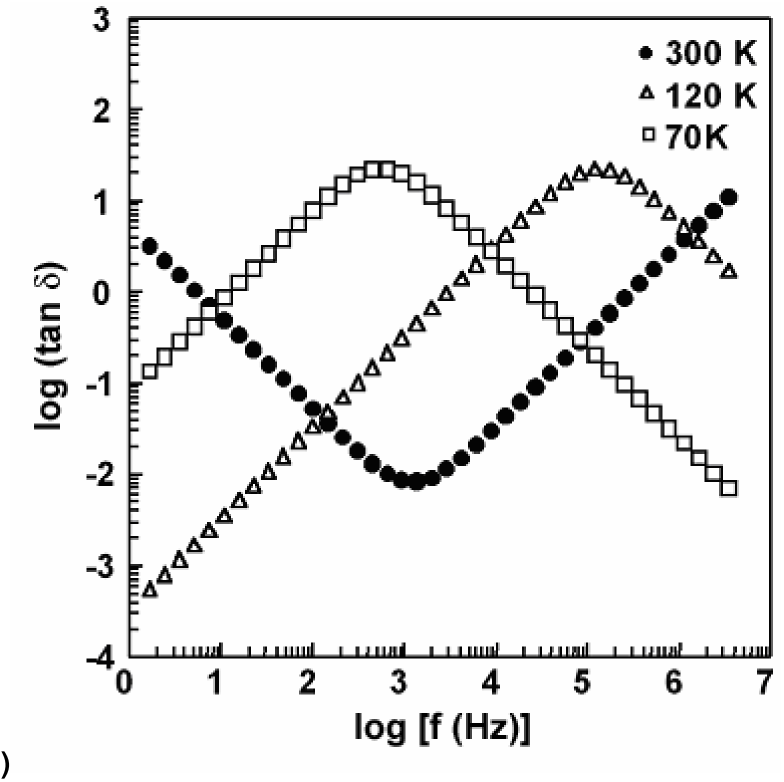

(c)

Figure 3.8 (contd): Spectroscopic plot of (c) tan *δ* at 300 K, 120 K and 70 K.

C', *C*'' and tan δ are plotted as a function of both frequency and temperature in Figures 3.9 (a), (b) and (c), respectively. The dispersion in *C*' and the peak in *C*'' have the same temperature dependence, decreasing exponentially with decreasing temperature. The interpretation based on an equivalent circuit of 2 parallel *RC* elements in series is simple but easily obfuscated when data are obtained using fixed frequency/variable temperature measurements, as shown by the white lines in Figure 3.9. In this case, a frequency of 128 kHz was selected as the fixed frequency. The data for C_1 appear to show a “transition” from high capacitance at room temperature to low capacitance at sub-ambient temperatures, the onset of which occurs at ~ 225 K. Referring to Figure 3.9 (b), it can be seen that the peak in *C*'' versus frequency, corresponding to ω_c, tends towards the fixed measuring frequency of 128 kHz as temperature decreases from 300 K. At ~ 225 K, ω_c corresponds to a frequency of ~ 128 kHz and so a maximum occurs in the fixed frequency measurements of *C*'', coincident with the onset of the decrease in C' observed in Figure 3.9 (a). Similarly, fixed frequency measurements of tan δ, Figure 3.9 (c), exhibit a maximum at ~ 110 K, associated with ω_d tending towards the fixed measuring frequency as temperature decreases. At ~ 110 K, ω_d corresponds to a frequency of ~ 128 kHz, resulting in a maximum in the fixed frequency tan δ measurements. If a higher frequency were to be selected for fixed frequency measurements then, upon cooling, changes in *C*', *C*'' and tan δ would appear to occur at higher temperatures.

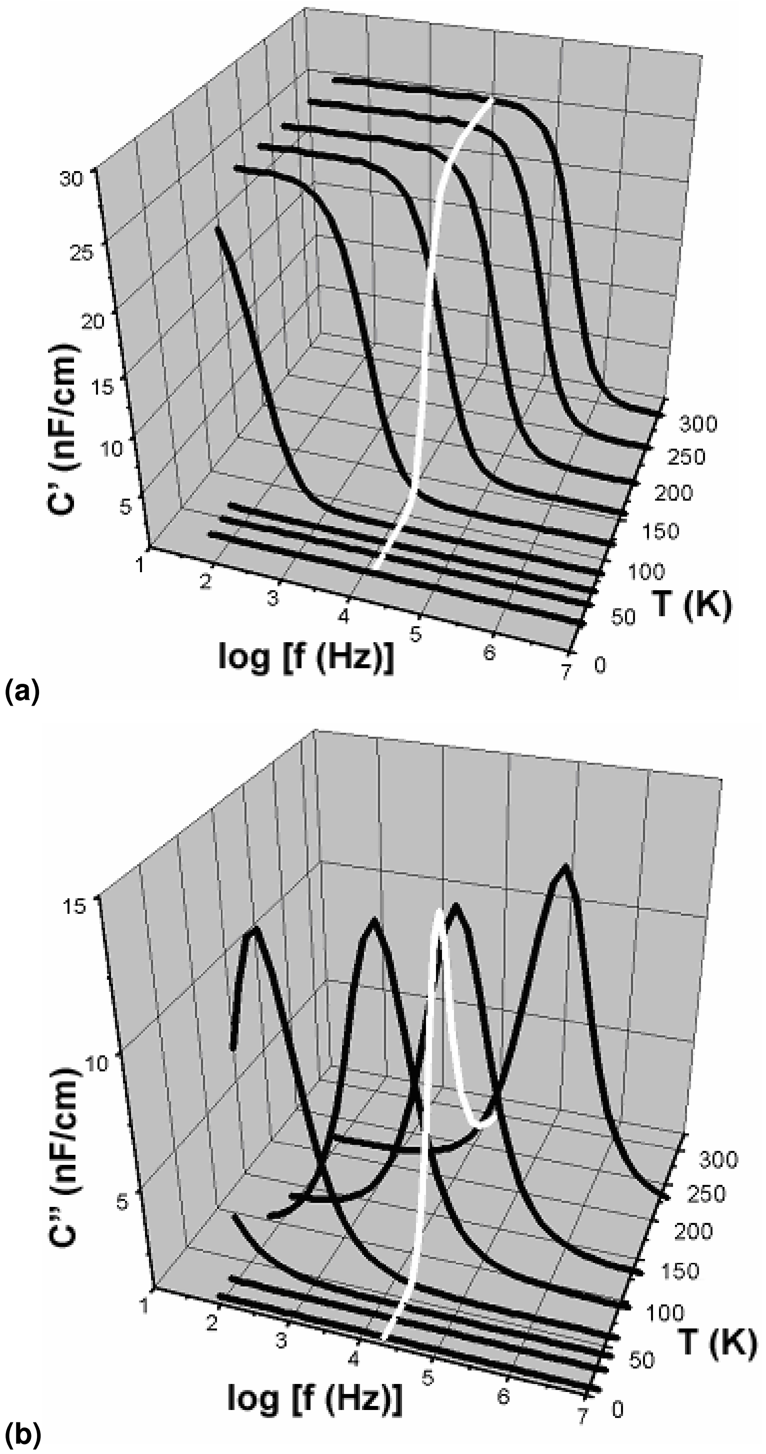

Figure 3.9: Simulated (a) C' and (b) C'' versus frequency and temperature, showing apparent fixed frequency behaviour at 10 kHz as the white curve.

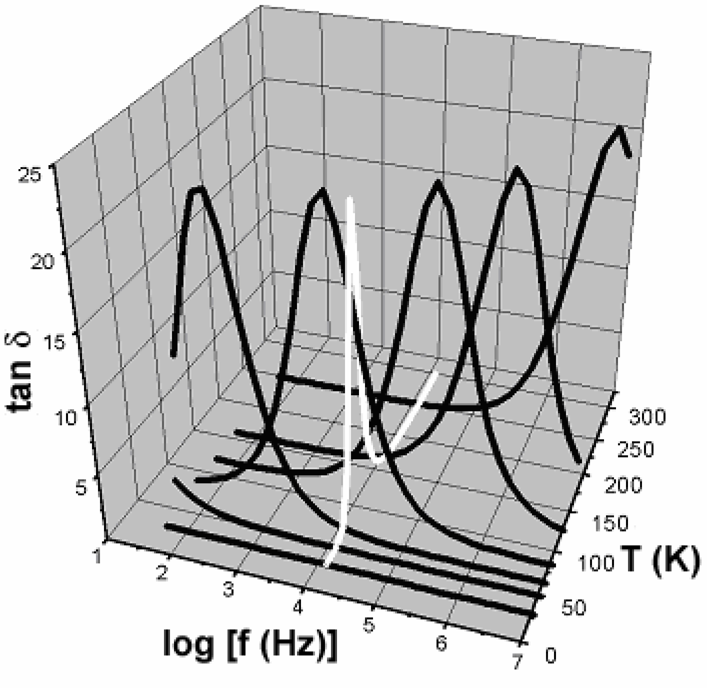

(c)

Figure 3.9 (contd): Simulated (c) tan δ versus frequency and temperature, showing apparent fixed frequency behaviour at 10 kHz as the white curve.

The simulations of an equivalent circuit corresponding to an IBLC provide a simple model for characterising materials with grain boundary barrier layer capacitances using impedance spectroscopy and demonstrates how the impedance characteristics may result in artefacts in selected frequency measurements of *C'*, *C"* and tan δ.

References

1. J.T.S. Irvine, D.C. Sinclair, A.R. West, "Electroceramics: Characterisation by Impedance Spectroscopy." Advanced Materials, 1990, **2**(3), 132-138
2. D.C. Sinclair, F.D. Morrison, A.R. West, "Application of Combined Impedance and Electric Modulus Spectroscopy to Characterise Electroceramics." International Ceramics, 2000,(2), 33-37
3. A.R. West, D.C. Sinclair, N. Hirose, "Characterisation of Electrical Materials, Especially Ferroelectrics, by Impedance Spectroscopy." Journal of Electroceramics, 1997, **1**(1), 65-71
4. J. Fleig, J. Maier, "A Finite Element Study on the Grain Boundary Impedance of Different Microstructures." Journal of the Electrochemical Society, 1998, **145**(6), 2081-2089
5. J. Fleig, J. Maier, "The Impedance of Ceramics with Highly Resistive Grain Boundaries: Validity and Limits of the Brick Layer Model." Journal of the European Ceramic Society, 1999, **19**, 693-696
6. Fleig, J., "The Influence of Non-Ideal Microstructures on the Analysis of Grain Boundary Impedances." Solid State Ionics, 2000, **131**, 117-127
7. D.C. Sinclair, T.B. Adams, F.D. Morrison, A.R. West, "$CaCu_3Ti_4O_{12}$: One-Step Internal Barrier Layer Capacitor ." Applied Physics Letters, 2002, **80**(12), 2153-2155
8. T.B. Adams, D.C. Sinclair, A.R. West, "Giant Barrier Layer Capacitance Effects in $CaCu_3Ti_4O_{12}$." Advanced Materials, 2002, **14**(18), 1321

4. Impedance Spectroscopy of $CaCu_3Ti_4O_{12}$ Ceramics

4.1. Introduction

Recent investigations into the electrical properties of $CaCu_3Ti_4O_{12}$ by Homes and Subramanian [1, 2] were discussed in Section 1.3.4. The observation of high permittivity at ambient temperatures and an apparent relaxor-like (*i.e.* frequency dependent) transition to a low permittivity state at sub-ambient temperatures were a common theme in their publications. It was speculated that such behaviour was attributable to either a new "exotic" polarisation mechanism facilitated by the octahedral tilt system ($a^+a^+a^+$, corresponding to $Im3$ space group symmetry) or a barrier layer capacitance arising from insulating layers at grain boundaries and/or twin boundaries. Conclusive evidence for either case, however, was not forthcoming.

In this Chapter, impedance spectroscopy data were used to identify the bulk response, associated with the intrinsic electrical properties of the $CaCu_3Ti_4O_{12}$ grains, and characterise possible extrinsic responses that may arise from insulating surface layers and/or electrode contact phenomena. Preliminary investigations into the pO_2 dependence of the electrical properties are made to elucidate the conductivity mechanism(s) in the bulk and grain boundary regions. The stability of $CaCu_3Ti_4O_{12}$ was investigated by weight loss experiments (TGA) of reacted powder samples in air and H_2 – Ar atmospheres.

By modifying the processing route and replacing hand-grinding with planetary ball milling, it was possible to produce fully dense $CaCu_3Ti_4O_{12}$ ceramics with either fine-grained (~ 5 – 10 μm) microstructures or, when sintered for an extended period of time, coarse-grained (~ 100 – 300 μm) microstructures. The compositions of coarse-grained ceramics were analysed by EPMA. The influence of grain size on the electrical properties of $CaCu_3Ti_4O_{12}$ was then investigated by impedance spectroscopy.

4.2. Experimental

4.2.1. Opening Investigations

Single-phase powders of $CaCu_3Ti_4O_{12}$ were prepared by the mixed oxide route from appropriate quantities of $CaCO_3$, TiO_2 and CuO. Powders were mixed with acetone in an agate mortar & pestle and reacted (twice) overnight in air at 1000 °C on Pt foil. A sample of the reacted powder was analysed by X-ray Diffraction (Hagg-Guinier camera, Cu-Kα_1 radiation, 40 kV, 30 mA). Pellets were prepared by sintering uniaxially cold-pressed 10 mm diameter compacts in air at 1115 °C overnight and were found to be 85 % - 95 % of the theoretical X-ray density. One pellet was reground and analysed by XRD. Au electrodes were sputtered onto the major pellet faces prior to electrical measurements, which were performed over the range 5 Hz – 13 MHz with a sinusoidal signal of amplitude 100 mV using a Hewlett-Packard Impedance Analyser, model 4192A. Locating the conductivity jig in a tube furnace facilitated high temperature impedance measurements and an Oxford Instruments Cryostat facilitated sub-ambient temperature measurements. All data were corrected for pellet geometry and analysed using commercial software (Z-view, version 1.5). The sample was then post-annealed in N_2 at 1000°C for 6 h (heating rate 5 °C/min, cooling rate 2.5 °C/min) and the RT impedance re-measured. Two powder samples (~ 8 mg) were analysed by TGA (Stanton Redcroft model STA1500) from RT to 1100°C in air and H_2 – Ar atmospheres, respectively. The samples were subsequently analysed by XRD (STOE Stadi-P, Cu kα_1 radiation, 40 kV, 40 mA).

4.2.2. Grain Size Dependence

Appropriate amounts of reagent grade $CaCO_3$, CuO and TiO_2 were mixed in a planetary ball mill with acetone using an agate pot and balls (a mixture of 5 and 10mm balls) at 250 rpm for 20 min. After drying, the powder (~ 10 g) was reacted in air overnight at 1000 ^{o}C on Pt foil and then milled again at 250 rpm for 30 min prior to a second reaction at 1000 ^{o}C. The powder was then planetary ball-milled at 250 rpm for 60 min. XRD (Hagg-Guinier camera, Cu-Kα_1 radiation, 40 kV, 30 mA) of a powder sample was used to assess phase purity. A Coulter LS130 laser size analyser showed a bimodal particle size distribution for the powder at ~ 0.4 and 6 μm and a d_{50} value of ~ 3.4 μm. $CaCu_3Ti_4O_{12}$ powder compacts were pressed in a 10mm steel die at 0.5 tonnes and were sintered at 1115 ^{o}C in air for 1, 3, 5, 8 and 24 h, respectively, and furnace-cooled to room temperature. Pellet densities were calculated from the mass and dimensions of the pellets and all were > 95% of the theoretical X-ray density. Scanning Electron Microscopy (Camscan mark 2) was performed at 20 kV on as-prepared pellet surfaces that were Au sputter-coated prior to examination. A sample sintered for 24 hours was prepared as an optically-transparent section using standard techniques and characterised by EPMA (Cambridge Scientific Instruments Microscan 9; beam voltage and current were 15 kV and 4 nA, respectively, and pure Cu metal, wollastonite ($CaSiO_3$), rutile (TiO_2) and quartz (SiO_2) standards were used to identify Cu, Ca, Ti and Si, respectively). Electrical property characterisation was performed using impedance spectroscopy as described above. Prior to measurement, the major pellet faces were lightly polished with SiC paper and InGa (~ 60:40 mole ratio) electrodes applied.

4.3. Results & Discussion

4.3.1. Opening Investigations

The XRD pattern for the reacted powder was fully indexed to the pattern reported in [3], Figure 4.1 being a typical example for $CaCu_3Ti_4O_{12}$ as measured using high resolution XRD. The unit cell parameter, *a*, was determined to be 7.39547(19) Å.

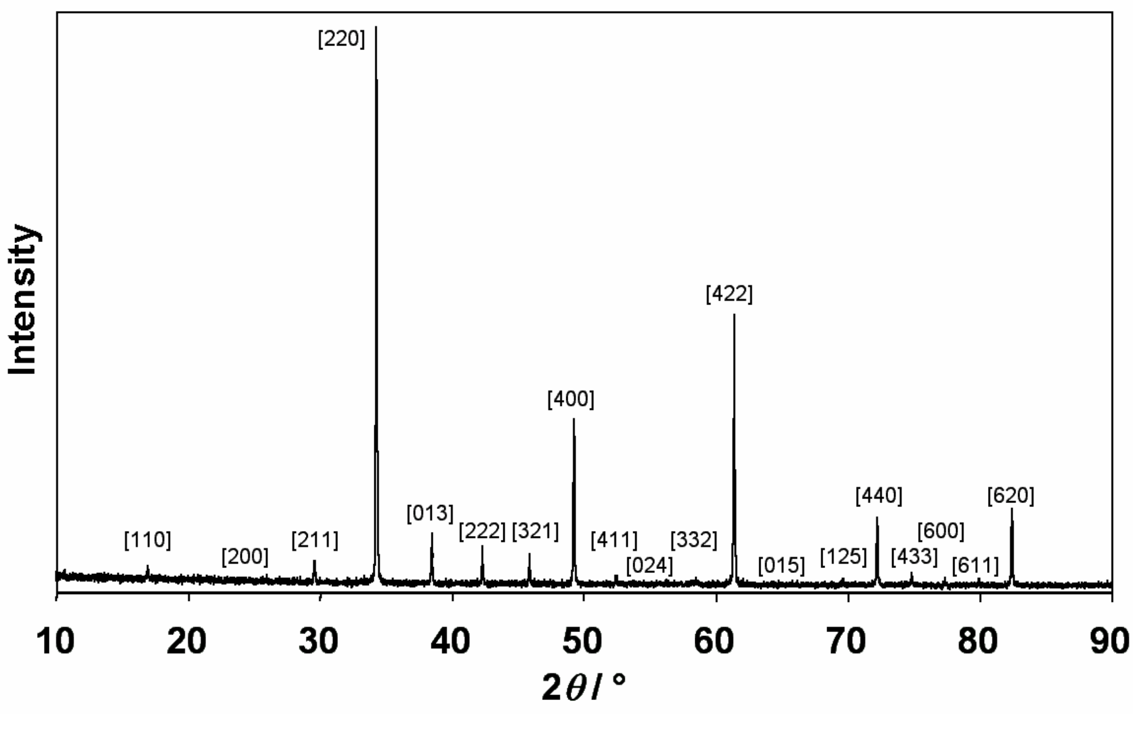

Figure 4.1: Typical XRD pattern for $CaCu_3Ti_4O_{12}$ powders and reground ceramics.

Figure 4.2 (a) shows the variation in real capacitance, *C'*, with frequency between ~ 100 K and 250 K for a $CaCu_3Ti_4O_{12}$ ceramic. At 250 K, the data show a plateau with *C'* ~ 1.7 nF.cm (equivalent to a relative permittivity, *ε'*, value of ~ 18,700) over most of the frequency range but drops dramatically in the MHz region. With decreasing temperature, the magnitude of the plateau remains constant but the dramatic drop in C' occurs at increasingly lower frequencies until, at temperatures below 150 K, a second, high frequency plateau with C ~ 10 pF (ε' ~ 110) is observed.

The frequency dependence of C' is indicative of an electrically heterogeneous microstructure in which the bulk material in the grains is electrically (and chemically) discrete from that of the grain boundaries. As discussed in Chapter 3, for such a system, data can often be modelled on an ideal equivalent circuit consisting of two parallel *RC* elements connected in series, one *RC* element for the bulk and the other for the grain boundary response. Each *RC* element gives rise to (ideally) a semicircular arc in impedance complex plane plots, Z^*, and a plateau in spectroscopic plots of the real component of the permittivity (or C'). The grain and grain boundary responses can be identified by the magnitude of C associated with each arc which, based on the brickwork layer model, are typically of the order of pF and nF, respectively. The position of the arcs in the frequency spectrum depends on their relaxation times, τ; at the arc maxima, the relationship $\omega_{\max}RC = 1$ holds. In general, τ for grain boundary regions is much larger than for the bulk and the grain boundary response is relaxed out at lower frequencies than bulk effects. Often, *RC* elements have $\omega_{\max}$ values that lie outside the available frequency range, especially if they represent either insulating regions with high R or semiconducting regions with low R. In such cases, only parts of arcs may be observed.

When measured at a fixed frequency, e.g. 100 kHz, C' appears to show a transition from a high capacitance state at high temperature to a low capacitance state at low temperature, Figure 4.2 (b). This is not due to changes in the polarisation mechanism arising from structural distortions, as observed in ferroelectric crystals, but is associated with the changing frequency range of the bulk and grain boundary plateaus in the C' spectroscopic plot. The apparent dielectric phenomenon reported by Subramanian and Homes[1, 2] is therefore explained by an electrical heterogeneous microstructure. The resultant artefacts observed in fixed frequency C' measurements only *appear* to be similar to relaxor-ferroelectric behaviour.

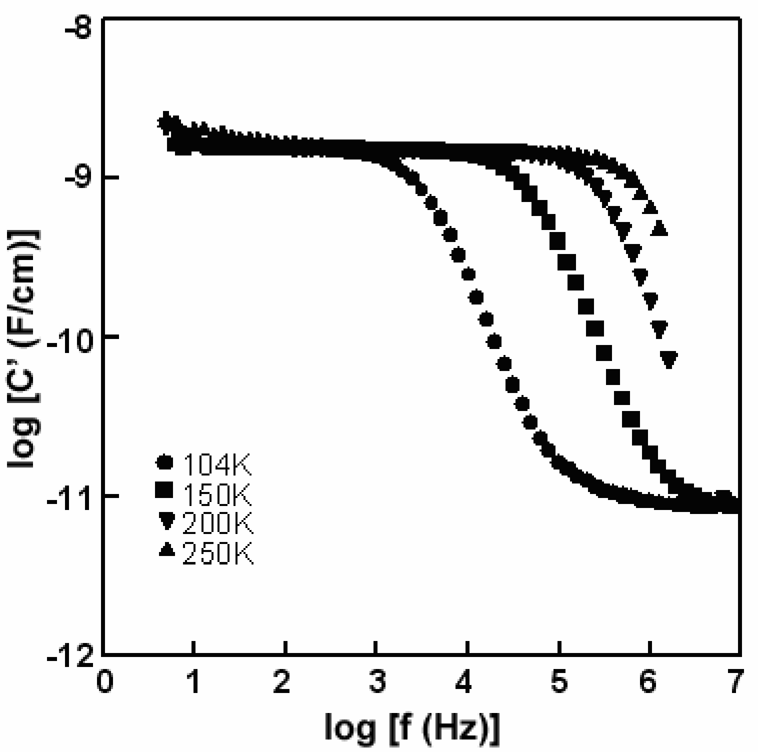

(a)

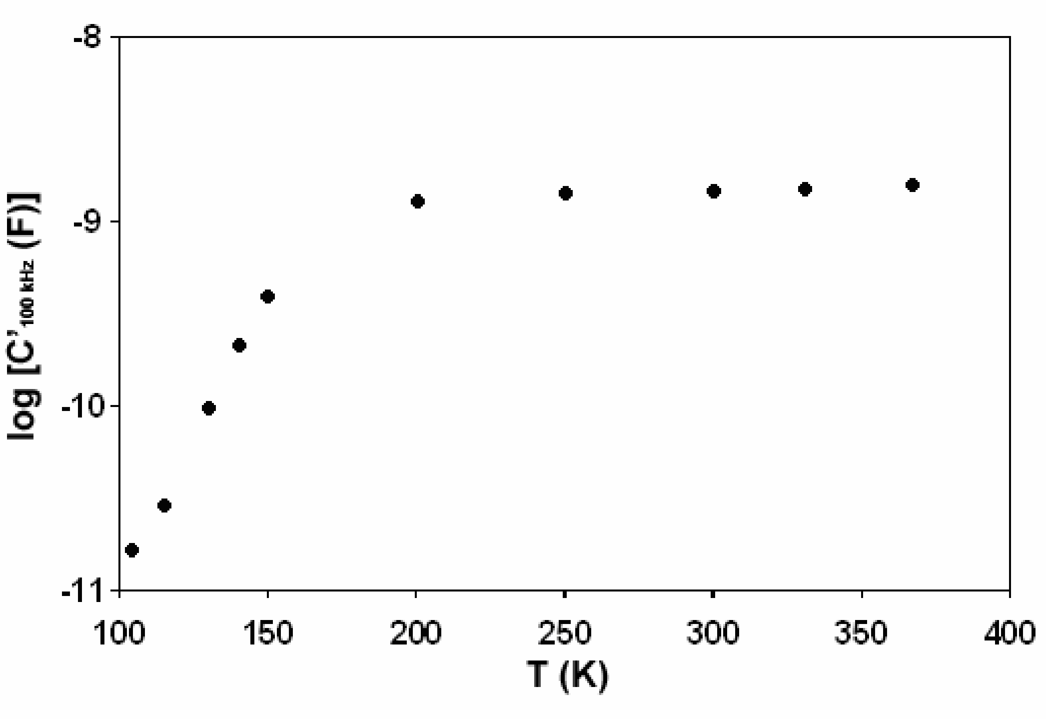

(b)

Figure 4.2: (a) spectroscopic plot of C' for $CaCu_3Ti_4O_{12}$ at sub-ambient temperatures and (b) variation in C' at 100 kHz with temperature.

A Z^* plot for $CaCu_3Ti_4O_{12}$ ceramics at room temperature (~ 25 – 30 °C) contains a large arc with non-zero intercept at high frequencies, Figure 4.3 (a). Based on an equivalent circuit consisting of two parallel *RC* elements in series, the non-zero intercept indicates the presence of an arc with $\omega_{\max}$ higher than the maximum frequency measured (10^7 Hz). This component has a resistance of 62 Ω.cm; although it is not possible to calculate its capacitance, it is clearly < 250 pF/cm. The large arc with $f_{\max}$ ~ 1000 Hz has R ~ 0.45 MΩ.cm and C ~ 2.2 nF/cm. The response did not change significantly on polishing the pellet faces. The room temperature data therefore indicate $CaCu_3Ti_4O_{12}$ ceramics prepared in air to consist of moderately insulating grain boundary regions with semiconducting grains.

Z^* plots for measurements above and below 300 K show the bulk (R_b) and grain boundary (R_{gb}) resistances to be thermally activated; low temperature data confirm the presence of the expected high frequency (bulk) arc, e.g., at 104 K R_b ~ 25 kΩ.cm and C_b ~ 9 pF/cm, Figure 4.3 (b). At these temperatures, $R_{gb} >> 10^7$ Ω.cm and $\omega_{\max} << 10^2$ Hz and therefore, only a small section of the grain boundary arc is observed, as a steep incline at low frequencies, Figure 4.3 (b).

Conductivity data, σ, where $\sigma = R^{-1}$, were obtained from the bulk, σ_b, and grain boundary, σ_{gb}, components and plotted against reciprocal temperature in Arrhenius format, Figure 4.4. Both obey the Arrhenius law with activation energies of 0.08(2) eV and 0.60(2) eV, respectively. This low value for the bulk activation energy is consistent with that observed for other semiconducting titanate perovskites, such as La-doped $BaTiO_3$. C_b showed little variation with temperature from ~ 9 pF/cm (ε' ~ 110) at 104 K and is comparable to other tilted, titanate perovskites, such as $CaTiO_3$ and other isostructural $ACu_3Ti_4O_{12}$ and $A'_{2/3}Cu_3Ti_3FeO_{12}$ compounds where A = Cd and A' = Bi, Y, etc. C_{gb} remained relatively constant at ~ 1.7 nF/cm over the range 150 – 400 K.

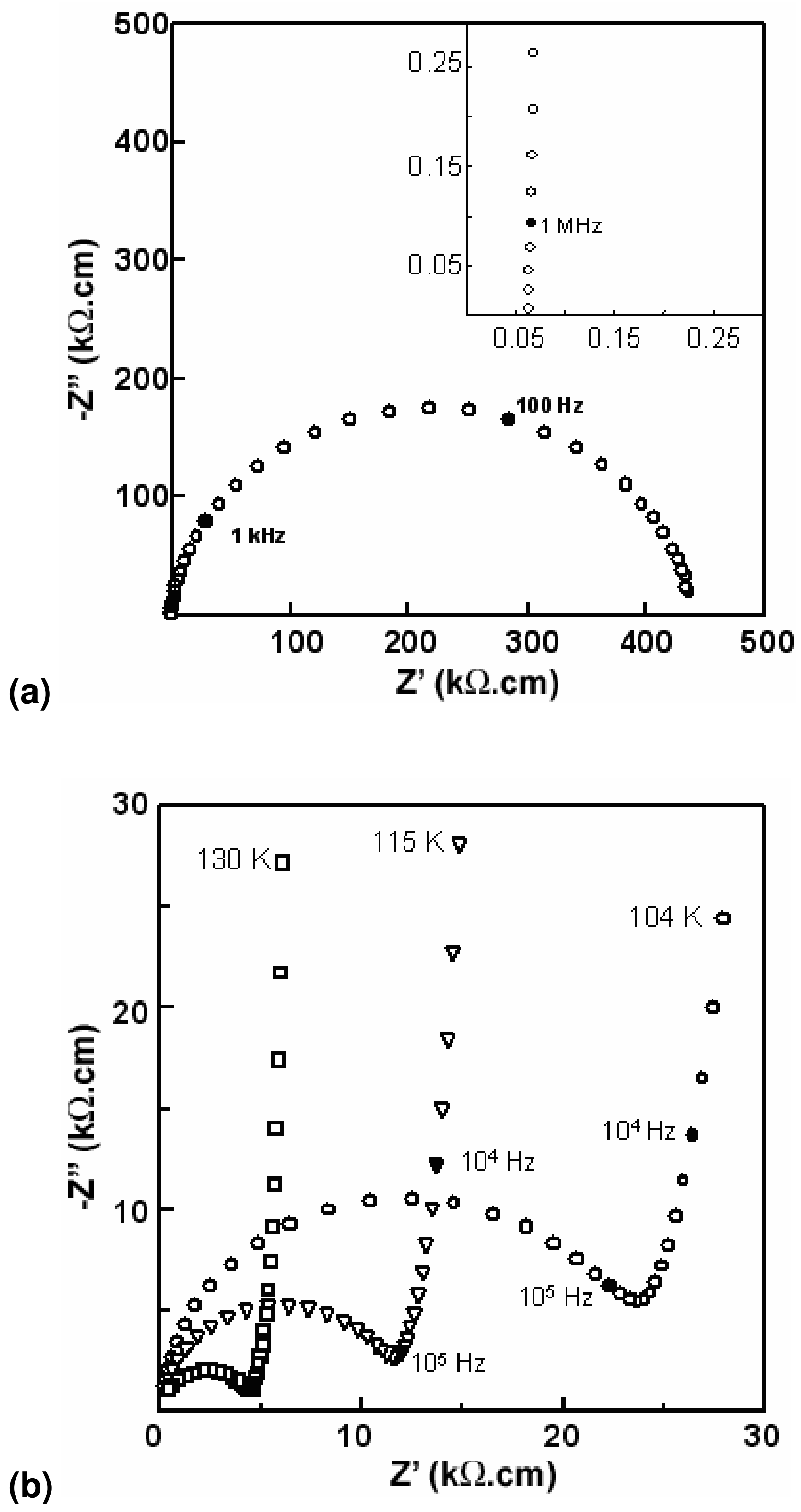

Figure 4.3: (a) Z* plot of $CaCu_3Ti_4O_{12}$ at room temperature showing non-zero intercept (inset), (b) Z* plot of $CaCu_3Ti_4O_{12}$ showing bulk response at low temperatures.

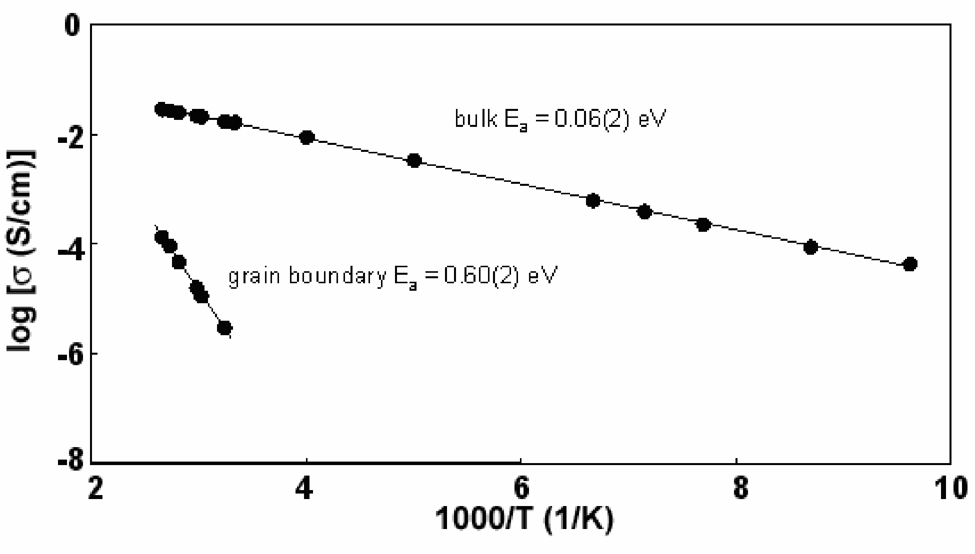

Figure 4.4: Arrhenius conductivity plot for $CaCu_3Ti_4O_{12}$.

Heat treatment of prefired pellets in N_2 at 1000℃ caused a significant change in the room temperature Z^* plot, as shown in Figure 4.5. The high frequency, non-zero intercept corresponding to R_b increased slightly to ~ 130 Ω.cm, compared to Figure 4.3 (a), whereas R_{gb} decreased by two orders of magnitude to ~ 7 kΩ.cm. This shows R_{gb} depends on the oxygen partial pressure of the atmosphere in which ceramics are processed. In particular, the difference in electrical properties of samples heated in air and N_2 demonstrates that limited reoxidation of the grain boundaries must occur on cooling from the sintering temperature to produce thin, insulating layers within the ceramics which give rise to the high and essentially temperature-independent permittivity observed in the kHz region. The apparent increase in R_b may be attributable to inductive effects in the conductivity jig above 2 MHz due to the low impedance of the sample, < ~ 7kΩ.cm.

Based on this simple model of semiconducting perovskite grains with a bulk permittivity of ~ 100, and with thin, oxidised insulating grain boundaries, there is no need to infer a complex dipole relaxation model associated with the crystal structure to explain the capacitance behaviour observed in Figure 4.2. Instead, it can be rationalised and modelled on that expected for an IBLC.

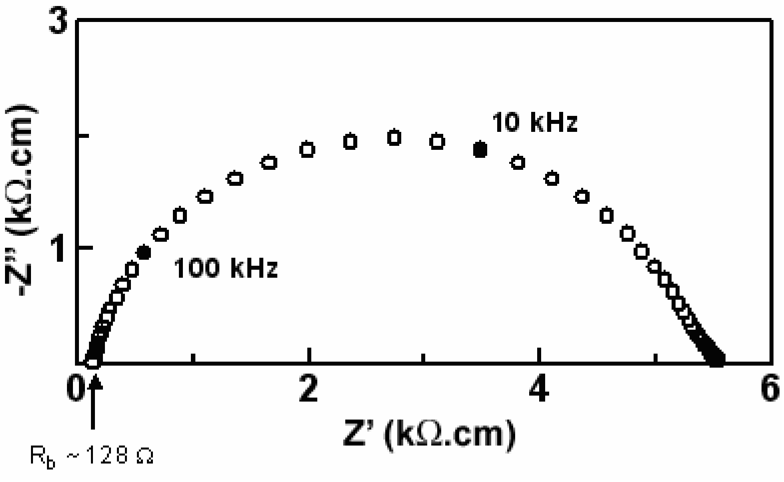

Figure 4.5: Z* plot of $CaCu_3Ti_4O_{12}$ at room temperature after post-annealing at 1000°C in N_2.

The semiconductivity of the grains may arise from a small amount of oxygen loss during ceramic processing in air at elevated temperatures, as is known to occur in other titanate-based materials. Alternatively, the grains may be oxygen stoichiometric and exhibit intrinsic semiconductivity, as occurs in the structurally related $CaCu_3Mn_4O_{12}$.

It was not possible to quantify the amount of oxygen loss from the grain boundaries (and bulk) during sintering; thermogravimetric (TG) studies in air to 1100 °C showed no significant weight loss on heating or weight gain on cooling; this suggests, but does not prove, that the departure from oxygen stoichiometry is small. Hydrogen reduction TG, Figure 4.6, showed the samples to commence losing weight at ~ 330 °C. The weight loss ceases to increase above 680 °C, at which point ~ 7 - 8 % of the original mass has been lost.

XRD of the remaining powder following the TGA experiment, Figure 4.7, revealed no trace of the original $CaCu_3Ti_4O_{12}$ phase. The remaining sample consisted of $CaTiO_3$, TiO_2 (Rutile) and metallic Cu indicating that heat treatment at 1100 °C in H_2 - Ar resulted in complete decomposition of $CaCu_3Ti_4O_{12}$.

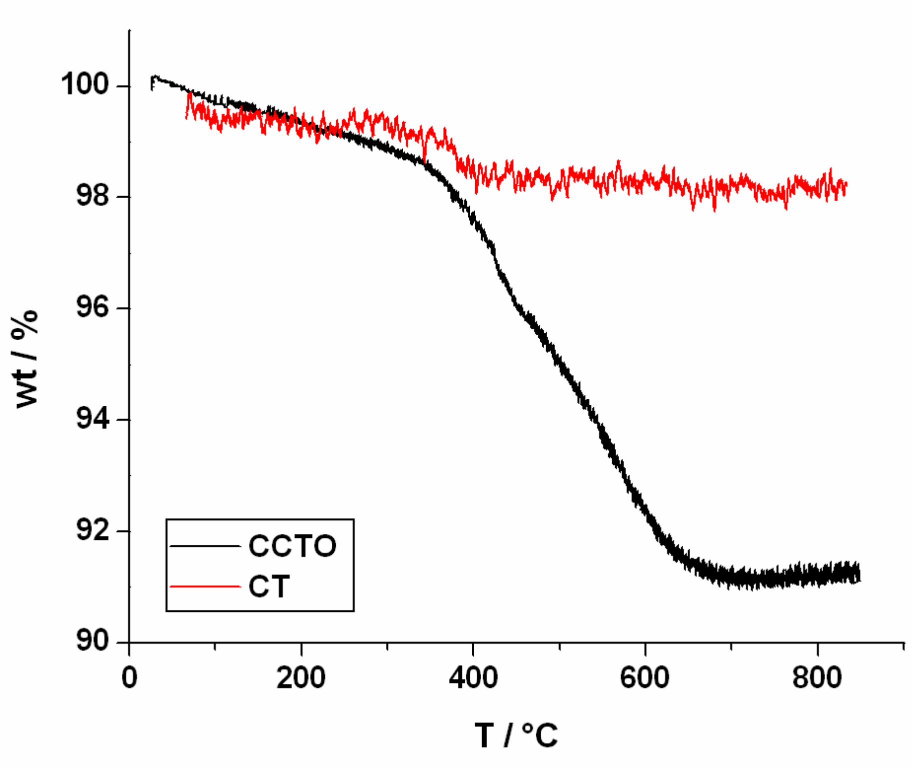

Figure 4.6: TG behaviour of $CaCu_3Ti_4O_{12}$ (black curve) and $CaTiO_3$ (red curve) powder heated to 850 °C in H_2-Ar atmosphere.

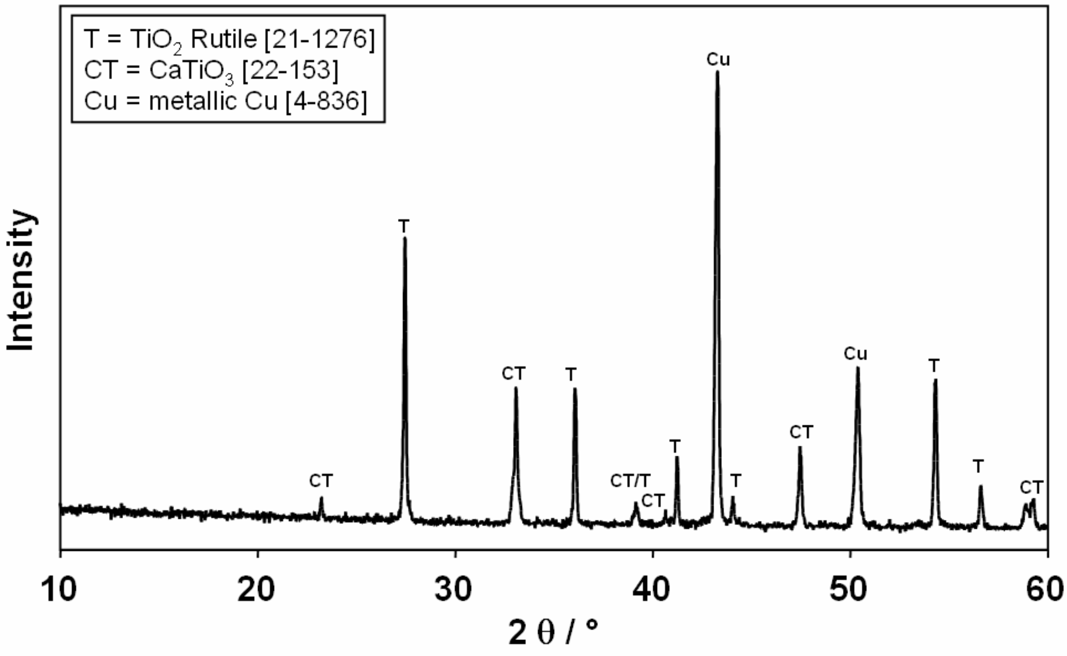

Figure 4.7: XRD pattern of phase mixture following TGA of $CaCu_3Ti_4O_{12}$ powder heated to 1100 °C in H_2-Ar atmosphere.

The overall decomposition reaction may, therefore, be described by:

$$CaCu_3Ti_4O_{12} \rightarrow CaTiO_3 + 3TiO_2 + 3Cu + 1\tfrac{1}{2}O_{2(g)}$$

The molar mass of $CaCu_3Ti_4O_{12}$ is 614.33 and the oxygen lost as a result of reduction of Cu^{2+} to Cu^0 (metallic) corresponds to a molar mass of 48, *i.e.* ~ 7.8 % of the total weight of $CaCu_3Ti_4O_{12}$ and thus fully accounts for the 7 - 8 % weight loss observed in the H_2 - Ar TGA experiment, Figure 4.6.

This ease of reduction in H_2 - Ar is in marked contrast to the behaviour of many $ATiO_3$ perovskites, such as $CaTiO_3$ (TGA data for this phase shown as the red trace in Figure 4.7), that are stable under similar atmospheres and temperatures in excess of 1400 °C, and provides indirect evidence that $CaCu_3Ti_4O_{12}$ may lose small amounts of oxygen to become semiconducting when heated in air at > 1000 °C. The oxygen-loss mechanism may be related to the unusual crystal structure in which a small cation with a low coordination number, *i.e.* Cu, occupies the A site in the perovskite lattice. Alternatively, $CaCu_3Ti_4O_{12}$ may not tolerate significant oxygen non-stoichiometry and instead decomposes directly to $CaTiO_3$, TiO_2 and Cu metal.

4.3.2. Grain Size Dependence

Secondary electron images of the as-sintered surfaces of the 1 hr sample, Figures 4.8 (a) and 4.8 (b), show a fine (~ 5 – 10 μm) grained, fully dense microstructure, suggesting that the final stage of sintering is reached after less than 1 h at sintering temperatures of ~ 1115 °C. Although the morphology of the as-sintered surfaces were not necessary representative of the bulk, it was not possible to reveal grain boundary texture of polished cross-sections (see Chapter 6) or fracture surfaces. However, given that many perovskite-related ceramics (e.g. $BaTiO_3$) often require sintering temperatures in excess of 1300 °C and dwell times greater than 6 h to reach the final stages of sintering, it is apparent that dense $CaCu_3Ti_4O_{12}$ ceramics can be sintered rapidly at relatively low temperatures. Rapid densification is more typical of a liquid phase sintering (LPS) system, in which transport of material into pores occurs by solution-precipitation, as opposed to solid state sintering (SSS) where transport occurs by diffusion of atoms via vacancies in the lattice, as described in Section 2.1.4.5. If LPS was the predominant sintering mechanism then it is possible that reactions between $CaCu_3Ti_4O_{12}$ and SiO_2 (arising from contamination by the milling media) and/or decomposition products are possible origins of the liquid phase.

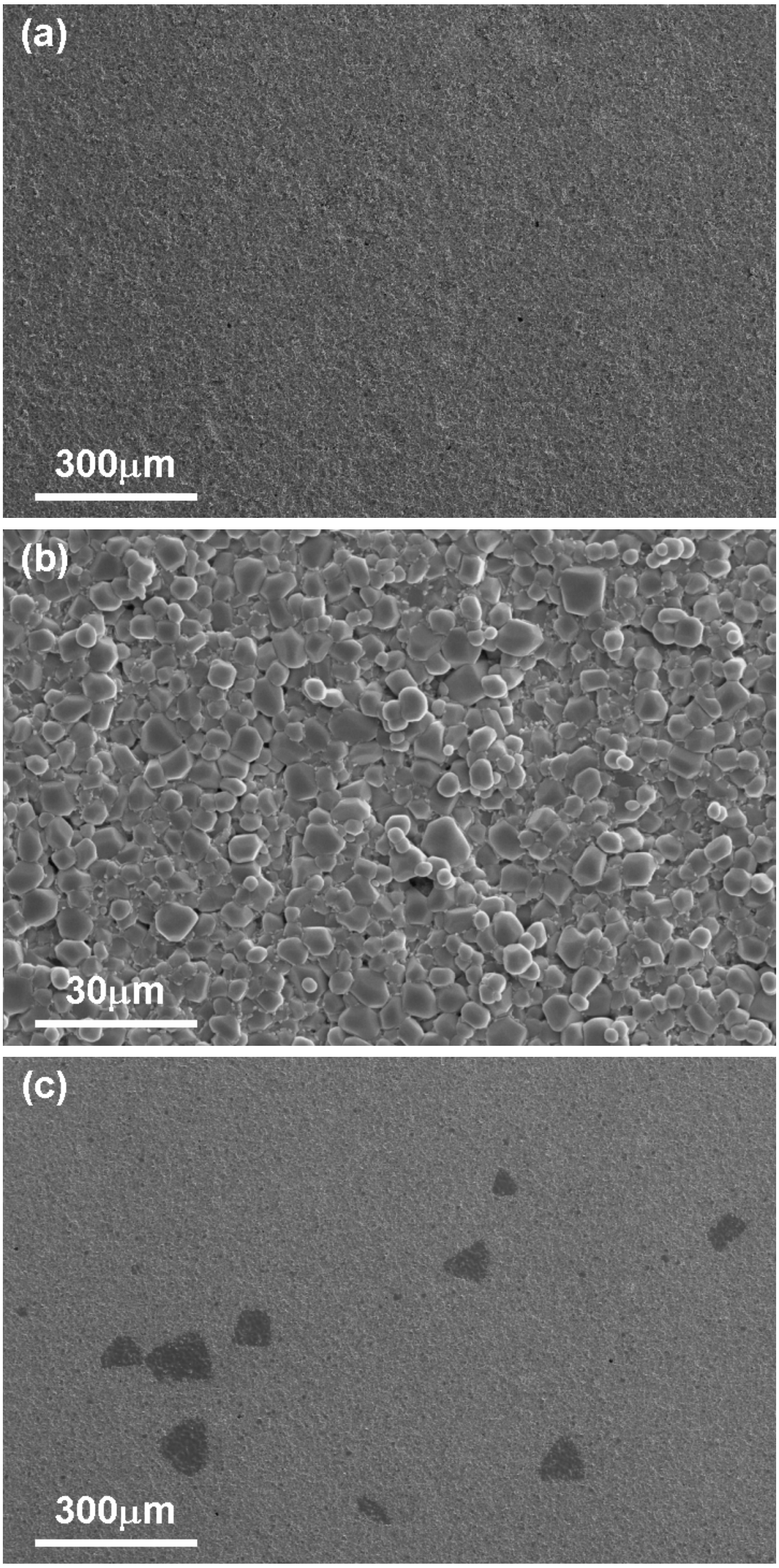

Figure 4.8: SEM images (SEI mode) showing microstructure of $CaCu_3Ti_4O_{12}$ ceramics sintered for 1 hour (a-b), 5 h (c), 8 h (d) and 24 h (e-f). Continued overleaf…

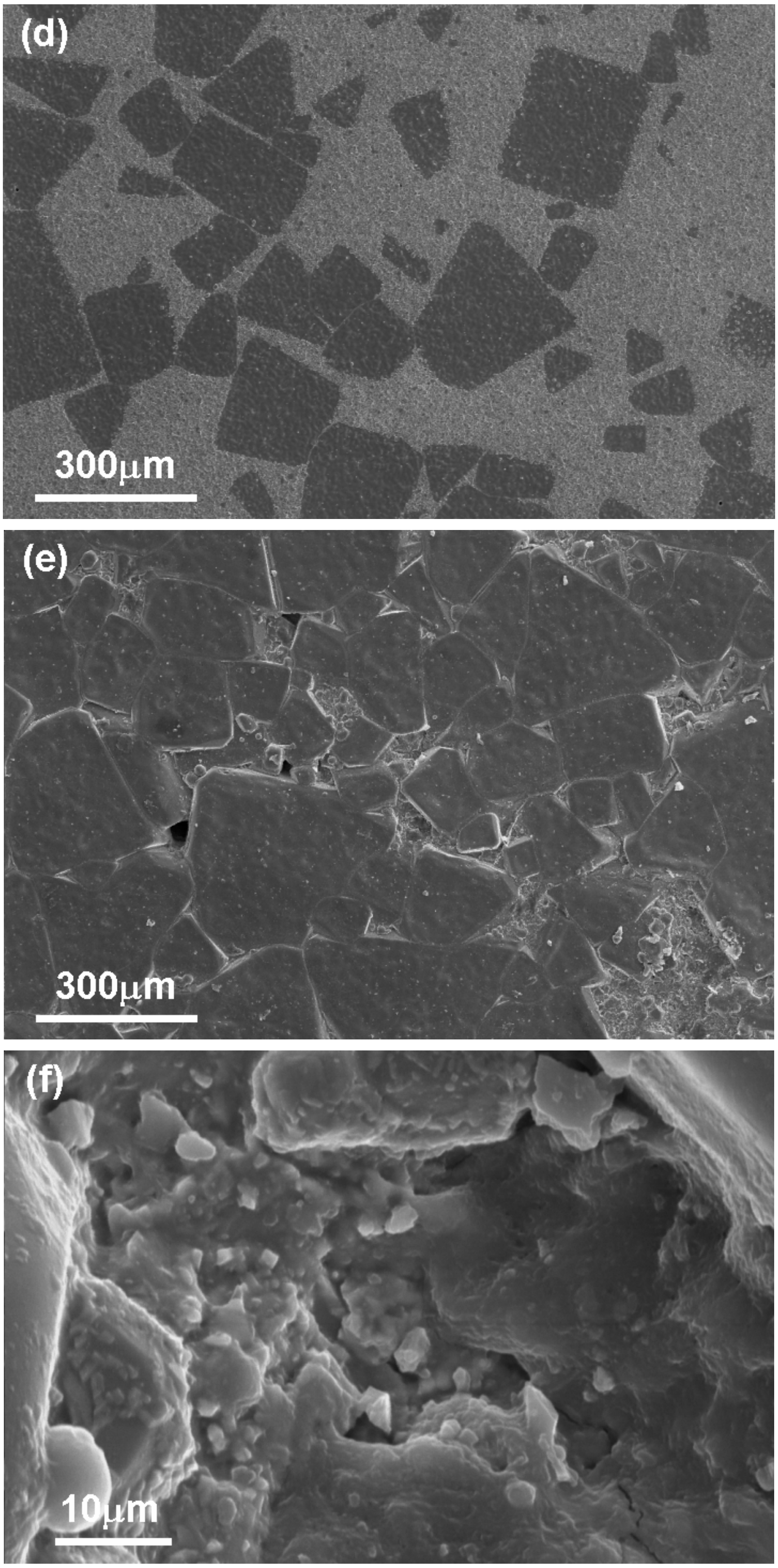

Figure 4.8: Continued.

Sintering for more than 1 h results in abnormal grain growth, whereby certain grains grow rapidly to sizes significantly greater than the mean grain size, as shown in Figure 4.8 (c) for a sample sintered for 5 h, contrary to the power law equation for normal growth, Equation 2.1. The large grains are isolated from one another by the 'matrix' of fine grains and appear darker, with grain sizes in the order of ~ 100 μm. Samples sintered for 8 h exhibit a greater number of large grains, some of which have become interconnected although the matrix of fine grains is still evident and a number of grains exceeded 300 μm in diameter. Samples sintered for 24 h, Figure 4.8 (d), were composed almost entirely of large grains of diameter ~ 50 – 300 μm. However, a higher magnification image, Figure 4.8 (e), reveals fine grains and (possibly) a second phase at grain boundary junctions and voids between the large grains, shown at higher magnification in Figure 4.8 (f). The rapid densification, smooth grain morphology, rapid abnormal grain growth and possible second phase precipitates at grain boundary junctions strongly suggest that the densification of $CaCu_3Ti_4O_{12}$ ceramics at 1115 °C had occurred by LPS.

A coarse-grained pellet was characterised by EPMA to analyse the stoichiometry of the bulk phase and to identify and subsequently determine the composition of secondary phases. Backscattered Electron Imaging (BEI) revealed dark spherical precipitates of ~ 5 μm diameter, Figure 4.9 (a). Figure 4.9 (b) is an elemental map corresponding to Si, of the same area shown in Figure 4.9 (a), and shows that the precipitates are a Si-rich phase. A secondary phase was also observed at grain boundary triple junctions (not shown). Quantitative data were collected from the matrix, precipitate and triple junction phases and shown in Tables 4.1 – 4.3.

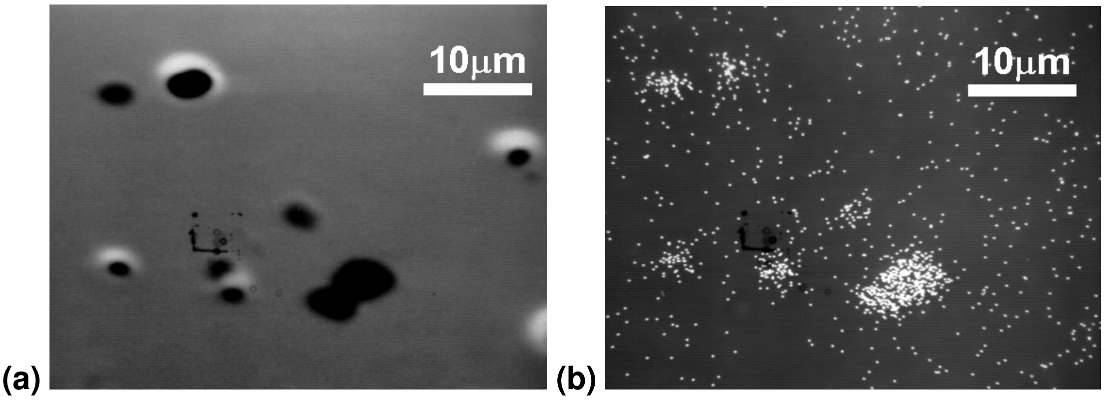

Figure 4.9: Precipitate phase in pellet sintered for 24 hours at 1115°C in air: (a) backscattered electron image and (b) X-ray map corresponding to silicon.

Element	Raw El wt%	Corrected El wt%	Oxide wt%	Stoichiometry
Si	0.05	0.06	0.12	0.0119
Ca	7.51	6.54	9.15	0.9791
Ti	32.74	32.23	53.76	4.0395
Cu	27.03	30.88	38.65	2.9171
O	32.67	30.29	0.00	
TOTAL	100.00	100.00	101.68	7.9476

Table 4.1: EPMA quantitative data of the matrix phase.

Element	Raw El wt%	Corrected El wt%	Oxide wt%	Stoichiometry
Si	13.43	13.75	29.41	0.9577
Ca	21.47	20.11	28.14	0.9817
Ti	23.44	25.17	41.99	1.0282
Cu	1.22	1.50	1.88	0.0462
O	40.44	39.47	0.00	
TOTAL	100.00	100.00	101.42	3.0138

Table 4.2: EPMA quantitative data of the precipitate phase.

Element	Raw El wt%	Corrected El wt%	Oxide wt%	Stoichiometry
Si	0.06	0.07	0.16	0.0148
Ca	0.07	0.06	0.08	0.0084
Ti	0.72	0.65	1.09	0.0760
Cu	83.71	87.19	98.09	7.6735
O	15.44	12.03	0.00	
TOTAL	100.00	100.00	99.42	7.7727

Table 4.3: EPMA quantitative data of the grain boundary triple point phase.

The composition of the main phase, Table 4.1, accurate to +/-0.02, was $Ca_{0.98}Cu_{2.92}Ti_{4.04}O_{12}$ containing 0.012 mols SiO_2. The spherical precipitates were determined to be of sphene ($CaTiSiO_5$) and the grain boundary triple junction phase, was determined to be Cu_2O containing 0.076 mols TiO_2.

The EPMA data revealed samples made from planetary ball milled powder were SiO_2 contaminated. However, the contaminant Si cations appear to have segregated, forming $CaTiSiO_5$ precipitates, rather than become incorporated into the $CaCu_3Ti_4O_{12}$ lattice (by substitution, for instance). Furthermore, the EPMA data suggest that limited decomposition of $CaCu_3Ti_4O_{12}$ occurred when heated to 1115 °C in air to form precipitates of Cu_2O and $CaTiSiO_5$.

Z^* plots for pellets sintered for 3 h and 24 h are shown in Figures 4.10 (a) and (b), respectively. Both show a large, semi-circular arc with a non-zero intercept on the Z' axis at high frequencies (see insets in Figures 4.10 (a) and (b)). All impedance data could be interpreted in terms of an equivalent circuit of two parallel *RC* elements connected in series. One *RC* element corresponds to the semiconducting grains which gives rise to the non-zero intercept of ~ 70 Ω.cm, Figure 4.10 (a) and ~ 30 Ω.cm, Figure 4.10 (b) in the Z^* plots. The other corresponds to the 'leaky' grain boundary regions which give rise to the large arc of ~ 4.2 MΩ.cm, Figure 4.10 (a) and 0.18 MΩ.cm, Figure 4.10 (b) for pellets sintered for 3 hrs and 24 hrs, respectively. f_{max} values for the grain boundary impedance were determined from Z^* plots for the 3 hrs and 24 hrs samples as being ~ 40 Hz and ~ 25 Hz. Using the relationship $\omega_{\mathrm{max}}RC = 1$, C_{gb} values of ~ 0.95 nF/cm and ~ 35.37 nF/cm for the 3 and 24 h samples, respectively. Since the effective permittivity, $\varepsilon'_{\mathrm{eff}}$, of an internal barrier layer capacitor arises from the grain boundary capacitance, $\varepsilon'_{\mathrm{eff}}$ values of ~ 10,700 and ~ 399,500 are obtained for the 3 h and 24 h samples, respectively.

Z^* plots for the 3 h sample are comparable with those for samples sintered for 1 h and 5 h, as shown in Table 4.4, and data for the 24 h sample are comparable with those for sample sintered for 8 h. The rapid coarsening between 5 and 8 h, therefore results in an increase in C_{gb} of ~ 1 order of magnitude and a similarly substantial decrease in R_{gb}. The trend of f_{max} to decrease from 100 to 25 Hz for 1 and 24 h samples, respectively, indicates that either the grain boundary composition is changing or that, as the microstructure deviates from the brick layer model, current detours are responsible for the apparent change in f_{max}.

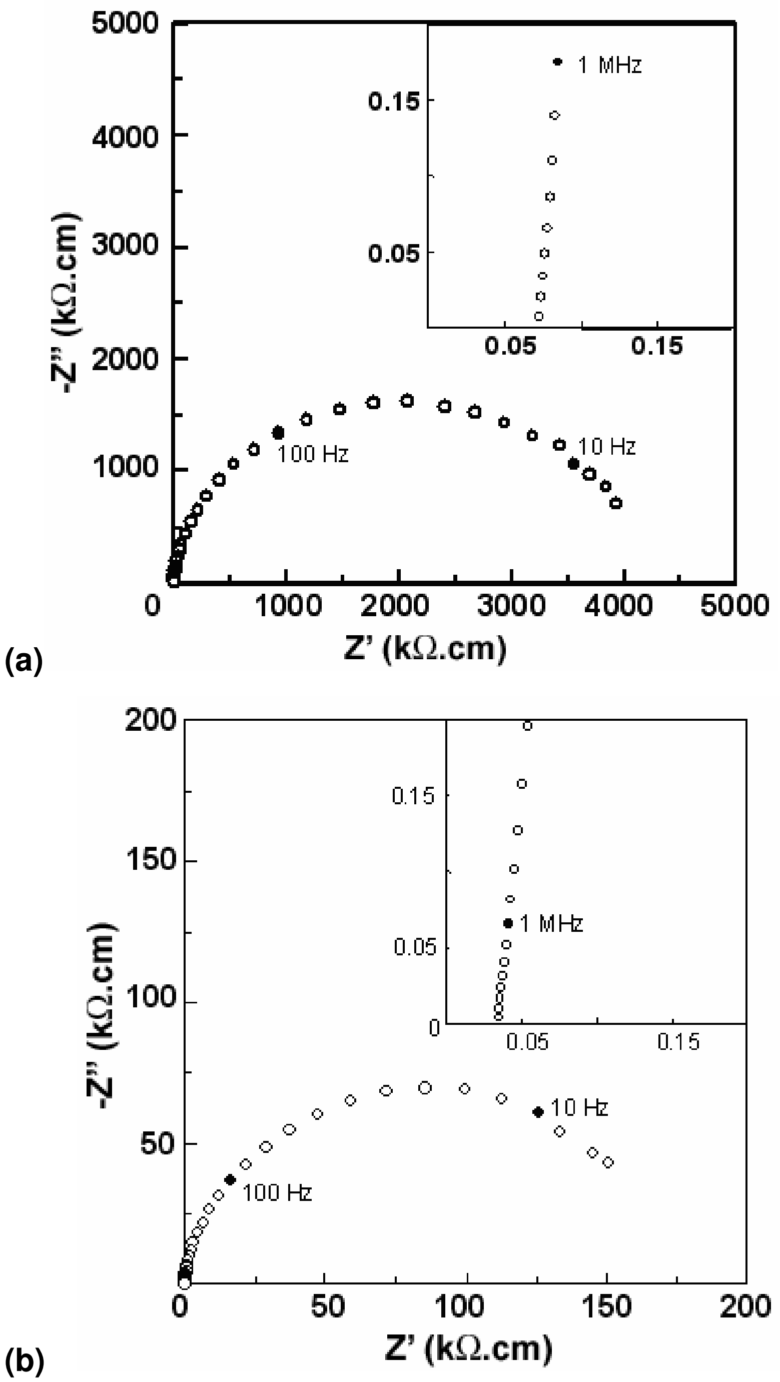

Figure 4.10: Z* plots typical of fine-grained (a) and coarse-grained (b) $CaCu_3Ti_4O_{12}$.

Sample	R_b / Ω	R_{gb} / kΩ	C_{gb} / nF	f_{max} / Hz
1 hr	79	2,100	0.76	100
3 hr	70	4,200	0.95	40
5 hr	54	2,600	1.22	50
8 hr	35	150	26.53	40
24 hr	30	180	35.37	25

Table 4.4: Impedance characteristics of $CaCu_3Ti_4O_{12}$ ceramics sintered for 1 – 24 h at 1115 °C in air.

Conductivity data, obtained at temperatures between RT and ~ 100 °C, for samples sintered for 1, 8 and 24 h are plotted in Arrhenius format in Figure 4.11. Both the bulk and grain boundary responses in all samples obey the Arrhenius law within this temperature range, allowing activation energies for bulk and grain boundary conductivity to be determined. The activation energies, E_a, for bulk and grain boundary conductivity for the 1 h sample were 0.07(2) eV and 0.63(2) eV, respectively. The E_a values for the 8 h sample were found to be 0.05(2) eV and 0.62(2) eV for the bulk and grain boundaries, respectively. In the 24 h sample, the bulk and grain boundary activation energies were 0.06(2) eV and 0.62(2) eV, respectively. For all samples, the grain boundary activation energy appears to be independent of sintering time.

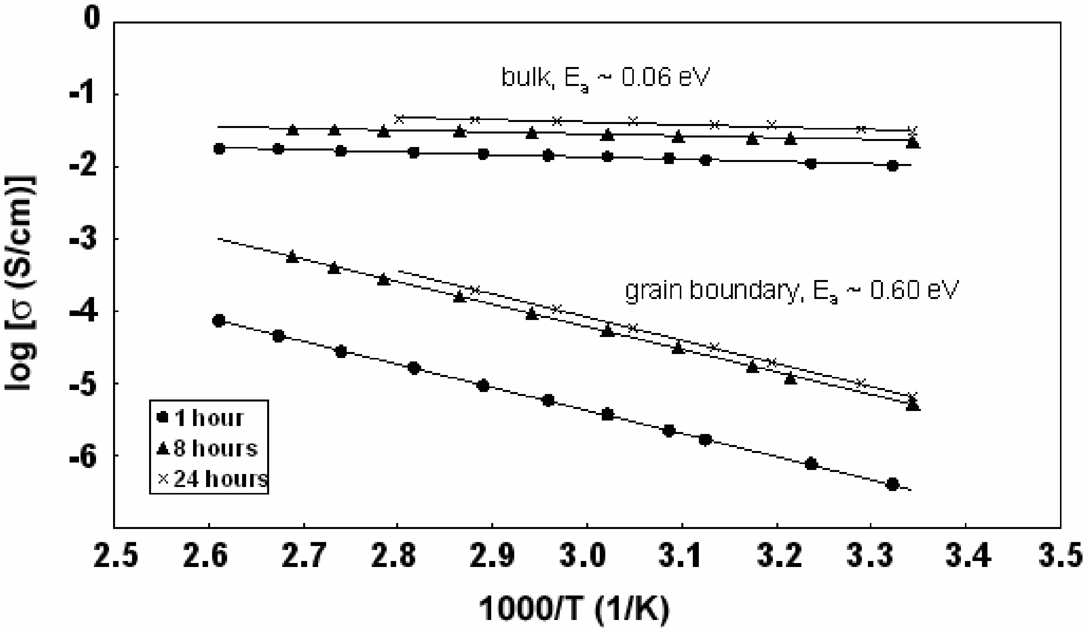

Figure 4.11: Arrhenius-type conductivity plots for fine and coarse-grained $CaCu_3Ti_4O_{12}$.

The low frequency plateau centred at ~ 10 kHz in the spectroscopic plots of the real component of the complex capacitance, C', Figure 4.12 (a) corresponds to a capacitance of ~ 0.8 nF/cm and ~ 25 nF/cm for pellets sintered for 3 and 24 h, respectively. These capacitances, when converted to effective permittivity, give values of ~ 9,000 and ~ 280,000, respectively. In the same way, capacitance data were obtained for samples sintered for 1, 5 and 8 h. At 10 kHz, capacitance values of 0.65 nF/cm and 1.04 nF/cm were measured for the 1 and 5 h samples, corresponding to $\varepsilon'_{\mathrm{eff}}$ values of ~ 7,300 and ~ 11,800, respectively. For the 8 hr sample a capacitance of 15.78 nF/cm was measured, corresponding to $\varepsilon'_{\mathrm{eff}}$ ~ 178,200. Such values are comparable with C_{gb} values determined from Z^* plots.

If the samples were electrically homogeneous, then these values would represent true bulk permittivities. They do not, however, but are instead controlled by the geometry of the grain boundary regions. The $\varepsilon'_{\mathrm{eff}}$ values taken from the intermediate-frequency plateaux show very little variation over the temperature range 150 – 400 K. The variation in tan δ with frequency at room temperature for the same samples indicates minimum values of ~ 0.1 at ~ 2 kHz and ~ 0.04 at ~ 20 kHz, respectively, Figure 4.12 (b).

These data indicate that sintering between 1 and 5 h at 1115°C in air imparts a slight coarsening of the microstructure since, if the IBLC model is correct for $CaCu_3Ti_4O_{12}$ ceramics, larger grains result in a thinner overall grain boundary layer. As such, R_{gb} decreases and C_{gb} increases with increasing grain size. Between 5 and 8 h sintering time, R_{gb} decreases and C_{gb} increases by nearly 1 order of magnitude, suggesting rapid coarsening of the microstructure. Between 8 and 24 h, however, the rate of change is less marked. The differences in Z^* plots on sintering time is reflected in the conductivity data. When plotted in Arrhenius form, σ_{gb} for all samples (1, 8 and 24 h shown as typical examples) have similar activation energies of ~ 0.60 eV, suggesting that any changes in grain boundary composition do not have a significant effect on conductivity. Furthermore, the f_{max} values reported at room temperature are similar in terms of their magnitude for all samples, indicating little difference in grain boundary composition in samples sintered between 1 and 24 h. The lower grain boundary conductivity of the 1 h sample is related to the larger volume fraction of grain boundaries present in this sample compared to the large grained samples obtained for sintering periods of > 5 h.

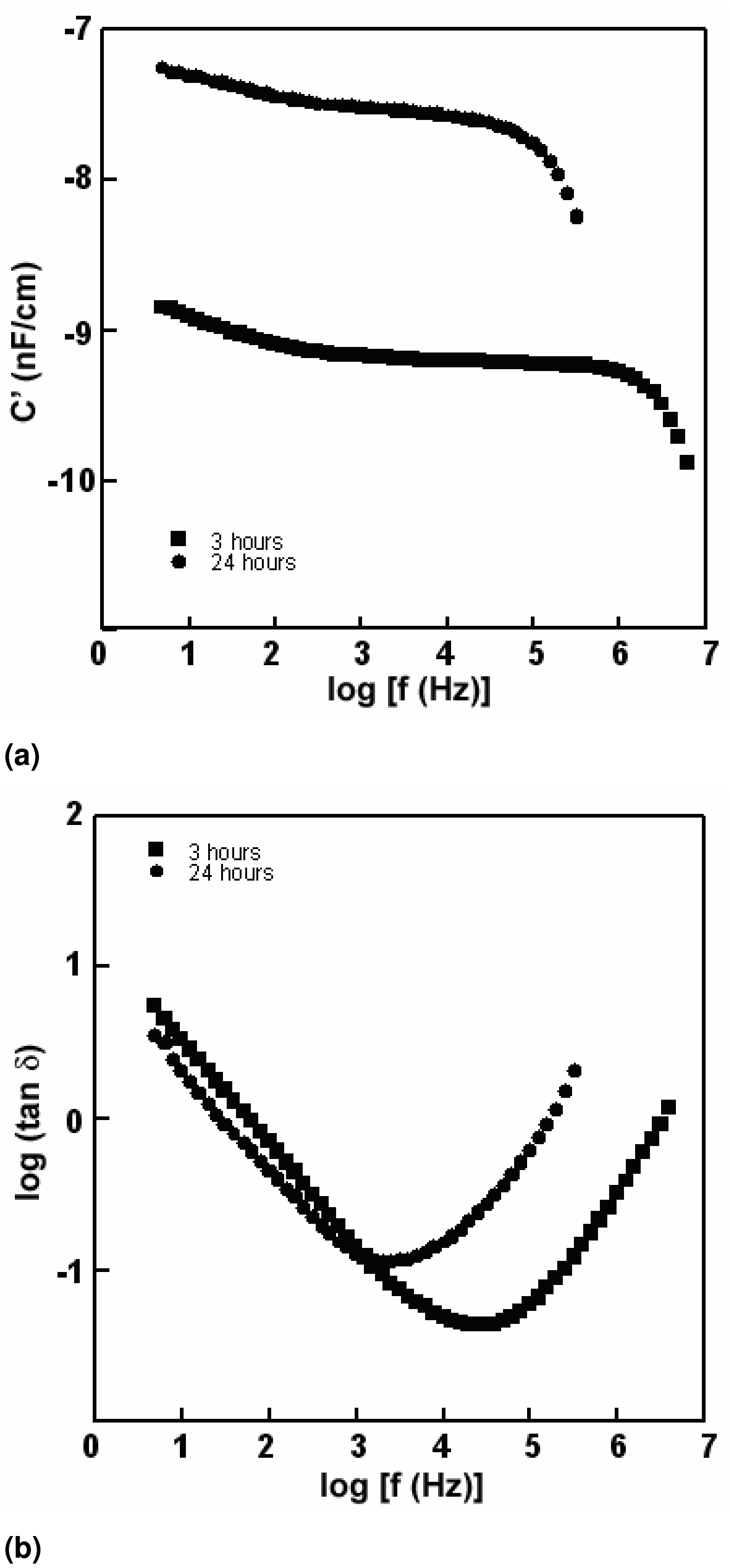

Figure 4.12: Spectroscopic plot of (a) C' and (b) tan δ for $CaCu_3Ti_4O_{12}$ pellets sintered for 3 and 24 h.

The evolution of the ceramic microstructure for sintering times between 1 and 24 h is in good agreement with the evolution of the electrical microstructure described earlier, in which the effective permittivity is enhanced from ~ 10^4 for samples sintered for 1 – 5 h, to ~ 10^5 for samples sintered between 8 and 24 h. This enhancement is clearly linked to differences in ceramic microstructure and in particular, to the average grain size as all pellet densities were > 95% of the theoretical X-ray density. The 'giant' effective permittivity value for ceramics sintered for 24 h is, therefore, associated with the presence of either thin, reoxidised grain boundary regions on the outer surfaces of the large semiconducting grains or to a secondary phase at the grain boundaries. Further work is needed to distinguish these possibilities; however, both models produce Schottky barriers and associated space charge regions that penetrate only the outer regions of the large semiconducting grains and which results in $\varepsilon'_{\text{eff}}$ values > 100,000 for large-grained ceramics. Ceramics with small average grain sizes, ~ 5 μm, such as those sintered for 3 h have a larger fraction of their volume taken up by Schottky barriers and this results in an increase in the effective thickness of the charge storage regions which produces smaller values of $\varepsilon'_{\text{eff}}$.

A disadvantage of large grained microstructures for IBLC ceramics is their lower threshold to voltage breakdown and higher tan δ values. As shown in Figure 4.12 (b), tan δ is frequency dependent and although the loss at 1 kHz is ~ 0.1 it would be desirable to have lower values (< 0.01) and less frequency dependent behaviour, especially at higher frequencies. Also, EPMA reveals second phase precipitates of sphene and Cu_2O in the grains and at grain boundary junctions, respectively. As an insulating phase, isolated sphene particles would not be expected to impart anomalies in the impedance measurements whereas the Cu_2O precipitates are, presumably, semiconducting and may introduce detours in the current pathway, making analysis based on the bricklayer model less reliable.

4.4. Conclusions

$CaCu_3Ti_4O_{12}$ powders were prepared by solid state reaction. In the opening investigations, these powders were milled using an agate mortar and pestle. Ceramics were produced by sintering at 1115 °C and electrical properties measured using impedance spectroscopy. The impedance data indicated the presence of an electrically heterogeneous microstructure whereby the grains were semiconducting and exhibited relatively low permittivity (ε' ~ 120) whereas the grain boundaries were insulating and of high permittivity (ε' > 10,000). This high permittivity arises from the grain boundary geometry and, as such, these are "effective" permittivity values since they are not representative of the intrinsic permittivity of the grain boundary phase. Neither bulk nor grain boundary permittivity values displayed any significant temperature dependence, suggesting that both are non-ferroelectric in origin. The temperature dependence of the bulk and grain boundary conductivity was found to obey the Arrhenius law with activation energies of 0.06(2) eV and 0.60(2) eV, respectively.

$CaCu_3Ti_4O_{12}$ was shown to be sensitive to pO_2; post-annealing samples at 1000 °C in flowing N_2 reduced the grain boundary resistance by several orders of magnitude; TGA experiments for powder samples in H_2 - Ar atmospheres exhibited significant weight loss at relatively low temperatures, and complete decomposition of the parent phase at temperatures > ~ 400 °C.

To investigate grain size dependence, $CaCu_3Ti_4O_{12}$ samples were prepared from planetary ball milled powders. These samples sintered readily and were nearly fully dense after only 1 hr of sintering. The impedance data were comparable with those obtained from samples produced in the opening investigations. The grain boundary impedance was found to be sensitive to sintering time, whereby the effective permittivity increased and the *dc* resistance decreased as sintering time was extended. The bulk conductivity and grain boundary activation energy, however, did not change significantly. SEM revealed abnormal grain growth in samples sintered for > 5 hr and so the grain boundary impedance was shown to depend strongly on the geometry of the grain boundaries, in which increasing grain size results in a thinner overall grain boundary layer. Although it is possible to achieve effective permittivities of ~ 10^5 by sintering for > 8 hr, the electrical properties exhibit unfavourable characteristics including high tan δ values and lower *dc* resistance. These samples also appear to contain a second phase that may facilitate rapid sintering, *i.e.* by liquid phase sintering, and abnormal coarsening of the microstructure.

References

1. C.C. Homes, T. Vogt, S.M. Shapiro, S. Wakimoto, A.P. Ramirez, “Optical Response of High-Dielectric-Constant Perovskite-Related Oxide.” Science, 2001, **293**(5530), 673-676.
2. M.A. Subramanian, D.Li, N. Duan, B.A. Reisner, A.W. Sleight, “High Dielectric Constant in $ACu_3Ti_4O_{12}$ and $ACu_3Ti_3FeO_{12}$ Phases”, Journal of Solid State Chemistry, 2000, **151**, 323.
3. B. Bochu, M.N. Deschanvres, J.C Joubert, A. Collomb, J. Chenevas, M. Marezio, “Synthese et caracterisation d'une serie de titanates Perowskites isotypes de $(CaCu_3)(Mn_4)O_{12}$”, Journal of Solid State Chemistry, 1979, **29**, 291-298.
4. F.D. Morrison, D.C. Sinclair., A.R. West, “Characterization of Lanthanum-Doped Barium Titanate Ceramics Using Impedance Spectroscopy”, Journal of the American Ceramic Society, 2001, **84**(3), 531-538.
5. R. Weht, W.E.Pickett, Physics Review B, 2002, **65**, 014415.
6. C. Pecharroman, F.E. Beltran, J.F. Bartolome, S. Lopez-Esteban, J.S. Moya, “New Percolative $BaTiO_3$-Ni Nanocomposites With A High And Frequency-Independent Dielectric Constant (ε_r approximate to 80,000)”, Advanced Materials, 2001, **13**, 1541.

5. Effect of Electrode Material, Applied Field and Sample Thickness on Impedance of $CaCu_3Ti_4O_{12}$ Ceramics

5.1. Introduction

Schottky barriers are commonly observed at grain boundary regions of semiconducting materials[1, 2], as described in Section 1.3.3.1. The barrier can typically be characterised as a grain boundary impedance since it is both resistive (in comparison to the bulk) and of high capacitance due to the grain boundary geometry. The back-to-back double Schottky barrier is illustrated schematically in Figure 5.1 for the grain boundary of a generic *n*-type semiconductor. The barrier height, Φ_b, introduced in Section 1.3.3.1, and hence grain boundary resistance, R_{gb}, decreases under applied field (*i.e.* by applying a *dc* bias voltage, V) according to Equations 1.6 and 1.7, respectively. It is therefore possible to reduce the observed grain boundary resistance by applying a *dc* bias whilst taking the impedance measurement. In effect, the *ac* signal from the impedance analyser is superimposed onto a *dc* bias of specified magnitude. The field is applied across the entire sample rather than individual grain boundaries, and so the sensitivity of grain boundary resistance to *dc* bias will be lower for a finer grained sample of equivalent geometry.

Under zero applied field, the width of both barriers (the depletion width, w) varies with barrier height, Φ_b, according to:

$$w = \left(\frac{2\Phi_b \varepsilon'}{qN_d} \right)^{1/2} \qquad (5.1)$$

where q is the electron charge, ε' is relative permittivity and N_d is the concentration of donor ions[3]. The capacitance associated with the depletion region, per unit area, is given by:

$$C_0 = \left(\frac{\varepsilon' qN_d}{8\Phi_b} \right)^{1/2} \qquad (5.2)$$

Under an applied field, the barrier becomes asymmetrical such that the depletion width in the reverse direction, w_r, increases whereas the depletion width in the forward direction, w_f, decreases according to Equations 5.3 and 5.4, respectively.

$$w_r = \left(\frac{\varepsilon'}{qN_d}\right)^{1/2}\left(\sqrt{4\Phi_b^2 + V^2} - V\right)^{1/2} \tag{5.3}$$

$$w_f = \left(\frac{\varepsilon'}{qN_d}\right)^{1/2}\left(\sqrt{4\Phi_b^2 + V^2} + V\right)^{1/2} \tag{5.4}$$

It was shown by Li *et al.* [3] that, under an applied field, the capacitance associated with the depletion region, C, is given by:

$$\left(\frac{1}{C^2} - \frac{1}{2C_0^2}\right)^2 = \frac{4}{(\varepsilon' qN_d)^2}\left(4\Phi_b^2 + V^2\right) \tag{5.5}$$

Since the magnitude of V is significantly greater than Φ_b, C decreases with increasing dc bias and a linear relation should be observed between $(1/C^2 - 1/2C_0^2)^2$ and V^2 as reported for $BaTiO_3$-based PTC thermistors[3]. Mukae reported a similar trend for ZnO-based varistors[4], in which the relation between capacitance, applied voltage and barrier height was:

$$\left(\frac{1}{C} - \frac{1}{2C_0}\right)^2 = \frac{2}{(\varepsilon' qN_d)}\left(\Phi_b + V\right) \tag{5.6}$$

In both Equations 5.5 and 5.6, the units of capacitance are in $\mathrm{Fcm^{-2}}$ and the applied voltage, V, is the *dc* bias divided by the number of grain boundaries parallel to the electrodes.

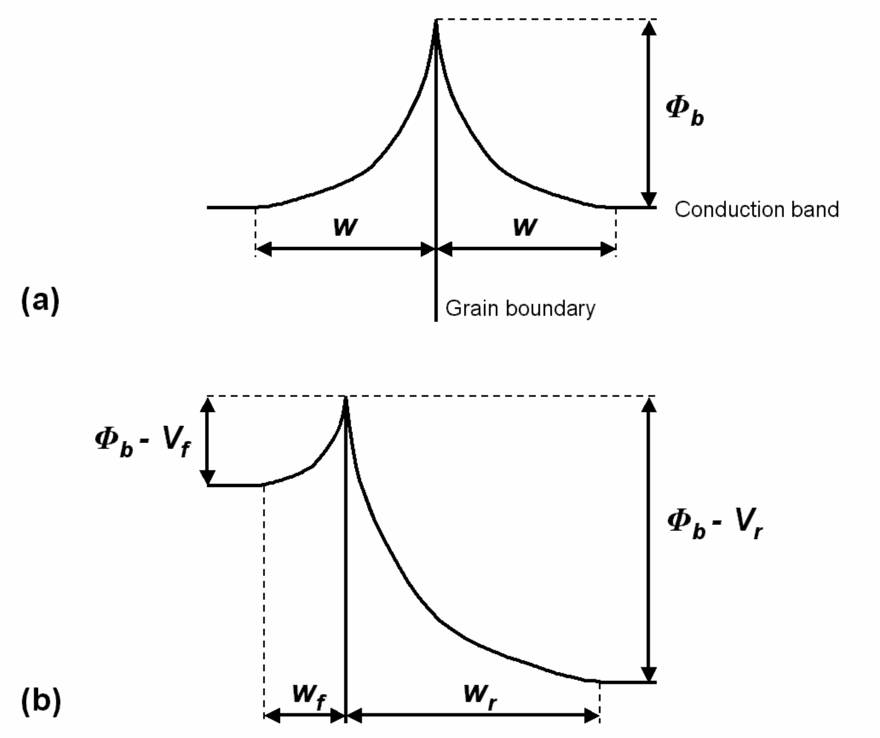

Figure 5.1: Schematic illustration of a back-to-back double Schottky barrier at a single grain boundary when (a) $V = 0$ and (b) $V > 0$.

Schottky barriers may also be present at the electrode-sample interface and tend to arise because of a mismatch in Fermi levels between the bulk and electrode materials. For example, PTCR devices based on semiconducting $BaTiO_3$ exhibit electrode-sample Schottky barrier impedances when noble metals are used as electrodes[5]. As with Schottky barriers at grain boundaries, the barrier height can be lowered by applying a *dc* bias. The barrier may be eliminated by using electrodes composed of metals or alloys with Fermi levels similar to that of the bulk material. In the case of semiconducting $BaTiO_3$, a 60:40 mole ratio of In:Ga alloy is well known to give Ohmic contact and avoids Schottky barrier impedances associated with electrode contacts.

A further implication for electrical property measurements of IBLC-like electrical microstructures is that, provided the data are corrected for sample geometry (*i.e.* pellet thickness and cross sectional area of the electrodes) the electrical properties should be independent of the pellet thickness providing the thickness is at least an order of magnitude greater than the grain size. In such a case, the change in the number of grain boundaries per unit volume would not be large enough to have any noticeable impact on the geometry-corrected data, as shown in Figure 5.2 (a). If the sample thickness is comparable to the grain size, however, then the number of grain boundaries per unit volume will be significantly lower than for thicker samples, Figure 5.2 (b). In the extreme case, Figure 5.2 (c), no grain boundaries would be present and the only source of impedance would be the semiconducting bulk material.

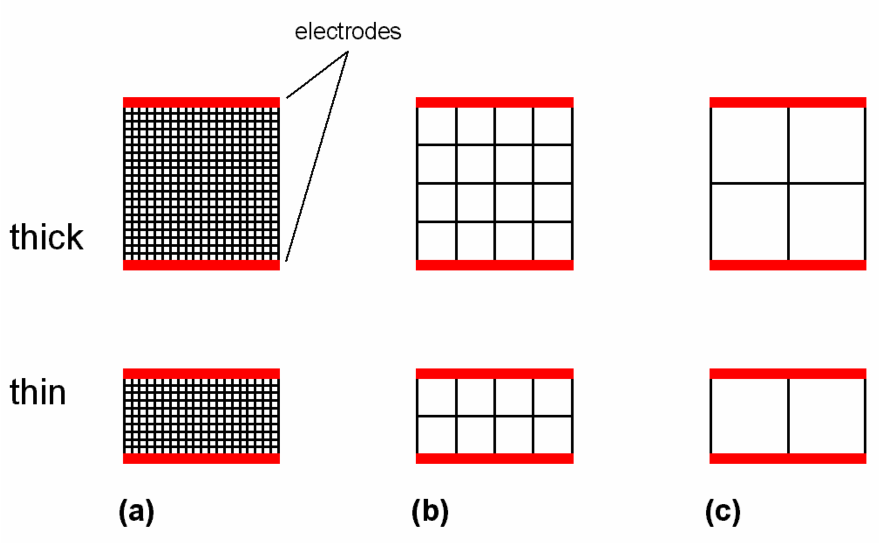

Figure 5.2: Schematic diagram of grain boundaries in thick and thin samples containing (a) small, (b) medium and (c) large grains.

In the previous Chapter, impedance spectroscopy (IS) was used to show that CCTO ceramics are electrically heterogeneous with an electrical microstructure similar to that of an IBLC. The data can be modelled, to a first approximation, on an equivalent circuit consisting of two parallel *RC* elements connected in series; one for the insulating grain boundary regions ($R_{gb}C_{gb}$) and the other for the semiconducting bulk regions (R_bC_b). At room temperature, Z^* plots of dense CCTO ceramics processed in air consist of a large arc with a non-zero intercept at high frequencies. Using this approach, the bulk resistance, R_b, can be estimated as the magnitude of the non-zero intercept whereas the grain boundary resistance, R_{gb}, can be estimated from the diameter of the large arc. The grain boundary capacitance, C_{gb}, can then be calculated using the relationship $\omega R_{gb}C_{gb} = 1$ at the arc maximum. Alternatively, C_{gb} can be estimated directly from complex electric modulus (M^*) plots or from the peak height of the Debye peak associated with element $R_{gb}C_{gb}$ in spectroscopic plots of the imaginary component of the electric modulus (M''), as described in Chapter 3 and elsewhere[6, 7].

In this Chapter the influence of electrode material, *dc* bias and pellet thickness on the IS response of coarse- (24 h) and fine-grained (3 h) CCTO ceramics will be reported. This allows discrimination of the grain boundary response from any significant electrode contact phenomenon and provides further evidence that CCTO ceramics have an IBLC-type electrical microstructure.

5.2. Experimental

Fine- and coarse-grained CCTO ceramics with average grain-sizes of ~ 3 - 5 and ~ 100 - 300 μm, respectively and pellet density ~ 95% of the theoretical X-ray density were prepared by sintering single-phase CCTO powder as pellets in air at 1115 °C for 3 and 24 h, respectively, as described in the Chapter 4.

For the electrode material experiment, Au-electrodes were sputtered on each pellet face of a coarse-grained ceramic with a current of 20 mA for 8 minutes using an Emscope EM400 sputter coating unit. Impedance measurements were taken with an applied voltage of 100 mV using a Hewlett-Packard 4192A impedance analyser over the frequency range 5 Hz – 2 MHz at selected temperatures between room temperature (RT) and ~ 100 °C. At each temperature, further impedance measurements were taken with a *dc* bias of 5, 10 and 15 V. The Au-sputtered electrodes were removed and replaced by InGa (60:40 mol ratio). Impedance measurements were again taken between RT and ~ 100°C at 0, 5, 10 and 15 V *dc*. The InGa electrodes were then removed and replaced by Au-sputtered electrodes using the method described above. RT impedance measurements were taken from 0 to 15 V *dc* at 1 V intervals. The Au-sputtered electrodes were removed, replaced by InGa electrodes and RT impedance measurements were again taken between 0 and 15 V *dc* at 1 V intervals. This procedure was repeated for fine-grained ceramics. All IS data were corrected for pellet geometry and ZView 2 software used for data analysis.

For the sample thickness experiment, InGa (60:40 mol ratio) electrodes were applied to a coarse-grained pellet of thickness, *t* ~ 1.9 mm and the RT impedance measured. The electrodes were removed and the pellet thinned by polishing with SiC paper. The geometric correction factor was recalculated, InGa electrodes re-applied and the RT impedance measured. This process was repeated until the pellet thickness was ~ 0.2 mm. The experiment was then repeated on a fine-grained ceramic.

5.3. Results

5.3.1. Electrode Materials

A typical Z^* plot for a coarse-grained ceramic with Au-sputtered and InGa electrodes at ~ 85 ^{o}C is shown in Figure 5.3 (a). The data can be interpreted in the same way as in Chapter 4, showing R_{gb} and R_b (inset in Figure 5.3 (a)) to have values of ~ 45 – 50 kΩ.cm and ~ 20 Ω.cm, respectively, irrespective of the electrode material. In both cases, C_{gb} ~ 22 nF/cm using the relationship $\omega RC = 1$ at the arc maximum. This temperature is chosen to illustrate typical IS data as the low frequency arc maximum associated with the grain boundary response for this sample was below the lower limit of the impedance analyser at RT. Real capacitance, C', versus frequency for the same data are plotted in Figure 5.3 (b). Based on the interpretation in Chapter 4, the high capacitance plateau in the kHz region corresponds to a grain boundary capacitance of ~ 22 – 15 nF/cm, and the dispersion in the MHz region signifies the presence of conducting grains. Data collected with InGa electrodes are nearly identical to those collected using Au electrodes.

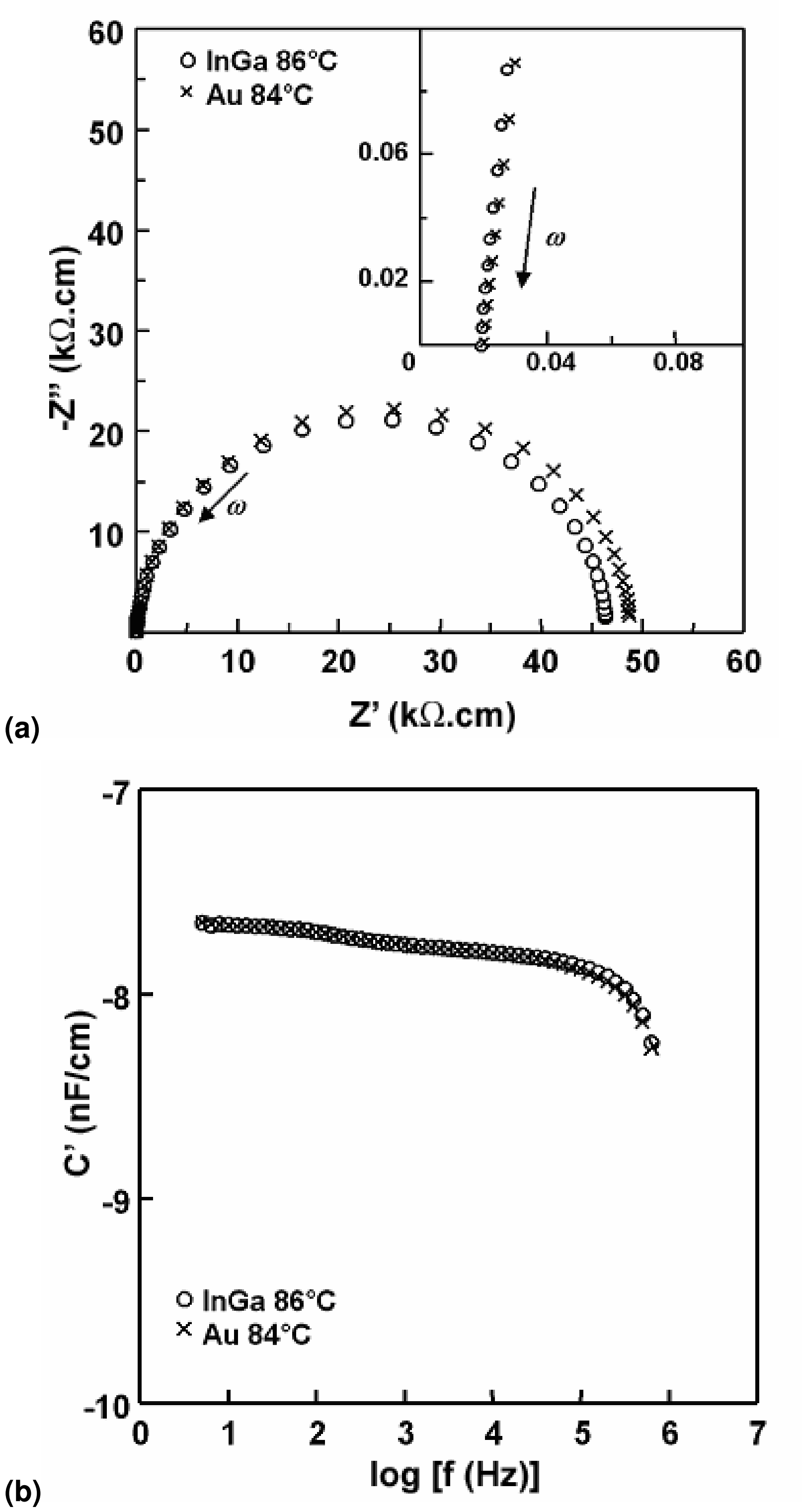

Figure 5.3: (a) *Z plot (85 °C) of coarse-grain sample with InGa electrodes and Au electrodes and (b) corresponding *C'* spectroscopic plot.**

An Arrhenius-type plot of R_b^{-1} and R_{gb}^{-1} against temperature for the two different electrode materials is shown in Figure 5.4 and reveals excellent agreement for R_b and R_{gb} over the measured temperature range. In both cases, the activation energies for bulk and grain boundary conduction are 0.06(2) and 0.66(2) eV, respectively.

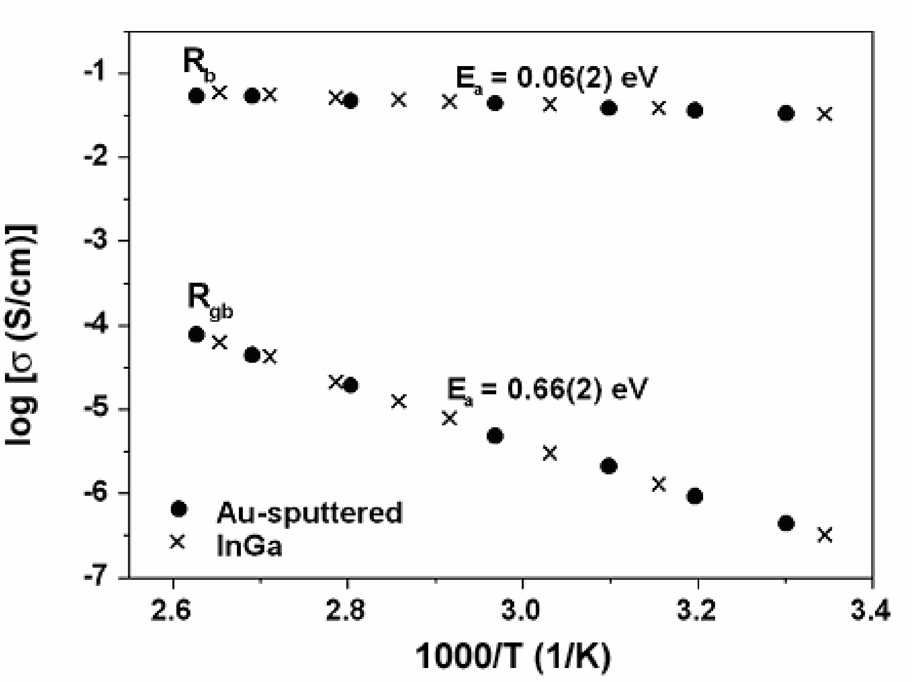

Figure 5.4: Arrhenius plot of conductivity data for CCTO samples with InGa or Au electrodes.

5.3.2. *dc* Bias

Typical Z^* plots for a coarse-grained ceramic with InGa electrodes at 86 °C with a *dc* bias of 0, 5, 10 and 15 V are shown in Figure 5.5 (a). R_{gb} decreased significantly with increasing *dc* bias from 43 kΩ.cm with no *dc* bias to 10 kΩ at 10 V whereas R_b ~ 20 Ω.cm and was independent of the *dc* bias. The corresponding *M"* spectroscopic plots, Figure 5.5 (b), show the Debye peak height associated with the grain boundary response to increase slightly with increasing *dc* bias, indicating C_{gb} decreased with increasing bias.

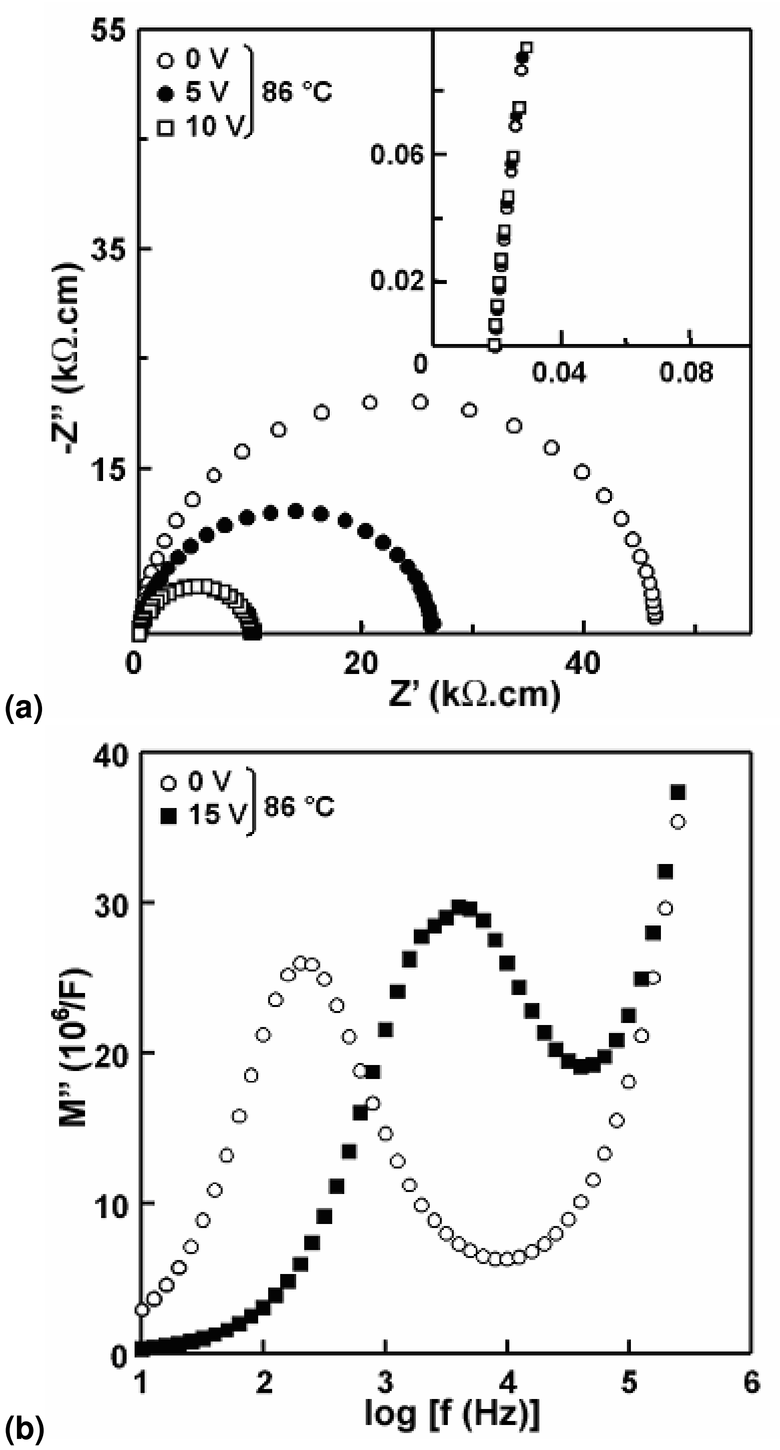

Figure 5.5: (a) *Z plot of data obtained for a coarse grained ceramic with a dc bias of 0 – 10 V and (b) corresponding *M''* data with a dc bias of 0 – 15 V.**

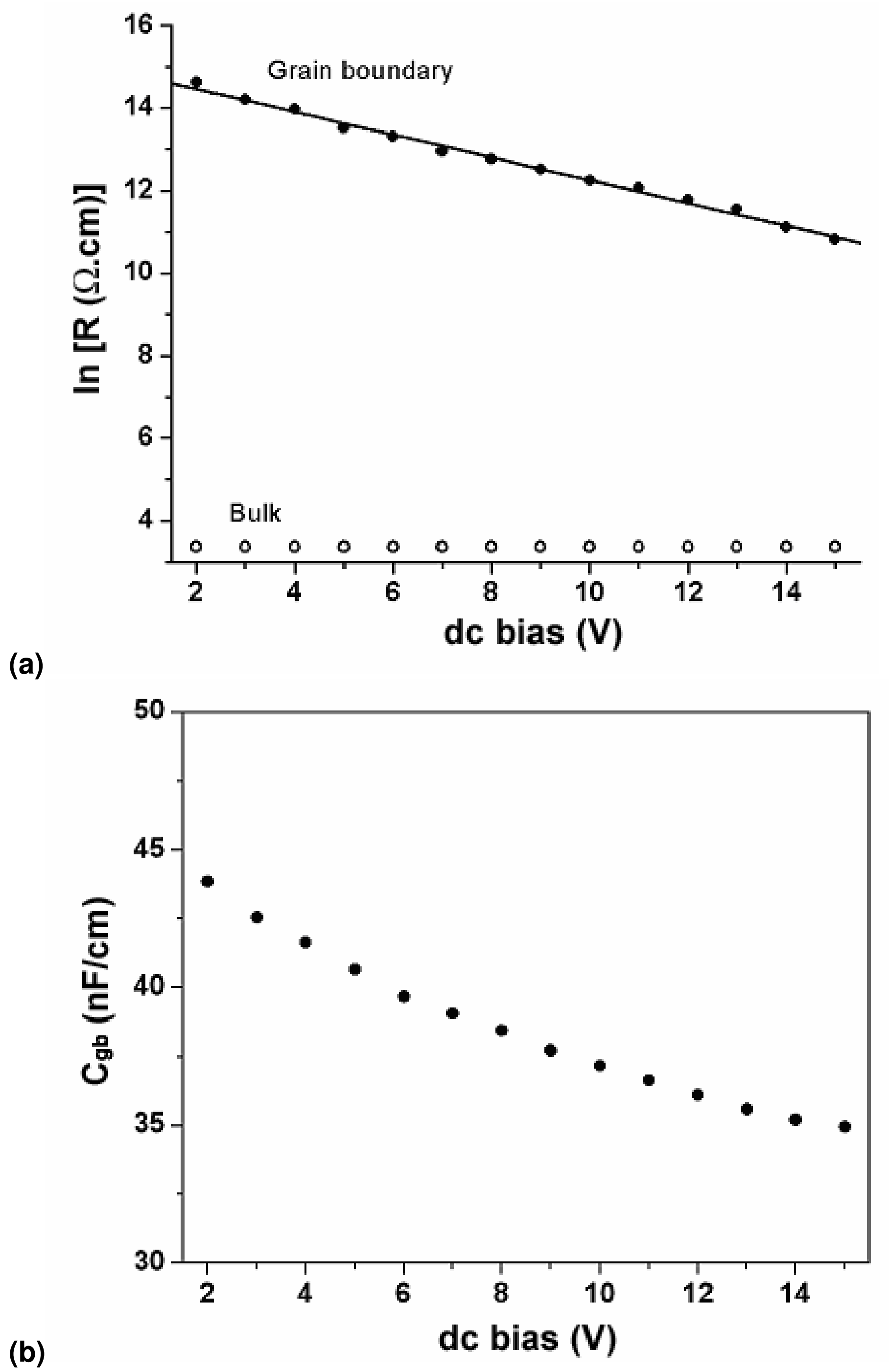

Figure 5.6: (a) ln (R_{gb}) and ln (R_b) versus *dc* bias and (b) C_{gb} versus *dc* bias for a coarse grained ceramic. ***Note: below a dc bias of 2 V it was not possible to observe the arc maximum in the Z* plot (and therefore the corresponding Debye peak maximum in the M'' spectroscopic plots) as it occurred below the lower frequency limit of the impedance analyser, therefore data for R_{gb} and C_{gb} are restricted to dc bias ≥ 2V.***

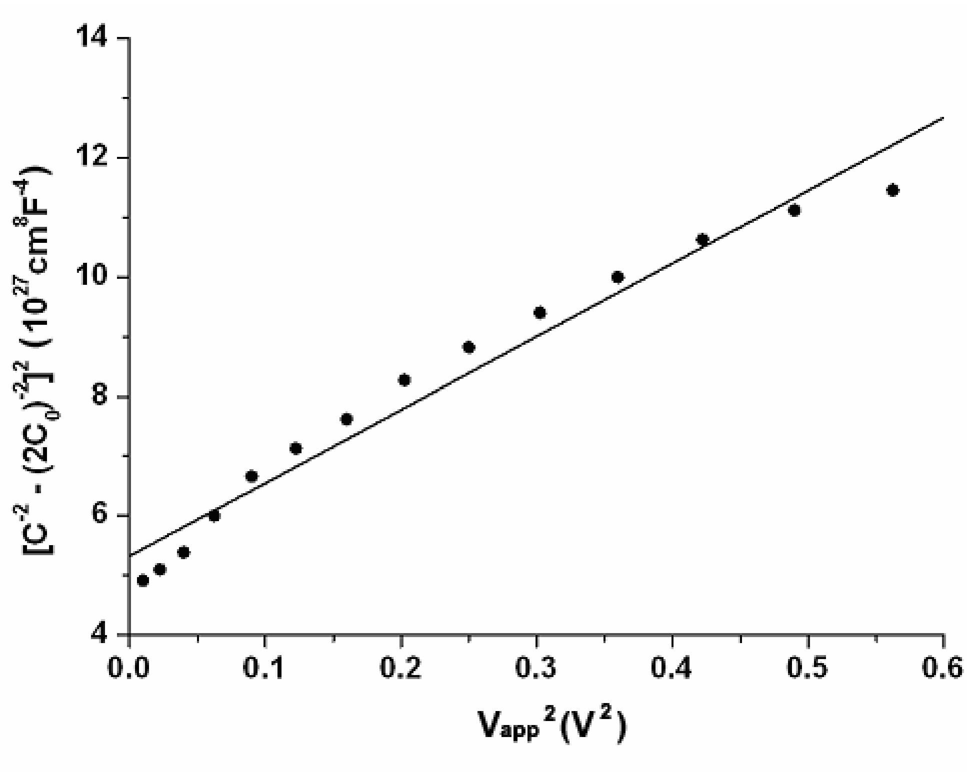

Figure 5.7: Plot of the voltage dependence of grain boundary capacitance in the form suggested by Li [3] for a coarse grained ceramic.

The voltage dependence of R_b, R_{gb} and C_{gb} at RT for the same coarse-grained sample are shown in Figures 5.6 (a) and (b), respectively. R_b ~ 25 Ω.cm and was independent of the *dc* bias whereas R_{gb} displayed an exponential decrease with increasing bias. The filled-line in Figure 5.6 (a) represents a linear fit to the R_{gb} data with an agreement factor (R^2) of > 0.99. C_{gb} was determined from *M"* plots and showed a decrease from ~ 42 nF/cm at 2 V *dc* to a near constant value of ~ 35 nF/cm at 15 V *dc*, Figure 5.6 (b).

The grain boundary capacitance data were also plotted in the form suggested by Li [3], Figure 5.7, corresponding to Equation 5.5. Capacitance values were converted to units of Fcm^{-2} by removing the geometric factor (thickness / area) correction and dividing by the electrode area. The number of grain boundaries was estimated as 20, based on previous SEM data. The data were fitted by linear regression with an agreement factor (R^2) of 0.96. Analysis of Equation 5.5 revealed that:

$$\text{y-axis intercept} = \frac{16\phi^2}{(\varepsilon' q N_d)^2} \qquad (5.7)$$

$$\text{slope} = \frac{4}{(\varepsilon' q N_d)^2} \qquad (5.8)$$

hence intercept/slope $= 4\phi^2$ (5.3)

and so the barrier height at zero applied field was calculated from the intercept divided by the slope. The intercept and slope were determined by linear regression to be ~ 5.32×10^{27} cm^8F^{-4} and 12.25×10^{27} $cm^8F^{-4}V^{-2}$, respectively, hence the barrier height was calculated from the model of Li et al [3] as ~ 0.43 eV.

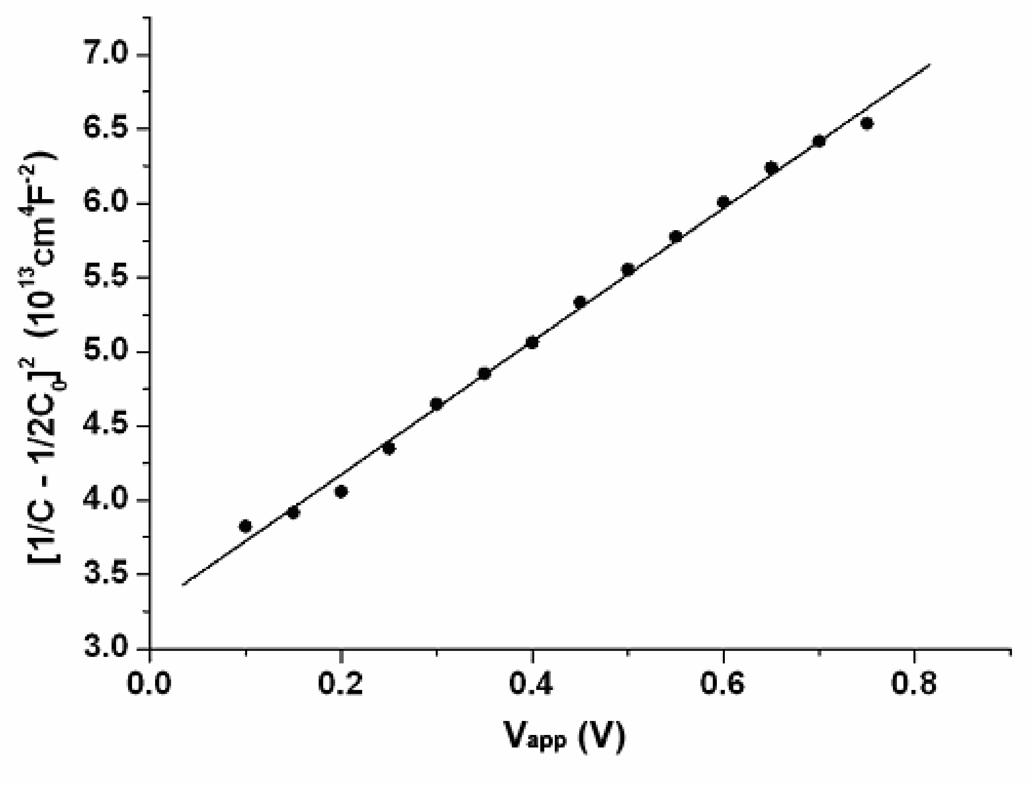

Figure 5.8: Plot of the voltage dependence of grain boundary capacitance in the form suggested by Mukae [4] for a coarse-grained ceramic.

Similarly the barrier height was also calculated using the model of Mukae *et al* [4], Equation 5.6. The data in Figure 5.8 were fitted by linear regression with an agreement factor, $R^2 > 0.99$. The intercept and slope were 3.28×10^{13} cm^4F^{-2} and 4.48×10^{13} $cm^4F^{-2}V^{-1}$, respectively, hence the barrier height according to the model of Mukae was calculated to be ~ 0.73 eV.

Arrhenius-type plots of R_{gb}^{-1} against temperature for 0, 5, 10 and 15 V *dc* bias show the grain boundary resistance to decrease systematically with increasing bias and, additionally, the activation energy for the grain boundary conduction process to decrease systematically from 0.66(2) eV with no *dc* bias to 0.46(2) eV at 15 V *dc* bias, Figure 5.9.

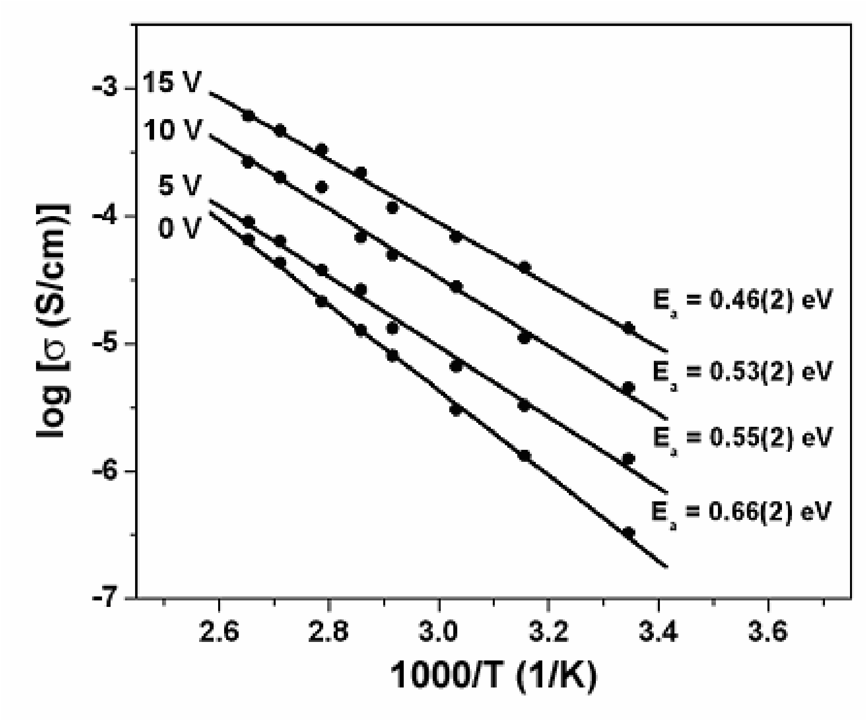

Figure 5.9: Arrhenius plot of grain boundary conductivity as a function of *dc* bias for a coarse grained ceramic.

In contrast, fine-grained ceramics displayed very weak voltage dependence at RT, Figure 5.10. For example, R_{gb} decreased from ~ 4 MΩ.cm (no *dc* bias) to ~ 2.5 MΩ.cm at 4 V and remained constant up to 15 V *dc*. Similarly, no detectable change was observed in C_{gb} as a function of *dc* bias.

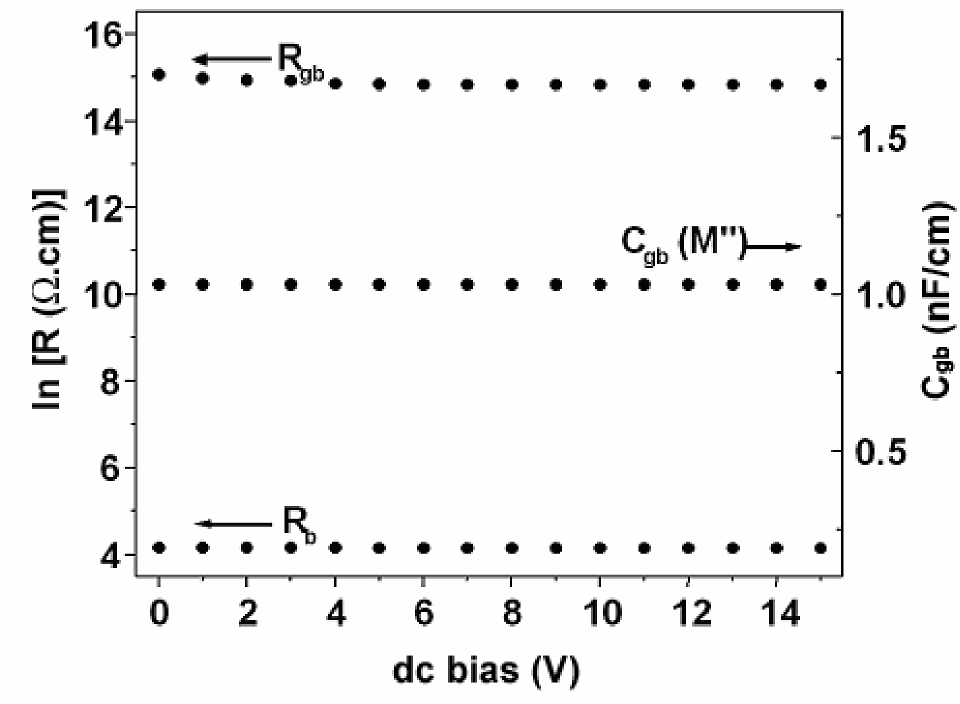

Figure 5.10: Dependence of ln (R_{gb}), ln (R_b) and C_{gb} for a fine-grained ceramic as a function of *dc* bias.

5.3.3. Sample Thickness

A coarse-grained ceramic of initial thickness ~ 1.9 mm with R_{gb} ~ 4 MΩ.cm, R_b ~ 25 Ω.cm and C_{gb} ~ 17.5 nF/cm at RT was polished to a final thickness of ~ 0.34 mm. Polishing the pellet to a thickness of ~ 0.6 mm caused R_{gb} to decrease slightly to ~ 1.6 MΩ.cm, and increased C_{gb} to ~ 21 nF/cm without significant change in R_b, Figure 5.11 (a). Polishing to ~ 0.4 mm resulted in a more noticeable change in electrical properties, whereby R_{gb} decreased by nearly 2 orders of magnitude to ~ 32 kΩ.cm and C_{gb} increased to ~ 29 nF/cm. For a final pellet thickness of ~ 0.34 mm, R_{gb} ~ 40 Ω.cm, R_b ~ 25 kΩ.cm and C_{gb} ~ 27 nF/cm. It is noteworthy that the time constant for the grain boundary response, τ_{gb}, (where $\tau_{gb} = R_{gb}C_{gb}$) was 0.03 s and remained constant for thicknesses > 0.5 mm. Below 0.5 mm, however, a significant decrease in τ_{gb} was observed to 0.005 s for $t < 0.4$ mm.

For a fine-grained ceramic of initial thickness ~ 1.4 mm, R_b ~ 80 Ω.cm, R_{gb} ~ 4 MΩ.cm and C_b ~ 0.98 nF/cm at RT. Polishing to a final pellet thickness of ~ 0.3 mm reduced R_{gb} slightly to ~ 2.5 MΩ.cm, although R_b remained unchanged and no significant variation in C_{gb} was observed, Figure 5.11 (b). For this sample, τ_{gb} was 0.002 s and independent of thickness.

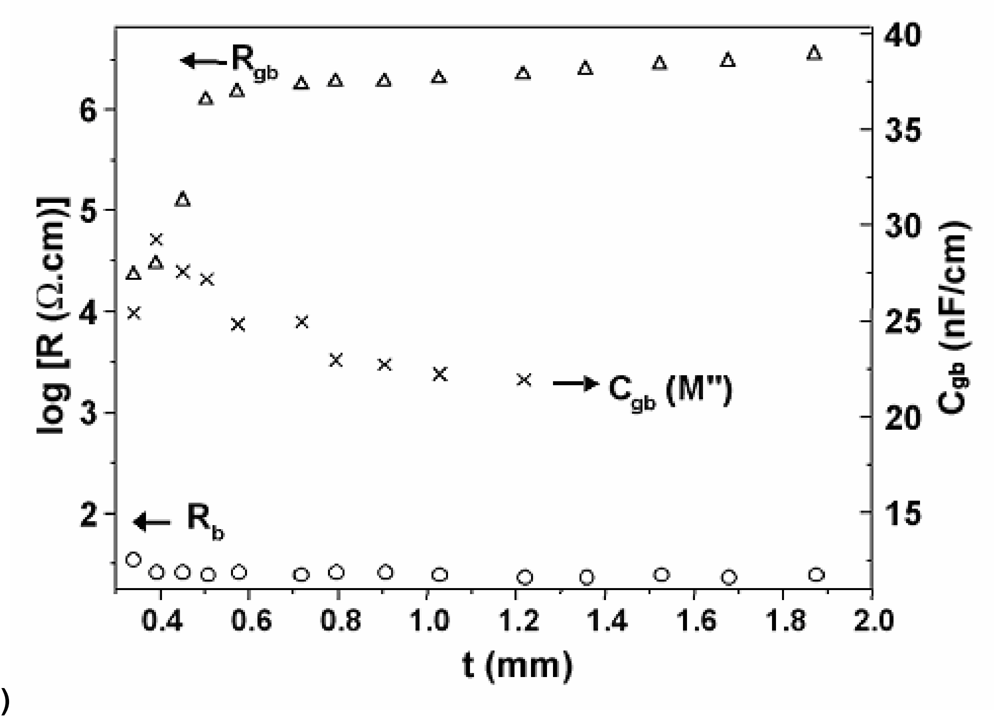

(a)

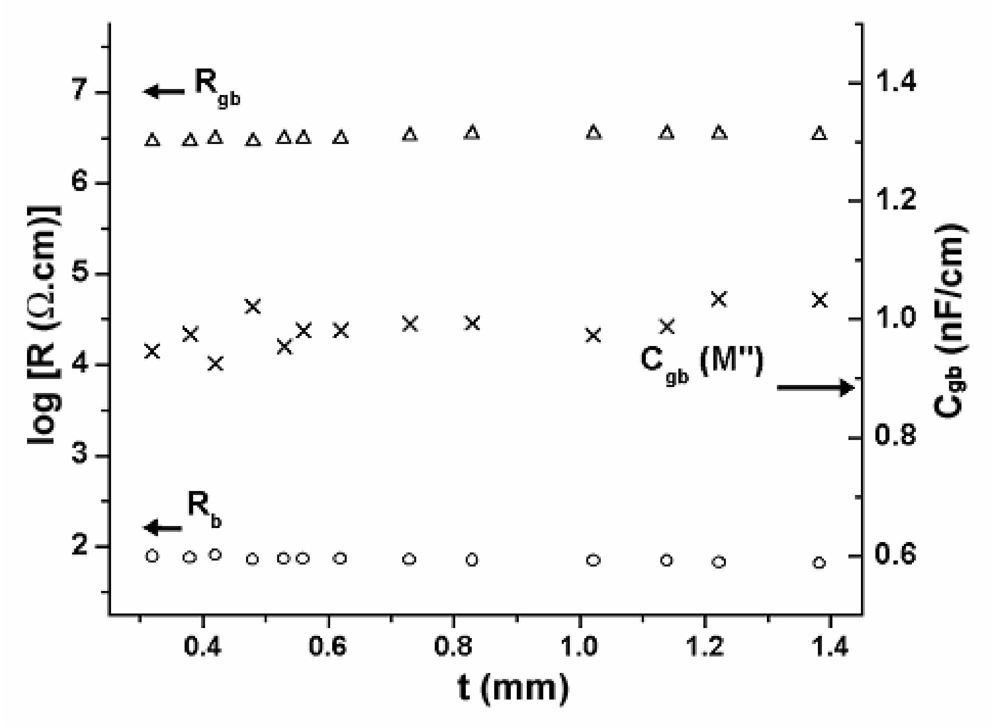

(b)

Figure 5.11: R_{gb}, R_b and C_{gb} for (a) a coarse-grained ceramic and (b) a fine-grained ceramic as a function of thickness.

5.4. Discussion

The voltage dependence of coarse-grained CCTO ceramics appears to fit the Schottky barrier model, in which R_{gb} exhibits a strong dependence on *dc* bias whereas R_b does not. The Arrhenius plot showed a significant decrease in grain boundary activation energy with increasing *dc* bias. Again, this is expected for a Schottky barrier model in which the activation energy is associated with the potential barrier height and, as such, exhibits a proportional decrease with increasing *dc* bias. Furthermore, the voltage dependence was comparable for both InGa and Au-sputtered and, given the different Fermi-levels of these two materials, the impedance data were not influenced by any possible electrode contact phenomenon.

C_{gb} also decreased with increasing *dc* bias; although this trend was anticipated by Equation 5.5, these data did not result in a perfect linear fit of $(1/C^2 - 1/C_0^2)^2$ versus V^2 suggested by Li *et al.*[3]. This may be a further indication of the heterogeneous nature of the grain boundary network in $CaCu_3Ti_4O_{12}$ ceramics, in which ideal behaviour cannot be observed due to a distribution of grain boundary electrical properties and/or an inhomogenous potential distribution attributable to a distribution of grain sizes. However, the extracted potential barrier height of 0.43 eV is comparable in terms of order of magnitude to previous values determined for grain boundary activation energy. When the data were plotted according to the model of Mukae *et al* [4], a barrier height of 0.73 eV was determined, in good agreement with the activation energy values determined for $CaCu_3Ti_4O_{12}$ ceramics. Furthermore, linear regression indicated a significantly improved fit for the model of Mukae *et al* [4] ($R^2 > 0.99$ for Mukae *et al*, as opposed to $R^2 = 0.96$ for Li *et al*).

The fine-grained CCTO ceramics exhibited no such dependence on R_{gb} since the number of grain boundaries per unit volume was much greater than for the coarse-grain ceramics. As such, fine grain ceramics have a thicker effective insulating layer than the coarse-grained ceramics and so, in the case of fine-grained ceramics, the electric field across each grain boundary was considerably less than in a coarse-grained sample for an equivalent *dc* bias. A larger *dc* bias would, therefore, be required to observe significant changes in R_{gb} in fine-grained ceramics.

As mentioned in Chapter 3, the geometry of the grain boundaries cannot be corrected for using standard impedance techniques. The implication for CCTO ceramics is that the grain boundary impedance remains independent of thickness provided the sample thickness is much greater than the grain size. As the sample becomes progressively thinner and comparable to the grain size, the number of grain boundaries per unit volume rapidly decreases with the result that the "corrected" values of R_{gb} and C_{gb} appear to suddenly decrease and increase, respectively. In the case of the coarse-grained ceramics, where the grain size is ~ 100 μm - ~ 300 μm, the sample thickness is initially ~ 1.6 mm, *i.e.* less than an order of magnitude greater than the grain size. As the sample is thinned, R_{gb} steadily decreases and C_{gb} steadily increases as the number of grain boundaries per unit volume decreases. A sudden change in R_{gb} occurs when the sample has been thinned to ~ 0.6 mm. At this point, the number of grain boundaries per unit volume has rapidly decreased and it may be that only one active grain boundary existed between the electrodes. The slight variation in R_b and fluctuations in R_{gb} and C_{gb} are believed to be a consequence of both inaccuracies in measuring the progressively smaller pellet dimensions and heterogeneous grain boundary geometry and composition.

Fine-grained ceramics exhibit no such trend in R_{gb} and C_{gb} since the typical grain size for these samples is ~ 1 μm - ~ 10 μm and the final sample thickness remained ~ 2 orders of magnitude greater than the grain size. In this case the number of grain boundaries per unit volume would remain constant until the sample thickness became comparable with the 10 μm grain size.

The variation in the time constant with sample thickness observed in the coarse-grained ceramics cannot, therefore, be entirely explained through a simple BL-model interpretation. It seems likely that the microstructure of coarse-grained ceramics may result in an inhomogeneous potential distribution, in which "islands" of fine-grained material may be present in a coarse-grained matrix and/or there may different types of grain boundary conductivity in these ceramics, see Figure 3.6. Such behaviour has been simulated in the finite element analysis studies of Fleig and Maier [8, 9] and has shown that the low frequency arc associated with the "grain boundary" response shows significant deviation from the simple BL model. This may explain the variation in the τ_{gb} values for the coarse-grained ceramics.

The findings presented here support the IBLC model for $CaCu_3Ti_4O_{12}$ but are in conflict with a similar study reported recently by Lunkenheimer *et al.* [10]. They observed that the choice of electrode material (polished brass plates pressed on the major pellet faces, silver 'paint' and sputtered silver) had a significant effect on the observed electrical response at frequencies < 1 MHz while changes in the sample thickness had no significant effect. It was concluded that neither internal barrier layers nor intrinsic polarisation mechanisms resulted in high permittivity. Instead, the high permittivity arose from Schotky-diodes at the electrode/sample interfaces. There are, however, two major shortcomings with the Lunkenheimer study that cast doubt on their conclusions, particularly when viewed alongside the results presented here: 1) the difference in electrode coverage area provided by the various electrodes used in their study is likely to be the major contributing factor to the *change* in the observed electrical properties, but does not suggest that contact potential at the sample and electrode is the origin of the high permittivity plateau. 2) no mention was made of the grain size of these samples and so the change in sample thickness from 0.69 mm to 0.24 mm may be insignificant.

5.5. Conclusions

From the dependence of impedance on applied *dc* bias, the grain boundary impedance in CCTO ceramics appears to arise from Schottky barriers formed at the grain boundary interface. As expected, the effect is strongly dependent upon grain size since, in coarse-grained ceramics, the grain boundary resistance decreased by nearly 2 orders of magnitude by application of 15 V *dc*, whereas fine-grained ceramics require significantly higher voltages to exhibit an observable change. The response of coarse-grained ceramics to an applied field was almost identical when measurements were made using either Au-sputtered or InGa electrodes which, combined with the earlier grain size dependence work, strongly supports the grain boundary barrier layer in favour of an electrode-sample interface effect.

The change in impedance characteristics with sample thickness is also dependent upon grain size. For a coarse-grained sample, the grain boundary resistance decreases rapidly and the capacitance increases rapidly as the sample thickness is reduced to become comparable with the grain size. No such effect was observed in fine-grained samples because the final thickness was at least an order of magnitude higher than the sample thickness. The thickness dependence of the coarse-grained samples also appeared to be influenced by inhomogeneous potential distribution.

In conclusion, the apparent high permittivity of CCTO ceramics is a consequence of Schottky-barriers behaving as thin, insulating layers at the grain boundaries (or possibly external surfaces in the case of single crystals) and the so-called “dielectric phenomena” reported for these materials are merely artefacts of selected frequency measurements.

5.6. References

1. G. Blatter, F. Greuter, "Carrier transport through grain boundaries in semiconductors." Physical Review B, 1986, **33**(6), 3952-3966
2. F. Greuter, G. Blatter, "Electrical properties of grain boundaries in polycrystalline compound semiconductors." Semiconductor Science & Technology, 1990, **5**, 111-137
3. Y.G. Li, S.G. Cho, "Capacitance-voltage relation for ceramics with positive temperature coefficient of resistance." Journal of Applied Physics, 2002, **91**(7), 4535-4537
4. K. Mukae, K. Tsuda, I. Nagasawa, "Capacitance-Voltage Characteristics of ZnO Varistors." Journal of Applied Physics, 1979, **50**, 4475-4476
5. D.P. Cann, C.A. Randall, "The Thermochemistry and Non-Ohmic Contact Electrical Characteristics of a BaTiO3 PTCR Ceramics." I.E.E.E. Transactions of Ultrasonics, Ferroelectrics and Frequency Control, 1997, **44**(6), 1405-1408
6. D.C. Sinclair, F.D. Morrison, A.R. West, "Application of Combined Impedance and Electric Modulus Spectroscopy to Characterise Electroceramics." International Ceramics, 2000,(2), 33-37
7. J.T.S. Irvine, D.C. Sinclair, A.R. West, "Electroceramics: Characterisation by Impedance Spectroscopy." Advanced Materials, 1990, **2**(3), 132-138
8. J. Fleig, J. Maier, "The Impedance of Ceramics with Highly Resistive Grain Boundaries: Validity and Limits of the Brick Layer Model." Journal of the European Ceramic Society, 1999, **19**, 693-696
9. J. Fleig, "The Influence of Non-Ideal Microstructures on the Analysis of Grain Boundary Impedances." Solid State Ionics, 2000, **131**, 117-127
10. P. Lunkenheimer, R. Fichtl, S.G. Ebbinghaus, A. Loidl, "Nonintrinsic origin of the colossal dielectric contasts in CaCu3Ti4O12." Physical Review B, 2004, **70**, 172102

6. Decomposition Reactions in $CaCu_3Ti_4O_{12}$

6.1. Introduction

In Chapter 4, a powder sample of $CaCu_3Ti_4O_{12}$ was shown, using TGA, to undergo complete decomposition upon heating to 800 °C in a flowing 5 % H_2 – 95 % Ar atmosphere, Figure 4.6. Under the same conditions, many other titanate phases such as $CaTiO_3$ and $BaTiO_3$ would be expected to exhibit only a low level of oxygen non-stoichiometry, as opposed to a total collapse of the structure. EPMA data also revealed the presence of Cu_2O and $CaTiSiO_5$ precipitates in ceramics sintered for 24 h at 1115 °C in air, suggesting that a limited decomposition process also occurred during sintering.

Thermal instability at temperatures < ~ 1000 °C in both ambient and low pO_2 atmospheres is a common observation in cuprate-based perovskites, such as high $\boldsymbol{T_c}$ superconductors. Kim [1] characterised the thermal stability of $YBa_2Cu_3O_{7-x}$ in H_2 - Ar gas using TGA and reported total decomposition to Cu, $Ba_3Y_4O_9$ and BaO. It seems likely, therefore, that the partial decomposition of $CaCu_3Ti_4O_{12}$ during sintering and total collapse during H_2 – Ar TGA, as described in Chapter 4, could primarily be attributable to the instability of Cu^{2+} at high temperatures.

Titanate-based perovskites such as $BaTiO_3$ are well known to loose oxygen when heated to > 1000 °C. La-doped $BaTiO_3$ phases exhibit an *n*-type conductivity mechanism and so the room temperature resistivity can be decreased from > 10^7 Ω.cm to ~ 1 - 10 Ω.cm as a result of losing small (< 1 at%) quantities of oxygen [2, 3]. The effect of oxygen loss in *n*-type $Ba_{1-x}La_xTi_{1-x/4}O_3$ ceramics was investigated by Morrison *et al.* [3] by heat treating ceramics in O_2, Ar and air then slow cooling or quenching to room temperature; the electrical properties were then characterised using IS. It was found that ceramics remained insulating after heat treatment in O_2 while ceramics heated in air or Ar exhibit electrical heterogeneities associated with semiconducting bulk material and insulating grain boundaries. It was also found that insulating layers could be present at external surfaces in ceramics that were quenched from > 1200 °C in air and/or Ar. Furthermore, the grain boundary response in certain ceramics could be characterised as a composite of two types of grain boundary regions with differing resistivities, associated with an inhomogeneous distribution of oxygen through the grain boundary network.

In this Chapter, the decomposition behaviour of $CaCu_3Ti_4O_{12}$ ceramics was investigated using XRD and SEM in conjunction with EDS after the ceramics were sintered in air at 1115 ℃ and heat-treated in a low pO_2 atmosphere at 1000 ℃. The effect of heat-treating $CaCu_3Ti_4O_{12}$ ceramics in both low and high pO_2 atmospheres was then characterised by IS to investigate the sensitivity of the bulk and grain boundary impedances to oxygen loss and thereby determine a possible conductivity mechanism.

6.2. Experimental

6.2.1. Decomposition Reactions in Air and N_2.

Reacted $CaCu_3Ti_4O_{12}$ powder was prepared from planetary ball milled powder and fine- and course-grained $CaCu_3Ti_4O_{12}$ ceramics were cold-pressed and sintered for 3 and 24 h, respectively, in air, as described in Section 4.2.2. Ceramics were prepared for SEM by mounting in resin and polishing sections perpendicular to the major pellet faces. The polished ceramics were carbon coated and analysed using a Jeol JSM-6400 SEM and Link Analytical EDS. The as-sintered surface of a 24 h ceramic was analysed by XRD, then ground with SiC paper and re-measured; the process was repeated until the sample was ~ 80 % of the original thickness. 3 h and 24 h ceramics were then heat-treated in N_2 for 6 h at 1000 ℃ (heating rate 5 ℃/min, cooling rate 2.5 ℃/min) on Pt foil. SEM ceramics were prepared and analysed as before. A 3 h heat-treated ceramic was analysed by XRD as a function of thickness as described above.

6.2.2. Effect of Post-Annealing on Electrical Properties

$CaCu_3Ti_4O_{12}$ ceramics were prepared as per Section 6.2.1 and sintered for 3 and 24 h in air. A 3 h sample was prepared for electrical property measurements by IS (Hewlett Packard 6192A) and InGa (60:40) electrodes applied. IS measurements were taken between RT and ~ 100 ℃. The electrodes were removed and sample post annealed at 600 ℃ in N_2 for 6 h (heating rate 5 ℃/min, cooling rate 2.5 ℃/min) on Pt foil. After cooling to RT, the surface was lightly reground with SiC paper, InGa electrodes re-applied and the electrical properties re-measured. Electrical property measurements were also made after annealing at 800 ℃, 900 ℃ and 1000 ℃ in N_2, then after annealing at 600 ℃, 800 ℃, 900 ℃ and 1000 ℃ in O_2. The experiment was repeated for the 24 h sample.

6.3. Results & Discussion

6.3.1. Decomposition Reactions

SEM images of as-sintered ceramics, viewed as a cross-section perpendicular to the major pellet faces, are shown in Figure 6.1. Backscattered electron imaging (BEI) was used to contrast variations in composition such that regions containing heavy elements (such as Cu) were observed as light areas and regions containing relatively light elements (e.g. Ti) were observed as darker areas. Figures 6.1 (a) and 6.1 (b) are low and high magnification images, respectively, of a 3 h ceramic. At low magnification, the sample appears homogeneous without large-scale flaws, such a fissures, or pores over 5 μm in diameter. At high magnification a fine-grained texture (< 10 μm grain size) is evident and the pore structure, seen as black voids, is closed. The remaining pores are small (1 – 5 μm) and the shape of the pore boundaries would indicate that pore shrinkage ceased before the sample was cooled to room temperature. The final stage of sintering for $CaCu_3Ti_4O_{12}$ prepared from planetary ball milled powders was, therefore, reached within 3 h of sintering at 1115 °C in air. A secondary phase was observed as bright precipitates in a number of pores and, in particular, at grain boundary junctions.

Figures 6.1 (c) and 6.1 (d) are low and high magnification images, respectively, of a 24 h ceramic. The low magnification image reveals the pore structure to be coarser than the 3 h ceramic with pores sizes up to 30 μm, suggesting that bloating has occurred as a result of air or gas evolved by volatilisation becoming trapped within the sample during the final stage of sintering. At high magnification, the grain structure is coarser than the 3 h ceramic although it was not possible to accurately measure the grain size since the grain boundaries were not etched. The grain size study in Chapter 4 would suggest the grains are between 100 μm and 300 μm in diameter. Secondary phases were detected as bright precipitates at grain boundary junctions, Figure 6.1 (d), as observed in 3 h ceramics, and also as dark spherical precipitates of ~ 5 μm diameter.

EDS of the bulk phase are given in Figure 6.2 (a) as a typical example for both the 3 and 24 h ceramics. The observed peaks correspond to known peak positions for Ca, Cu and Ti. Although the EDS data do not provide a direct means to quantify the composition of a particular region, these data are representative of the bulk $CaCu_3Ti_4O_{12}$ phase analysis performed by EPMA and described in Chapter 4. Figure

6.2 (b) shows typical EDS data for the bright phase observed at grain boundary junctions in 3 and 24 h ceramics. The two major peaks were found to correspond to known peak positions for Cu and secondary peaks corresponded to Si, Ca and Ti. These data are commensurate with the Cu_2O phase detected by EPMA. The presence of Si, Ca, and Ti may arise from the precipitate itself, or from surrounding material if the interaction volume exceeds the volume of the precipitate. The EDS data in Figure 6.2 (c) are typical of the dark phase observed in the 24 h sample, with major peaks corresponding to Si, Ca and Ti, and a minor peak corresponding to Cu. The morphology and composition (according to the EDS data) appear to correspond to the $CaTiSiO_5$ (sphene) precipitates observed by EPMA and described in Chapter 4. The Cu signal may arise from incorporation of Cu into the sphene lattice or as a result of interaction of the primary beam with the surrounding area.

XRD data obtained from a 3 h sample are shown in Figure 6.3. All reflections, with the exception of the small peak at ~ 36 °, were found to correspond to the pattern obtained in previous experiments (Figure 4.1) and reported in the literature for $CaCu_3Ti_4O_{12}$. The one minor peak observed at ~ 36 ° in the as-sintered pellet surface may correspond to Cu_2O precipitates at the surface. Upon removal of the pellet surface, the extra peak was not present, suggesting that the secondary phase had been removed upon polishing the pellet surface.

(a)

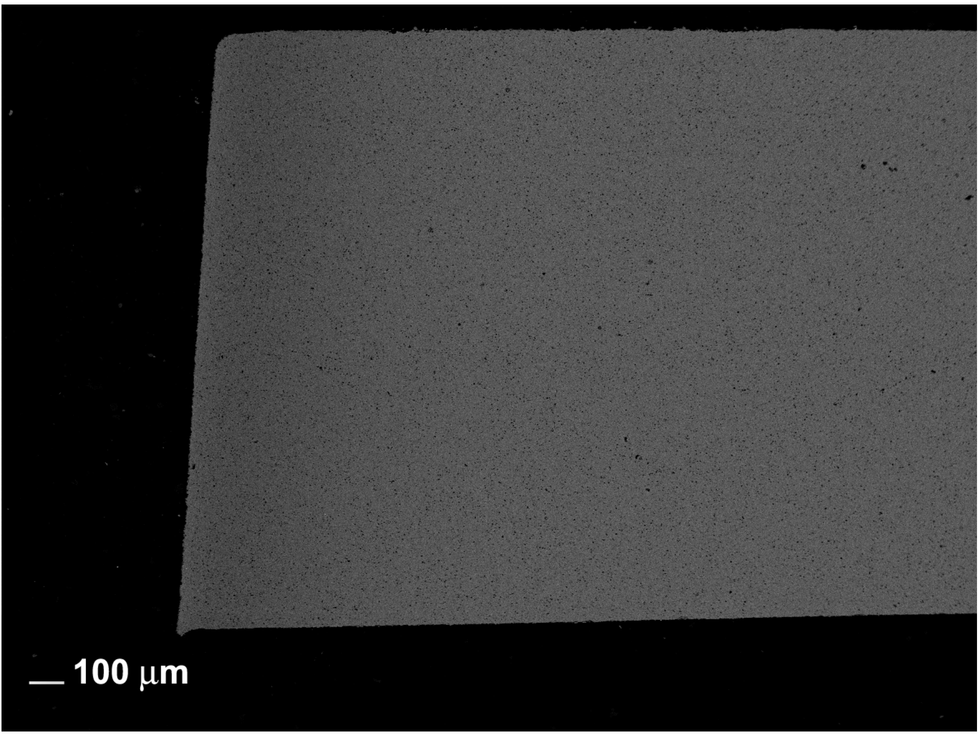

(b)

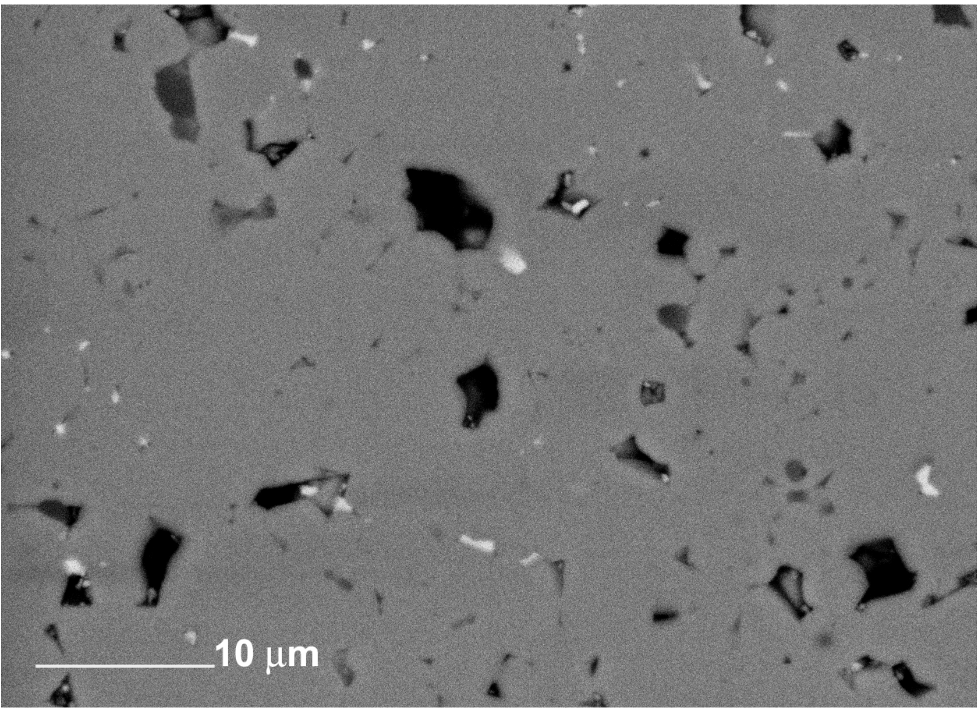

Figure 6.1: BEI SEM showing cross section of a 3 h ceramic at (a) low magnification and (b) high magnification (contd overleaf).

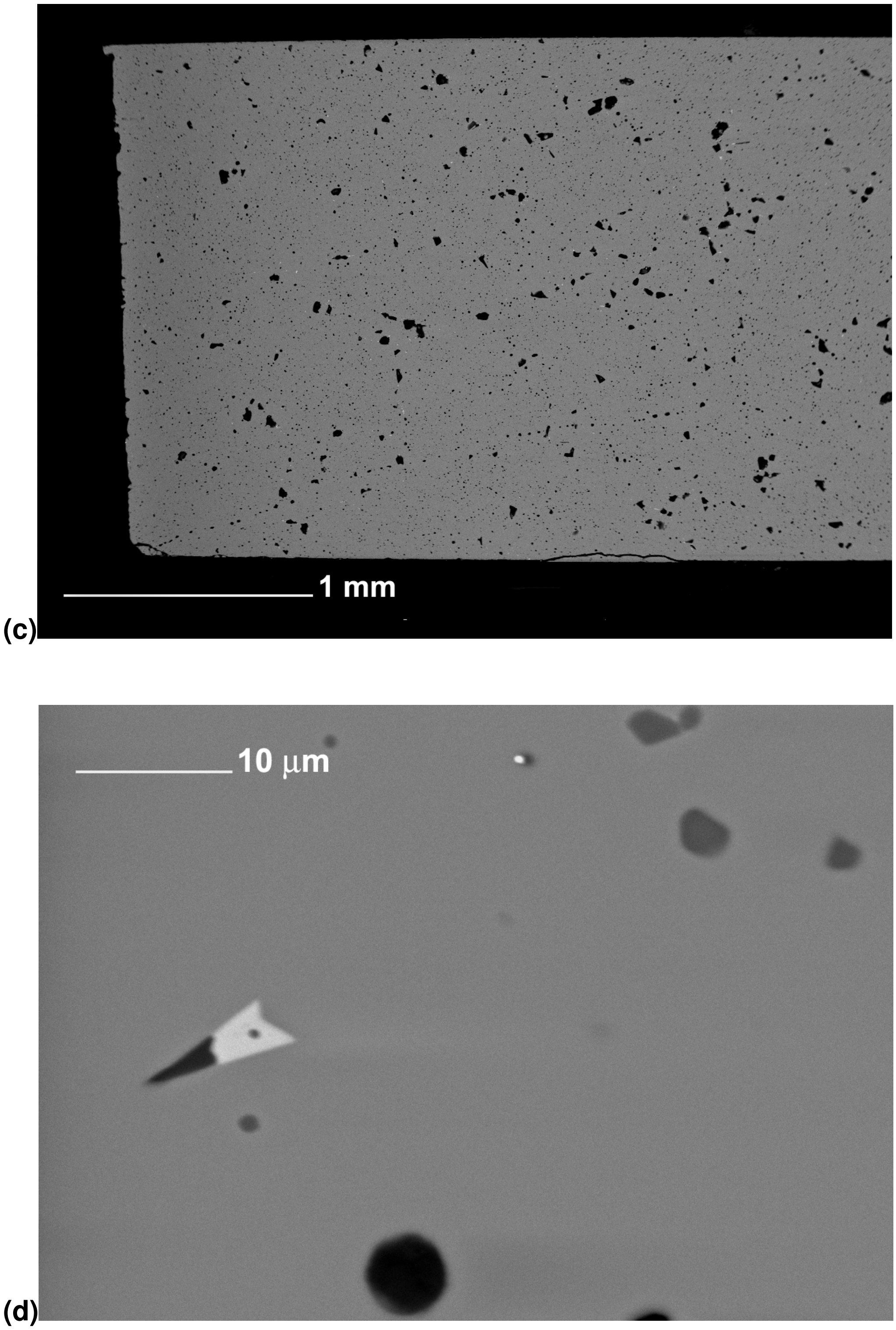

Figure 6.1 (contd): BEI SEM showing cross-section of a 24 h ceramic at (c) low magnification and (d) high magnification.

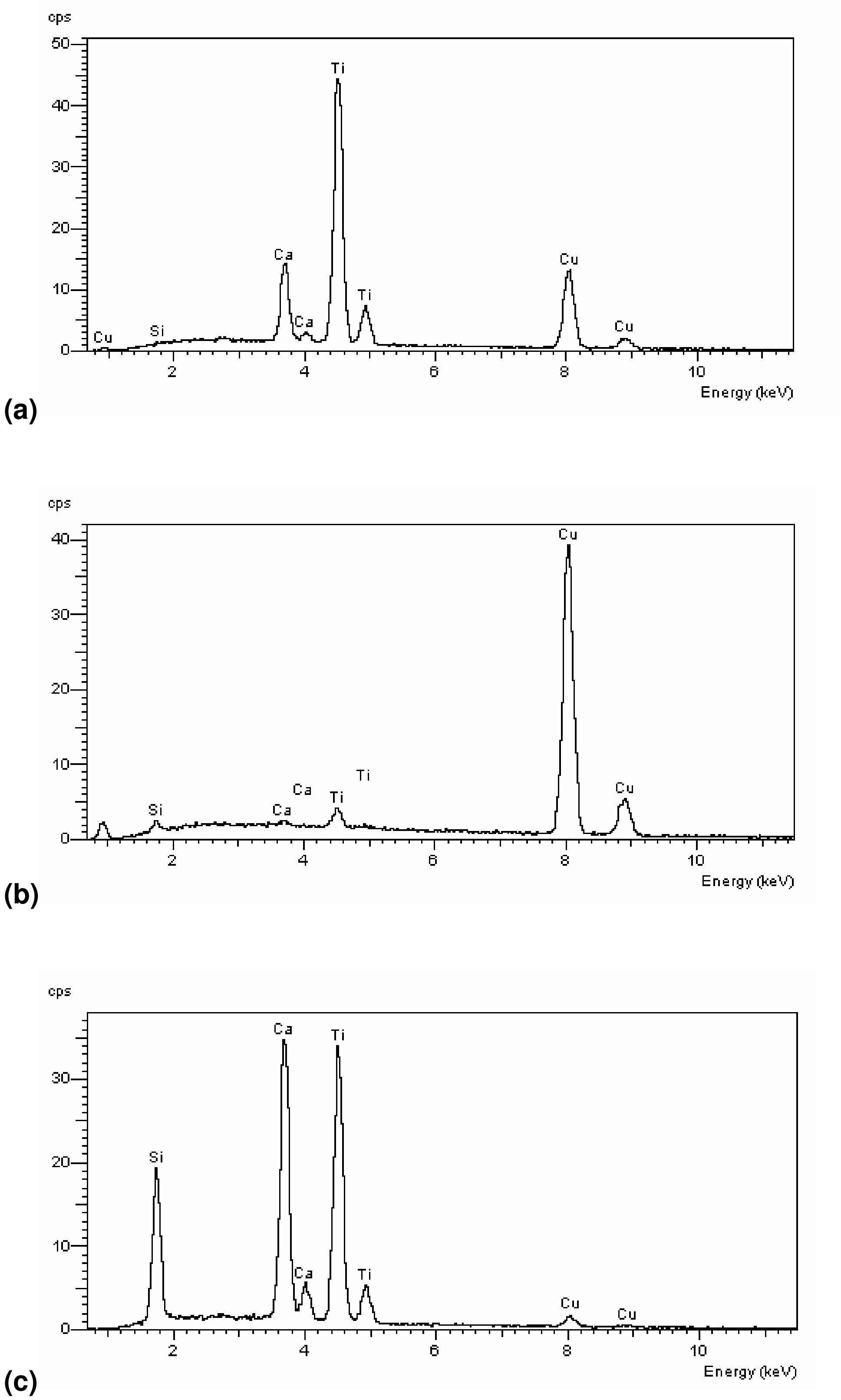

Figure 6.2: Typical EDS spectra of (a) bulk $CaCu_3Ti_4O_{12}$ phase, (b) bright precipitate and (c) dark precipitate for 3 and 24 h ceramics.

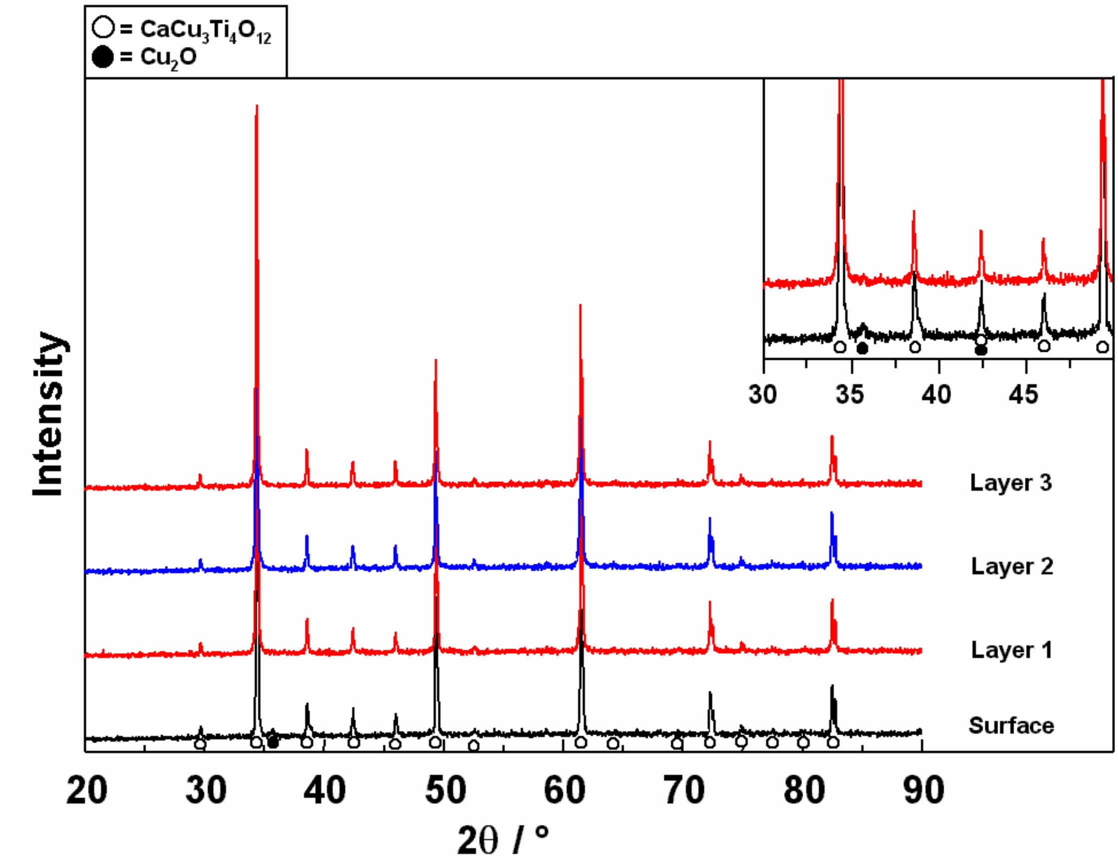

Figure 6.3: XRD patterns obtained layer-by-layer from a 3 h sample.

Low magnification BEI images of a 3 and 24 h ceramic post annealed in N_2 for 6 h at 1000 °C are shown in Figure 6.4 (a) and 6.4 (b), respectively. The image contrast reveals 2 compositionally distinct layers surrounding the bulk $CaCu_3Ti_4O_{12}$ material in both ceramics; these layers appear to form a “decomposition zone”. Figures 6.4 (c) and 6.4 (d) are high magnification images showing the interface between the outer two layers in the 3 and 24 h ceramic, respectively. The outermost layer was a highly porous (~ 50 %), “coral-like” structure of ~ 1 µm diameter interconnected strands. This structure forms the matrix of an inner layer in which the pores are filled with a phase that appears brighter (and therefore composed of heavier element(s)) than the matrix. In both ceramics, the thickness of the layers varies greatly such that, for the 3 h ceramics, the outer layer can penetrate to ~ 100 µm into the sample or, conversely, the inner layer can extend from the bulk interface, through the outer layer and to the pellet surface. The thickness of the decomposition zone as a whole was relatively constant in both ceramics. For the 3 h ceramic, the decomposition zone thickness was ~ 150 µm at the major pellet faces, increasing to ~ 200 – 300 µm along the pellet circumference. The decomposition zone was thinner in the 24 hr sample, ~ 100 – 150 μm.

Typical EDS data for the bright precipitate phase and matrix phase observed in the decomposition zone are shown in Figure 6.5 (a) and 6.5 (b), respectively. The bright phase corresponds to a copper-rich phase that, from previous data, is likely to be Cu_2O. The presence of Ca and Ti may, as before, arise from incorporation into the Cu_2O lattice or beam interaction with surrounding material. Similarly, the dark matrix corresponds to a Si-Ca-Ti phase. Such a "phase" may in fact be a finely textured mixture of oxides (e.g. $CaTiO_3$, TiO_2 and $CaTiSiO_5$) or a single Si-Ca-Ti-oxide.

The interface between the inner layer and the bulk material is shown in Figure 6.4 (e) and 6.4 (f) for the 3 and 24 h ceramics, respectively. For both ceramics, the interface is clearly defined by a fine texture of Cu_2O striations originating from the $CaCu_3Ti_4O_{12}$ grains and, below the interface, the microstructure is comparable both in terms of grains size, porosity and distribution of secondary phase(s) to that of the as-sintered ceramics in Figure 6.1 (b) and 6.1 (d). A major difference between the 3 and 24 h sample is that the texture was less striated in the 3 hr sample, such that the striations extend for 5 – 10 μm before coalescing into a more 'globular' morphology. The inner layer of the 24 h sample, however, was entirely striated between the interface with the outer layer and the interface with the bulk material.

The phases contained within the decomposition zone and the bulk material for the 3 h sample post-annealed in N_2 at 1000 °C were characterised by XRD after grinding successive layers away. As-sintered $CaCu_3Ti_4O_{12}$ pellets were black in colour, whereas samples post-annealed at 1000 °C in N_2 were white. By grinding through the sample with SiC paper, it was found that the white appearance of the surface quickly changed to an orange colour. Upon further grinding, a change to a dark brown colour and finally to black was observed. The different colours seemed to correspond to the 2 layers in the decomposition zone and the bulk material below, with white being the outer layer, orange-brown being the inner layer and black being the bulk $CaCu_3Ti_4O_{12}$. XRD data were obtained firstly from the untouched white surface. Data were then re-collected after: grinding until a change from white to orange was observed, regrinding until the orange colour darkened, regrinding until the colour changed to black and a final grinding to ensure no further changes in colour occurred. The results are shown in Figure 6.6.

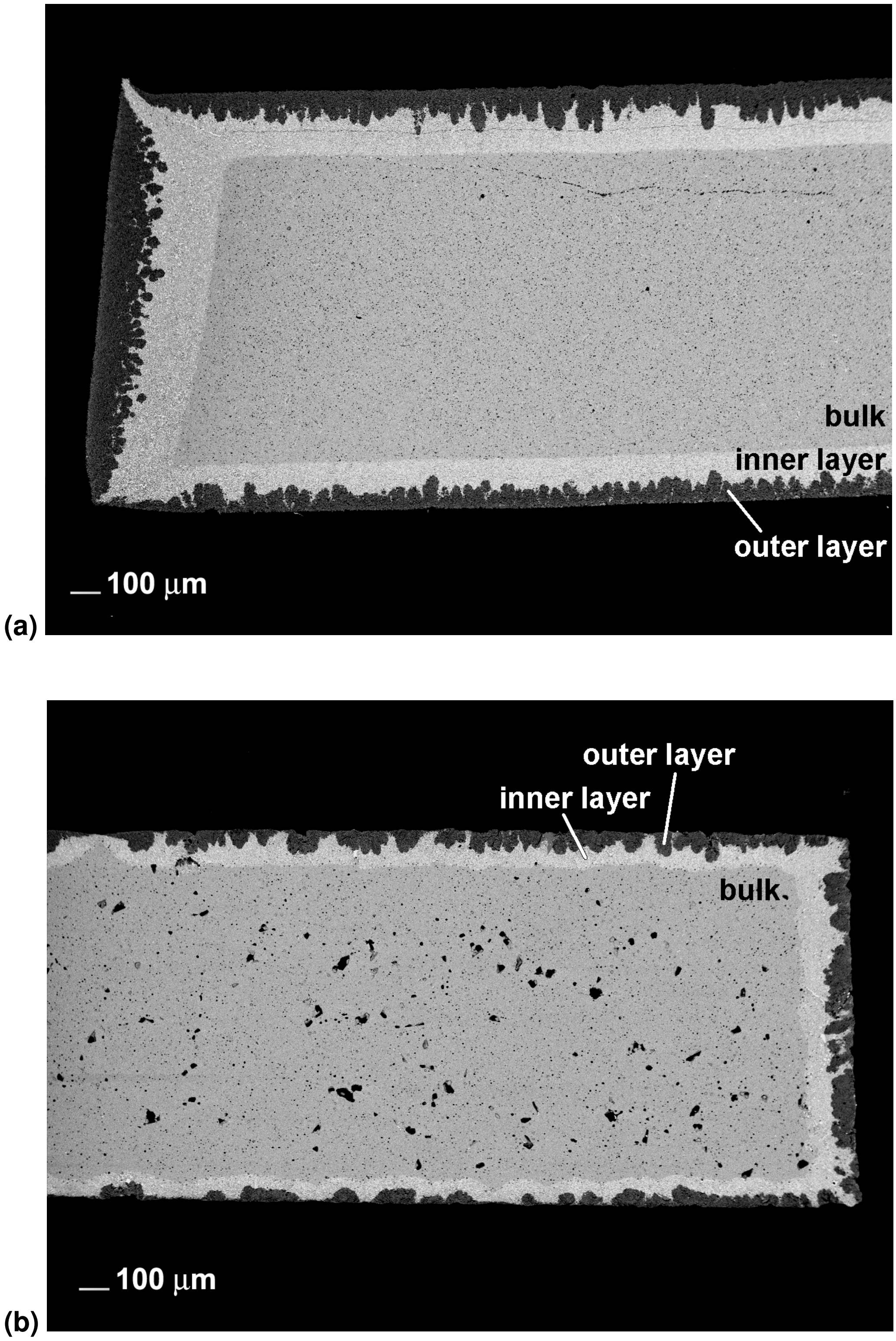

Figure 6.4: Low magnification BEI SEM of (a) 3 and (b) 24 h sample in cross-section after post annealing at 1000 °C in N_2 (contd. overleaf).

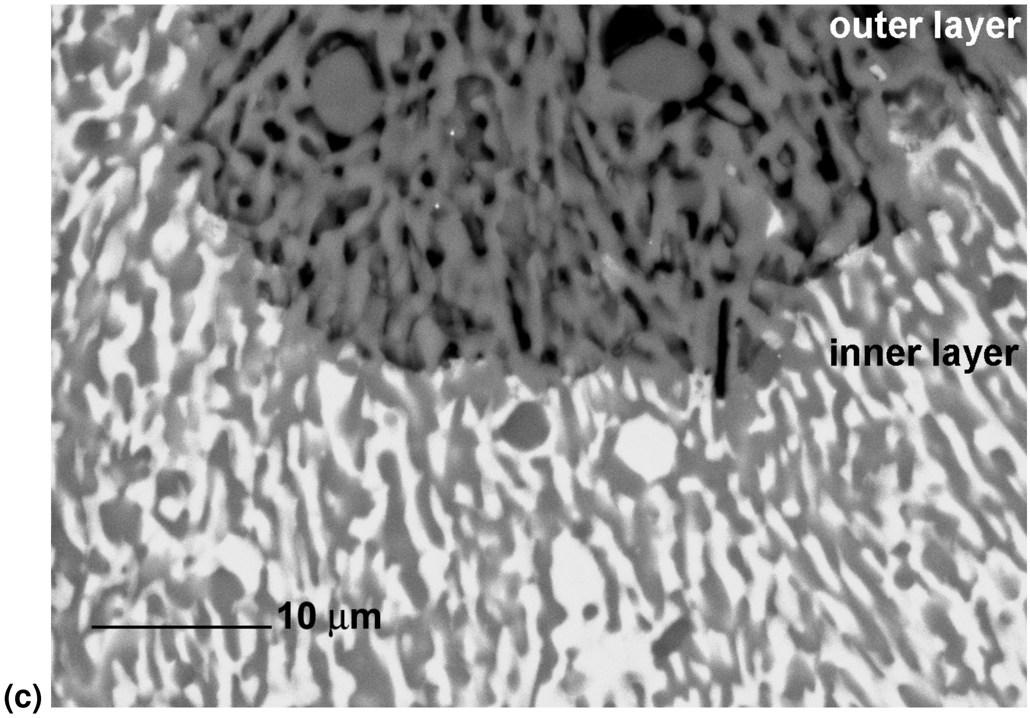

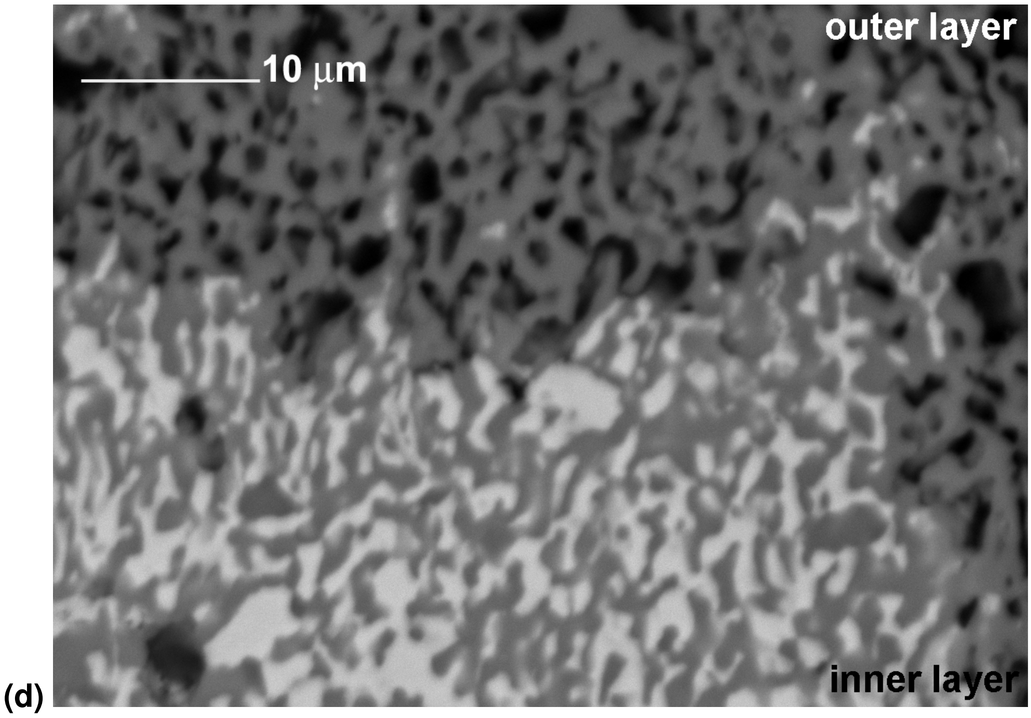

Figure 6.4 (contd.): BEI SEM showing the interface between the outer and inner layers of the decomposition zone in (c) a 3 h ceramic and (d) a 24 h ceramic after annealing at 1000 °C in N_2 (contd. overleaf).

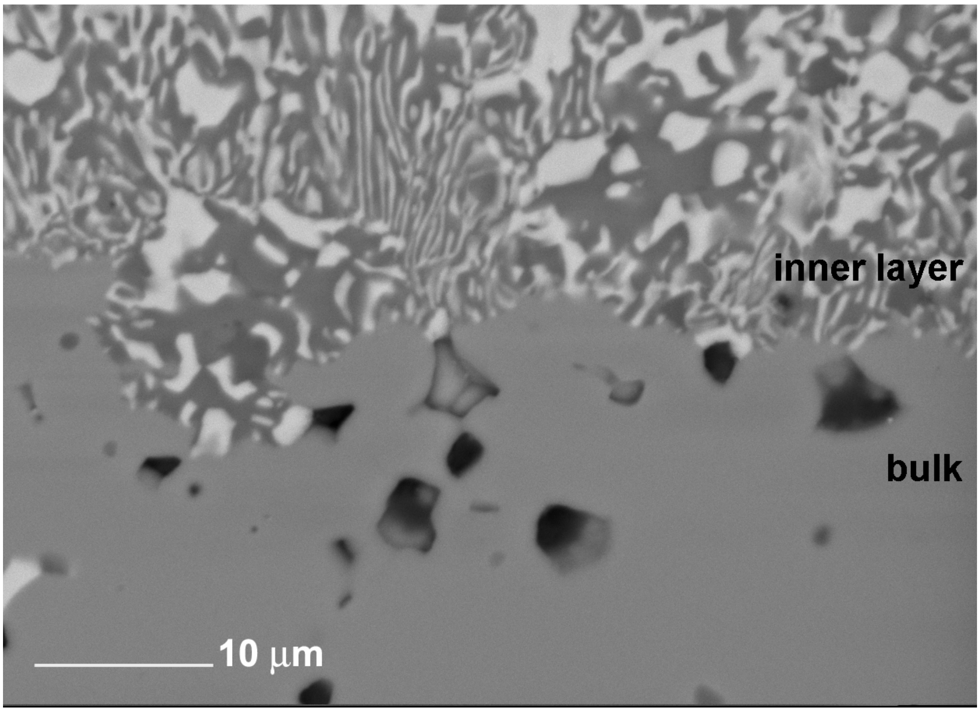

(e)

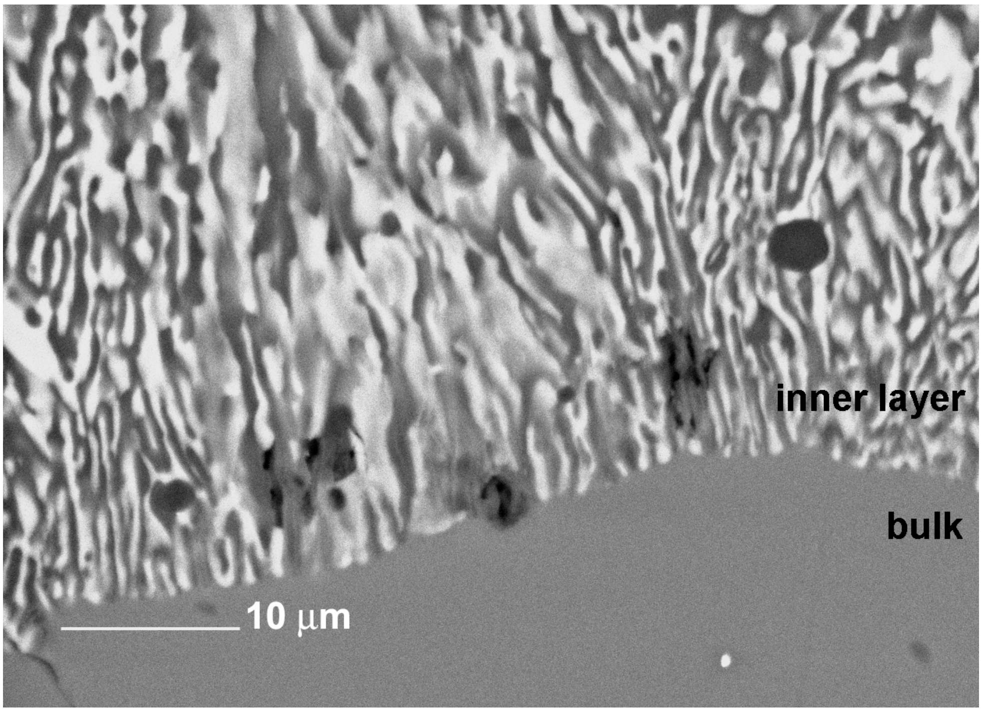

(f)

Figure 6.4 (contd.): BEI SEM showing the interface between the bulk phase and the inner layer of the decomposition zone of (e) a 3 h ceramic and (f) a 24 h ceramic.

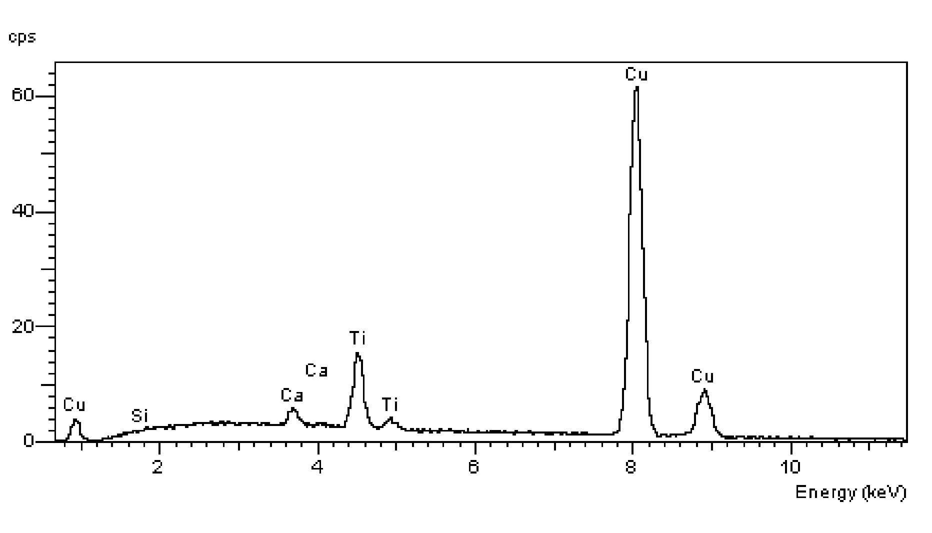

(a)

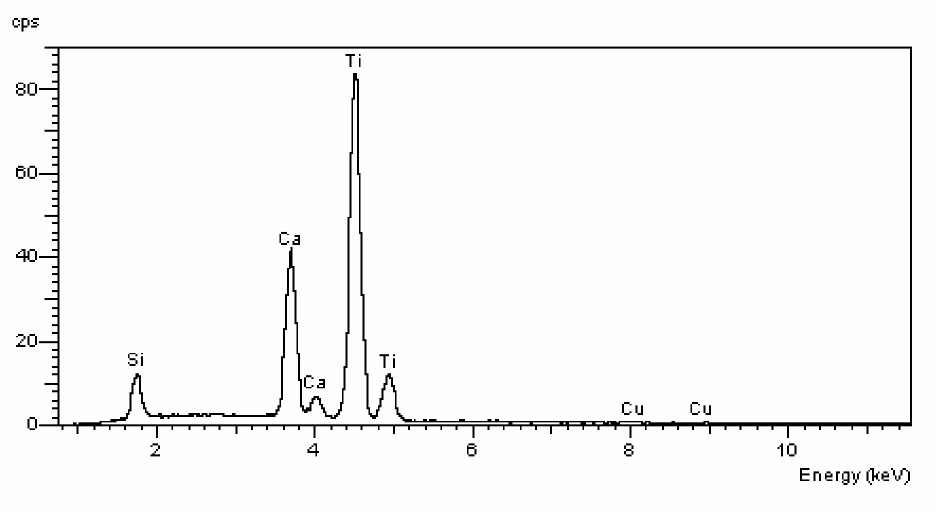

(b)

Figure 6.5: Typical EDS spectra from (a) the bright precipitate phase in the inner layer of the decomposition zone and (b) the matrix phase in the inner and outer layer.

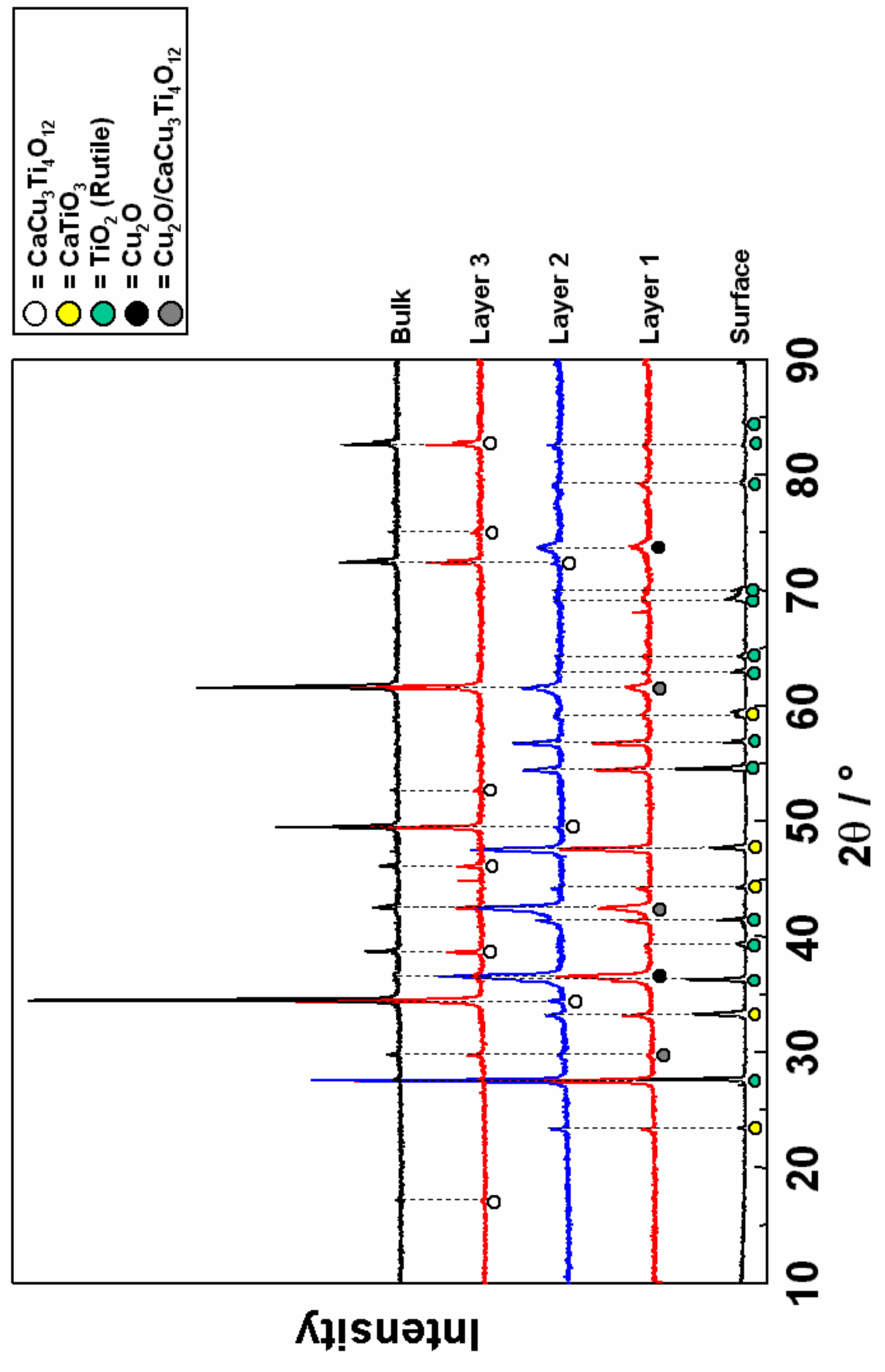

Figure 6.6: XRD data for a 3 h sample annealed at 1000 °C and analysed layer-by-layer.

Reflections observed from the surface correspond to TiO_2 (rutile) and $CaTiO_3$, in agreement with EDS data obtained from the outer layer and inner layer matrix. No evidence for sphene or crystalline SiO_2 was forthcoming in the XRD data, suggesting that the Si detected by EDS was either present in an amorphous silicate phase or incorporated into the TiO_2 and/or $CaTiO_3$ lattice, or in such small quantities that it could not be detected by laboratory XRD. The change from white to orange coincides with the observation of extra reflections corresponding to Cu_2O. This confirms that the major precipitate phase of the inner layer is Cu_2O and that an outer layer "coral" structure of TiO_2 and $CaTiO_3$ also forms the matrix of the inner layer. Further grinding, until the change in colour from orange to dark brown, yields major reflections in the XRD pattern corresponding to $CaCu_3Ti_4O_{12}$ with Cu_2O, TiO_2 and $CaTiO_3$ impurity phases. After further re-grinding, all reflections were found to correspond to $CaCu_3Ti_4O_{12}$.

The decomposition processes occurring in $CaCu_3Ti_4O_{12}$ at 1000 °C in N_2 are summarised schematically in Figure 6.7. At the interface of the bulk phase and the decomposition zone, $CaCu_3Ti_4O_{12}$ decomposes into a phase mixture of $CaTiO_3$, Cu_2O and TiO_2 (this discussion is simplified to exclude oxygen loss from the bulk phase and/or secondary phases). The inner layer contains the reaction products, in which $CaTiO_3$ and TiO_2 coexist as matrix structure and Cu_2O as a precipitate within that matrix. At the interface between the outer and inner layers of the decomposition, volatilisation of Cu_2O occurs, leaving the $CaTiO_3$-TiO_2 matrix to form the porous outer layer.

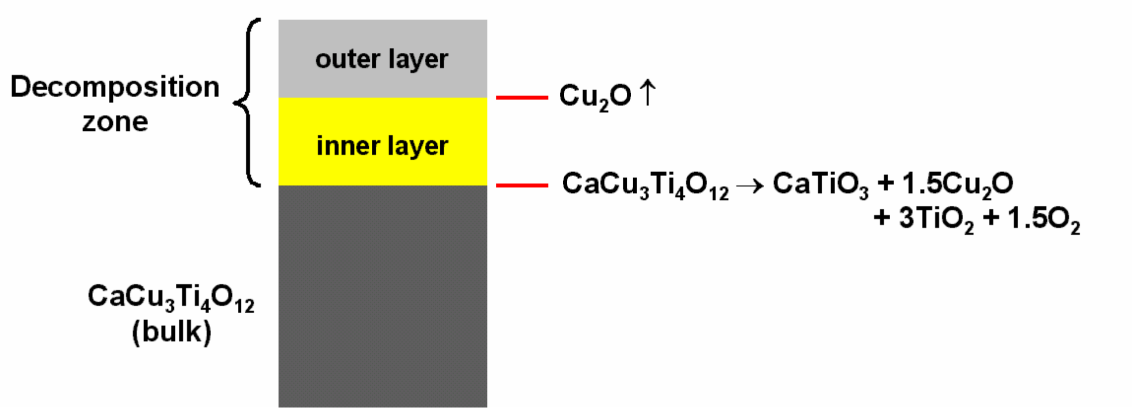

Figure 6.7: Schematic illustration of decomposition reactions occurring in $CaCu_3Ti_4O_{12}$ ceramics at 1000 °C in N_2.

Such large scale decomposition processes were not observed in as-sintered ceramics, although isolated precipitates of Cu_2O and $CaTiSiO_5$ were observed in ceramics sintered for 3 hrs and 24 hrs.

6.3.2. Effect of Post-Annealing on Electrical Properties

6.3.2.1. Fine-grained Ceramic

Figure 6.8 (a) is a Z^* plot of data collected from a sample sintered for 3 h at 1115 °C in air, featuring a single arc corresponding to the grain boundary impedance and a non-zero intercept at high frequencies associated with the bulk response. At 48 °C, R_{gb} ~ 600 kΩ.cm, R_b ~ 61 Ω.cm and f_{max} ~ 250 Hz, hence C_{gb} was calculated using the relation $\omega_{max}RC = 1$ and found to be ~ 1.1 nF/cm. These data are comparable with data previously obtained for 3 h ceramics, Chapter 4. No significant change in R_b or R_{gb} occurred following heat treatment at 600 °C in N_2. Post annealing in N_2 at 800 °C resulted in a reduction of R_{gb} to ~ 210 kΩ.cm and an increase in f_{max} to ~ 600 Hz. C_{gb} was calculated as ~ 1.2 nF/cm and R_b displayed a slight increase to ~ 65 Ω.cm (not shown).

Figure 6.8 (b) shows the Z^* plot of the ceramic after heat treatment in N_2 at 900 °C. R_{gb} and R_b decreased to ~ 85.6 kΩ.cm and ~ 55 Ω.cm, respectively, whereas f_{max} increased to ~ 1.5 kHz; C_{gb} was 1.2 nF/cm. The most significant change in the grain boundary impedance was observed following post-annealing at 1000 °C in N_2, Figure 6.8 (c). Prior to measurement, the decomposition zone, described in the previous section, was removed by grinding the major pellet faces and pellet circumference with SiC paper. The non-zero intercept was still evident, associated with the bulk response where R_b ~ 60 Ω but the grain boundary arc corresponded to R_{gb} and f_{max} values of ~ 170 Ω.cm and ~ 300 kHz, respectively; C_{gb} was ~ 3.1 nF/cm.

The above data are summarised in Table 6.1, highlighting the sensitivity of R_{gb} and $f_{max(gb)}$ to heat treatment in comparison to the relatively unaffected R_b and C_{gb} values. Heat-treating the ceramic at 1000 °C in N_2 resulted in R_{gb} decreasing by a factor of ~ 3500 and $f_{max(gb)}$ increasing by a factor of ~ 1200 from their respective as-sintered values. This is in contrast with the fluctuations in R_b by +/- 5 Ω.cm from the as-sintered value and the approximate threefold increase in C_{gb}. These data suggest the reduction in R_{gb} was not due to a change in grain boundary geometry since C_{gb} remained relatively constant. Instead, the condition $\omega RC = 1$ was maintained due to the substantial increase in $f_{max(gb)}$; such behaviour may be a consequence of changes in the chemical composition of the grain boundary phase.

Heat Treatment	R_b **(Ω.cm)**	R_{gb} **(kΩ.cm)**	$f_{max(gb)}$ **(kHz)**	C_{gb} **(nF/cm)**
As-sintered	61	600	0.25	1.1
800 ℃ in N_2	65	210	0.62	1.2
900 ℃ in N_2	55	85.6	1.50	1.2
1000 ℃ in N_2 then reground	60	0.17	300	3.1

Table 6.1. Impedance characteristics of a fine-grained $CaCu_3Ti_4O_{12}$ ceramic following several heat treatments.

Figure 6.8 (d) is a spectroscopic plot of *C'* corresponding to IS data obtained from the ceramic in the as-sintered state and following post annealing in N_2 at 900 ℃ and 1000 ℃. The data exhibit a high capacitance plateau in the kHz region, attributable to the grain boundary response, as discussed in Chapter 4, and the onset of dispersion in the MHz range to a low capacitance plateau associated with the bulk response. In the as-sintered state, the capacitance of the plateau is ~ 0.75 nF/cm when measured at 100 kHz, and increases at low frequencies to ~ 1.42 nF/cm at 40 Hz. The grain boundary impedance does not, therefore, exhibit ideal Debye-like behaviour but is typical of the inhomogeneous grain boundary responses observed in previous chapters.

Heat treatment in N_2 appears to further decrease the level of homogeneity in the grain boundary response such that, after post-annealing at 900 ℃ in N_2, the values of *C'* at 40 Hz and 100 kHz increased slightly to ~ 0.85 nF/cm and ~ 2.18 nF/cm, respectively. After heat treatment at 1000 ℃ in N_2, the high capacitance plateau was still observable in the kHz region where *C'* at 100 kHz was measured as ~ 1.9 nF/cm. The high frequency dispersion appears to occur at lower frequencies than previously observed and this may be associated with instrumentation problems, most likely originating from inductance within the ceramic and/or the conductivity jig.

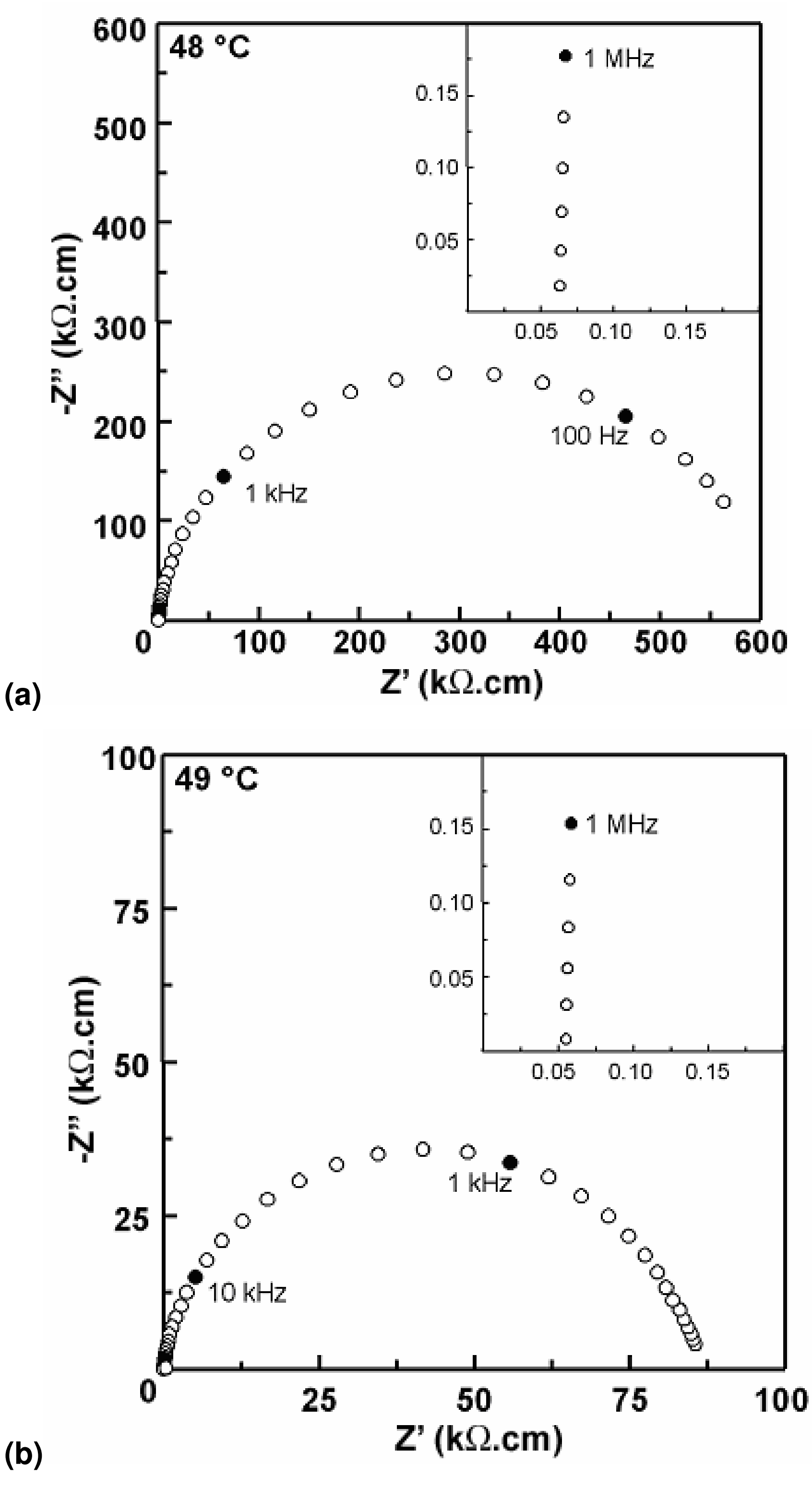

Figure 6.8: Z* plot of a 3 h ceramic (a) as-sintered and (b) post annealed at 900 °C in N_2 and measured at ~ 48 °C (contd overleaf).

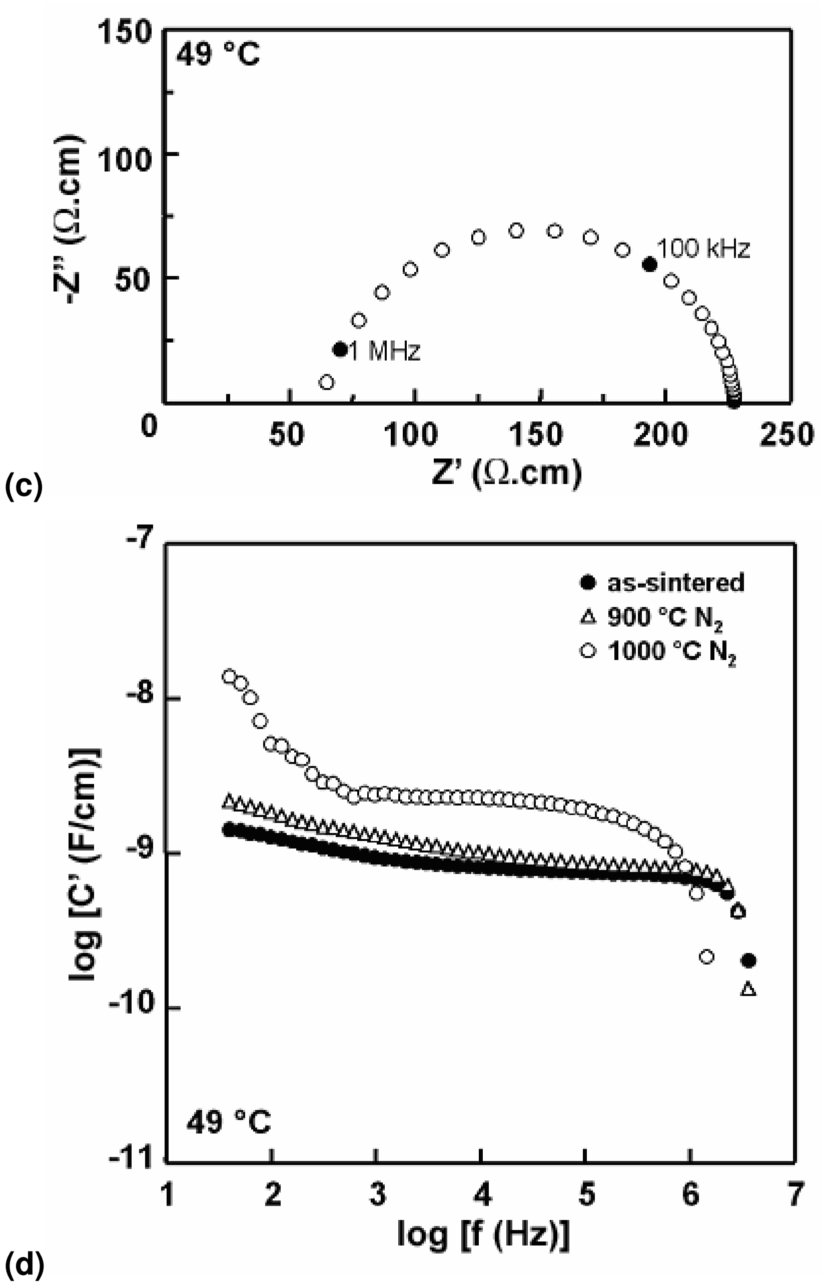

Figure 6.8 contd: (c) Z* plot of a 3 h ceramic after annealing at 1000 °C in N_2 and (d) C' spectroscopic plot of a 3 h ceramic as-sintered, post annealed at 900 °C and 1000 °C in N_2, measured at ~ 48 °C.

After heat treatment at 600 °C in O_2, no significant change was observed in Z^* plots. Figure 6.9 (a) is a Z^* plot of data collected following heat treatment at 800 °C in O_2. A single arc was observed at 51 °C corresponding to an electroactive element with R_{gb} ~ 55 kΩ.cm and $f_{max(gb)}$ ~ 280 Hz; C_{gb} was therefore calculated as ~ 10.3 nF/cm. The corresponding spectroscopic plot of *C'*, Figure 6.9 (b), shows the value of *C'* is more dependent on frequency than in previous measurements, exhibiting a sharp decrease between *dc* and 10 kHz, from 14.60 nF/cm to 5.53 nF/cm, respectively.

At high frequencies, the non-zero intercept in Z^* associated with R_b was observed and found to correspond to R_b ~ 75 Ω.cm, insert Figure 6.9 (a). At this scale, however, a high frequency arc, labelled “HF”, was partially resolved in Z^* plots. Although accurate values of R_{HF} and $f_{max(HF)}$ for this arc cannot be extracted, it was possible to “hand-fit” the data and estimate such values. For this high frequency arc, R_{HF} and $f_{max(HF)}$ were estimated to be ~ 300 Ω.cm and ~ 200 kHz, respectively; C_{HF} was then determined to be ~ 3 nF/cm. These values are comparable with those obtained for the grain boundary arc observed in Z^* after post annealing at 1000 °C in N_2, Figure 6.8 (c).

Heat treatment at 800 °C has, therefore, restored $f_{max(gb)}$ to the same order of magnitude as was observed in the as-sintered state, although the high frequency distortion of the grain boundary arc in Z^*, Figure 6.9 (a), and enhanced frequency-dependence of *C'* observed in Figure 6.9 (b) would suggest that the homogeneity of the grain boundary response has further degenerated. It seems likely that the HF arc observed in Figure 6.9 (a) may correspond to the pellet interior, where the grain boundary resistivity is lower than at the pellet surface. This argument is commensurate with a simple diffusion-type model, in which the grain boundary composition at the ceramic surface is readily modified by incorporation and/or volatilisation of ions, since diffusion of ions to and from the surface requires much less time than diffusion to and from the interior.

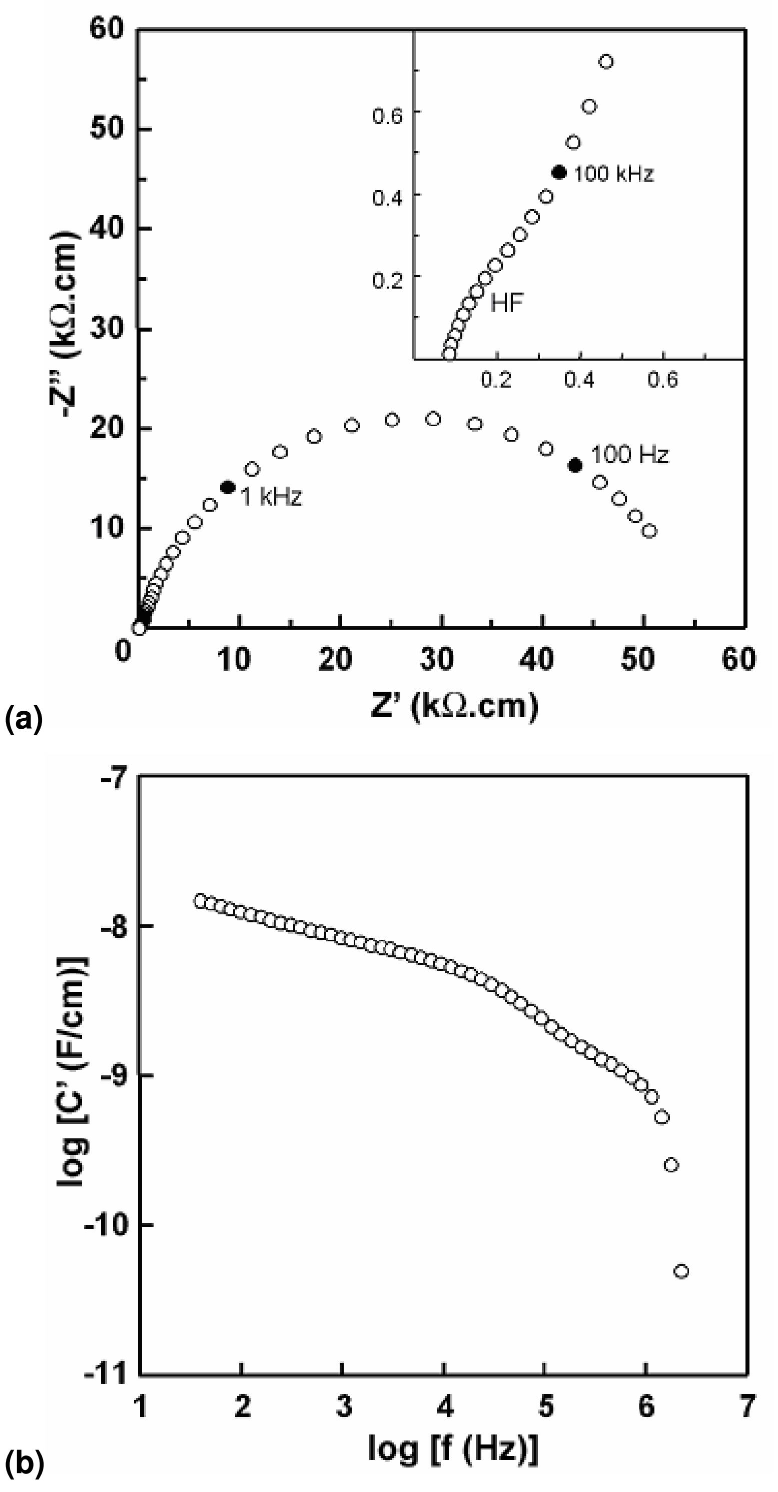

Figure 6.9: (a) Z* of a 3 h ceramic after annealing at 800 °C in O_2 and (b) corresponding C' spectroscopic plot.

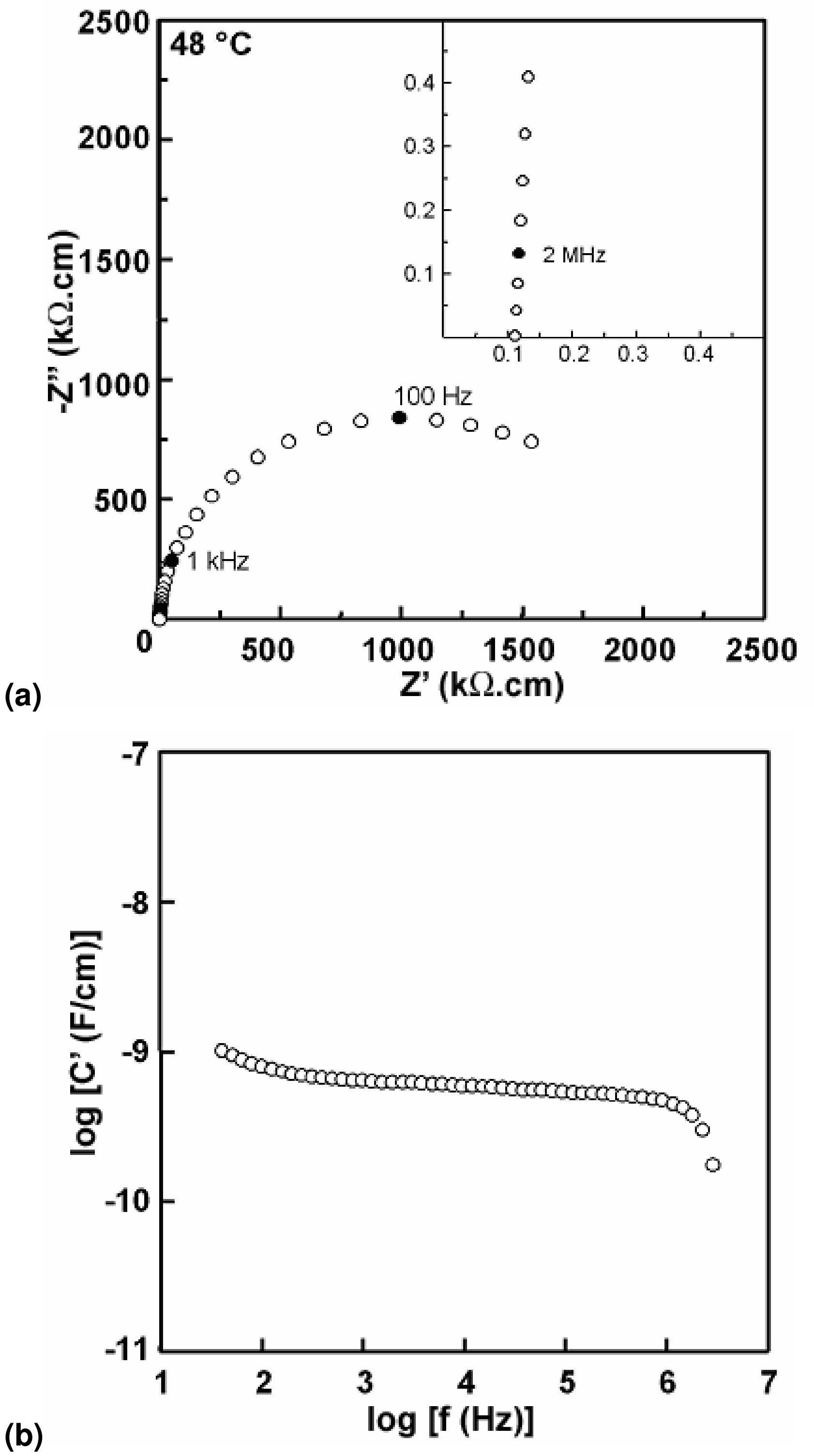

Figure 6.10: (a) Z* of a 3 h ceramic after annealing at 1000 °C in O_2 and (b) corresponding C' spectroscopic plot (contd. overleaf).

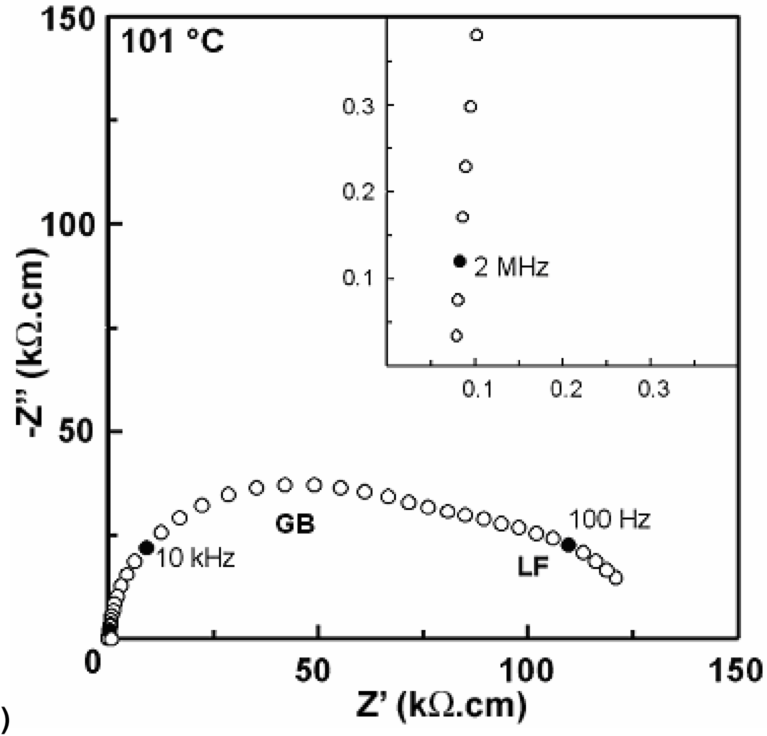

(c)

Figure 6.10: (contd.): Z* plot of a 3 h ceramic after post annealing at 1000 °C in O_2. The data were collected at a higher temperature (100 °C as opposed to 50 °C in previous figures).

After heat treatment at 1000 °C in O_2, the Z^* plot at 48 °C revealed a partially resolved low frequency arc as shown in Figure 6.10 (a). It was possible to hand fit a value of ~ 2 MΩ.cm for R_{gb} and, since $f_{max(gb)}$ was found to be ~ 100 Hz, a value of ~ 0.80 nF/cm was estimated for C_{gb}. Figure 6.10 (b) shows the spectroscopic plot of C' for the same measurement. C' at 100 kHz was ~ 0.55 nF/cm, in agreement with the C_{gb} value estimated from the Z^* plot in Figure 6.10 (a) and previously obtained data for the as-sintered ceramic. Within the measured frequency range, the impedance data when measured at ~ 50 °C were more typical of a homogenous grain boundary response. At higher temperatures, however, a second low frequency arc (labelled LF) was observed in Z^* plots, and shown in Figure 6.10 (c) for 101 °C. At this temperature, the two arcs were sufficiently resolved to allow R_{LF}, $f_{max(LF)}$ and C_{LF} to be estimated. R_{LF} was hand-fitted to a value of ~ 50 kΩ.cm and $f_{max(LF)}$ was ~ 160 Hz, such that C_{LF} was calculated to be ~ 20 nF/cm. Although these impedance data allow only speculation as to the origin of the LF arc, the magnitude of the capacitance excludes intrinsic polarisation phenomena associated with the bulk phase, suggesting the origin to be a grain boundary impedance.

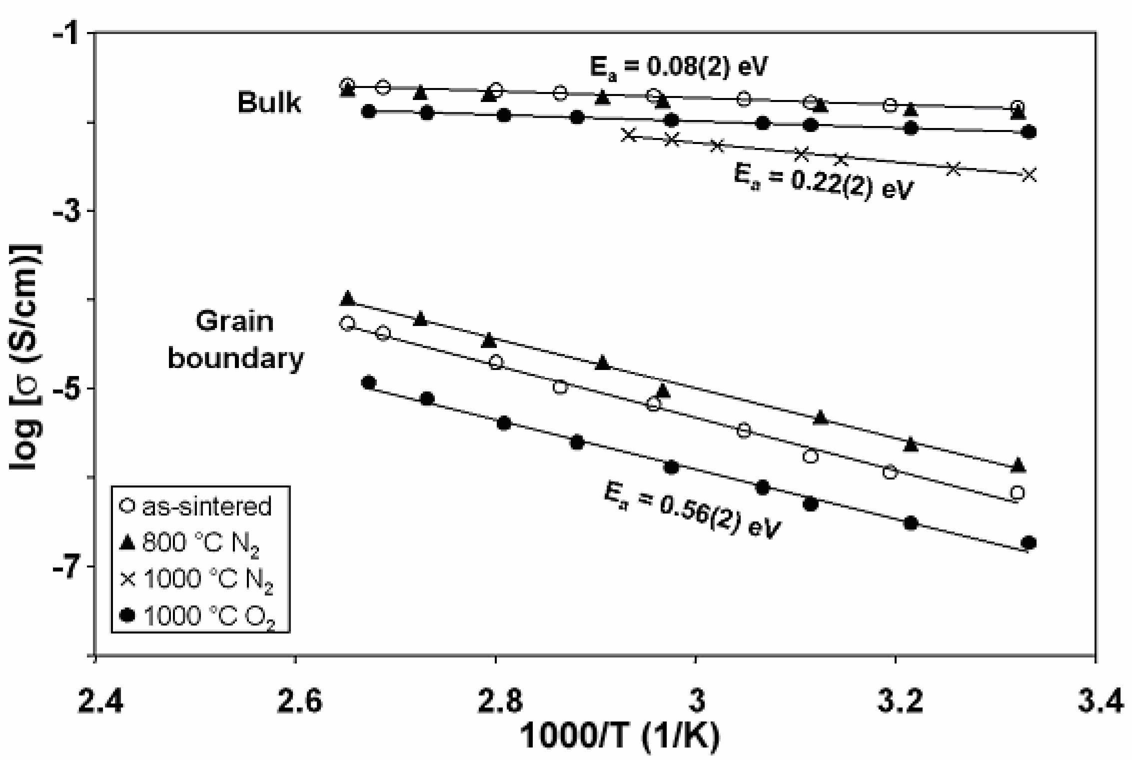

Figure 6.11: Arrhenius conductivity plot of a 3 h ceramic as-sintered and after post annealing at 800 ℃ and 1000 ℃ in N_2, then 1000 ℃ in O_2.

Conductivity data are plotted in Arrhenius format in Figure 6.11 for the ceramic as-sintered, post annealed at 800 ℃ in N_2, 1000 ℃ in N_2 and 1000 ℃ in O_2. Bulk conductivity data were unavailable after post annealing at 1000 ℃ in N_2 due to obfuscation of the data by inductive effects at high frequencies. Grain boundary conductivity data obtained after annealing at 1000 ℃ in O_2 were determined by hand-fitting the grain boundary arc in order to exclude the LF arc. In the as-sintered state, the bulk and grain boundary activation energies were found to be ~ 0.08(2) eV and ~ 0.56(2) eV, respectively. Such values are comparable with those obtained previously for $CaCu_3Ti_4O_{12}$ ceramics (Chapter 4), and did not change significantly after heat treatment at 800 ℃ in N_2 or 1000 ℃ in O_2. Following heat treatment at 1000 ℃ in N_2, the activation energy was ~ 0.22 eV; this value is likely to correspond to a combination of bulk and grain boundary conductivities, since the bulk and grain boundary impedances are comparable in terms of their order of magnitude.

Although the conductivity of the grain boundaries may vary over several orders of magnitude depending on pO_2 and annealing temperature, the activation energy remains relatively unaffected and so the change in conductivity is primarily attributable to a change in the number of charge carriers, rather than changes in the electronic band structure of the grain boundary interface. Since the grain boundary conductivity was increased by annealing at high temperature in N_2 and decreased by annealing at high temperatures in O_2, the grain boundary interface appears to exhibit an *n*-type conduction mechanism as described in Section 1.3.1.1. In the case of $CaCu_3Ti_4O_{12}$ ceramics in a low pO_2 atmosphere, oxygen in the grain boundary lattice becomes increasingly volatile at high temperatures. Oxygen can be removed from the grain boundary regions according to the following reaction:

$$O^{2-}_{\text{lattice}} \rightarrow 2e^- + V_O'' + 1/2O_{2(\text{gas})} \qquad (6.1)$$

whereby oxygen vacancies are created and electrons remain in the solid and result in conductivity, presumably by reduction of Ti, i.e. $Ti^{4+} + e^- \rightarrow Ti^{3+}$, as is widely believed to occur in *n*-type $BaTiO_3$[2, 3].

As shown in Figure 6.12, the oxygen has to diffuse through the grain boundary network to the surface of the ceramic before volatilising into the atmosphere. Similarly, when the ceramic is heated in a high pO_2 atmosphere, oxygen is adsorbed at the ceramic surface before diffusing into the ceramic interior via the grain boundary network. Oxygen is incorporated into the vacant sites and, according to the following reaction, recombines with the electrons associated with the oxygen vacancy, reducing the number of charge carriers and so decreasing the conductivity.

$$1/2O_{2(\text{gas})} + 2e^- + V_O'' \rightarrow O^{2-}_{\text{lattice}} \qquad (6.2)$$

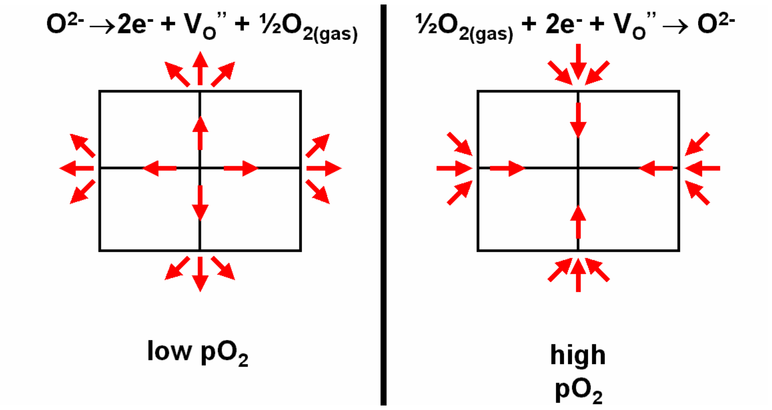

Figure 6.12: Schematic diagram of oxygen diffusion via a grain boundary network.

Diffusion along the grain boundaries often results in an inhomogeneous distribution of oxygen in the grain boundary network, since sites near the surface are more easily reduced or oxidised than those in the interior. The inhomogeneous nature of the grain boundary response was observed in previous impedance measurements, and may in part be attributable to oxygen enriched grain boundary regions near the surface. Since such a region would have thin layer geometry and higher resistivity than interior grain boundaries, a high capacitance, low frequency impedance may be expected resulting in distortion of the C_{gb} plateau at low frequencies.

Alternatively, dependence of conductivity upon pO_2 may be attributable to partial decomposition of $CaCu_3Ti_4O_{12}$ at the grain surfaces under low pO_2. This may occur if the $CaCu_3Ti_4O_{12}$ structure is intolerant to significant oxygen non-stoichiometry, as suggested in a recent study of non-stoichiometry in $SrCu_3Ti_4O_{12}$ by Li *et al.* [4]. It was proposed that partial reduction of Cu^{2+} to Cu^+ occurred during solid state reaction and during sintering, with charge compensation provided by partial occupation of the Cu-site by Ti^{4+}, *i.e.*:

$$3Cu^{2+} \rightarrow 2Cu^+ + Ti^{4+} \qquad (6.3)$$

On cooling, Cu^+ oxidises to Cu^{2+} with electrons entering the Ti 3d conduction band, according to:

$$6Cu^+ + 6Ti^{4+} \rightarrow 6Cu^{2+} + 6Ti^{3+} \qquad (6.4)$$

And so the stoichiometry can be described by the general formula $Ca(Cu^{2+}_{1-x}Ti^{4+})_3(Ti^{4+}_{4-6x}Ti^{3+}_{6x})O_{12}$. In this respect, n-type semiconductivity could be induced for phases having very small (< 0.001) values of x.

6.3.2.2. Coarse-grained Ceramic

Figure 6.13 (a) is a Z^* plot of a pellet sintered for 24 hours at 1115 °C in air. The large arc in the kHz range corresponds to a grain boundary impedance with R_{gb} ~ 0.4 MΩ.cm, f_{max} ~ 12 Hz and corresponding C_{gb} ~ 33.2 nF/cm. At high frequencies a non-zero intercept was observed, inset Figure 6.13 (a), corresponding to the impedance of the bulk $CaCu_3Ti_4O_{12}$ phase with R_b ~ 30 Ω.cm. In the 100 kHz range, the grain boundary data appear distorted, possibly as a result of the presence of an impedance similar to the HF arc observed in Figure 6.10 (a). After heat treatment at 800 °C in N_2, the Z^* plot revealed a significant decrease in R_{gb} to ~ 15.5 kΩ.cm, Figure 6.13 (b). f_{max} increased to ~ 280 Hz, and C_{gb} was calculated as ~ 36.7 nF/cm. The insert showing the non-zero intercept at high frequencies reveals a slight decrease in R_b to ~ 25 Ω.cm.

The Z^* plot in Figure 6.13 (c) shows the impedance response after heat treatment at 1000 °C in N_2. The low frequency arc corresponds to a resistance of ~ 5 - 6 Ω.cm and, below ~ 10 kHz, -*Z*'' was zero and *Z*' was fixed at 38 Ω.cm, indicating behaviour as an ideal resistor with no measurable reactance. The overall impedance of the ceramic was considered too small for accurate impedance measurements using the previously stated apparatus; it is clear, however, that post annealing at 1000 °C in N_2 has a significant effect on the grain boundary response.

C' data for a ceramic as-sintered and post annealed at 800 °C and 1000 °C in N_2 are shown in the spectroscopic plot in Figure 6.13 (d). In the as-sintered state, the grain boundary impedance resulted in a plateau in the kHz region and the onset of dispersion at higher frequencies to the low capacitance bulk plateau. The grain boundary plateau is slightly distorted such that *C*' at *dc* was ~ 35 nF/cm, whereas, at 10 kHz, C' ~ 24 nF/cm. As before, these data are indicative of an inhomogeneous grain boundary response.

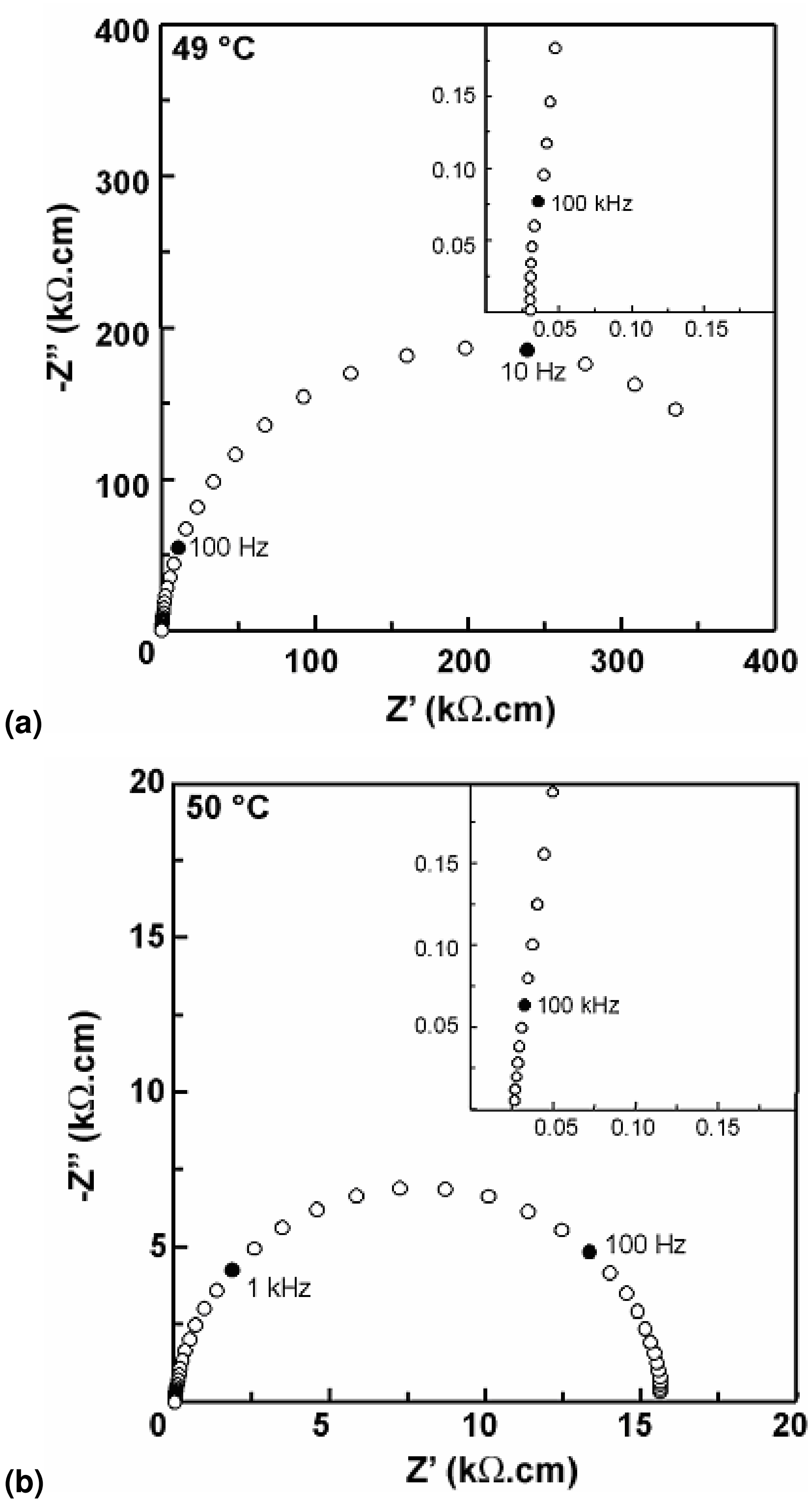

Figure 6.13: Z* plot of a 24 h pellet (a) as-sintered and (b) post annealed at 800 °C in N_2 (contd. overleaf).

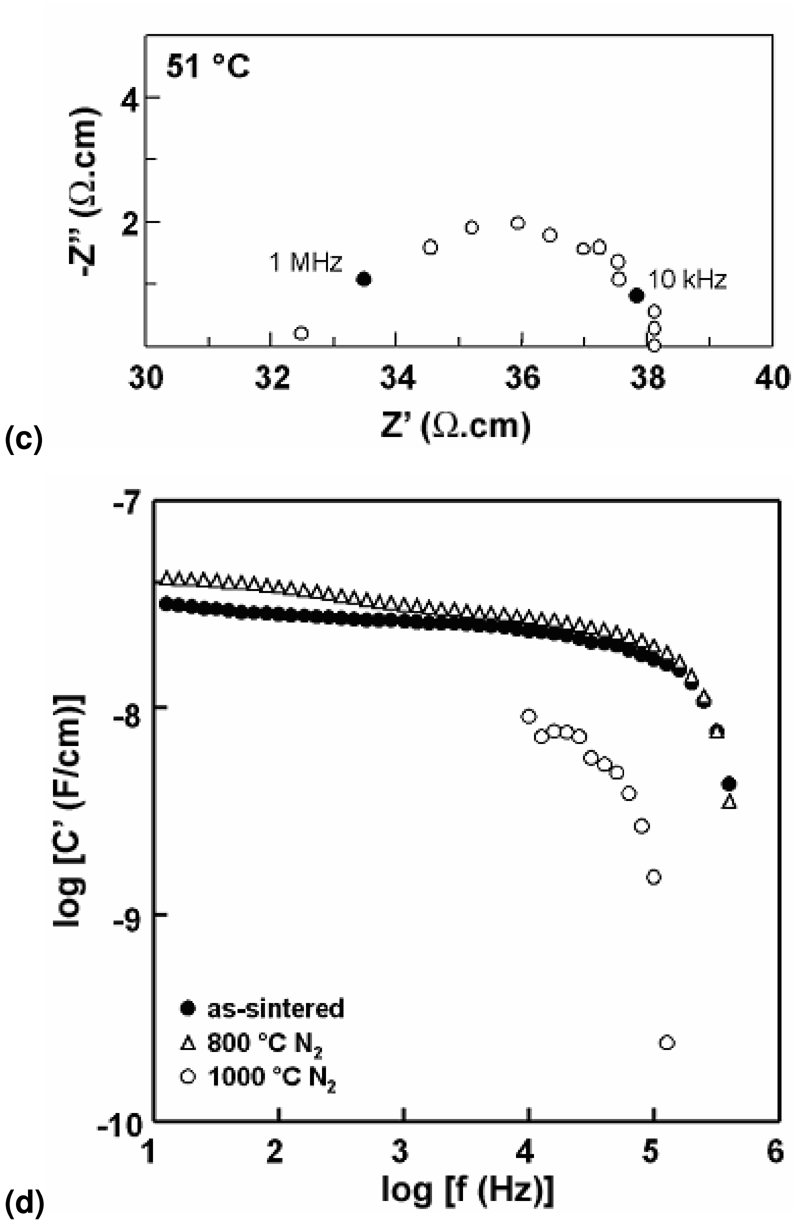

Figure 6.13 (contd.): Z* plot of a 24 h ceramic post annealed at 1000 °C in N_2 and (b) C' spectroscopic plot of a 24 h ceramic as-sintered, post annealed at 1000 °C in N_2 and post annealed at 1000 °C in O_2.

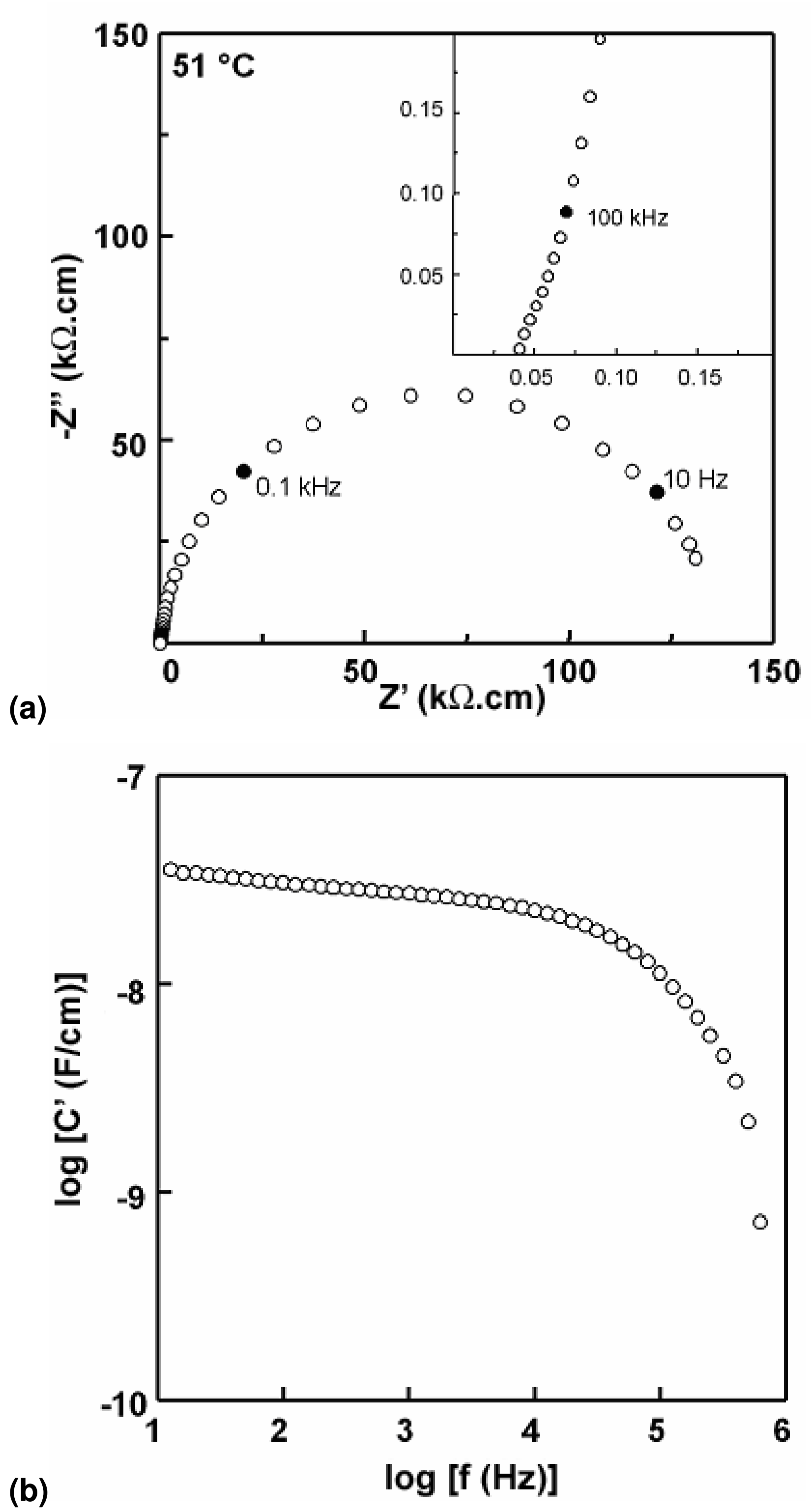

Figure 6.14: (a) Z^* plot of a 24 h ceramic post annealed at 1000 °C in O_2 and (b) corresponding *C'* spectroscopic plot.

After post annealing at 800 °C in N_2, an increase in *C'* was observed, particularly at low frequencies, comparable with observations made from the previous fine-grained ceramic and suggest the level of inhomogeneity in the grain boundary response was increased by heat treatment in N_2. *C'* data were not available below ~ 10 kHz after annealing at 1000 °C in N_2 due to the instrumentation difficulties described earlier. However, an apparent dispersion to the bulk plateau was observed at ~ 200 kHz, as shown in Figure 6.13 (d).

Figure 6.14 (a) shows the Z^* plot after post annealing at 1000 °C in O_2. The data are comparable with those obtained for the ceramic in the as-sintered state, featuring a grain boundary-type impedance (R_{gb} ~ 135 kΩ.cm, f_{max} ~ 35 Hz, C_{gb} ~ 33.7 nF/cm) and a non-zero intercept at high frequencies corresponding to R_b ~ 35 Ω.cm. Furthermore, the distortion in the 100 kHz range described in the previous data was again observed. The equivalent *C'* spectroscopic plot in Figure 6.14 (b) corresponds to the grain boundary impedance with *C'* at 100 kHz ~ 22.5 nF/cm and exhibits the onset of dispersion to the bulk plateau in the MHz range.

As for the fine-grained ceramic, R_{gb} and $f_{max(gb)}$ were found to be highly sensitive to heat treatment in N_2 and O_2 atmospheres at temperatures > 800 °C, whereas R_b and C_{gb} remained unaffected. It is apparent, therefore, that the grain boundary phase in coarse-grained ceramics exhibits the same *n*-type conduction mechanism as presumed to exist in the fine-grained ceramics.

Although *C'* in the spectroscopic plot shown in Figure 6.14 (b) appears to increase with decreasing frequency along the grain boundary plateau, the effect is less marked than that observed in the *C'* data obtained following annealing of a 3 h ceramic under equivalent conditions. In the 3 h ceramic, high temperature data revealed a further grain boundary-type impedance element labelled "LF" in the Z^* plot in Figure 6.10 (c). For the 24 hr ceramic, however, only one arc was observed in Z^* throughout the entire temperature range, suggesting that reoxidation of the coarse-grained ceramic was more homogenous than for the fine-grained ceramic. Since ceramics sintered for 24 h have a coarse grain structure (100 - 300 μm grains, as opposed to 1 - 10 μm in the 3 h ceramics), the diffusion pathways for oxygen migration are presumably shorter and less tortuous than in the 3 h ceramic, reducing the kinetic barrier for diffusion of O^{2-} ions within the grain boundary network. As such, a homogeneous distribution of O^{2-} ions was more easily maintained in the 24 h ceramic.

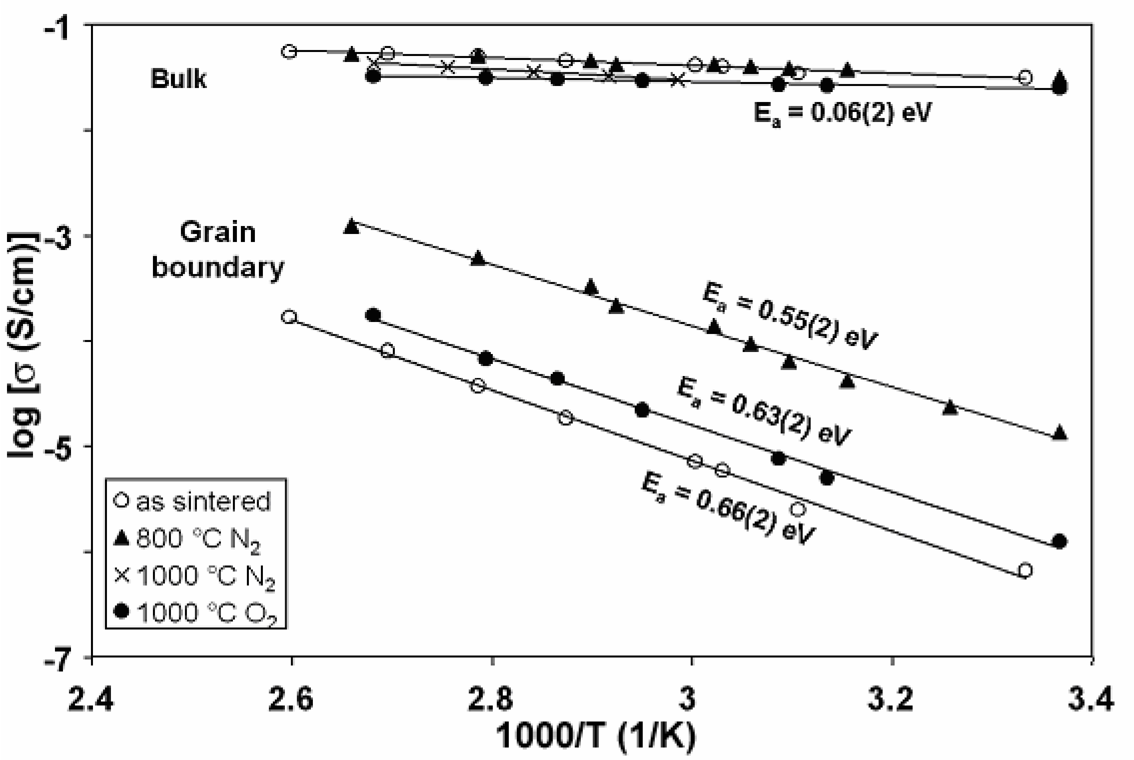

Figure 6.15: Arrhenius conductivity plot for a 24 h ceramic as-sintered and post annealed at 800 °C and 1000 °C in N_2 then post annealed at 1000 °C in O_2.

Conductivity data for the 24 h ceramic in the as-sintered state, after heat treatment at 900 °C and 1000 °C in N_2, and after post annealing at 1000 °C in O_2 are plotted in the Arrhenius form in Figure 6.15. *dc* conductivity data were collected after annealing at 1000 °C in N_2 using a Hewlett-Packard E2378A multimeter. Analysis of the data collected prior to annealing yielded activation energies of 0.06(2) eV and 0.66(2) eV for the bulk and grain boundary conductivity, respectively; such values were commensurate with previous data. After annealing at 800 °C in N_2, grain boundary conductivity increased by approximately one order of magnitude and the corresponding activation energy decreased to ~ 0.55(2) eV. The bulk conductivity, however, was unaffected. The *dc* conductivity was bulk-like in terms of magnitude with an activation energy of ~ 0.10(2) eV after annealing at 1000 °C in N_2. As for the 3 h ceramic, this activation energy value is attributable to a combination of both bulk and grain boundary conductivity. After annealing at 1000 °C in O_2, the grain boundary conductivity was similar to data collected for the as-sintered state.

R_{gb} and R_b are plotted against annealing conditions in Figure 6.16 to summarise the Z^* data obtained from the 24 h ceramic (this was not possible for the 3 h ceramic due to the convoluted nature of the grain boundary impedance, particularly after heat treatment in O_2). The grain boundary impedance in the 24 hr ceramic exhibit a strong dependence on pO_2 at temperatures > 800 ℃. Annealing between 800 ℃ and 900 ℃ in N_2 can increase the grain boundary conductivity by one or two orders of magnitude in both types of ceramic.

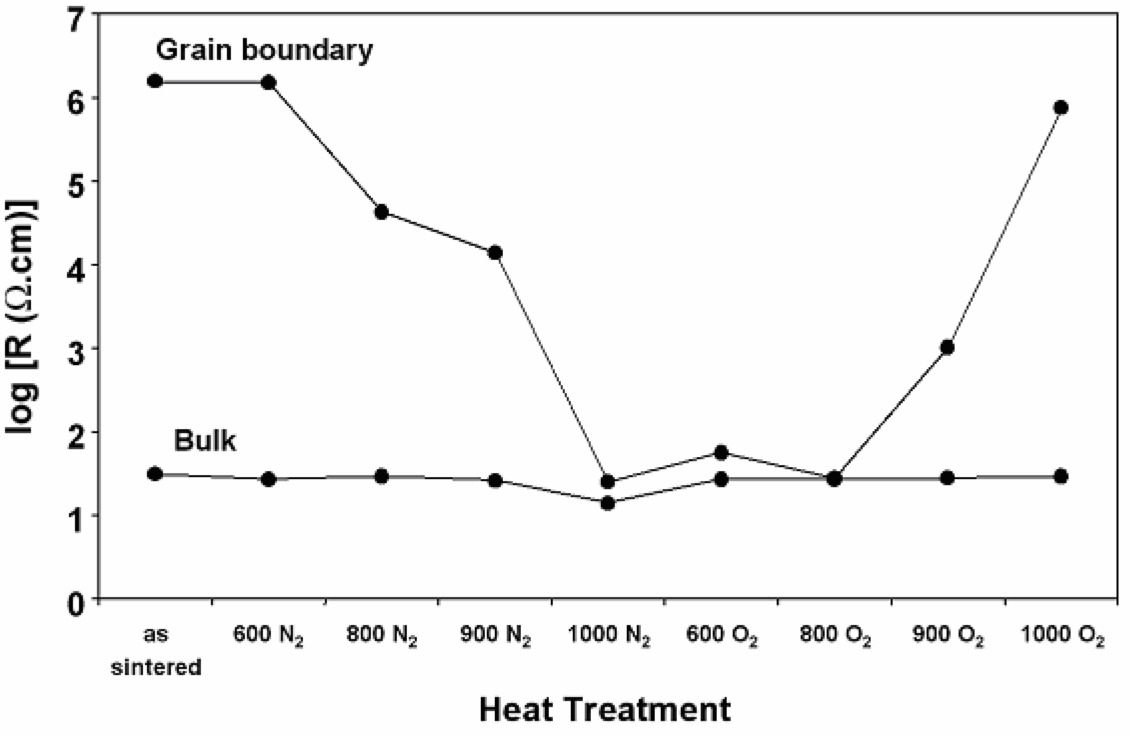

Figure 6.16: R_{gb} and R_b of a 24 h ceramic as-sintered and post annealed (room temperature measurements).

Given that it was possible to effectively eliminate the grain boundary impedance by post annealing at 1000 ℃ in N_2, and subsequently restore the impedance by post annealing at 1000 ℃ in O_2, conductivity in the grain boundary network would seem to occur via an *n*-type mechanism, although this interpretation does not account for the apparent insensitivity of the bulk $CaCu_3Ti_4O_{12}$ in both the 3 hr and 24 hr ceramics to pO_2. Possible explanations are that the oxygen stoichiometry of the bulk was unaffected by the annealing conditions (as such it would be impossible to distinguish between *n*-type and *p*-type conductivity) or that $CaCu_3Ti_4O_{12}$ exhibits an intrinsic conduction mechanism, as observed in the structurally-related $CaCu_3Mn_4O_{12}$.

6.4. Conclusions

The partial decomposition of $CaCu_3Ti_4O_{12}$ to Cu_2O and $CaTiSiO_5$ was characterised by SEM and XRD for ceramics prepared in air at 1115 °C. The secondary phases were present in ceramics sintered for 3 and 24 h. They appear as isolated precipitates in a matrix of $CaCu_3Ti_4O_{12}$ and are evenly distributed throughout the ceramics. Heat treatment at 1000 °C in N_2, however, resulted in large-scale decomposition of $CaCu_3Ti_4O_{12}$ to TiO_2, $CaTiO_3$ and Cu_2O in both 3 and 24 h ceramics. This reaction appeared to have commenced at the ceramic surface and progressed with time into the ceramic such that a decomposition zone was observed, surrounding the apparently stoichiometric $CaCu_3Ti_4O_{12}$ interior. The decomposition zone itself was divided into an outer layer near the pellet surface, consisting of a fine, coral-like structure of $CaTiO_3$ and TiO_2, and an inner layer adjacent to the $CaCu_3Ti_4O_{12}$ interior consisting of the same coral-like structure but with the pores filled by a Cu_2O-rich phase.

IS data revealed the grain boundary impedance to be sensitive to heat treatment in N_2 and O_2 at > 600 °C. R_{gb} could be decreased by several orders of magnitude by heating in N_2 at temperatures up to 900 °C. After annealing at 1000 °C in N_2, and removal of the decomposition zone, the total resistance of both ceramics was $< 50\ \Omega$, indicating R_{gb} comparable to R_b. Subsequent heating in O_2 increased R_{gb} suggesting the grain boundary phase exhibits an *n*-type conduction mechanism. An alternative explanation is based on partial decomposition of $CaCu_3Ti_4O_{12}$ under low pO_2 conditions, resulting in an increase in conductivity, followed by reformation under high pO_2 conditions, resulting in a decrease in conductivity. The exact origin of the semiconductivity (e.g. by oxygen loss or the decomposition mechanism of Li [4]) remains unknown.

The impedance data suggest that reoxidation did not occur homogeneously throughout the ceramic and so data could not necessarily be modelled on a simple circuit of 2 parallel *RC* elements connected in series. The bulk impedance, however, remained insensitive to heat treatment, suggesting that either oxygen loss does not occur in the bulk or, alternatively, that the bulk exhibits a conductivity mechanism that is insensitive to small amounts of oxygen loss.

References

1. Kim, J.-S., "The decomposition reaction of $YBa_2Cu_3O_{7-x}$ in hydrogen reduction." Materials Letters, 1996, **27**, 259-262
2. F.D. Morrison, D.C. Sinclair, A.R. West, "An Alternative Explanation for the Origin of the Resistivity Anomaly in La-Doped $BaTiO_3$." Journal of the American Ceramic Society, 2001, **84**(2), 474-476
3. F.D. Morrison, D.C. Sinclair, A.R. West, "Characterization of Lanthanum-Doped Barium Titanate Ceramics Using Impedance Spectroscopy." Journal of the American Ceramic Society, 2001, **84**(3), 531-538
4. J. Li, M.A. Subramanian, H.D. Rosenfeld, C.Y. Jones, B.H. Toby, A.W. Sleight, "Clues to the Giant Dielectric Constant of $CaCu_3Ti_4O_{12}$ in the Defect Structure of "$SrCu_3Ti_4O_{12}$"." Chemistry of Materials, 2004, **16**, 5223-5225

7. Synthesis & Characterisation of $CaCu_3Ti_4O_{12}$ Analogues

7.1. Introduction

Reports of high permittivity in perovskite-structured phases with body-centred cubic *Im*3 space group symmetry are not limited to $CaCu_3Ti_4O_{12}$. In 2000, Subramanian *et al* [1] also reported room temperature, single frequency permittivity values in excess of 1000 for a number of phases of general formulae $ACu_3Ti_4O_{12}$ and $ACu_3Ti_3FeO_{12}$. Certain phases, such as $LaCu_3Ti_3FeO_{12}$, had, however, low permittivity values of ~ 30 – 50. Later in 2002, Subramanian and Sleight [2] reported similar data for such phases, including those of general formulae $A_{2/3}Cu_3Ti_4O_{12}$ and $Na_{1/2}A_{1/2}Cu_3Ti_4O_{12}$. These data are summarised in Table 7.1.

Phase	**ε'**	**tan δ**
$CdCu_3Ti_4O_{12}$	409	0.093
$La_{2/3}Cu_3Ti_4O_{12}$	418	0.060
$Sm_{2/3}Cu_3Ti_4O_{12}$	1,665	0.048
$Dy_{2/3}Cu_3Ti_4O_{12}$	1,633	0.040
$Y_{2/3}Cu_3Ti_4O_{12}$	1,743	0.049
$Bi_{2/3}Cu_3Ti_4O_{12}$	1,871	0.065
$Na_{1/2}La_{1/2}Cu_3Ti_4O_{12}$	3,560	0.074
$Na_{1/2}Sm_{1/2}Cu_3Ti_4O_{12}$	1,426	0.083
$Na_{1/2}Gd_{1/2}Cu_3Ti_4O_{12}$	1,645	0.074
$Na_{1/2}Dy_{1/2}Cu_3Ti_4O_{12}$	1,854	0.085
$Na_{1/2}Yb_{1/2}Cu_3Ti_4O_{12}$	2,048	0.059
$Na_{1/2}Y_{1/2}Cu_3Ti_4O_{12}$	1,783	0.064
$Na_{1/2}Bi_{1/2}Cu_3Ti_4O_{12}$	2,454	0.094
$BiCu_3Ti_3FeO_{12}$	692	0.082
$LaCu_3Ti_3FeO_{12}$	44	0.339
$NdCu_3Ti_3FeO_{12}$	52	0.325
$SmCu_3Ti_3FeO_{12}$	52	0.256
$GdCu_3Ti_3FeO_{12}$	94	0.327
$YCu_3Ti_3FeO_{12}$	33	0.308
$Cu_3Ti_3FeO_{12}$	244	0.254
$CdCu_3Ge_4O_{12}$	34	0.064

Table 7.1: Reported fixed frequency permittivity and tan δ values of various phases with the $CaCu_3Ti_4O_{12}$ structure, after Subramanian *et al.* [1, 2]

Subramanian and Sleight also calculated permittivity values for selected phases using the Clausius-Mossotti relationship, Equation 7.1, where Nj and αj are the concentration and polarisability of ion j, respectively [3].

$$\frac{\varepsilon-1}{\varepsilon+1}=\frac{1}{3\varepsilon_0}\sum N_j\alpha_j \qquad (7.1)$$

The calculated values for all phases isostructural to $CaCu_3Ti_4O_{12}$ were < ~ 90 (the calculated bulk permittivity of $CaCu_3Ti_4O_{12}$ was 49), indicating that the observed high permittivity may not be associated with the bulk response, or that these phases exhibited a novel polarisation mechanism. For $CdCu_3Ti_4O_{12}$, the calculated permittivity was 56. αj values were based on those reported by Shannon [4], i.e. 3.2 and 3.4 Å^3 for Ca^{2+} and Cd^{2+}, respectively. Shannon reports that polarisability of Na^+ and Bi^{3+} as 1.8 and 6.0 Å^3 (the notably high polarisability of Bi^{3+} is attributable to the lone pair $6s^2$ orbital), respectively, and so it may be predicted that $Na_{1/2}Bi_{1/2}Cu_3Ti_4O_{12}$ exhibits a permittivity greater than $CaCu_3Ti_4O_{12}$ and $CdCu_3Ti_4O_{12}$.

The previous chapters demonstrated that the high apparent permittivity observed in $CaCu_3Ti_4O_{12}$ ceramics originated from a grain boundary capacitance. The bulk permittivity could not be measured over the typical frequency range of 10 Hz – 1 MHz since the bulk was semiconducting, such that its time constant was so low that f_{max} associated with bulk relaxation processes was > 10^7 Hz, which is above the frequency limit of most impedance analysers and fixed frequency LCR meters. When measured at temperatures below ~ 100 K, however, the time constant of the bulk was higher and within the measuring range (< 1 MHz), such that the bulk permittivity could be obtained.

Since the phases listed in Table 7.1 were all commensurate with *Im*3 space group symmetry it may be reasonable to assume that ferroelectricity was not the origin of the high reported permittivity values. If a barrier-layer capacitor model could also be applied to these samples, then the reported high permittivities may be attributed to a grain boundary capacitance. Where phases have been reported as being of low (< 100) permittivity, then it may be speculated that the bulk resistance is significantly greater than in so-called "high permittivity" phases, such that the time constant of the bulk phase is within measuring range at room temperature, allowing the low bulk permittivity to be obtained at < 1 MHz.

In this Chapter, the electrical properties of $CdCu_3Ti_4O_{12}$ and $Na_{1/2}Bi_{1/2}Cu_3Ti_4O_{12}$ ceramics will be investigated using Impedance Spectroscopy in order to probe the electrical heterogeneity of the samples and determined whether the permittivity values reported by Subramanian *et al* [1, 2] correspond to intrinsic or extrinsic responses.

7.2. Experimental

~ 5 g batches of $CdCu_3Ti_4O_{12}$ and $Na_{1/2}Bi_{1/2}Cu_3Ti_4O_{12}$ were prepared in covered platinum crucibles by solid state reaction in air at 950 ℃ for 6 hrs and 1000 ℃ for 6 hrs (heating and cooling rates were 5 ℃/min). $CdCu_3Ti_4O_{12}$ and $Na_{1/2}Bi_{1/2}Cu_3Ti_4O_{12}$ pellets were uniaxially pressed in a 5 mm diameter steel die and sintered in covered platinum crucibles in air at 1000 ℃ and 1050 ℃ for 6 hrs, respectively. Selected pellets were ground using an agate pestle & mortar in acetone and characterised by XRD (STOE Stadi-P diffractometer). Other pellets were characterised for grain morphology and porosity by SEM of Au-sputter coated pellet surfaces. For electrical property measurements, pellets were prepared as in previous chapters with InGa electrodes and impedance measurements made using Agilent 4192A and Solartron 1296 analysers in conjunction with an non-inductively-wound furnace (for high temperature measurements) and Oxford Cryostat for measurements between 77 K and 300 K.

7.3. Results & Discussion

Powder XRD data for the reacted $CdCu_3Ti_4O_{12}$ and $Na_{1/2}Bi_{1/2}Cu_3Ti_4O_{12}$ are shown in Figure 7.1. All peak positions were indexed to space group Im3 with lattice parameter a = 7.38987(15) Å for $CdCu_3Ti_4O_{12}$ and a = 7.4179(7) Å for $Na_{1/2}Bi_{1/2}Cu_3Ti_4O_{12}$. Relative peak intensities were found to correspond to the XRD pattern obtained for $CaCu_3Ti_4O_{12}$, shown in Figure 7.1. These data would suggest that both phases are analogous in terms of crystal structure to $CaCu_3Ti_4O_{12}$, described by the general formula $A'A''_3B_4O_{12}$. In the case of $CdCu_3Ti_4O_{12}$, therefore, Cd occupies the *A*' site whereas $Na_{1/2}Bi_{1/2}Cu_3Ti_4O_{12}$ is more complex, having Na and Bi sharing the *A*' site in a 1:1 ratio (the degree of ordering between Na and Bi ions cannot be fully discerned using the XRD data).

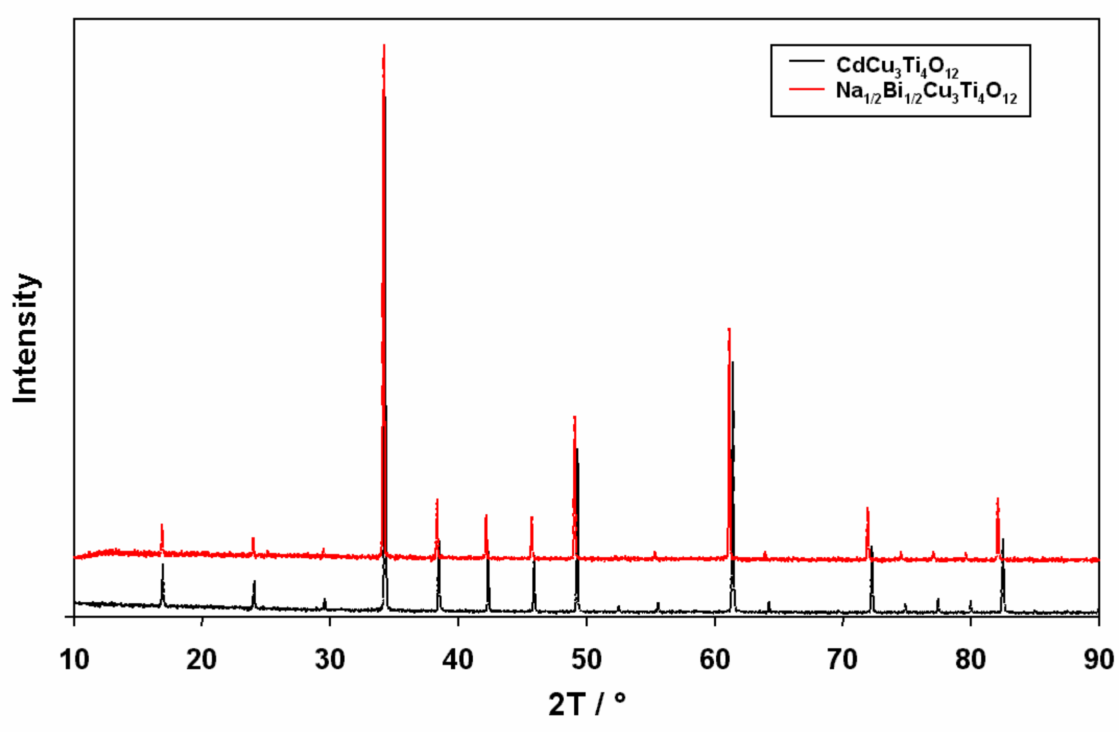

Figure 7.1: Powder XRD data for $CdCu_3Ti_4O_{12}$ and $Na_{1/2}Bi_{1/2}Cu_3Ti_4O_{12}$

XRD data from $CaCu_3Ti_4O_{12}$ were refined in Chapter 4 with Im3 space group symmetry and the lattice parameter, *a*, was reported as 7.39547(19) Å. The unit cell parameters for $CaCu_3Ti_4O_{12}$, $CdCu_3Ti_4O_{12}$ and $Na_{1/2}Bi_{1/2}Cu_3Ti_4O_{12}$ are shown in Table 7.1, together with ionic radii of the *A*' cation according to Shannon [5].

Phase ($A'Cu_3Ti_4O_{12}$)	*A*' radius / Å	Observed *a* / Å
Ca^{2+}	1.34	7.39547(19)
Cd^{2+}	1.31	7.39878(15)
$Na^{+}_{1/2}Bi^{3+}_{1/2}$	1.28 (average)*	7.4179(7)

Table 7.1: Structural data for $CaCu_3Ti_4O_{12}$ and analogues. **** ionic radii data for 12-coordinate Bi^{3+} were unavailable and so this average value was calculated using the ionic radii for 8-coordinate Bi^{3+}. It is likely that this value, therefore, is an over-estimate.***

Cd^{2+} is reported as having a slightly smaller ionic radius than Ca^{2+} and so it may be expected that the unit cell volume for $CdCu_3Ti_4O_{12}$ is less than that of $CaCu_3Ti_4O_{12}$. However, the estimated effective ionic radii of the *A*' site (1.28 Å) in $Na_{1/2}Bi_{1/2}Cu_3Ti_4O_{12}$ is significantly smaller than that of both $CaCu_3Ti_4O_{12}$ and $CdCu_3Ti_4O_{12}$, yet the observed unit cell is significantly larger. Furthermore, comparing lattice parameter values reported by other groups for $CaCu_3Ti_4O_{12}$ reveals a wide variance of values for this phase: 7.4035(5), 7.39347(3), 7.3798(1) Å were reported by Subramanian and Sleight [2], Subramanian *et al* [1] and Moussa *et al* [6], respectively. Such variance may be attributable to slight variations in stoichiometry (e.g. through oxygen loss and/or cation nonstoichiometry) arising from different processing conditions.

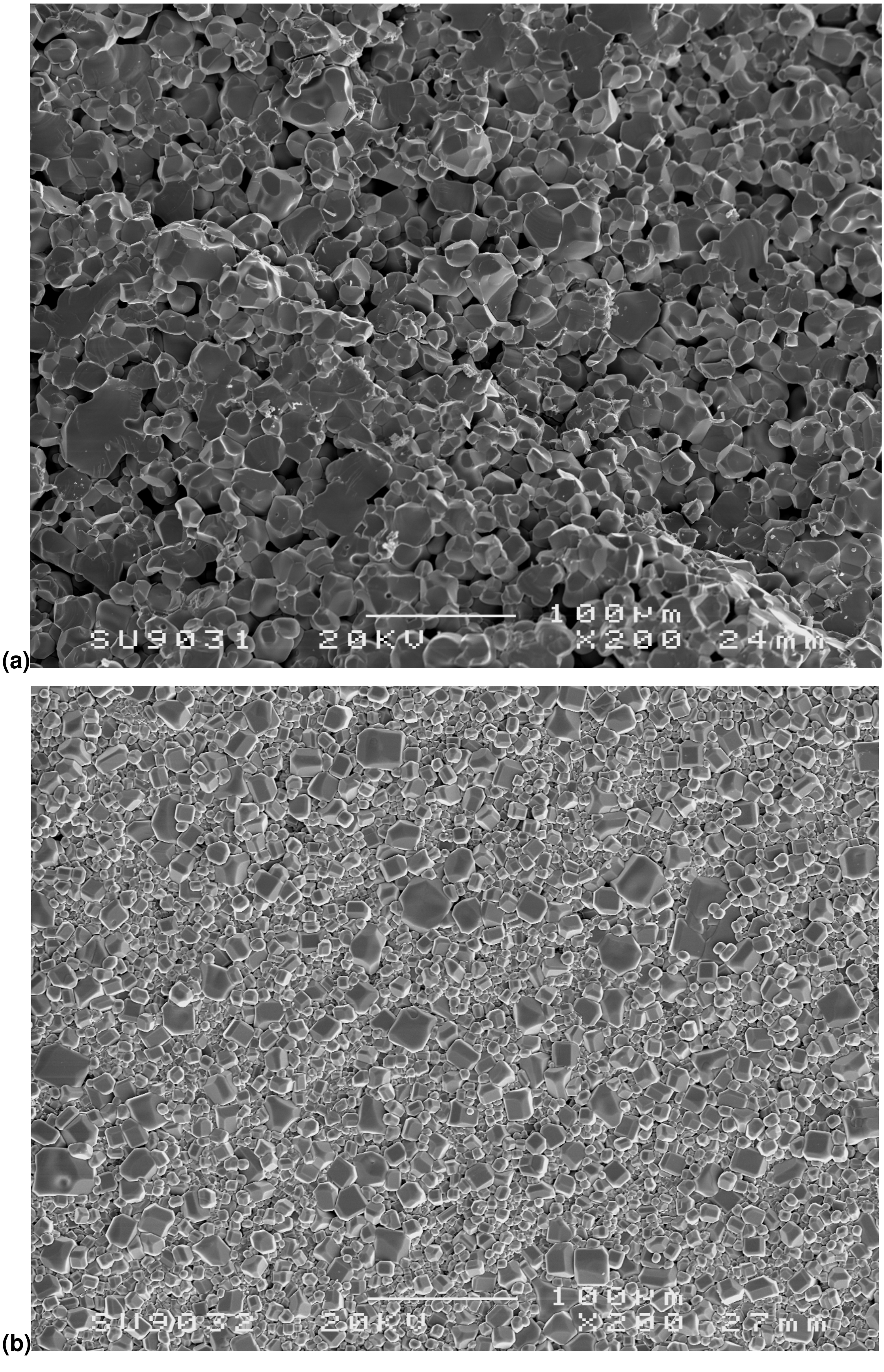

Figure 7.2: SEM images of (a) $Na_{1/2}Bi_{1/2}Cu_3Ti_4O_{12}$ and (b) $CdCu_3Ti_4O_{12}$ sintered pellets.

Figures 7.2 (a) and 7.2 (b) are SEM images of sintered $Na_{1/2}Bi_{1/2}Cu_3Ti_4O_{12}$ and $CdCu_3Ti_4O_{12}$ pellets, respectively. The grain size of the $Na_{1/2}Bi_{1/2}Cu_3Ti_4O_{12}$ sample was ~ 25 – 50 μm and the microstructure appeared to be relatively well sintered. Pellet densities were > 90 % of the calculated theoretical X-ray density. The grain size distribution of the $CdCu_3Ti_4O_{12}$ was bimodal in nature, such that the microstructure comprised of large grains of sizes ~ 25 – 50 μm in a matrix of finer grains of < ~ 5 μm diameter. These samples also appeared to be well sintered with relative densities calculated to be > 90 % of the calculated theoretical X-ray density.

The impedance response of the $Na_{1/2}Bi_{1/2}Cu_3Ti_4O_{12}$ sample at 330 K is shown in the Z^* formalism in Figure 7.3 (a). The low frequency arc centred at ~ 100 Hz corresponds to a parallel RC element where R ~ 850 kΩ.cm and C ~ 1.9 nF/cm (ε' ~ 21,500), according to equation 3.16. At high frequencies, a non-zero intercept was observed as shown in the insert in Figure 7.3 (a) corresponding to an element with f_{max}, associated with time constant, τ, outside the range of the impedance analyser. For this element, however, R was determined from the intercept with the Z' axis as being ~ 80 Ω.cm. C' data for the sample at 330 K are shown in Figure 7.3 (b), featuring a high capacitance plateau at frequencies < 1 MHz corresponding to a capacitance of ~ 1.5 – 2 nF/cm. Above 1 MHz, a dispersion to low capacitance was observed.

According to the barrier layer capacitor model proposed for $CaCu_3Ti_4O_{12}$ in Chapter 4, the low frequency arc in Z^* corresponds to the grain boundary response and the high frequency non-zero intercept corresponds to semiconducting bulk response. By cooling $Na_{1/2}Bi_{1/2}Cu_3Ti_4O_{12}$ ceramics to sub-ambient temperatures, it was possible to resolve an arc in Z^* corresponding to the bulk impedance as shown in Figure 7.4 (a). The bulk resistance, R_b, was hand-fitted to ~ 110 kΩ.cm and the bulk capacitance, C_b, was calculated according to Equation 3.16 and found to be ~ 29 pF/cm (ε' ~ 330). Corresponding C' data are given in Figure 7.4 (b) and reveal a high capacitance plateau at < 100 Hz and a low capacitance plateau at > 100 kHz. The high capacitance plateau corresponds, therefore, to a grain boundary capacitance of ~ 1.8 nF (ε' ~ 20,300) and the low capacitance to a bulk capacitance of ~ 21 pF/cm (ε' ~ 237), in reasonable agreement with values obtained from Z^* plots.

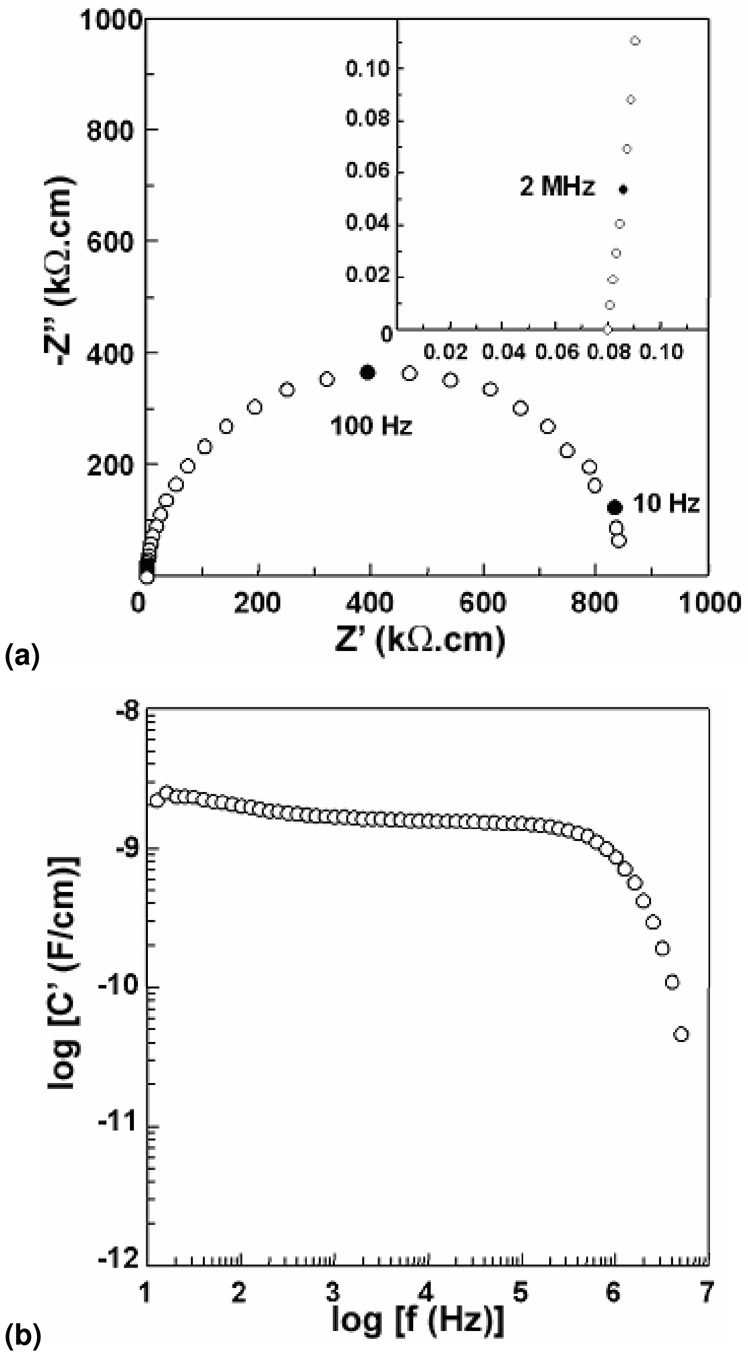

Figure 7.3: Impedance data for $Na_{1/2}Bi_{1/2}Cu_3Ti_4O_{12}$ at 330 K represented in (a) Z^* formalism and (b) a spectroscopic plot of C'.

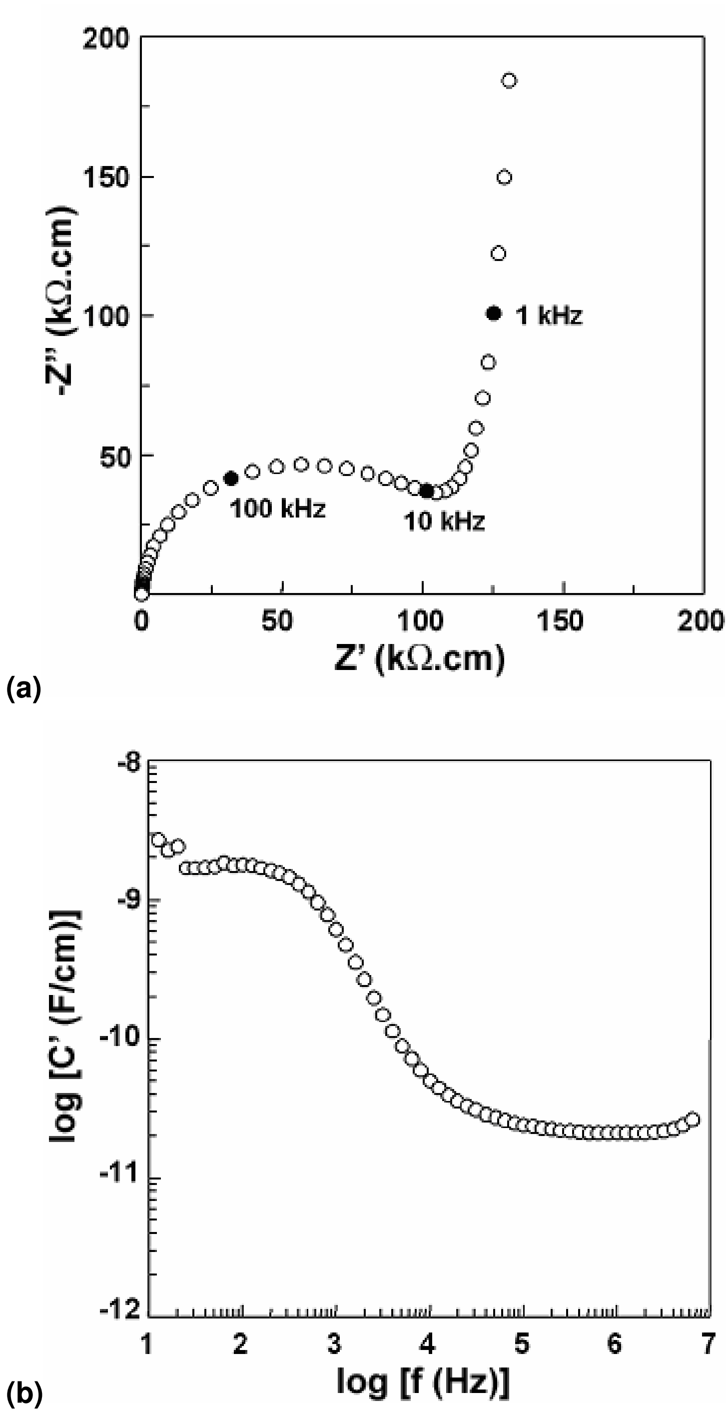

Figure 7.4: Impedance data for $Na_{1/2}Bi_{1/2}Cu_3Ti_4O_{12}$ at 78 K represented in (a) *Z formalism and (b) a spectroscopic plot of *C'*.**

Figures 7.5 and 7.6 represent impedance measurements of the $CdCu_3Ti_4O_{12}$ sample at ~ 380 and 78 K, respectively. The low frequency (< 100 Hz) impedance data in Figure 7.5 were obtained using a Solartron 1260 impedance analyser. The Z* plot in Figure 7.5 (a) features a single arc corresponding to a parallel *RC* element, with *R* ~ 1.6 GΩ.cm and *C* was calculated to be ~ 1.6 nF/cm (ε' ~ 18,000) using Equation 3.16. As observed in $CaCu_3Ti_4O_{12}$ and $Na_{1/2}Bi_{1/2}Cu_3Ti_4O_{12}$ at ambient temperatures, a non-zero intercept at frequencies in the MHz range corresponds to a bulk-like impedance, R_b ~ 60 Ω.cm. *C'* data, Figure 7.5 (b), feature plateau at *C'* ~ 1.7 – 0.6 nF/cm, corresponding to the capacitance of the single arc observed in *Z** with the onset of a dispersion at high frequencies to the bulk plateau. The data obtained using the Solartron do not overlap perfectly with data obtained from the Agilent analyser, suggesting a slight discrepancy in the measuring accuracy of the two systems and/or a difference in the experimental conditions under which the two measurements were made. The magnitude of the observed capacitance suggests that the response originated from a grain-boundary capacitance, although the grain boundary resistance and time constant values are several orders of magnitude greater than was observed in both $Na_{1/2}Bi_{1/2}Cu_3Ti_4O_{12}$ and $CaCu_3Ti_4O_{12}$ samples at equivalent temperatures.

The impedance data collected at 78 K, Figure 6, indicate that the $CdCu_3Ti_4O_{12}$ sample also fit the internal barrier-layer capacitor model. The bulk response was observed as a high frequency arc in *Z**, Figure 7.6 (a), with R_b ~ 250 kΩ.cm and C_b ~ 16 pF/cm (ε' ~ 180). In Figure 7.6 (b), a high capacitance plateau associated with the grain boundary response was observed at < 1 kHz and a low capacitance plateau was observed at > 100 kHz associated with the bulk response.

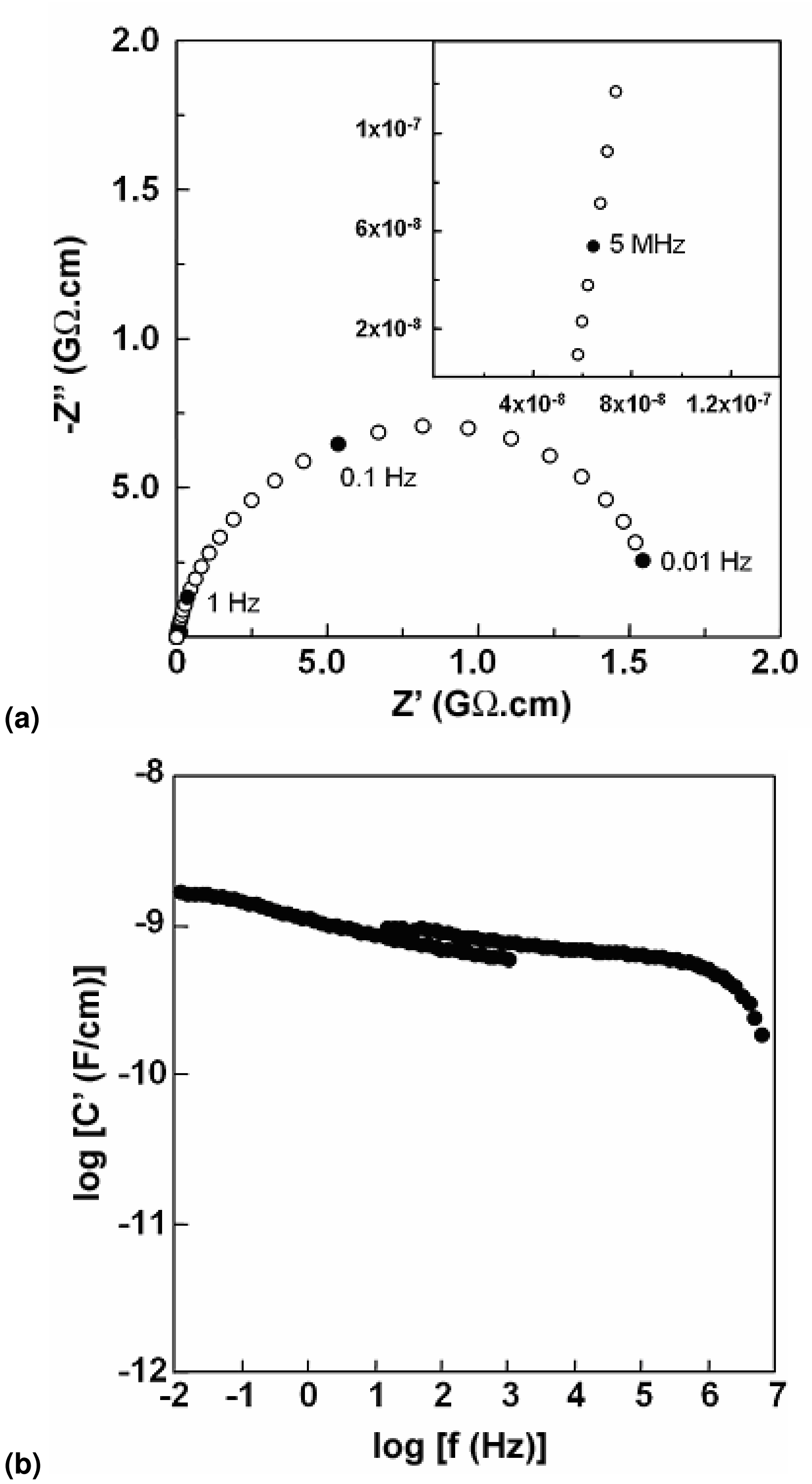

Figure 7.5: Low frequency impedance data for $CdCu_3Ti_4O_{12}$ at 380 K represented in (a) *Z formalism and (b) a spectroscopic plot of *C'*.**

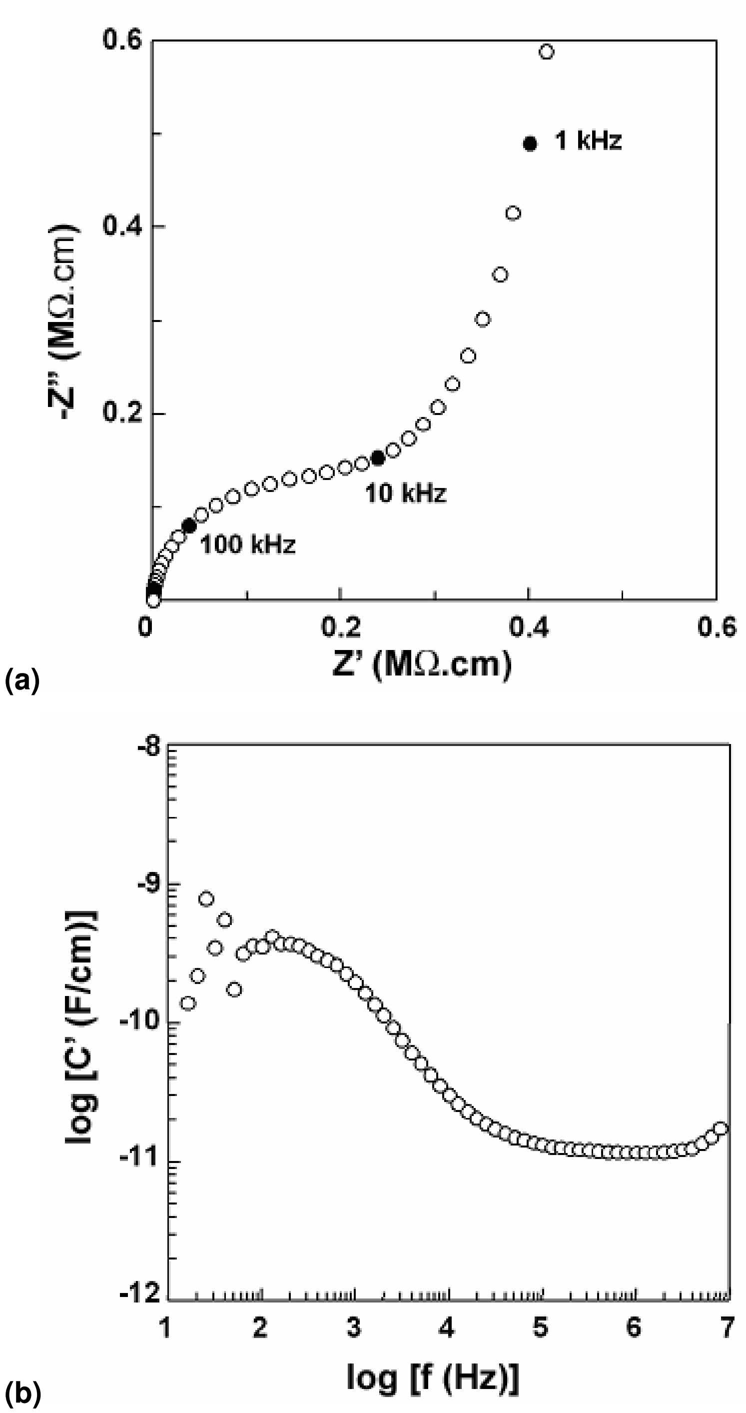

Figure 7.6: Impedance data for $CdCu_3Ti_4O_{12}$ at 78 K represented in (a) *Z formalism and (b) a spectroscopic plot of *C'*.**

Conductivity data for the bulk and grain boundary responses of the $CdCu_3Ti_4O_{12}$ and $Na_{1/2}Bi_{1/2}Cu_3Ti_4O_{12}$ samples are plotted in Figure 7.7. The activation energy of the grain boundary conductivity was determined to be 0.89(2) eV and 0.49(2) eV for $CdCu_3Ti_4O_{12}$ and $Na_{1/2}Bi_{1/2}Cu_3Ti_4O_{12}$, respectively. The grain boundary activation energy for $Na_{1/2}Bi_{1/2}Cu_3Ti_4O_{12}$ is comparable with the values observed for $CaCu_3Ti_4O_{12}$ in previous chapters, whereas the grain boundary activation energy of $CdCu_3Ti_4O_{12}$ is considerably higher. This would indicate that the high grain boundary resistance of $CdCu_3Ti_4O_{12}$ (when compared to that of $CaCu_3Ti_4O_{12}$ and $Na_{1/2}Bi_{1/2}Cu_3Ti_4O_{12}$) was not primarily due to the fine grain size of the $CdCu_3Ti_4O_{12}$ but due to a lower intrinsic conductivity of the grain boundary "phase".

The bulk conductivity of both $Na_{1/2}Bi_{1/2}Cu_3Ti_4O_{12}$ and $CdCu_3Ti_4O_{12}$ appear to fall into 2 regimes of temperature dependence. Above ~ 150 K, the bulk activation energy is 0.08(2) eV for both phases and, below 150 K, it decreases to 0.05(2) eV and 0.06(2) eV for $Na_{1/2}Bi_{1/2}Cu_3Ti_4O_{12}$ and $CdCu_3Ti_4O_{12}$, respectively. Changes in activation energy as a function of temperature may be indicative of structural phase transitions or changes in conduction mechanism; the two possibilities need not be mutually exclusive. It is clear, however, that above 150 K, the bulk conductivity behaviour of both phases was comparable to $CaCu_3Ti_4O_{12}$.

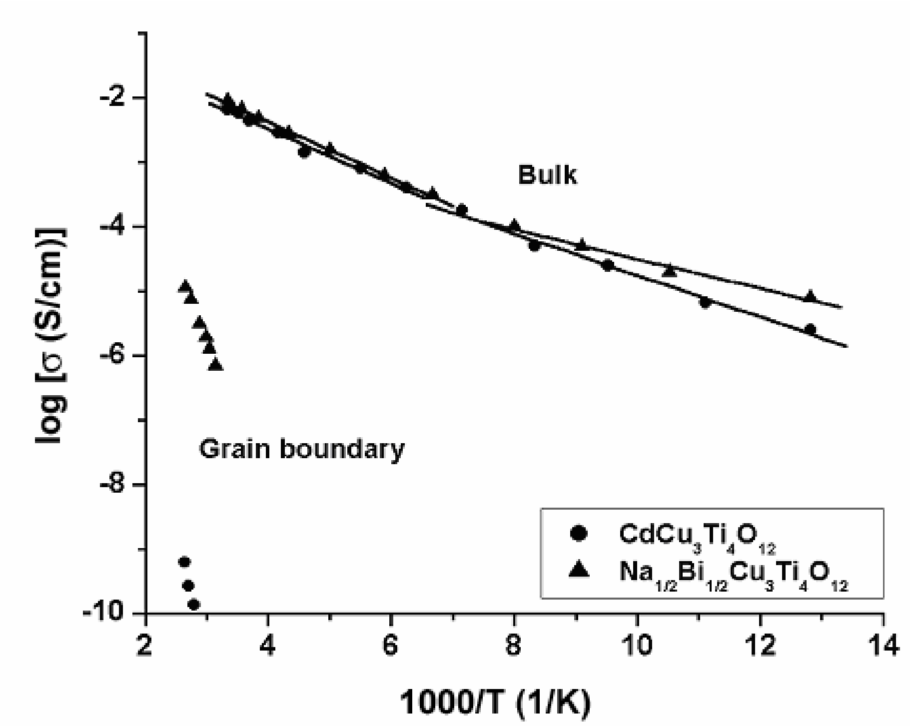

Figure 7.7: Arrhenius plot of bulk and grain boundary conductivity for $CdCu_3Ti_4O_{12}$ and $Na_{1/2}Bi_{1/2}Cu_3Ti_4O_{12}$ samples.

These data (T > 150 K) are summarised in Table 7.2 with predicted *f_{max}* values for the bulk response at room temperature (in each case, *f_{max}* was determined from the relation *ωRC* = 1, the room temperature *R* value and the *C* value measured at < 100

K). This time, the bulk permittivity values have been corrected for the parasitic capacitance of the conductivity jig (1.9 pF/cm, equivalent to an effective permittivity of ~ 20).

Non-ferroelectric phases generally have permittivity values < 100 unless the temperature of the sample is close to that of a phase transition. Having accounted for the jig capacitance, the bulk permittivity of $CdCu_3Ti_4O_{12}$ and $Na_{1/2}Bi_{1/2}Cu_3Ti_4O_{12}$ are significantly higher than expected. One possible explanation for the high bulk permittivity values is the possibility of a phase transition to a ferroelectric mode at sub-ambient temperatures.

	Permittivity*		**Activation Energy / eV**		**Bulk f_{max} / Hz**
Sample	**Bulk**	**Grain Boundary****	**Bulk**	**Grain Boundary**	**(predicted RT)**
$CaCu_3Ti_4O_{12}$	82	10k – 300k	0.06	0.60	285G
$CdCu_3Ti_4O_{12}$	160	21.5k	0.08	0.89	69G
$Na_{1/2}Bi_{1/2}Cu_3Ti_4O_{12}$	310	32.3k	0.08	0.49	62G

* as derived from Z*

** refers to *apparent* permittivity

Table 7.2: Summary of electrical property data of $CaCu_3Ti_4O_{12}$, $CdCu_3Ti_4O_{12}$ and $Na_{1/2}Bi_{1/2}Cu_3Ti_4O_{12}$.

From the predicted room temperature f_{max} values, it was apparent that the bulk permittivity cannot be measured below 1 MHz, since f_{max} is of the order of 10^{10} Hz for $CdCu_3Ti_4O_{12}$ and $Na_{1/2}Bi_{1/2}Cu_3Ti_4O_{12}$. The permittivity value of 2,454 reported by Subramanian for $Na_{1/2}Bi_{1/2}Cu_3Ti_4O_{12}$ is clearly attributable, therefore, to a grain boundary capacitance. However, Subramanian [1] also reported a permittivity of 409 for $CdCu_3Ti_4O_{12}$ and this value is comparable in terms of magnitude for the observed bulk permittivity of 180 shown in Table 7.2. At present, this result cannot be explained but may be related to a different ceramic microstructure (*e.g.* lower pellet density) or different bulk/grain boundary composition for the samples prepared in this study compared to that of Subramanian.

7.4. Conclusions

It has been shown that the IBLC-like electrical properties of $CaCu_3Ti_4O_{12}$ were also observed in two isostructural phases: $CdCu_3Ti_4O_{12}$ and $Na_{1/2}Bi_{1/2}Cu_3Ti_4O_{12}$ (diffraction data did not facilitate understanding of the degree of ordering between Na and Bi in this phase). Although the observed grain boundary capacitances were both equivalent to

$CaCu_3Ti_4O_{12}$ in terms of order of magnitude, the grain boundary resistance of $CdCu_3Ti_4O_{12}$ was significantly greater and had a a higher activation energy. At room temperature, the bulk resistance of $CdCu_3Ti_4O_{12}$ and $Na_{1/2}Bi_{1/2}Cu_3Ti_4O_{12}$ could be estimated from the non-zero intercept in Z^* and was also found to be equivalent to that of $CaCu_3Ti_4O_{12}$. Low temperature conductivity data revealed a non-linearity in the temperature dependence of the bulk conductivity in both $CdCu_3Ti_4O_{12}$ and $Na_{1/2}Bi_{1/2}Cu_3Ti_4O_{12}$, with a change in activation energy at ~ 140 – 150 K, the origin of which is unknown. It is suggested that reports of high permittivity in phases investigated by Subramanian [1] were in fact attributable to a grain boundary capacitance. Only phases reported as having low permittivity may be regarded as being representative of the bulk response. However, the origin of the bulk permittivity and the composition of the grain boundary phase(s) still need to be established.

References

1. M.A. Subramanian, D. Li, N. Duan, B.A. Reisner, A.W. Sleight, Journal of Solid State Chemistry, 2000, **151**, 323
2. M.A. Subramanian, A.W. Sleight, "$ACu_3Ti_4O_{12}$ and $ACu_3Ru_4O_{12}$ perovskites: high dielectric constants and valence degeneracy." Solid State Sciences, 2002, **4**, 347-351
3. C. Kittel, *Introduction to Solid State Physics*. 7th ed. 1996: Wiley.
4. R.D. Shannon, "Dielectric polarizabilities of ions in oxides and fluorides." Journal of Applied Physics, 1993, **73**(1), 348-366
5. R.D. Shannon, "Revised Effective Ionic Radii and System Studies of Interatomic Distances in Halides and Chalcogenides." Acta Crystallographica A, 1976, **32**, 751-767
6. S.M. Moussa, B.J. Kennedy, "Structural studies of the distorted perovskite $Ca_{0.25}Cu_{0.73}TiO_3$." Materials Research Bulletin, 2001, **36**, 2525-2529

8. Conclusions & Further Work

8.1. Conclusions

The electrical properties of $CaCu_3Ti_4O_{12}$ ceramics were investigated using impedance spectroscopy in order to determine the origin of the high permittivity discussed in Chapter 1. It was found that the high permittivity was not an intrinsic property of $CaCu_3Ti_4O_{12}$ but in fact arose from the capacitance of the grain boundaries in the sample. $CaCu_3Ti_4O_{12}$ samples were found to have an electrical microstructure of low permittivity, semiconducting grains surrounded by thin and insulating grain boundaries. Based on the brick–layer (BL) model, the response could be approximated to an equivalent circuit of 2 parallel resistor-capacitor (*RC*) elements connected in series. Each *RC* element represents the impedance of the bulk and grain boundary regions, respectively. Since the grain boundaries are considerably thinner than the grains, the capacitance of these regions is much greater; this "effective permittivity" is controlled mainly by the geometry of the grain boundaries (*i.e.* grain size and grain boundary thickness).

By varying the sintering time, it was possible to produce pellets with various grain size distributions. This allowed the electrical properties to be correlated with the microstructure. For sintering times < 5 h, grain sizes of ~ 1 – 5 μm were observed and the effective permittivity values of these samples were of the order of $10^3 – 10^4$. For sintering times > 8 h, abnormal grain growth occurred such that the grain size became bimodal with grain sizes of 1 – 10 μm and 50 - 300 μm. Effective permittivity values in excess of 10^5 were observed in these samples. The impedance (corrected for sample geometry) of the fine grained samples was independent of sample thickness whereas the impedance of the coarse grained samples exhibited a non-linear dependence on sample thickness. In part, this was due to a rapid decrease in the number of active grain boundaries between the electrodes when the sample thickness became comparable to the grain size, but also because these samples, having a bimodal grain size distribution, violated the brick layer model.

Impedance measurements of coarse-grained $CaCu_3Ti_4O_{12}$ ceramics where also performed with a *dc* bias, such that an electric field was applied across the sample during the measurement. The grain boundary resistance decreased exponentially with increasing *dc* bias. This behaviour is consistent with a back-to-back double Schottky barrier system existing at the grain-grain interfaces, in which the voltage drop across each grain boundary arising from the *dc* bias lowers the potential barrier height for conduction through the grain boundary. The grain boundary capacitance was found to decrease with increasing *dc* bias and a linear relationship between $[1/C_{gb} - 1/2C_0]^2$ and V_{app} (where C_{gb} and C_0 are the grain boundary capacitance under *dc* bias and without dc bias, respectively, in $\mathrm{Fcm^{-2}}$) was observed. From this relationship, the barrier height was determined to be ~ 0.77 eV. Fine grained $CaCu_3Ti_4O_{12}$ ceramics exhibited no such behaviour at *dc* bias < 15 V since the voltage drop across each grain boundary was significantly less than in the coarse-grained samples.

Thermo-gravimetric analysis of $CaCu_3Ti_4O_{12}$ powders revealed that, in 5 % H_2 – 95 % Ar atmospheres, decomposition occurs at temperatures > ~ 350 °C. After cycling to 800 °C, the phase decomposed to $CaTiO_3$, TiO_2 and Cu. This was in marked contrast to other perovskite-structured phases, such as $CaTiO_3$, that remain stable (or become slightly oxygen-deficient) under similar conditions. Limited decomposition was also observed in samples sintered in air, although the decomposition products ($CaTiSiO_5$, TiO_2 and Cu_2O) were found to occur in isolated 'islands' within the $CaCu_3Ti_4O_{12}$ matrix. Samples were annealed in N_2 and measured by impedance spectroscopy. The grain boundary resistance was decreased by several orders of magnitude after annealing at 1000 °C in N_2, and could be restored to its as-sintered state by subsequent annealing at 1000 °C in O_2. This behaviour was commensurate with an *n*-type conduction mechanism in the grain boundary phase, in which oxygen loss results in injection of electrons into the conduction band, increasing the conductivity. Annealing at 1000 °C in N_2 also resulted in the formation of "decomposition zones" at the pellet surfaces surrounding the bulk material.

Two phases isostructural with $CaCu_3Ti_4O_{12}$ were synthesised: $CdCu_3Ti_4O_{12}$ and $Na_{1/2}Bi_{1/2}Cu_3Ti_4O_{12}$. Ceramic samples of both phases exhibited similar electrical properties to $CaCu_3Ti_4O_{12}$ and could also be approximated on an internal barrier layer capacitor-type model in which the observed high permittivity in fact arises from a grain boundary capacitance. This would suggest that these phases share a common conductivity mechanism that has yet to be fully understood.

8.2. Further Work

Since electrically heterogeneous ceramics find widespread application in electronic devices (see Chapter 1), $CaCu_3Ti_4O_{12}$ and structural analogous may have many commercial applications. A great deal of further investigation must be carried out, however, in order to fully understand and control their properties. Such work may include:

High resolution TEM and chemical analysis (EELS) to characterise the grain-grain interfaces in $CaCu_3Ti_4O_{12}$ ceramics

Synthesis and characterisation of doped-$CaCu_3Ti_4O_{12}$ and solid solutions between $CaCu_3Ti_4O_{12}$ and analogous phases

Further annealing/doping studies to isolate the bulk conductivity mechanism

Electronic and magnetic property measurements at temperatures < 80 K

Detailed analysis of impedance data (< 80 K) to establish an equivalent circuit model for the bulk response and then to analyse data at > 80 K to 'build-up' the equivalent circuit to include the grain boundary response

Further work is also required to establish the origin of the high permittivity reported for $Na_{1/2}Bi_{1/2}Cu_3Ti_4O_{12}$

Appendix

A1. Derivation of *Z**, *M**, *Y**, *ε** and tan *δ* for 2 Parallel *RC* Elements in Series

RC elements connected in series, so find *Z** by addition of Z^*_1 and Z^*_2:

$$Z^* = \frac{R_1}{(\omega R_1 C_1)^2 + 1} + \frac{R_2}{(\omega R_2 C_2)^2 + 1} - j\left(R_1 \frac{\omega R_1 C_1}{(\omega R_1 C_1)^2 + 1} + R_2 \frac{\omega R_2 C_2}{(\omega R_2 C_2)^2 + 1} \right) \tag{A1.1}$$

Then derive electric modulus by combining Equations 3.3 and A2.1:

$$M^* = j\omega C_0 \left[\frac{R_1}{(\omega R_1 C_1)^2 + 1} + \frac{R_2}{(\omega R_2 C_2)^2 + 1} - j\left(R_1 \frac{\omega R_1 C_1}{(\omega R_1 C_1)^2 + 1} + R_2 \frac{\omega R_2 C_2}{(\omega R_2 C_2)^2 + 1} \right) \right] \tag{A1.2.1}$$

$$= \omega C_0 \left[R_1 \frac{\omega R_1 C_1}{(\omega R_1 C_1)^2 + 1} + R_2 \frac{\omega R_2 C_2}{(\omega R_2 C_2)^2 + 1} \right] + jC_0 \left[\left(\frac{1}{C_1} \right) \frac{\omega R_1 C_1}{(\omega R_1 C_1)^2 + 1} + \left(\frac{1}{C_2} \right) \frac{\omega R_2 C_2}{(\omega R_2 C_2)^2 + 1} + \right] \tag{A1.2.2}$$

Since $Y^* = Z^{*-1}$, it can be written:

$$Y^* = (Z_1^* + Z_1^*)^{-1} = \left(\frac{1}{Y_1^*} + \frac{1}{Y_2^*} \right)^{-1} = \frac{Y_1^* Y_2^*}{Y_1^* + Y_2^*} \tag{A1.3.1}$$

And so admittance can be derived from equations A1.3.1 and 3.24.1:

$$\mathrm{Y}^* = \frac{\left(\frac{1}{R_1} + j\omega C_1 \right)\left(\frac{1}{R_2} + j\omega C_2 \right)}{\left(\frac{1}{R_1} + \frac{1}{R_2} \right) + j\omega (C_1 + C_2)} \times \frac{\left(\frac{1}{R_1} + \frac{1}{R_2} \right) - j\omega (C_1 + C_2)}{\left(\frac{1}{R_1} + \frac{1}{R_2} \right) - j\omega (C_1 + C_2)} \tag{A1.3.2}$$

$$= \frac{\left(\frac{1}{R_1} + j\omega C_1\right)\left(\frac{1}{R_2} + j\omega C_2\right)\left[\left(\frac{1}{R_1} + \frac{1}{R_2}\right) - j\omega(C_1 + C_2)\right]}{\left(\frac{1}{R_1} + \frac{1}{R_2}\right)^2 + \omega^2 (C_1 + C_2)^2} \qquad \text{(A1.3.3)}$$

$$\begin{aligned} = \Bigg[& \frac{1}{R_1 R_2}\left(\frac{1}{R_1} + \frac{1}{R_2}\right) + j\omega\left(\frac{C_2}{R_1} + \frac{C_1}{R_2}\right)\left(\frac{1}{R_1} + \frac{1}{R_2}\right) - \omega^2 C_1 C_2 \left(\frac{1}{R_1} + \frac{1}{R_2}\right) \\ & - \frac{j\omega}{R_1 R_2}(C_1 + C_2) + \omega^2 (C_1 + C_2)\left(\frac{C_2}{R_1} + \frac{C_1}{R_2}\right) + j\omega^3 C_1 C_2 (C_1 + C_2) \Bigg] \\ & \div \left[\left(\frac{1}{R_1} + \frac{1}{R_2}\right)^2 + \omega^2 (C_1 + C_2)^2\right] \end{aligned} \qquad \text{(A1.3.4)}$$

Let $Y' = \dfrac{\frac{1}{R_1 R_2}\left(\frac{1}{R_1} + \frac{1}{R_2}\right) + \omega^2 C_1 C_2 \left(\frac{1}{R_1} + \frac{1}{R_2}\right) + \omega^2 (C_1 + C_2)\left(\frac{C_2}{R_1} + \frac{C_1}{R_2}\right)}{\left(\frac{1}{R_1} + \frac{1}{R_2}\right)^2 + \omega^2 (C_1 + C_2)^2}$ (A1.3.5)

Let $jY'' = \dfrac{j\omega\left(\frac{C_2}{R_1} + \frac{C_1}{R_2}\right)\left(\frac{1}{R_1} + \frac{1}{R_2}\right) - \frac{j\omega}{R_1 R_2}(C_1 + C_2) + j\omega^3 C_1 C_2 (C_1 + C_2)}{\left(\frac{1}{R_1} + \frac{1}{R_2}\right)^2 + \omega^2 (C_1 + C_2)^2}$ (A1.3.6)

Permittivity is then be derived by combining Equations A1.3.2 and 3.2:

$$\varepsilon^* = \frac{\left(\frac{1}{R_1} + j\omega C_1\right)\left(\frac{1}{R_2} + j\omega C_2\right)}{\left(\frac{1}{R_2} + \frac{1}{R_1}\right) + j\omega(C_1 + C_2)} \times \frac{-j\omega C_0\left(\frac{1}{R_2} + \frac{1}{R_1}\right) - j\omega^2 C_0 (C_1 + C_2)}{-j\omega C_0\left(\frac{1}{R_2} + \frac{1}{R_1}\right) - j\omega^2 C_0 (C_1 + C_2)} \qquad \text{(A1.4.1)}$$

$$\begin{aligned}=&\left[-\omega^2 C_0(C_1+C_2)\left(\frac{1}{R_1}+j\omega C_1\right)\left(\frac{1}{R_2}+j\omega C_2\right)\right.\\&\left.\quad -j\omega C_0\left(\frac{1}{R_1}+\frac{1}{R_2}\right)\left(\frac{1}{R_2}+j\omega C_1\right)\left(\frac{1}{R_1}+j\omega C_2\right)\right]\\&\qquad\div\left[\omega^2 {C_0}^2\left(\frac{1}{R_1}+\frac{1}{R_2}\right)^2+\omega^4 {C_0}^2(C_1+C_2)^2\right]\end{aligned}\tag{A1.4.2}$$

$$\begin{aligned}=&\left[-\omega^2 C_0(C_1+C_2)\left(\frac{1}{R_1R_2}+\frac{j\omega C_2}{R_1}+\frac{j\omega C_1}{R_2}-\omega^2 C_1C_2\right)\right.\\&\left.\quad -j\omega C_0\left(\frac{1}{R_1}+\frac{1}{R_2}\right)\left(\frac{1}{R_1R_2}+\frac{j\omega C_2}{R_1}+\frac{j\omega C_1}{R_2}-\omega^2 C_1C_2\right)\right]\\&\qquad\div\left[\omega^2 {C_0}^2\left(\frac{1}{R_1}+\frac{1}{R_2}\right)^2+\omega^4 {C_0}^2(C_1+C_2)^2\right]\end{aligned}\tag{A1.4.3}$$

Let $\varepsilon'=$

$$\begin{aligned}&\left[-\omega^2 C_0(C_1+C_2)\left(\frac{1}{R_1R_2}\right)+\omega^4 C_1C_2C_0(C_1+C_2)\right.\\&\left.\quad +\omega C_0\left(\frac{1}{R_1}+\frac{1}{R_2}\right)\left(\frac{\omega C_2}{R_1}+\frac{\omega C_1}{R_2}\right)\right]\\&\qquad\div\left[\omega^2 {C_0}^2\left(\frac{1}{R_1}+\frac{1}{R_2}\right)^2+\omega^4 {C_0}^2(C_1+C_2)^2\right]\end{aligned}\tag{A1.4.4}$$

$$=\frac{-\left(\frac{C_1+C_2}{R_1R_2}\right)+\omega^2 C_1C_2(C_1+C_2)+\left(\frac{1}{R_1}+\frac{1}{R_2}\right)\left(\frac{C_2}{R_1}+\frac{C_1}{R_2}\right)}{C_0\left(\frac{1}{R_1}+\frac{1}{R_2}\right)^2+\omega^2 C_0(C_1+C_2)^2}\tag{A1.4.5}$$

Let $j\varepsilon''=$

$$\begin{aligned}&\left[j\omega^2 C_0(C_1+C_2)\left(\frac{\omega C_2}{R_1}+\frac{\omega C_1}{R_2}\right)\right.\\&\left.\quad -j\omega C_0\left(\frac{1}{R_1}+\frac{1}{R_2}\right)\left(\frac{1}{R_1R_2}-\omega^2 C_1C_2\right)\right]\\&\qquad\div\left[\omega^2 {C_0}^2\left(\frac{1}{R_1}+\frac{1}{R_2}\right)^2+\omega^4 {C_0}^2(C_1+C_2)^2\right]\end{aligned}\tag{A1.4.6}$$

$$= \frac{-j(C_1+C_2)\left(\frac{\omega C_2}{R_1}+\frac{\omega C_1}{R_2}\right)-\frac{j}{\omega}\left(\frac{1}{R_2}+\frac{1}{R_2}\right)\left(\frac{1}{R_1R_2}\right)+j\omega C_1C_2\left(\frac{1}{R_1}+\frac{1}{R_2}\right)}{C_0\left(\frac{1}{R_1}+\frac{1}{R_2}\right)^2+\omega^2C_0(C_1+C_2)^2} \qquad \text{(A1.4.7)}$$

tan δ is therefore deduced by re-writing Equations A1.4.5 and A1.4.7:

$$\varepsilon' = \frac{1}{\omega}\times\frac{R_1+R_2}{(R_1R_2)^2}+\omega\left(\frac{C_1{}^2}{R_2}+\frac{C_2{}^2}{R_1}\right) \qquad \text{(A1.5.1)}$$

$$\varepsilon'' = \frac{C_1}{R_2{}^2}+\frac{C_2}{R_1{}^2}+\omega^2C_1C_2(C_1+C_2) \qquad \text{(A1.5.2)}$$

and deriving tan δ according to Equation 3.4:

$$\tan\delta = \frac{\frac{1}{\omega}\times\frac{R_1+R_2}{(R_1R_2)^2}+\omega\left(\frac{C_1{}^2}{R_2}+\frac{C_2{}^2}{R_1}\right)}{\frac{C_1}{R_2{}^2}+\frac{C_2}{R_1{}^2}+\omega^2C_1C_2(C_1+C_2)} \qquad \text{(A1.5.3)}$$

Multiply both sides by $\omega(R_1R_2)^2$

$$= \frac{R_2+R_1+\omega^2C_1{}^2R_1{}^2R_2+\omega^2C_2{}^2R_1R_2{}^2}{\omega C_1R_1{}^2+\omega C_2R_2{}^2+\omega^3C_1{}^2C_2R_1{}^2R_2{}^2+\omega^3C_1C_2{}^2R_1{}^2R_2{}^2} \qquad \text{(A1.5.4)}$$

$$= \frac{R_1+R_2+R_1(\omega R_1C_1)^2+R_2(\omega R_2C_2)^2}{\omega R_1{}^2C_1+\omega R_2{}^2C_2+\omega R_2{}^2C_2(\omega R_1C_1)^2+\omega R_1{}^2C_1(\omega R_2C_2)^2} \qquad \text{(A1.5.5)}$$

A2. Frequency Dependence of *Z**, *M**, *Y**, *ε** and tan *δ* for 2 Parallel *RC* Elements in Series

Inspection of the expressions derived for *Z*' and *M*' (equations A1.1 and A1.2.2, respectively) reveals two Debye functions corresponding to the frequency of maximum loss of each parallel *RC* element in the circuit, $\omega_{max(1)}$ and $\omega_{max(2)}$. If it is assumed that $R_2 >> R_1$ and $C_2 >> C_1$, then $\tau_2 >> \tau_1$ and so $\omega_{max(2)} << \omega_{max(1)}$. In other words, as frequency increases from 0 and tends to ∞, the observed low frequency peak corresponds to $\omega_{max(2)}$ and the high frequency peak corresponds to $\omega_{max(1)}$, for both *Z*' and *M*'. It can also be seen that the magnitudes of *Z*' at $\omega_{max(1)}$ and $\omega_{max(2)}$ correspond to $R_1/2$ and $R_2/2$, respectively. Similarly, the magnitudes of *M*' at $\omega_{max(1)}$ and $\omega_{max(2)}$ correspond to $C_0/2C_1$ and $C_0/2C_2$, respectively. Further analysis proves that, in *Z*', the positive inflexion between $\omega_{max(1)}$ and $\omega_{max(2)}$ corresponds to ω_d while the positive inflexion in *M*' between $\omega_{max(1)}$ and $\omega_{max(2)"}$ corresponds to ω_b:

For *Z*', the positive inflexion occurs when the $\omega R_1{}^2C_1$ term becomes dominant, *i.e.*:

$$\frac{\omega R_2{}^2C_2}{(\omega R_2{}^2C_2)^2+1}=\omega R_1{}^2C_1 \qquad \text{(A2.1.1)}$$

$$\frac{1}{\omega C_2}=\omega R_1{}^2C_1 \qquad \text{(A2.1.2)}$$

$$\omega^2=\frac{1}{R_1{}^2C_1C_2} \qquad \text{(A2.1.3)}$$

$$\therefore \omega=\frac{1}{R_1(C_1C_2)^{\frac{1}{2}}}=\omega_d \qquad \text{(A2.1.4)}$$

Similarly for *M*', the positive inflexion occurs when:

$$\omega R_1=\frac{\omega R_2}{(\omega R_2C_2)^2+1} \qquad \text{(A2.2.1)}$$

$$R_1=\frac{1}{\omega^2R_2C_2{}^2} \qquad \text{(A2.2.2)}$$

$$\omega^2 = \frac{1}{C_2{}^2 R_1 R_2} \tag{A2.2.3}$$

$$\therefore \omega = \frac{1}{C_2 (R_1 R_2)^{1/2}} = \omega_b \tag{A2.2.4}$$

The Debye peak in both Y'' and ε'' corresponding to the parasitic series circuit was discussed previously. Further confirmation of their association with the parasitic circuit is given by determining the magnitude of Y'' and ε'' at ω_C. Y'' at ω_c can be rewritten since, at this frequency, the second and third terms in the numerator cancel and, as mentioned earlier, the denominator terms are equal:

$$Y'' = \frac{\omega_C \left(\frac{C_2}{R_1} + \frac{C_1}{R_2}\right)\left(\frac{1}{R_1} + \frac{1}{R_2}\right)}{2\left(\frac{1}{R_1} + \frac{1}{R_2}\right)^2} = \frac{\frac{1}{R_1 C_2}\left(\frac{C_2}{R_1} + \frac{C_1}{R_2}\right)}{2\left(\frac{1}{R_1} + \frac{1}{R_2}\right)} = \frac{1/R_1{}^2 + 1/R_1 R_2 C_2}{2/R_1 + 2/R_2} \tag{A2.3.1}$$

$$\therefore Y'' \sim \frac{1/R_1{}^2}{\frac{2}{R_1} + \frac{2}{R_2}} = \frac{1}{\frac{2R_1{}^2}{R_1} + \frac{2R_1{}^2}{R_2}} = \frac{1}{2R_1 + \frac{2R_1{}^2}{R_2}} \sim \frac{1}{2R_1} \tag{A2.3.2}$$

Similarly, ε'' at ω_c can be rewritten:

$$\varepsilon'' = \frac{(C_1 + C_2)\left(\frac{\omega_c C_2}{R_1} + \frac{\omega_c C_1}{R_2}\right)}{2\omega_c{}^2 C_0 (C_1 + C_2)^2} \tag{A2.4.1}$$

$$\therefore \varepsilon'' = \frac{\frac{C_1 C_2}{R_1} + \frac{C_1{}^2}{R_2} + \frac{C_2{}^2}{R_1} + \frac{C_1 C_2}{R_2}}{2\omega_c C_0 (C_1 + C_2)^2} \sim \frac{\frac{C_1 C_2}{R_1} + \frac{C_2{}^2}{R_1}}{2\omega_c C_0 (C_1 + C_2)^2} \tag{A2.4.2}$$

$$= \frac{C_1 C_2 + C_2{}^2}{2R_1 \omega_c C_0 (C_1 + C_2)^2} = \frac{C_1 C_2 + C_2{}^2}{\frac{2C_0 (C_1 + C_2)^2}{C_2}} = \frac{C_2 (C_1 C_2 + C_2{}^2)}{2C_0 (C_1 + C_2)^2} \sim \frac{C_2}{2C_0} \tag{A2.4.3}$$

As frequency increases from ω_c to ∞, *Y*’ initially decreases before a positive inflection to ∞. The frequency of this inflection corresponds to ω_d, as shown:

Analysis reveals the positive inflection to occur when the 1st and third terms in the numerator of *Y*’ are equal, i.e.:

$$\omega\left(\frac{C_2}{R_1}+\frac{C_1}{R_2}\right)\left(\frac{1}{R_1}+\frac{1}{R_2}\right)=\omega^3 C_1 C_2 (C_1+C_2) \qquad \text{(A2.5.1)}$$

$$\omega^2=\frac{1}{R_1}\left(\frac{C_2}{R_1}+\frac{C_1}{R_2}\right)+\frac{1}{R_2}\left(\frac{C_1}{R_2}+\frac{C_2}{R_1}\right) \qquad \text{(A2.5.2)}$$

$$=\frac{\dfrac{C_2}{R_1}+\dfrac{C_1}{R_2}}{R_1 C_1 C_2 (C_1+C_2)}+\frac{\dfrac{C_2}{R_1}+\dfrac{C_1}{R_2}}{R_2 C_1 C_2 (C_1+C_2)} \qquad \text{(A2.5.3)}$$

$$\sim\frac{\dfrac{C_2}{R_1}+\dfrac{C_1}{R_2}}{R_1 C_1 C_2 (C_1+C_2)} \qquad \text{(A2.5.4)}$$

$$=\frac{1}{R_1{}^2 C_1 (C_1+C_2)}+\frac{C_1}{R_1 R_2 C_1 C_2 (C_1+C_2)} \qquad \text{(A2.5.5)}$$

$$\sim\frac{1}{R_1{}^2 C_1 (C_1+C_2)} \qquad \text{(A2.5.6)}$$

$$=\frac{1}{R_1{}^2 C_1{}^2+R_1{}^2 C_1 C_2}\sim\frac{1}{R_1{}^2 C_1 C_2} \qquad \text{(A2.5.7)}$$

$$\therefore \omega=\frac{1}{R_1 (C_1 C_2)^{1/2}}=\omega_d \qquad \text{(A2.5.8)}$$

Below ω_c, *Y*’ tends to 0 as frequency tends to 0. Conversely, ε’ tends to 0 when frequency increases from ω_c to ∞. As frequency tends to 0 from ω_c, ε’ initially decreases before a positive inflection to ∞. The frequency of the inflection corresponds to ω_b, as shown:

Analysis shows that the first and second terms of the numerator are equal at the point of inflection, i.e.:

$$(C_1 + C_2)\left(\frac{\omega C_2}{R_1} + \frac{\omega C_1}{R_2}\right) = \frac{1}{\omega}\left(\frac{1}{R_1} + \frac{1}{R_2}\right)\left(\frac{1}{R_1 R_2}\right) \tag{A2.6.1}$$

$$(C_1 + C_2)(\omega C_2 R_2 + \omega C_1 R_2) = \frac{1}{\omega}\left(\frac{1}{R_1} + \frac{1}{R_2}\right) \tag{A2.6.2}$$

$$C_1 C_2 R_1 R_2^{\,2} + C_1^{\,2} R_1^{\,2} R_2 + C_2^{\,2} R_2^{\,2} R_1 + C_1 C_2 R_1^{\,2} R_2 = \frac{1}{\omega^2}(R_1 + R_2) \tag{A2.6.3}$$

$$C_1 C_2 R_1 R_2^{\,2} + C_2^{\,2} R_2^{\,2} R_1 \sim \frac{1}{\omega^2}(R_1 + R_2) \tag{A2.6.4}$$

$$\omega^2 = \frac{R_1 + R_2}{C_1 C_2 R_1 R_2^{\,2} + C_2^{\,2} R_2^{\,2} R_1} \tag{A2.6.5}$$

$$\sim \frac{1}{C_1 C_2 R_1 R_2 + C_2^{\,2} R_2 R_1} = \frac{1}{R_1 R_2 (C_2^{\,2} + C_1 C_2)} \tag{A2.6.6}$$

$$\sim \frac{1}{R_1 R_2 C_2^{\,2}} \tag{A2.6.7}$$

$$\therefore \omega = \frac{1}{C_2 (R_1 R_2)^{1/2}} = \omega_b \tag{A2.6.8}$$

Having defined the characteristic frequencies in a circuit of 2 parallel *RC* elements connected in series, the frequency dependence of the real terms are considered. At *dc*, the magnitude of Z' is $R_1 + R_2$, and remains constant until ω approaches $\omega_{max(2)}$. At intermediate frequencies between $\omega_{max(2)}$ and $\omega_{max(1)}$, Z' can be written as follows:

$$Z' \sim R_1 + \frac{R_2}{(\omega R_2 C_2)^2} \tag{A2.7}$$

since $(\omega R_1 C_1)^2 << 1$ and $(\omega R_2 C_2)^2 >> 1$. R_1 is also dominant over the $R_2/(\omega R_2 C_2)^2$, hence a plateau corresponding to R_1 may be observed in a plot of Z' vs ω, provided $\omega_{max(1)}$ and $\omega_{max(2)}$ are sufficiently resolved. As ω increases from $\omega_{max(1)}$ to ∞, Z' tends to 0.

As ω increases from *dc* to intermediate frequencies between $\omega_{max(1)}$ and $\omega_{max(2)}$, M' increases from 0 to C_0/C_2 since, below $\omega_{max(1)}$, M' can be written:

$$M' \sim \frac{(\omega R_2)^2 C_2 C_0}{(\omega R_2 C_2)^2} \sim \frac{C_0}{C_2} \qquad \text{(A2.8.1)}$$

Above $\omega_{max(2)}$ and tending to ∞, M' can be written:

$$M' = \frac{(\omega R_1)^2 C_1 C_0}{(\omega R_1 C_1)^2} + \frac{(\omega R_2)^2 C_2 C_0}{(\omega R_2 C_2)^2} \qquad \text{(A2.8.2)}$$

and so a high frequency plateau is observed corresponding to:

$$= \frac{C_0}{C_1} + \frac{C_0}{C_2} \qquad \text{(A2.8.3)}$$

At *dc*, Y' can be written:

$$Y' = \frac{\frac{1}{R_1 R_2}\left(\frac{1}{R_1} + \frac{1}{R_2}\right)}{\left(\frac{1}{R_1} + \frac{1}{R_2}\right)^2} = \frac{1}{R_1 + R_2} \qquad \text{(A2.9.1)}$$

corresponding to the low frequency plateau observed in a plot of Y' vs ω. As ω increases and approaches ω_c, Y' increases to a high frequency plateau at frequencies > ω_d. As ω tends to ∞, Y' can be written:

$$Y' = \frac{\omega^2 [C_1 + C_2]\left(\frac{C_2}{R_1} + \frac{C_1}{R_2}\right)}{\omega^2 [C_1 + C_2]^2} = \frac{\frac{C_2}{R_1} + \frac{C_1}{R_2}}{C_1 + C_2} \qquad \text{(A2.9.2)}$$

$$\sim \frac{1}{R_1} \qquad \text{(A2.9.3)}$$

The high frequency plateau in *Y'* therefore corresponds to $1/R_1$. Similarly, at *dc* ε' can be written:

$$\varepsilon' = \frac{\omega C_0\left(\frac{1}{R_1}+\frac{1}{R_2}\right)\left(\frac{\omega C_2}{R_1}+\frac{\omega C_2}{R_2}\right)}{\omega^2 C_0{}^2\left(\frac{1}{R_1}+\frac{1}{R_2}\right)^2} = \frac{\frac{C_2}{R_1}+\frac{C_2}{R_2}}{C_0\left(\frac{1}{R_1}+\frac{1}{R_2}\right)} \qquad \text{(A2.10.1)}$$

$$= \frac{C_2}{C_0\left(1+\frac{R_1}{R_2}\right)} + \frac{C_2}{C_0\left(1+\frac{R_2}{R_1}\right)} \qquad \text{(A2.10.2)}$$

$$\sim \frac{C_2}{C_0} \qquad \text{(A2.10.3)}$$

Hence the low frequency plateau observed in ε' vs ω corresponds to C_2/C_0. As frequency increases from ω_b to ω_d, ε' decreases to a high frequency plateau. As ω tends to ∞, ε' can be written:

$$\varepsilon' = \frac{\omega^4 C_1 C_2 C_0 (C_1 + C_2)}{\omega^4 C_0 (C_1 + C_2)^2} = \frac{C_1 C_2}{C_0 (C_1 + C_2)}$$

$$\sim \frac{C_1}{C_0} \qquad \text{(A2.10.4)}$$

and so the high frequency plateau in ε' corresponds to C_1/C_0.

Having previously defined the characteristic frequencies of tan δ as ω_b and ω_d, the magnitude of tan δ at ω_b *and* ω_d can be determined. At ω_b, tan δ can be written:

$$\tan\delta_b = \frac{R_2 + \omega_b R_2{}^2 C_2}{\omega_b R_2{}^2 C_2} \qquad \text{(A2.11.1)}$$

$$\sim \frac{2}{\omega_b R_2 C_2} \quad \text{since } R_2 \sim \omega_b R_2{}^2 C_2 \qquad \text{(A2.11.2)}$$

$$= \frac{2(R_1 R_2)^{1/2}}{R_2} \tag{A2.11.3}$$

At ω_d, can tan δ can be written:

$$\tan \delta_d = \frac{R_1(\omega_d R_2 C_2)^2}{\omega_d R_2{}^2 C_2 + \omega_d R_1{}^2 C_1 (\omega_d R_2 C_2)^2} \tag{A2.11.4}$$

$$\sim \frac{R_1(\omega_d R_2 C_2)^2}{\omega_d R_2{}^2 C_2} \text{ since } \omega_d R_2{}^2 C_2 \sim \omega_d R_1{}^2 C_1 (\omega_d R_2 C_2)^2 \tag{A2.11.5}$$

$$= \frac{(C_1 C_2)^{1/2}}{2C_1} \tag{A2.11.6}$$